universität
wien

MASTERARBEIT / MASTER'S THESIS

Titel der Masterarbeit / Title of the Master's Thesis

„Cryovolcanism on Enceladus"

verfasst von / submitted by

Dipl.-Ing. Dr. Wolfgang Sakuler, BSc

angestrebter akademischer Grad / in partial fulfilment of the requirements for the degree of

Master of Science (MSc)

Wien, 2021 / Vienna, 2021

Studienkennzahl lt. Studienblatt / degree programme code as it appears on the student record sheet:	A 066 861
Studienrichtung lt. Studienblatt / degree programme as it appears on the student record sheet:	Masterstudium Astronomie UG2002
Betreut von / Supervisor:	Univ.-Prof. Dr. Maria G. Firneis

Contents

Acknowledgements

I would like to thank my supervisor Univ.-Prof. Dr. Maria Firneis for the useful comments, remarks and engagement through the creation process of this master thesis, and for carefully reading and examining the manuscript.

Furthermore, I am also deeply grateful to Dr. Ruth-Sophie Taubner for many discussions about my thesis and for her insightful comments and suggestions. In addition, I want to thank Dr. Johannes Leitner for offering me such an interesting topic of investigation. I would also like to thank Viktor Bauer, MSc, for establishing the contact to a private sponsor supplying computing time on a high-performance machine for test simulations at the beginning of this work.

Finally, I would like to thank my family and my friends, who encouraged and supported me the last couple of years.

List of Figures

List of Tables

1. Introduction

Enceladus, the tiny moon of Saturn is one of the most exciting objects in our Solar System, as NASA's Cassini spacecraft has detected an anomalously high heat flow around the south polar region, and a plume of water vapor and ice particles emerging from fractures in this area. [Porco *et al.*, 2006, Spencer *et al.*, 2006, Hansen *et al.*, 2006, Waite *et al.*, 2006]. At least 101 geysers that might be connected to jet curtains were identified by analysing Cassini's data erupting from the small moon [Porco *et al.*, 2014, Spitale *et al.*, 2015].

The discovery of these cryovolcanic geysers makes Enceladus the first icy moon exhibiting a confirmed ongoing geological activity[1]. Jets of gas and icy grains are ejected from the fractures on the surface, where the gas has velocities up to 1000 $\mathrm{m\,s^{-1}}$ [Hansen *et al.*, 2011], thus exceeding the escape velocity of Enceladus ($v_{\mathrm{esc}} = 239\,\mathrm{m\,s^{-1}}$ [NASA, 2013]). The detection of sodium-salt-rich ice grains in the plume leads to the assumption that these grains have originated from a liquid water reservoir which is in contact with the rocky core of Enceladus [Postberg *et al.*, 2009, 2011, 2018; Nimmo and Porco 2014]. There are indications that this liquid reservoir is a subsurface ocean that is 8-30 km thick [Hsu *et al.*, 2015, Thomas *et al.*, 2016] located under an ice mantle of 2-40 km thickness [Hsu *et al.*, 2015, Čadek *et al.*, 2016, Le Gall *et al.*, 2017]. First it was assumed that the reservoir is only located at the south polar region, but measurements of Enceladus' physical libration support the picture that the icy crust is completely decoupled from the rocky core, thus suggesting that the subsurface water reservoir might be actually a global ocean than a localized polar sea [Thomas *et al.*, 2016].

The cryovolcanic activity of Enceladus supplies the bulk amount of material in Saturn's E-ring [Kempf *et al.*, 2008]. This ring that is located between the orbits of the moons Mimas and Titan [Hedman *et al.*, 2012] is the widest and one of the outermost rings of Saturn, which consists of icy grains with a narrow size distribution. The E-rings's anomalous vertical structure [Hillier *et al.*, 2007] (its thickness increases with distance from Saturn, but it has a local minimum at the orbit of Enceladus) is caused by the plume dynamics of the icy particles from the localized south polar origin on Enceladus [Kempf *et al.*, 2008].

The plume is also the origin of neutral water molecules and their dissociation products in the inner magnetosphere of Saturn [Esposito *et al.*, 2005, Cassidy and Johnson, 2010]. Additionally it is a source of water group ions [Tokar *et al.*, 2006] and a sink of low-energy electrons in the magnetospheric plasma [Jones *et al.*, 2006], thus, is also responsible for basic characteristics of Saturn's magnetosphere.

The plume also affects the reflection properties of several moons of Saturn. Those satellites that are located within the E-ring, namely Mimas, Tethys, Dione, Rhea and Enceladus, are among

[1] Observations by the Galileo spacecraft and by the Hubble space telescope indicate that a potential plume might also exist on Jupiter's moon Europa [Cook *et al.*, 2013, Jia *et al.*, 2018].

the brightest objects of the Solar System [Verbiscer *et al.*, 2007].

The Cassini spacecraft detected complex organic molecules in the plume's ejected material [Postberg *et al.*, 2018]. This observation, in addition to the fact that liquid water exists, and the occurance of hydrothermal activity give indications that the subsurface ocean of Enceladus might be a potentially habitable environment for extraterrestrial life.

Though the Cassini mission has doubtlessly shown the existence of cryovolcanic activities, many detail questions are still open:

(i) The exact physical mechanism behind the plume is still an open issue. Several physical models and hypotheses have been devised to explain the plume's origin: (a) the 'Cold Faithful' model, which suggests a heavily boiling, near-surface liquid water reservoir [Porco *et al.*, 2006], (b) the 'Frigid Faithful' or 'Clathrate Reservoir' hypothesis, which assumes the degassing of clathrates [Kieffer *et al.*, 2006, Gioia *et al.*, 2007], (c) the 'Shear Heating' model, where it is supposed that plume particles result from direct sublimation from warm ice [Nimmo *et al.*, 2007], and (d) the 'Deep Source' model, which seems to be the most prominent hypothesis, that states that a gas-particle mixture originating at depth by evaporation from a liquid-water reservoir is flowing through cracks and fractures in Enceladus' ice crust [Schmidt *et al.*, 2008, Ingersoll and Pankine, 2010, Nakajima and Ingersoll, 2016a, Ingersoll and Nakajima, 2016b, Postberg *et al.*, 2018]. These models will be described in detail in section 4.2. Possibly it is not only one single model which gives the final answer since no single theory is able to fully explain all processes and characteristics but it seems more realistic that a combination of several hypotheses describes the underlying physics more comprehensively [Taubner, 2012].

(ii) Another interesting open question concerns the type of energy source that generates the plume. Cassini's data suggest that the total heat flow has to be about 4.7 GW [Spencer *et al.*, 2013b, Ingersoll and Pankine, 2010, Spencer *et al.*, 2018]. However, it seems unlikely that this amount of power originates from tidal forces only, because some studies claimed that the heat produced by tidal forces does not exceed 1.1 GW [Spencer *et al.*, 2013b]. The puzzle might be solved by asssuming that either heat production and/or heat release show episodic behavior but none of these assumptions could be confirmed.

(iii) The geometrical form of the geyser eruptions is also an issue which is currently not fully clarified. Some authors interpret Cassini's observations of the plume emanating from the south-polar terrain, informally called 'tiger stripes', as discrete, single jets [Spitale and Porco, 2007, Porco *et al.*, 2014], while another study indicates that the eruptive activity might be explained by broad, continuous curtain-like eruptions [Spitale *et al.*, 2015]. Possibly the ice-particle plume might consist of a combination of both continuous curtains and discrete jets as the authors of a recent review paper suggest [Spencer *et al.*, 2018].

(iv) Several questions about the exact flow dynamics in the cracks and fractures that represent vents in the ice crust remain unanswered. It is not fully clear which flow regimes the water vapour actually undergoes. Also the details how waves do propagate within the vapor flow are still not known, e.g. whether shock waves are produced, or how dispersion relations of acoustic and porosity waves look like.

The discovery of Enceladus' plume and its present day on-going geologic activity make Enceladus an outstandingly interesting research object for astrobiology. The detection of water, sodium salts, complex macromolecular organic material [Waite *et al.*, 2017, Postberg *et al.*, 2018], nitrogen-bearing, oxygen-bearing, and aromatic low-mass organic compounds, which are ingredients of amino acids [Khawaja *et al.*, 2019], together with the strong indication of the existence of a subsurface liquid reservoir that is in contact with a warm rocky core raises Enceladus to a highly promising potential candidate for extraterrestrial life. Reactions on the bottom of Enceladus' subsurface ocean might be akin to the water/rock reactions that take place on Earth at hydrothermal vents located at sea ground. Hydrothermal vents and the chemical reactions occuring in their vicinities are considered as one possible explanation of the origin of life on Earth. Following this theory of a chemosynthetic origin of life, basically developed by Wächtershäuser (1992), it is assumed that life began on the surface of iron sulphides close to hydrothermal vents at high pressure and temperatures. Translating this hypothesis to Enceladus, it is imaginable that chemotrophic microorganisms might exist at the bottom of the subsurface ocean.

In this thesis the water vapor flow through the cracks and fractures within the ice mantle connecting the subsurface ocean to the surface is analysed via numerical simulations of the 2-dimensional and 3-dimensional Navier-Stokes equations that describe the motion of viscous fluid substances [Landau and Lifshitz, 1966]. The distributions of pressure and the 2-dim/3-dim velocity vector field inside the cracks have been computed for several vent channel structures. A finite element approach has been applied for constructing the geometries of the fractures. For the numerical simulations the open-source computing platform FEniCS (Finite Element Computational Software) has been employed ["FEniCS Project", Alnaes *et al.*, 2015, Logg *et al.*, 2012]. Simulations have been performed for different crack lengths and widths, and for various vent geometries, ranging from simple rectangles (2-dim) and cylinders (3-dim), up to more complicated structures with varying crack widths including throats, discontinuities, kinks (both 2-dim and 3-dim), zig-zag lines, and forking branches (in 2-dim).

A question which is also addressed in this treatise is which crack width and depth combinations produce physically reasonable situations where freezing inside the channel is avoided such that the water vapour flow can reach the moon's surface. For that purpose the heat loss along a crack vent within the ice mantle has been analysed. The thermodynamics in the ice channel is investigated considering a simple model of a cylindrical hollow pipe of length L and radius r surrounded by an infinitely extended block of ice. Differential equations are constructed for the temperature distribution $T(z)$ and solved for different boundary conditions. The effects on a gravitational term and additional external pressures are examined.

2. Enceladus

2.1 Basic Facts

Enceladus is the fourteenth and sixth-largest of the 62 known moons of Saturn, and one of the five mid-sized satellites, Mimas, Enceladus, Tethys, Dione, and Rhea (in order of increasing distance from the planet). It is about 500 km in diameter, so it is only approximately one-seventh the diameter of Earth's moon [Thomas *et al.*, 2007, Thomas, 2010]. The surface is mostly covered by clean, fresh ice, which is the reason for the large Bond albedo of 0.81. Since this number is one of the largest albedo values measured in the Solar System, Enceladus probably has the most reflective surface of any Solar System object. Basic orbital and physical characteristics of Enceladus are shown in Table 2.1.

The moon Enceladus was discovered on August 28, 1789 by Sir William Herschel with his new 1.2 m telescope during its first usage (this was worldwide the biggest telescope at that time) [USGS, 2015, Herschel, 1790, Herschel, 1795]. Though Enceladus is one of the brightest objects of the Solar System, the glare light of Saturn and its rings outshine the small satellite, thus, requiring a telescope with a larger diameter. The observations took place during the equinox of Saturn, when Earth is within the ring plane, resulting in a decrease of dazzling light, what makes the moon easier to observe.

Saturn's moons went nameless for many years. They were given just numerical names, based on their distance from the planet, Enceladus was called 'Saturn II'. It was John Herschel, the son of William Herschel, who suggested in his 1847 publication "Results of Astronomical Observations made at the Cape of Good Hope" that the satellites of Saturn be named after the giants of the Greek mythology, 'Titans' and 'Giants' [USGS, 2015]. These names were choosen by Herschel since Saturn (in Greek mythology Cronus) was the leader of the Titans (the two giant generations, 'Titans' and 'Giants', are often confused in the literature, e.g. Enceladus is a Giant, but Hyperion, Iapetus, Rhea, Tethys, Theia are Titans).

Herschel called the moon after the Giant Enceladus, who in Greek mythology is the offspring of Gaia (Earth) and Uranus (Sky), born from the blood that fell to Earth (fertilizing Gaia) when Uranus was castrated by their son Cronus (known to the Romans as Saturn). The Giant Enceladus was the opponent of Athena, Zeus, and Dionysos during the Gigantomachy, which was the war between the Giants and the Greek gods. According to the legend he was defeated by Athena, and she buried him alive under Mount Etna in Sicily. When volcano Etna erupted, it was considered to be the breath of Enceladus.

Geological features on the moon are named by the IAU (International Astronomical Union) after places and characters from the collection of West and South Asian stories known as "The Book of One Thousand and One Nights". Impact craters are named after the characters, whereas features, such as fossae, dorsa, planititiae, sulci, etc., are named after the places of the book, e.g. 'Aladdin' and 'Ali Baba' are the names of craters on the northern hemisphere, and the famous sulci in the the south pole region, unofficially called 'tiger stripes', where the plume emerges, are officially named 'Alexandria Sulcus', 'Cairo Sulcus', 'Baghdad Sulcus' and 'Damascus Sulcus'.

2.2 Space Missions to Enceladus

2.2.1 Voyager Spacecrafts

The mission of the two Voyager spacecrafts, Voyager 1 and Voyager 2, that were launched in 1977, was to study the planetary systems of Jupiter and Saturn. Before the Voyager mission not much was known about the tiny moon Enceladus because of its relative close orbit to Saturn. At that time only some basic physical properties of Enceladus could be estimated, like the total mass, the orbital characteristics, the bulk density, and its large albedo. However, due to measurements in the near-IR astronomers were fully aware that Enceladus' surface consists mainly of H_2O ice [Orton *et al.*, 2009].

The voyager spacecrafts encountered Enceladus in 1980 and 1981. They revealed Enceladus' extraordinary high albedo (0.81 bond albedo), which is probably the largest of any object in the Solar System, and its heterogenous surface terrains, that range from old, strongly cratered areas located at higher latitudes to young, tectonically distorted regions nearer to the equator [Smith *et al.*, 1982].

Ground-based observations have shown at that time that Saturn's E-ring was located around the orbit of Enceladus [Baum *et al.*, 1981]. The E-ring is an exceedingly wide and second-outermost ring of Saturn, located between the orbits of the moons Mimas and Titan. Mathematical models have shown that the lifetime of the μm-sized E-ring particles is rather short, resulting in an estimated lifespan of the E-ring between 10.000 and 1.000.000 years [Vittorio, 2006]. Thus, the E-ring has to be continously fed by particles to guarantee its stability. It was considered by several authors that geological activities on Enceladus were a possible source of these particles [Haff *et al.*, 1983, Pang *et al.*, 1984]. This view was additionally supported by the discovery of the neutral OH cloud by the Hubble Space Telescope in the 1990s [Shemansky *et al.*, 1993]. Therefore Enceladus was a high-priority target for a forthcoming project, the Cassini mission.

2.2.2 Cassini Spacecraft

The Cassini-Huygens mission, which was a joint program involving NASA, the European Space Agency (ESA), and the Italian Space Agency (ASI), was launched in October 1997 with the objective to explore the planet Saturn, its rings, and its moons. Cassini's scientific instruments and their particular jobs are described in Table 2.2. The spacecraft entered the Saturn orbit on July 1^{st}, 2004. Among the nine planned flybys of Saturn's satellites the prime mission included four flybys of Enceladus [ESA, 2019]. A list of all Enceladus flybys of the prime mission and the extended missions is shown in Table 2.3. The geometry of the closest flybys is depicted in Figure 2.1.

An important scientific discovery was done even before the spacecraft entered Saturn's orbit: observations with the UVIS (Ultraviolet Imaging Spektrograph) instrument revealed neutral O emission concentrated near Enceladus' orbit [Esposito *et al.*, 2005] which completed the previously detected neutral OH emission.

On February 17th 2005 the first close encounter took place at a minimum distance of 1260 km [Spencer *et al.*, 2009]. The flyby on July 2005 revealed the cryovolcanic active nature of Enceladus: the CIRS instrument detected anomalous thermal emission from the south polar area [Spencer *et al.*, 2006] located at the position of four prominent fractures, called the "tiger stripes" (see Figure 2.2 where an image taken by the ISS cameras is shown [Porco *et al.*, 2006]). The closest approach occurred on October 9th 2008, where the spacecraft flew over the moon at a minimum altitude of only 25 km. The closest flyby over the south pole terrain, which is the area of highest interest, took place on March 27th 2012, at a distance of 74 km.

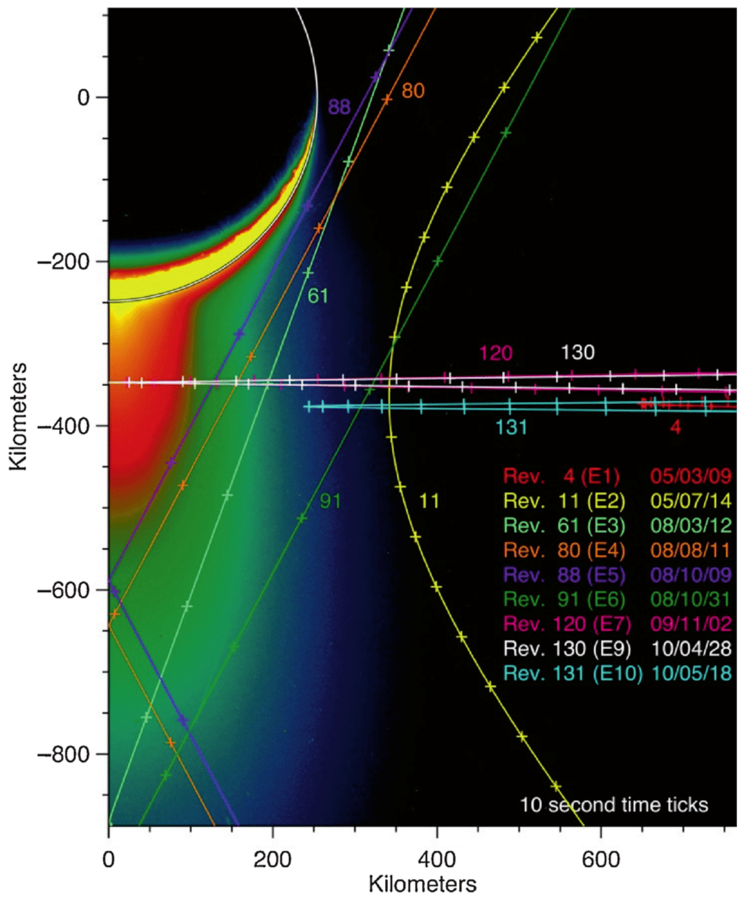

Figure 2.1: The paths of Cassini's nearest Enceladus flybys during Prime and Equinox mission are shown with respect to the south polar plume. The plume picture (taken on April 24th 2007) is expanded logarithmically.

Source: J.R. Spencer, *et al.*, 2009, *"Enceladus: An Cryovolcanic Satellite"* [Spencer *et al.*, 2009].

Cassini's INMS instrument detected a cloud of water vapor over the south polar region, and resolved a few percent of CO_2, CH_4, CO, and/or N_2 [Waite *et al.*, 2006]. At the same time another Cassini instrument, the CDA, measured a large amount of dust grains above the south pole [Spahn *et al.*, 2006]. Direct high resolution images of the dust plume were then taken by the ISS instrument on November 27th 2005, where several single jets could be resolved [Porco *et al.*, 2006]. Thus, it was obvious that there was indeed some cryovolcanic activity at the south pole area where

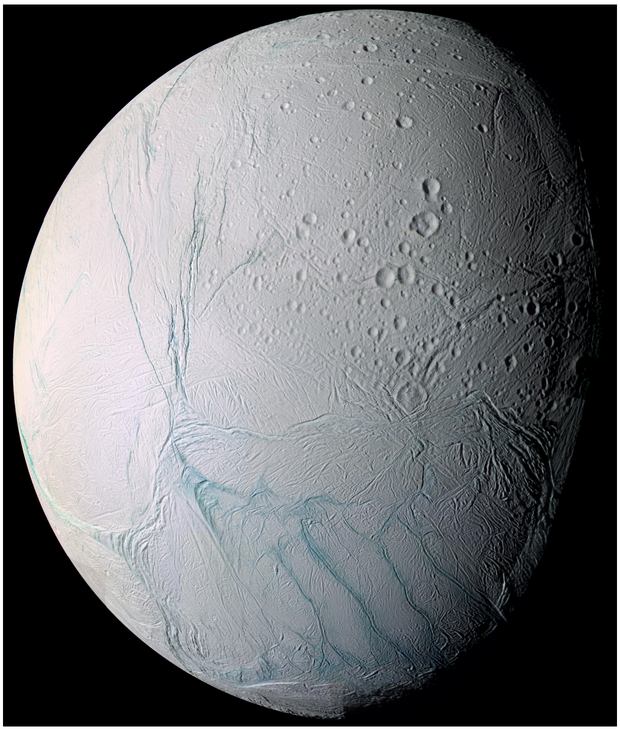

Figure 2.2: Global picture of Enceladus (in false colors) taken by the ISS cameras at the flyby on July 14$^{\text{th}}$ 2005. The four active "tiger stripe" fractures located at the lower part around the south pole are clearly seen as blue-green lines.
Source: NASA/JPL/SSI PIA06254, https://photojournal.jpl.nasa.gov/jpeg/PIA06254.jpg (accessed on July 27$^{\text{th}}$, 2021)

a plume of water vapor and ice grains, and other gases was erupting.

At a very close flyby on March 2008 the spacecraft penetrated the plume deeply and performed measurements with the INMS instrument of the gas composition, and with the CIRS instrument the thermal emission along the tiger stripes were viewed at high resolution [Spencer *et al.*, 2009].

After the original prime Cassini program two extended missions followed: the first extended mission was the "Equinox Mission" from mid-2008 to -2010, where Cassini performed seven additional close flybys, that included also flights through the plume.

Basic goals of this extended mission were [Seal and Buffington, 2009, Taubner, 2012]:

- retrieve a global map of Enceladus with a high resolution to get more insights into global tectonics and geological features,
- view the South Polar Terrain, especially the "Tiger Stripes" at very high resolution,
- perform high resolution IR measurements of hot spots to get a better understanding of the endogenous activity of Enceladus,
- investigate the dust and gas composition of the plume in more detail, and analyse its temporal changes,
- explore the gravity field during close passes to be able to gain deeper knowledge concerning the moon's internal composition and differentiation, and
- study the interplay between Enceladus, its plume, and its magnetic field.

The second extended mission was the “Solstice Mission” which lasted till September 2017, after the Saturnian northern summer solstice (which occurred in May 2017). This extension included twelve additional Enceladus flybys.

Objectives of this second extended mission were [Spilker, 2009, Taubner, 2012]:

- study the temporal variability of Enceladus' cryovolcanic activity, to get a deeper insight at which time scales (from hours to decades) the activities are changing and evolving,
- get a more detailed mapping of Enceladus' gravitational field to unveil the interior structure,
- trying to detect an intrinsic or induced magnetic field,
- perform additional plume penetrating close flybys to determine the composition of the plume's dust and gases [Waite *et al.*, 2008],
- get a detailed high resolution map of the surface thermal radiation, and
- detailed imaging of the surface and the plume.

The Cassini mission ended on September 15$^{\text{th}}$ 2017, when the spacecraft plunged into Saturn's atmosphere along a controlled de-orbiting trajectory.

2.3 Internal Structure and Composition

Enceladus has a bulk density of about 1.609 kg/m^3 [Porco *et al.*, 2006, Jacobson *et al.*, 2006, Taubner, 2012], which is larger than Saturn's other mid-sized icy moons, implying that it consists of ice and silicates, possibly also iron. The silicate rock fraction is higher than previously thought. Based on Cassini's observations and numerical simulations of Enceladus' thermal evolution it can be assumed that Enceladus is a differentiated body with a rocky core with a rock mass fraction of approx. 50-60 %, surrounded by an icy mantle [Schubert *et al.*, 2007], see Figure 2.3. According to the model of Schubert et al. (2007) differentiation took place early in the first million years after Enceladus' formation due to melting of ice by radiogenic heating (short-lived radioactivity, e.g. decay of ^{26}Al). When this phase ended (10-20 Myr after the formation of Enceladus), Enceladus was differentiated into a hot rocky core of about 150-170 km, a liquid water layer approximately 70 km thick, and a covering ice shell. In the two-layer model the density of the silicate core ranges from 2200 to 2500 kg/m^3, and the surface layer density is about 900-950 kg/m^3 [Nimmo and Porco, 2014]. The outer H_2O layer which consists mainly of ice may be partly liquid representing an ocean that seems to be a global one as recent studies suggest, which can be regarded as a third layer. [Nimmo and Pappalardo, 2006,Barr and McKinnon, 2007,Schubert *et al.*, 2007,Thomas *et al.*, 2016].

Estimations of the global mean thickness of the ice layer range between approxinately 20 and 100 km, where 'older' papers give higher values of about 50-100 km [Schubert *et al.*, 2007, Rappaport *et al.*, 2007], wheras more recent studies, based on gravity field measurements, libration data, and radar data, indicate that the ice mantle thickness might be somewhat smaller. The more realistic values are within a range of about 20-60 km [McKinnon, 2015, Thomas *et al.*, 2016, Kamata and Nimmo, 2017, Čadek *et al.*, 2016, Le Gall *et al.*, 2017]. In the vicinity of the South polar terrain, where temperature hot-spots are located, the ice shell might be even thinner, in the current literature values can be found ranging between 1.5 and 23 km, see Figures 2.4 and 2.5. An overview of the estimated ice shell thickness at the SPT given by different authors is shown in Table 2.4.

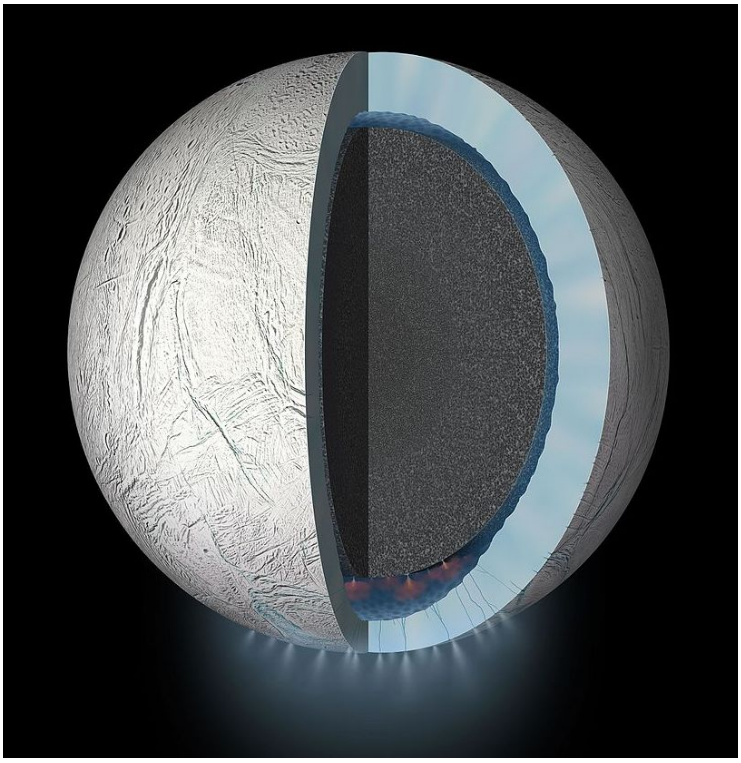

Figure 2.3: The illustration shows the interior of Enceladus with its three layer structure: the silicate rocky core (dark grey), the subsurface ocean (dark blue), and the water-ice-rich mantle (light blue); a plume is shown under the south pole.
Source: NASA/JPL, https://photojournal.jpl.nasa.gov/catalog/PIA20013 (accessed on July 27^{th}, 2021).

2.3.1 Subsurface Ocean

From gravity and topography data it can be concluded that a subsurface water reservoir under the South polar terrain (SPT) exists, or a global subsurface ocean that is thicker in the vicinity of the SPT [Nimmo and Porco, 2014, McKinnon, 2015, Thomas *et al.*, 2016, Kamata and Nimmo, 2017, Čadek *et al.*, 2016, Le Gall *et al.*, 2017, Beuthe, 2018]. Strongest indicator for the existence of an subsurface ocean is the active plume: a portion of the plume's icy particles are rich in NaCl, with a salt content comparable to the Earth's oceans [Postberg *et al.* 2009, 2011, 2018; Nimmo and Porco 2014], thus, it is assumed, that a subsurface salty liquid reservoir, either a local sea or even a global subsurface ocean, which is in direct contact with the silicate core, is the source of the plume [Spencer *et al.*, 2009]. The Cassini spacecraft also detected traces of organic compounds in the dust grains of the plume. Originally, only simple organic compounds (masses < 50 atomic mass units) have been observed [Waite *et al.* 2006, 2009; Postberg *et al.* 2009], however, a more recent study reports about observations of more complex macromolecular organic compounds with masses greater than 200 atomic mass units [Postberg *et al.*, 2018]. A more extensive compositional analysis of CDA mass spectra from organic-containing ice particles has been performed in a very recent study where spectral characteristics of low-mass nitrogen-bearing, oxygen-bearing, and aromatic organic compounds have been found [Khawaja *et al.*, 2019]. This compounds could be possible prerequisites for mineral-catalysed hydrothermal synthesis (Friedel-Crafts synthesis, [Friedel and Crafts, 1877]) of biologically substances at the warm ground of Enceladus' subsurface ocean.

The gravimetric measurements from Cassini's December 2010 flybys indicated that there might exist a liquid water ocean beneath the ice layer [Platt and Bell, 2014, Witze, 2014, Iess *et al.*, 2014]. It was assumed at that time that the subsurface ocean was located around the south pole only having a maximum depth of about 8-10 km [Hsu *et al.*, 2015].

But data obtained from libration measurements suggest that the icy crust is decoupled from the rocky core, thus favoring a global ocean having a depth about 26-31 km [Thomas *et al.*, 2016, Beuthe, 2018].

Cassini's CDA instrument detected nanometer-sized grains in the plume containing a large amount of silicon, which is most probably SiO_2 [Hsu *et al.*, 2015]. Composition and size of these particles indicate that their origin are hydrothermal activities within Enceladus which further supports the assumption that a liquid water reservoir that is in contact with the rocky core is the source for the plume [Hsu *et al.*, 2015, Spencer *et al.*, 2018]. The existence of the nanosilica particles constrains the conditions of the subsurface ocean to moderate salt content, an alkine pH value, and a rather warm temperature ($T \gtrsim 90°$ at the core-ocean interface) [Hsu *et al.*, 2015, Sekine *et al.*, 2015, Spencer *et al.*, 2018]. High alkine pH values of about a maximum 11-12 [Glein *et al.*, 2015] could be interpreted as an effect of serpentinization of chondritic rock where molecular hydrogen is produced, which serves as geochemical energy source feasable to synthesize (either abiotically or even biologically) organic molecules like the compounds that have been observed in the plume.

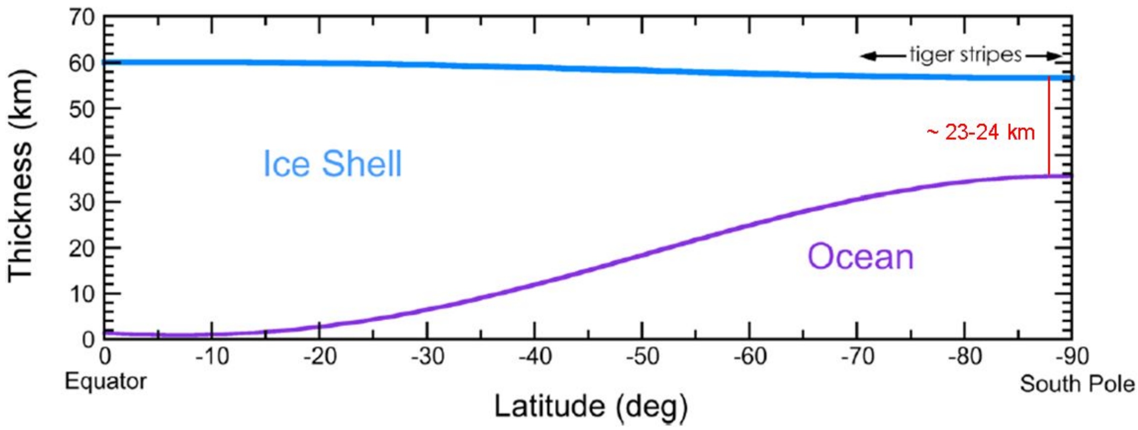

Figure 2.4: The ice shell/ocean thickness as function of latitude. The ice shell/ocean becomes thinner/thicker in the vicinity of the south polar terrain.
Source: adapted from Mc Kinnon, 2015, *"Effect of Enceladus's rapid synchronous spin on interpretation of Cassini gravity"* [McKinnon, 2015].

2.3.2 South Polar Terrain

The South Polar Terrain (SPT) is a region surrounding Enceladus' south pole, ranging up to 60° south latitude, having an area of the size of approx. 70 000 km^2 [Porco *et al.*, 2006]. This region represents a tectonically deformed area, which is covered by tectonic fractures and ridges [Porco *et al.*, 2006, Spencer *et al.*, 2009]. It has only a smaller number of considerable impact craters, which indicates that it is the youngest region on Enceladus' surface [Porco *et al.*, 2006].

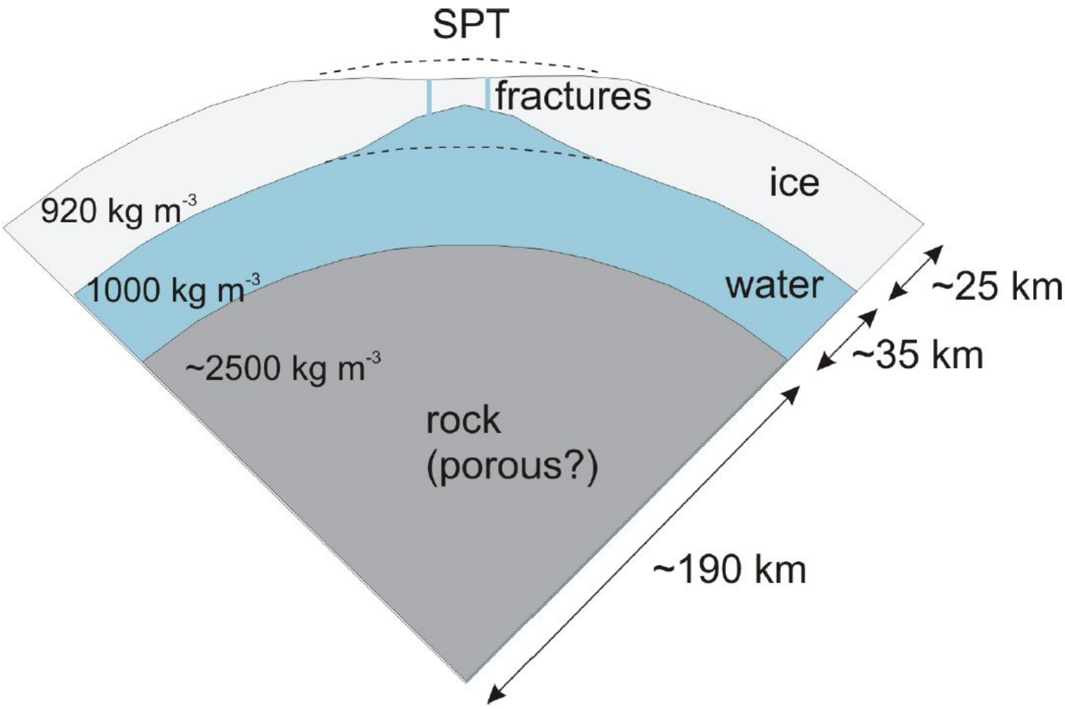

Figure 2.5: Enceladus' likely internal structure derived from gravity, topography and libration data. The ice shell thickness is reduced around the South Polar Terrain (SPT).
Source: F. Nimmo, *et al.*, 2017, *"The thermal and orbital evolution of Enceladus: observational constraints and models"* [Nimmo *et al.*, 2017].

The SPT is a geologically active area that stands out due to tectonically disrupted features and its unusual high albedo.

The edge of the south polar area is characterized by a structure of parallel, Y- and V-shaped ridges, edges and valleys [Porco *et al.*, 2006, Konstantinidis *et al.*, 2015, Giese *et al.*, 2017]. These tectonic structures and their detailed shapes, locations, and orientations might have been created by changes in the global shape of Enceladus, and could be interpreted as fold belts produced by horizontal compression [Porco *et al.*, 2006].

The most striking feature of the South Polar Terrain is a group of four fractures bounded by ridges, which are (unofficially) called "Tiger Stripes". These fractures are characteristically "about 500 m deep, 2 km wide, and 130 km in length, flanked on both sides by prominent 100-m-high ridges" [Porco *et al.*, 2006, Spencer *et al.*, 2009]. They were discovered by Cassini's Imaging Science Subsystem (ISS) camera on May 20$^{\text{th}}$ 2005. The four main Tiger Stripes are called "Alexandria Sulcus", "Baghdad Sulcus", "Cairo Sulcus", and "Damascus Sulcus", see Figure 2.6.

Data obtained from Cassini's Composite Infrared Spectrometer (CIRS) showed that the SPT is a hot spot area, see Figure 2.7 (mean temperature of about 85 K, the hottest SPT locations have temperatures between 114 and 157 K [Porco *et al.*, 2006]). This observation was very surprising since it was expected that the temperatures on Enceladus should be generally low (the estimated temperatures for the SPT had been ~ 68 K), and it was assumed that the temperatures around the poles are lower than at the equatorial zone (as on planets like Earth). These anomalous thermal emissions correlate with the location of the "Tiger Stripes". The SPT seems to be the thinnest

Figure 2.6: The four “Tiger Stripes” located at the South Polar Terrain.
Source: https://skyandtelescope.org/astronomy-news/how-moon-enceladus-got-its-stripes/ (accessed on July 27^{th}, 2021).

region of Enceladus' lithosphere and the Tiger Stripes might be the connection to the subsurface liquid reservoir [Collins and Goodman, 2007], the assumed ice-shell depth is about 1.5-23 km [McKinnon, 2015,Thomas *et al.*, 2016,Kamata and Nimmo, 2017,Čadek *et al.*, 2016,Le Gall *et al.*, 2017].

Thus, observations by Cassini made definitively clear that the Tiger Stripes are the origin of both the anomalous thermal emissions [Spencer *et al.*, 2006, Spencer and Nimmo, 2013a, Spencer *et al.*, 2018], see Figure 2.8, and the plume jets [Spitale and Porco, 2007, Porco *et al.*, 2014, Spitale *et al.*, 2015, Helfenstein and Porco, 2015, Spencer *et al.*, 2018], see Figure 2.9. The fractures are visible as dark linear patterns within the Tiger Stripes, but their internal structure cannot be resolved at Cassini ISS pictures since the highest possible resolution of this instrument is ∼10 m/pixel.

The water vapor and ice-particle plume consists of continous curtains [Spitale *et al.*, 2015] and at least 100 single jets [Porco *et al.*, 2014]. Exact positions on the surface of the origin of the discrete jets are generally not quite clearly detectable on the ISS images of the Tiger Stripes, some jet source locations might be related to local tectonic patterns, like cross-cutting fractures, ridges and grooves [Helfenstein and Porco, 2015, Spencer *et al.*, 2018]. Though the (spatially integrated) whole plume as such is clearly tidally modulated, some individual jets show timely variations that are not synchronous to the tidal oscillations of the whole plume [Porco *et al.*, 2014].

2.4 Thermal emissions

The total heat flow emerging from the Tiger Stripe region is an important geophysical parameter. However, it has turned out that it is very difficult to determine this quantity precisely. First calculations based on least square fits of CIRS data to blackbody curves, obtained for the complete south polar troughs at a wave number range of 600-1100 cm^{-1} in 2005, gave a heat flow of 5.8 ± 1.9 GW [Spencer *et al.*, 2006]. A subsequent study, which uses integrated data at lower wave number

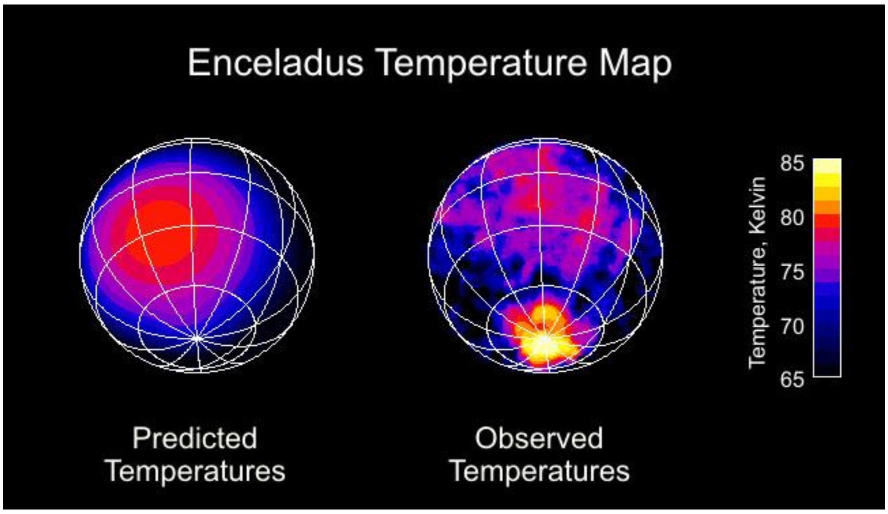

Figure 2.7: Temperature map of Enceladus (data taken by Cassini's CIRS instrument at $\lambda \sim 9 - 16.5\mu$m on July 14^{th}, 2005).

Source: NASA/JPL/GSFC, Photojournal: PIA06432, https://solarsystem.nasa.gov/resources/12631/enceladus-temperature-map (accessed on July 27^{th}, 2021).

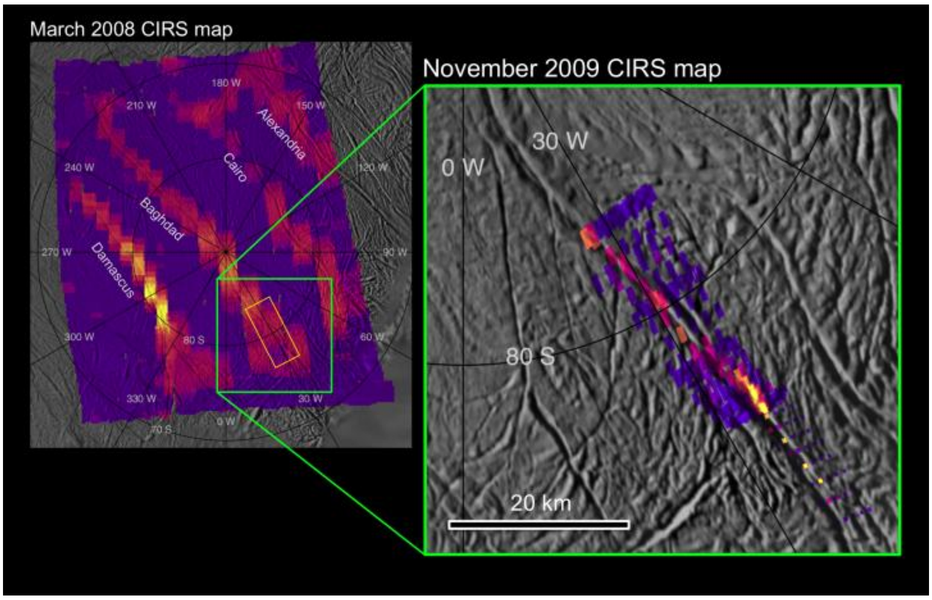

Figure 2.8: Heat maps of the South Polar Terrain (SPT) obtained by Cassini's CIRS instrument. The left-hand picture taken on March 2008 shows that the anomalous larger temperatures are located along the Tiger Stripes. The zoomed image on the right-hand side was taken during the November 21^{st} 2009 flyby and show very nicely that the highest temperatures are confined to a narrow region, which almost perfectly agrees with the position of the Baghdad Sulcus.

Source: NASA/JPL/GSFC, Photojournal: PIA12448, https://photojournal.jpl.nasa.gov/catalog/PIA12448 (accessed on July 27^{th}, 2021).

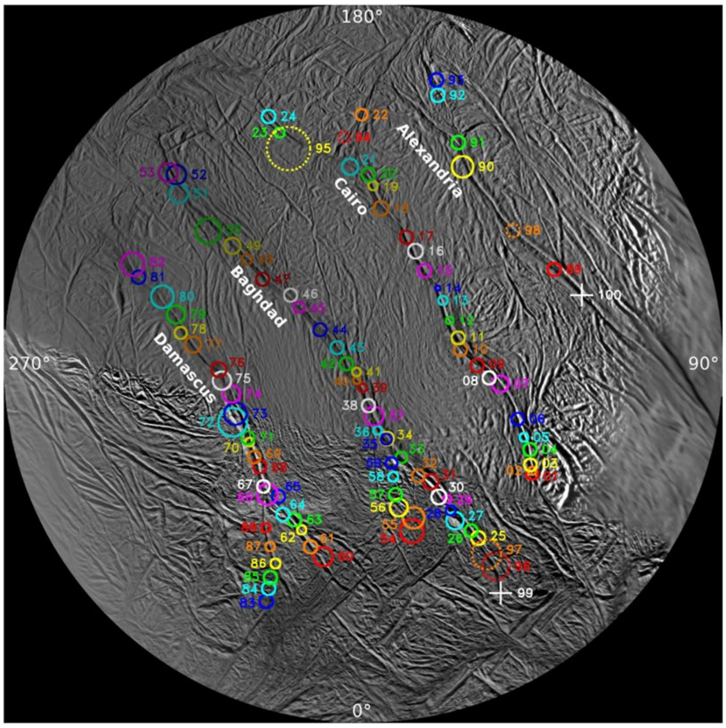

Figure 2.9: Polar stereographic basemap of Enceladus' South Polar Terrain (SPT) on which the locations of 100 plume jets are marked (color symbols).
Source: C. Porco *et al.*, 2014, *"How the Geysers, Tidal Stresses, and Thermal Emissions across the South Polar Terrain of Enceladus are related"* [Porco *et al.*, 2014].

10-600 cm^{-1}, produced a much higher heat flow value of 15.8 ± 3.1 GW [Howett *et al.*, 2011]. In that work a model-dependent subtraction of the "passive" component from reradiated sunlight has been performed. It seems likely that the "passive" contribution was underestimated in the employed model, which resulted in a value high above the (unknown) true value. In a more recent analysis higher spatial resolution data were used, and it produced a Tiger Stripe radiated heat flow of 4.2 GW [Spencer *et al.*, 2013b]. This value contains a passive contribution caused by reradiation of solar heat absorbed by the thermally anomalous areas ("thermal pedestal effect" [Veeder *et al.*, 1994]), which is in the order of $\sim$ 0.1 GW and has to be taken into account as correction from the total heat. Enceladus' power output also includes the latent heat of the escaping plume, which is $\sim$ 0.5 GW [Ingersoll and Pankine, 2010, Spencer *et al.*, 2018] and must be added to the 4.2 GW, thus giving a total heat generated output of $\sim$ 4.7 GW [Spencer *et al.*, 2013b, Ingersoll and Pankine, 2010, Spencer *et al.*, 2018]. This seems now to be a more realistic number, and it represents the currently accepted value within the scientific community.

Several mechanisms have been proposed for being responsible for the production of Enceladus' heat flow [Lissauer *et al.*, 1984, Wisdom, 2004, Spencer *et al.*, 2009, Schubert *et al.*, 2010]:

- Tidal Heating
- Radioactive Heating
- Chemistry

- Episodic Heat Release
- Episodic Heat Generation
- Spin-Orbit Libration.

The primary power source on Enceladus might be highly probably tidal heating. However, a study guesses that the expected heat, if created by tidal forces, cannot be larger than 1.1 GW [Spencer *et al.*, 2013b], and this is far smaller than the 4.7 GW, that were computed based on Cassini's data. The observed heat flow of 4.7 GW cannot be explained exclusively from tidal forces, thus the major origin of the heat remains a puzzle.

2.4.1 Tidal Heating

Tidal heating occurs when a satellite is in an eccentric orbit, since part of the mechanical energy related to the changing amplitude and location of the tidal bulge is transformed into heat [Spencer *et al.*, 2009]. Some problems arise when trying to apply this definition to Enceladus: (i) Tidal forces usually act symmetrically but on Enceladus cryovolcanic eruptions only occur in the SPT, no current activity has been detected in the north polar region [Schubert *et al.*, 2010]. However, a recent study indicates that there might have been some activity even on the northern hemisphere in the past [Robidel *et al.*, 2020]. (ii) Another problem arises when one compares Enceladus with Mimas. Tidal heating should be somewhat greater on Mimas than on Enceladus, since Mimas has a smaller distance to Saturn and also a larger eccentricity [Schubert *et al.*, 2010]. However, Mimas is strongly cratered and doesn't exhibit any cryovolcanism, thus, Enceladus must have an extra heat production mechanism, or these two moons had different initial conditions which caused them to evolve to very distinct final stages.

Currently Enceladus is in a 2:1 mean motion resonance with Dione [Murray and Dermott, 1999, Spencer *et al.*, 2009], i.e. Enceladus is performing two orbits of Saturn while Dione is completing one orbit. This resonance maintains Enceladus' non-zero eccentricity of $e = 0.0047$, that causes the tidal deformations.

A theory suggests that Enceladus might have migrated and increased the distance to Saturn [Schubert *et al.*, 2010]. During the movement Enceladus may have met resonant orbits with other Saturnian moons before it got locked to the present resonance with Dione [Meyer and Wisdom, 2007].

Another proposed mechanism assumes that before obtaining the resonance with Dione, Enceladus' was in a stable 2:1 mean-motion resonance with Saturn's moon Janus. The resulting angular momentum transfer could have sufficiently enhanced the eccentricity of Enceladus' orbit, that would lead to a heat production of about 4.5 GW [Lissauer *et al.*, 1984]. However, as was shown later, the model has some limitations [Peale, 2003], namely the resonance with Janus might have existed only for a certain period in the past, but on Enceladus several resurfacing episodes seem to have occurred, whereas the assumed resonance with Janus might only explain the most recent activity [Meyer and Wisdom, 2007]. Additionally a mass was assumed which was too high, thus, the heat production value resulting from a hypothetical Enceladus-Janus resonance has to be reduced accordingly.

The resonance model [Lissauer *et al.*, 1984] has been extended by adding other resonance combinations which could be responsible for the various resurfacing events on Enceladus [Meyer and Wisdom, 2007]. Four possible principal Enceladus-moon resonances could have occured in recent past:

3:2 Mimas-Enceladus, 4:3 Enceladus-Tethys, 2:1 Enceladus-Dione, and 2:1 Janus-Enceladus. Employing the formulae for the estimations of the equilibrium heat production rates as given in Meyer and Wisdom (2007), Taubner calculated the equilibrium heat production rates for the various Enceladus-moon resonances in her master-thesis [Taubner, 2012]. The values she obtained are smaller than the heat flux of 4.7 GW that was computed by Spencer *et al.* (2013), see Tab 2.5. Thus, it is obvious that equilibrium heating by tidal forces cannot be alone responsible for the heat flux observed by Cassini.

Though it is believed that tidal heating is highly probably the primary heat source for Enceladus, many issues, e.g. the exact value, and the time history of the heat source, and the position and type of the dissipation, are still not fully clear [Spencer and Nimmo, 2013a]. Enceladus has a differentiated structure, so tidal dissipation can occur in principle in the solid shell, the subsurface ocean, or the ice mantle, or in a combination/all of these locations.

The energy dissipation rate due to tidal heating is given by following relation [Peale and Cassen, 1978, Spencer *et al.*, 2009, Spencer and Nimmo, 2013a, Nimmo *et al.*, 2017]:

$$\dot{E} = \frac{21}{2}\frac{k_2}{Q}\frac{R_e^5\, G\, M_\mathrm{P}^2\, n}{a^6}\, e^2 \quad , \tag{2.1}$$

where G is the gravitational constant, M_P is the mass of Saturn, $n = 2\pi/P$ is the mean motion, P is the orbital period, a is the semimajor axis, R_e is the moon's radius, e is the moon's eccentricity, k_2 is the tidal Love number, which characterizes the flexing response of the moon to the tidal interaction, and Q is the dimensionless dissipation factor. The ratio k_2/Q indicates how the interior of the satellite reacts to the tidal forces, it strongly depends on the satellite's internal structure [Nimmo *et al.*, 2007, Nimmo *et al.*, 2017]. Bodies that are very elastic and dissipative have large k_2/Q values.

Evaluating equation 2.1 for Enceladus yields [Spencer and Nimmo, 2013a],

$$\dot{E} = 15\,\mathrm{GW}\left(\frac{k_2/Q}{0.01}\right)\left(\frac{e}{0.0047}\right)^2 \quad . \tag{2.2}$$

Isolated satellites in an eccentric orbit experience diurnal tides that dissipate energy internally causing the orbit to circularize in time. Thus, isolated moons are expected to evolve to a stage of near-zero eccentricity.

However, the situation changes when two satellites are in an eccentricity-type mean-motion resonance (MMR), like the Enceladus-Dione 2:1 MMR. Eccenticity growth due to the MMR competes with the circularization effect. If the satellites reach an equilibrium state such that the eccentricity remains constant an important result arises: the heat production rate is independent of the ratio k_2/Q, i.e. it is independent of the satellite structure. For Enceladus the equilibrium heat production can be readily calculated [Meyer and Wisdom, 2007], and is given by

$$\dot{E}_\mathrm{eq} = 1.1\,\mathrm{GW}\left(\frac{18\,000}{Q_p}\right) \quad . \tag{2.3}$$

Assuming that the time-averaged Q of Saturn exceeds 18 000 [Meyer and Wisdom, 2007], then the highest possible value of the (time-averaged) heat power of Enceladus caused by tidal dissipation is 1.1 GW. This is definitively smaller than the currently determined heat flow of 4.7 GW.

There are three+ possible solutions to this 'tidal heat production' problem [Nimmo *et al.*, 2017]:

1. Tidal heating on Enceladus is periodic, and Enceladus is currently generating heat to a larger amount than what is expected for the equilibrium case,

2. Enceladus creates heat at the equilibrium rate, but releases it episodically, or

3. $Q \ll 18\,000$ at this point in time.

The idea that Enceladus could produce heat episodically was investigated by Meyer and Wisdom (2008), and they concluded that such a scenario seems to be unlikely. However, a more recent study, which uses a slightly different approach, shows that for some parameter combinations, periodic heating could be possible [Shoji *et al.*, 2014, Nimmo *et al.*, 2017]. In Figure 2.10 a possible episodic heat generation is sketched, showing the periodic evolution of eccentricity, ice shell temperature, and subsurface ocean [Spencer and Nimmo, 2013a].

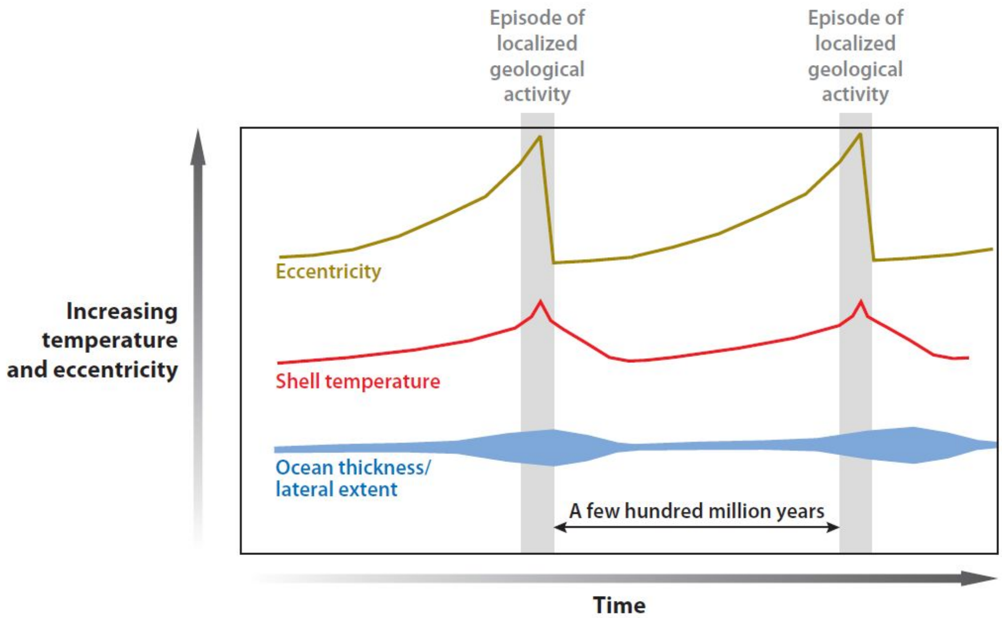

Figure 2.10: Schematic diagram illustrating the hypothesis of episodic heat generation in Enceladus, showing qualitatively the periodic behavior of eccentricity, ice shell temperature, and ocean thickness.
Source: J.R. Spencer and F. Nimmo, 2013a, *"An Active Ice World in the Saturn System"*.

Another hypothesis is that Enceladus produces heat at the time-averaged rate of 1.1 GW, however this heat is released episodically [Spencer and Nimmo, 2013a]. With simulations where numerical convection models are applied it is shown how this process could work [O'Neill and Nimmo, 2010], see Figure 2.11. The heat release episodes recur every 0.1-1 Gyr in that model, and they seem to be rather localized than global. The model of episodic heat release might be more promising than the idea of periodic heat production, but it raises the problem that it requires that Enceladus is presently observed at a very special time [Nimmo *et al.*, 2017].

Suggesting lower values of Q lead to unrealistic small values of the ages of Enceladus and Mimas, they must be much younger than the age of the Solar System in that case [Meyer and Wisdom, 2007] But a recent work shows that a low present-day Q does not necessarily require young satellites [Fuller *et al.*, 2016]. Proposing a scenario which the authors call "Resonance Locking", meaning

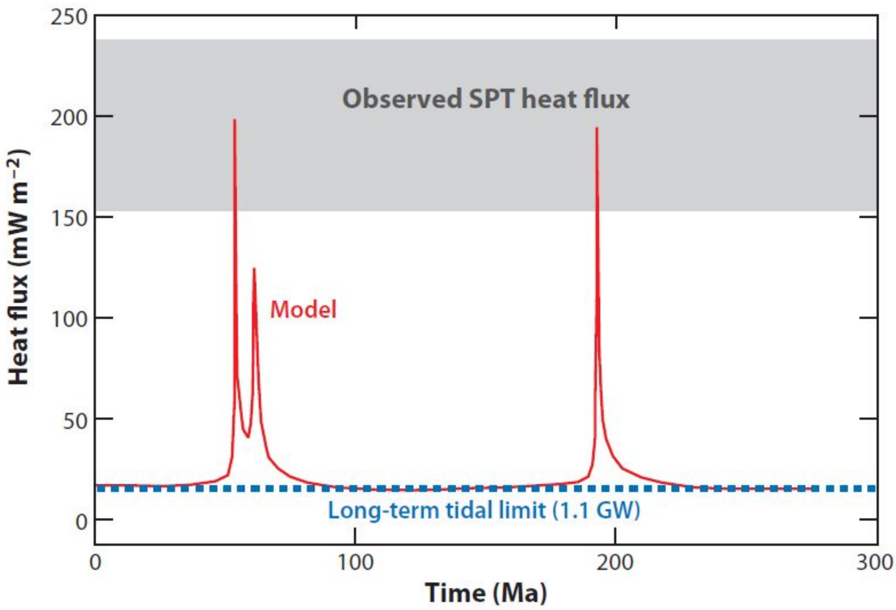

Figure 2.11: Possible episodic heat release in Enceladus as obtained by a numerical convection model [Spencer and Nimmo, 2013a, O'Neill and Nimmo, 2010]. High heat flux events (red peaks) coincidences with local yielding of the stagnant lid. The dashed blue line indicates the time-averaged rate of 1.1 GW.
Source: J.R. Spencer and F. Nimmo, 2013a, *"An Active Ice World in the Saturn System"*.

that the moon's orbital period being fixed to a certain resonance within Saturn, yields a present day value $Q = 1920$, which significantly raises today's heat production rate.

The small Q assumption, which results when employing the resonance locking scenario, might be the most promising solution of the 'tidal heat production' puzzle.

It is also still an open question where the tidal dissipation actually is located within Enceladus. Heating in the subsurface ocean has been discussed, but seems unlikely, because it requires obliquities which are unrealistically large [Chen and Nimmo, 2011]. The location of the tidal dissipation in the ice mantle could be either widely spread or could originate from heat produced by friction on particular fault segments [Nimmo *et al.*, 2007]. Regardless of this open detail, the large detected heat production rate strongly indicates the presence of (at least) a local subsurface ocean, because if the ice shell was connected seamlessly to the silicate core without any liquid sea in between, it would not deform strongly enough to produce the necessary observed tidal heat.

2.4.2 Radiogenic Heating

To estimate the heating rate originating from decays of radioactive nuclids, it can be assumed that Enceladus is made of material similar to that chondrites are built upon. Radiogenic isotopes contained in chondrites which are of interest are ^{232}Th, ^{235}U, ^{238}U, and ^{40}K. The present-day radiogenic heat release can be determined via Eq. 2.4 [Turcotte and Schubert, 2002]

$$H_{\mathrm{rad}} = H_{^{232}\mathrm{Th}} \cdot C_{^{232}\mathrm{Th}} + 0.0071 \cdot H_{^{235}\mathrm{U}} \cdot C_{^{235}\mathrm{U}} + \tag{2.4}$$

$$+ \; 0.9928 \cdot H_{^{238}\mathrm{U}} \cdot C_{^{238}\mathrm{U}} + 1.19 \cdot 10^{-4} H_{^{40}\mathrm{K}} \cdot C_{^{40}\mathrm{K}} \quad . \tag{2.5}$$

where C_i is the current concentration, and H_i the heat release of each nuclid. In Taubner (2012) an average value out of data from the literature [Czechowski and Leliwa-Kopystyński, 2005, Schubert *et al.*, 2007, Turcotte and Schubert, 2002, Schubert *et al.*, 1986] has been calculated, which is given by $\bar{H}_{\mathrm{rad}} \sim 0.34$. This value is at least one order of magnitude lower than the total power of 4.7 GW determined with Cassini's CIRS measured data [Nimmo *et al.*, 2017].

Though radiogenic heating might only contribute a smaller part to the whole heat flow, it could provide sufficient energy to keep a subsurface water reservoir liquid [Schubert *et al.*, 2007].

2.4.3 Alternative Heating Mechanisms

An alternative heat production mechanism proposed by Howett *et al.* (2011) is based on the assumption that "the orbital/tidal equilibrium of Enceladus is unstable", and that the current high heat flow value is a result of the recent changes of the orbital eccentricity.

Another alternative mechanism is provided by the secondary resonance spin-orbit libration model [Wisdom, 2004]. The authors developed a perturbative model of the secondary resonance. Calculating the tidal dissipation rate presuming that Enceladus is locked in this secondary resonance, gives a value 2 to 3 orders of magnitude larger than given by the usual tidal heating mechanism for a satellite in synchronous rotation. However, the prognosticated libration was not observed within detection limits of $\pm 1.5°$ [Porco *et al.*, 2006], that results in an upper limit of a heat production rate of 0.18 GW [Porco *et al.*, 2006], which is more than a factor 10 smaller than the measured Cassini value of 4.7 GW. Additionally, in Rappaport *et al.* (2007) it was shown that the large density of Enceladus is incompatible with this secondary resonance.

Property	**Value**
Semi-major axis	237 948 km [1]
Orbital eccentricity	0.0047 [1,2]
Orbital period	1.37 days [1]
Dimensions	513.2 x 502.8 x 496.6 km [1,3]
Mean radius	252.1 km [1,3]
Mass	1.08 x 10^{20} kg [1,4]
Bulk density	1.609 $\mathrm{kg\,m^{-3}}$ [1,3]
Surface gravity	0.113 $\mathrm{m\,s^{-2}}$
Escape velocity	239 $\mathrm{m\,s^{-1}}$ [1]
Albedo	1.375 (geometric) [5] or 0.81 (Bond) [6]

Table 2.1: Basic orbital and physical properties of Saturn's moon Enceladus.
Sources: [1] [NASA, 2013], [2] [Porco *et al.*, 2006], [3] [Roatsch *et al.*, 2009], [4] [Jacobson *et al.*, 2006], [5] [Verbiscer *et al.*, 2007], [6] [Howett *et al.*, 2010]

Name	Abbr	Task
Cassini Plasma Spectrometer	CAPS	investigated the plasma within and near Saturn's magnetic field, as well as Enceladus' plume.
Cosmic Dust Analyser	CDA	analyses ice and dust grains in and near the Saturnian system
Composite Infrared Spectrometer	CIRS	observed infrared radiation from surfaces, rings, and atmospheres of Saturn and its moons to investigate their temperatures, and compositions
Ion and Neutral Mass Spectrometer	INMS	explored composition of neutral and charged particles near Titan, Saturn and its moons to study their atmospheres
Imaging Science Subsystem	ISS	took images in near-infrared, visible, and near-ultraviolet light. The ISS consists of a wide-angle camera (WAC) and a narrow angle camera (NAC), both of which uses a charge-coupled device (CCD)
Dual-Technique Magnetometer	MAG	analyses Saturn's magnetic field, and its interplay with the solar wind, the moons and the rings of Saturn
Magnetospheric Imaging Instrument	MIMI	created images of Saturn's magnetosphere, and measured its interactions with the solar wind, satellites and rings
Cassini Radar	RADAR	created maps of Titans's surface. Radar waves could look through the opaque atmosphere of Titan, and displayed many surface details
Radio and Plasma Wave Science instrument	RPWS	measured natural radio signals stemming from Saturn, and plasma waves in the vicinity of Saturn
Radio Science Subsystem	RSS	analysed physical properties of atmospheres and ionospheres; explored rings and gravity fields of Saturn and its satellites
Ultraviolet Imaging Spectrograph	UVIS	took images of ultraviolet light reflected off an object; studied clouds and rings and their structure, chemistry and composition
Visible and Infrared Mapping Spectrometer	VIMS	took images of visible light and infrared wavelengths to investigate chemical compositions of moon's surfaces, atmospheres, and the rings

Table 2.2: Cassini Spacecraft Instruments.
Source: ESA, https://www.esa.int/Our_Activities/Space_Science/Cassini-Huygens/Cassini_instruments (accessed on July 27$^{\text{th}}$, 2021).

			Close approach		Geometry 1 h before encounter		Geometry 1 h after encounter	
Orbit, encounter name	Date and time (UT)	Speed ($km\,s^{-1}$)	Altitude (km)	Sub-spacecraft point	Sub-spacecraft point	Solar phase	Sub-spacecraft point	Solar phase
3, E0	2005/02/17 03:30	6.7	1,260	239 W, 51 N	318 W, 1 N	27	163 W, 3 N	159
4, E1	2005/03/09 09:08	6.6	497	304 W, 30 S	202 W, 1 S	45	41 W, 0 S	130
11, E2	2005/07/14 19:55	8.2	166	327 W, 22 S	197 W, 48 S	46	36 W, 47 N	132
61, E3	2008/03/12 19:06	14.4	47	135 W, 21 S	125 W, 70 N	114	327 W, 70 S	65
80, E4	2008/08/11 21:06	17.7	50	97 W, 28 S	87 W, 62 N	107	289 W, 63 S	72
88, E5	2008/10/09 19:06	17.7	25	97 W, 31 S	86 W, 62 N	107	289 W, 63 S	72
91, E6	2008/10/31 17:14	17.7	197	97 W, 26 S	86 W, 62 N	107	288 W, 63 S	72
120, E7	2009/11/02 07:41	7.7	99	159 W, 88 S	329 W, 1 S	174	170 W, 0 N	5
121, E8	2009/11/21 02:09	7.7	1,602	112 W, 82 S	189 W, 3 S	145	31 W, 3 S	33
130, E9	2010/04/28 00:10	6.5	99	147 W, 89 S	317 W, 1 S	172	159 W, 0 S	7
131, E10	2010/05/18 06:04	6.5	434	304 W, 34 S	201 W, 0 S	154	42 W, 1 S	27
136, E11	2010/08/13 22:31	6.9	2,550	29 W, 78 S	198 W, 17 S	153	39 W, 4 N	23
141, E12	2010/11/30 11:53	6.3	47	53 W, 62 N	315 W, 0 S	166	156 W, 0 S	14
142, E13	2010/12/21 01:08	6.3	47	232 W, 62 N	314 W, 0 S	166	156 W, 0 S	15
154, E14	2011/10/01 13:52	7.4	99	204 W, 89 S	192 W, 0 S	151	34 W, 1 S	28
155, E15	2011/10/19 09:23	7.5	1,229	114 W, 14 S	189 W, 0 S	154	36 W, 1 S	31
156, E16	2011/11/06 04:59	7.4	495	295 W, 30 S	193 W, 0 S	151	34 W, 0 S	29
163, E17	2012/03/27 18:29	7.2	82	191 W, 76 S	191 W, 0 N	160	32 W, 1 S	20
164, E18	2012/04/14 14:00	6.5	175	206 W, 49 S	191 W, 0 N	160	32 W, 1 S	20
165, E19	2012/05/02 09:31	7.6	73	291 W, 72 S	191 W, 0 N	159	32 W, 1 S	21
223, E20	2015/10/14 10:41	8.4	1,838	106 W, 78 N	185 W, 4 N	23	24 W, 4 N	148
224, E21	2015/10/28 15:22	8.5	48	66 W, 84 S	336 W, 0 N	41	177 W, 1 S	139
228, E22	2015/12/19 17:48	9.5	4,999	353 W, 88 S	342 W, 6 S	46	183 W, 10 S	144

Table 2.3: Cassini's close Enceladus flybys: Prime (blue), Equinox (green), and Solstice (yellow) missions.
Source: adapted from J.R. Spencer, *et al.*, 2009, *"Enceladus: An Active Cryovolcanic Satellite"*, page 685, Table 21.1.

Source	**Ice Shell Thickness @ SPT**
Mc Kinnon, 2015	23 km
Thomas *et al.*, 2016	7 - 13 km
Kamata & Nimmo, 2017	10 km
Čadek *et al.*, 2016	1.5 - 5 km
Le Gall *et al.*, 2017	2 km
Beuthe *et al.*, 2018	7 km
Average Value (by author)	***9.2 ± 7.5 km***

Table 2.4: Thickness of the ice mantle at the South polar terrain (SPT) as given by several authors. An average value is calculated by the present author.

Resonances	**2:1 Ence:Dione**	**3:2 Mimas:Ence**	**4:3 Ence:Tethys**	**2:1 Janus:Ence**
H_1 [10^9 W]	1.87262	0.75541	0.95777	0.01795
H_2 [10^9 W]	0.92230	0.32530	-0.41084	-0.03621

Table 2.5: Tidal Heat production rates at equilibrium for various resonance combinations as calculated by Taubner (2012).
Source: adapted from R.-S. Taubner (2012), "The possibility of the existence of a nitrogen cycle within Enceladus". Master thesis, University of Vienna, page 32, Table 2.4.

3. Potential Life on Enceladus

The detection of a plume of water vapour and icy particles erupting from the South Polar Terrain of Enceladus [Porco *et al.*, 2006, Dougherty *et al.*, 2006] together with several follow-up observations and analyses (e.g. [Hansen *et al.*, 2006, Spencer *et al.*, 2006]) led soon to the suggestion that the origin of the phenomenon is a subsurface liquid water reservoir [Porco *et al.*, 2006]. The discovery of sodium salts and organic components within the plume indicates that the subsurface ocean is in contact with Enceladus' hot rocky core. Hydrothermal vents might exist at the ocean's floor and provide energy for chemical reactions producing hydrothermal products, e.g. silica nanoparticles, sodium salts, complex organic compounds [Waite *et al.*, 2009, Hsu *et al.*, 2015, Postberg *et al.*, 2018, Khawaja *et al.*, 2019, Taubner *et al.*, 2020, Jebbar *et al.*, 2020]. The principal physical hydrothermal reactions at the interface between Enceladus' subsurface reservoir and its rocky core might be similar to those occuring at Earth in the vicinity of hydrothermal vents at ocean's floor. Hydrothermal vents and the chemical reactions around their locations are one possible explanation of the origin of life on Earth ("Wächtershäuser theory" [Wächtershäuser 1992], for a review of possible life in exooceans see [Taubner, 2018b, Taubner *et al.*, 2020, Jebbar *et al.*, 2020]). Thus, the tiny moon Enceladus is a highly interesting candidate for possible extraterrestrial life in our own Solar System.

3.1 Overview

The fundamental question 'How did life begin on Earth?' is still open and has not been completely answered at present days. Several theories and hypotheses exist trying to explain how life emerged on our planet. Basically, three main theories represent the most common explanations:

1. Panspermia Theory
2. "Primordial Soup" Theory
3. Chemosynthetic Origin

A categorical overview of the various hypotheses of the origin of life defined by Davis and McKay (2008) which has been modified and applied to the origin of possible life on Enceladus [McKay *et al.*, 2008] is shown in Figure 3.1.

3.1.1 Panspermia Theory

The Panspermia (Ancient Greek $\pi\tilde{\alpha}\nu$ (pan) meaning 'all', and $\sigma\pi\epsilon\rho\mu\alpha$ (sperma), meaning 'seed') states that life is distributed throughout the whole Universe, and is transported by asteroids, meteoroids, comets, planetoids, and possibly even by (extraterrestrial) spacecrafts contamined by microorganisms. The basic idea of Panspermia goes back to the Pre-Socratic Greek philosopher

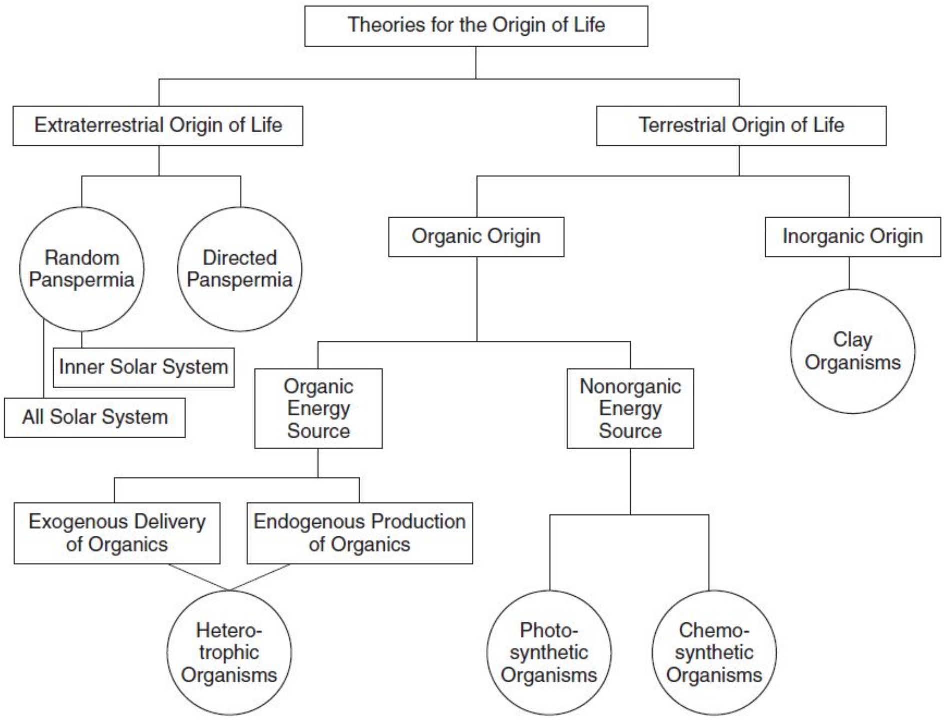

Figure 3.1: Categorical overview of the various assumptions of the origin of life on Earth from Davis and McKay [Davis and McKay, 1996] adapted to the origin of possible life on Enceladus (where two subcategories for random panspermia are added) [McKay *et al.*, 2008].
Source: C.P. McKay, *et al*, 2008, "The Possible Origin and Persistence of Life on Enceladus and Detection of Biomarkers in the Plume".

Anaxagoras (510-428 BC) [O'Leary, 2008]. A more scientific approach began in the 19$^{\text{th}}$ century when scientists like Lord Kelvin [Thomson (Lord Kelvin), 1871], Hermann von Helmholtz, and later the Swedish chemist Svante Arrhenius formulated the panspermia idea as a more elaborated hypothesis. In present time Fred Hoyle (1915-2001) and Chandra Wickramasinghe (born 1939) have been the strongest proponents of the panspermia theory [Hoyle and Wickramasinghe, 1981, Hoyle *et al.*, 1986, Wickramasinghe, 2009, Wickramasinghe, 2010, Wickramasinghe, 2011].

Panspermia theory states that microorganisms could be trapped in dust and debris when they were ejected into space after a collision between solar system bodies (planets, asteroids, planetesimals, comets, etc.) where at least one of the collisional bodies contains biological life. Some chemolithoautotrophic extremophilic microorganisms could endure the extreme conditions in space (temperature, radiation, ...) while being in a kind of dormant state and might survive their journey through space. Accidentently debris containing surviving members might collide with planets and under certain ideal conditions, e.g. if the microorganisms land in a liquid solvent, they might awaken from dormancy and start to proliferate in the new environment.

There are several proposed mechanisms of the panspermia hypothesis:

- Lithopanspermia: organisms travel on impact-expelled rocks from one planet to another either through interplanetary (within one solar system) or interstellar space (from one solar system to another).

- Radiopanspermia: microscopic life forms are propagated in space due to radiation pressure from stars.

- Accidental panspermia: assumption that life on Earth might originated accidentally by a pile of rubbish left on Earth spilled out by extraterrestrial beings [Gold, 1960].
- Directed panspermia: intentional spreading of bacterial seeds to other planets by an advanced extraterrestrial civilization, or intentianal spreading of microorganisms from Earth to other planets by humans [Crick and Orgel, 1973].

However, among scientists the Panspermia hypothesis is debated highly controversially: The proponents believe that it is indeed possible for extremophiles to withstand the extreme conditions in space long enough, on the other hand the opponents claim that the distances to travel in the galaxy (even within solar systems), and thus also the corresponding travel time, are far too long, such that life cannot survive the complete journey. The traveling time is so large that even the most resistant extremophile organism will be exposed to one or more fatal events that finally ends letally, e.g. strong ionizing radiation, strong gravitational or mechanical forces, extreme temperatures, etc.

From a basic perspective the Panspermia theory is also not satisfying as far as the ultimative question for the very origin of life is concerned. If life has been brought to Earth via spores traveling through space, these organisms must have been evolved somehow on a celestial body in our galaxy. The question where, when, and how life has actually developed remains still unanswered, thus the Panspermia hypothesis just defers this fundamental issue.

To be applied to Enceladus, McKay *et al.* (2008) introduced a distinction between (a) an "Inner Solar System" panspermia, where the source of microorganisms is restricted to a Solar System planet, e.g. Mars and Earth, and (b) an "All Solar System" panspermia, i.e. a Solar System wide panspermia, where the organisms stem from an extraterrestrial source. The first hypothesis supposes that life begins on Earth or Mars and is then transferred by meteorites to an outer body like Enceladus. However, this assumption might be improbable due to the large transit time to the outer Solar System which reduces the survival probability considerably. The second hypothesis, a Solar System wide panspermia, implies that every body in the Solar System would be seeded with life spores stemming from an other planetary system. Following the latter hypothesis, possible life on Enceladus would have the same bio-chemistry as life on Earth [McKay *et al.*, 2008]. But, even supposing that life on these Solar System bodies, Earth and Enceladus, would have the same origin, the evolutionary paths might be quite diverse due to different environmental conditions on these distinct bodies.

3.1.2 "Primordial Soup" Theory

The Primordial Soup, or Prebiotic Soup theory assumes that the basic building blocks of life originate from a "soup" of organic compounds that were created by abiotic synthesis [Oparin, 1924] or brought to Earth by comets around 4.2-4.0 billion years ago. The Primordial Soup hypothesis was first proposed by the Soviet biochemist Alexander Oparin in 1924 in his work "The Origin of Life" [Oparin, 1924], which was originally only available in Russian (the first English translation was published many years later in 1967 [Oparin, 1967]). Independently, the English scientist John Burdon Sanderson Haldane formulated his primordial soup theory in 1929 in an article also called "The origin of life" [Haldane, 1929]. Haldane introduced the term "soup" to describe the composition of organic material and water in the early Earth. According to the theory, carbon, hydrogen, ammonia, and water vapor reacted under energy supply to build the first organic compounds [Oparin, 1967, Haldane, 1929].

Today the theory is also called the "Heterotrophic origin of life theory" or the "Oparin-Haldane hypothesis". Its fundamentantal assumptions can be summarized as follows [Shapiro, 1987]:

1. Early Earth had possessed a chemically reducing atmosphere, containing methane (CH_4), ammonia (NH_3), carbon dioxide (CO_2), hydrogen (H_2), and water vapor (H_2O) that were basic raw materials for the evolution of life.

2. This atmosphere when exposed to energy (e.g. electrical discharges, flash of ligtning, ultraviolet light...) produced simple organic compounds, so-called monomers.

3. These monomers intermixed and formed a "soup" that might have concentrated in certain locations (oceanic vents, shorelines, etc.).

4. By further chemical reactions the compounds built more complex polymers, and finally, as ultimative step, life developed in the "soup".

In 1953 the American chemist Stanley Lloyd Miller with assistance from his supervisor Harold Urey performed a chemical experiment at the University of Chicago to test the hypothesis of Oparin and Haldene, which nowadays is well-known as the Miller-Urey experiment [Miller, 1953, Miller and Urey, 1959] (a schematic illustration of the experiment is shown in Figure 3.2).

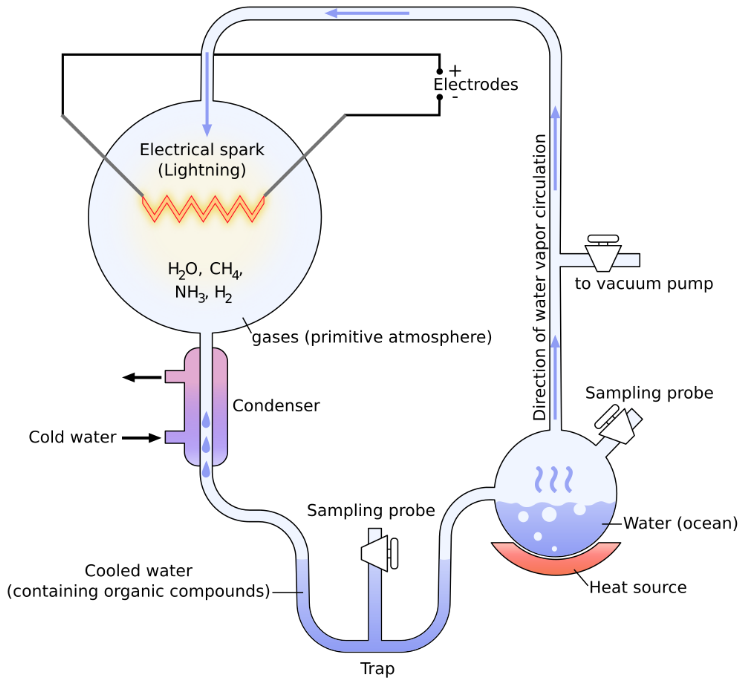

Figure 3.2: Schematic illustration of the Miller-Urey experiment of 1953 [Miller, 1953,Miller and Urey, 1959] that was conducted to test the Oparin-Haldane ("Primordial Soup") hypothesis [Oparin, 1924, Haldane, 1929].
Source: Wikipedia, 2021, file licensed under Creative Commons license, https://creativecommons.org/licenses/by-sa/3.0/ (accessed on July 27$^{\text{th}}$, 2021).

In this chemical experiment water was heated in a flask till it evaporated. The water vapor then entered a larger flask and was mixed with CH_4, NH_3, and molecular H_2, which should represent the primitive anaerobic early Earth atmosphere according to the assumption at that time. The water vapor gas mixture was then exposed to electrical sparks that were continously fired by surrounding electrodes, and which should simulate lightning in the primitive atmosphere. Finally, as last step of the continous cycle, the gas mixture was cooled and condensed back into the first flask. After one day running several cycles, the solution accumulated in the flask had turned pink in color, and after running for approximately one week, Miller identified a substantial amount of organic material. Employing paper chromatography, he detected five biologically important amino acids in the solution [Miller, 1953]: glycine, α-alanine, β-alanine, aspartic acid, and α-aminobutyric acid (the first three were positively identified, whereas the latter two were less certain).

An analogous mechanism on Enceladus is possible, provided Enceladus has a subsurface liquid reservoir which is rich in organic compounds. Recent detections of organic material like CH_4 [Waite *et al.*, 2009], and even complex compounds [Postberg *et al.*, 2018] might support this theory.

3.1.3 Chemosynthetic Origin

Another approach how life could have begun on Earth is the hydrothermal vent hypothesis which might be valid for Enceladus as well. Following this assumption, life has a chemosynthetic origin at hydrothermal vents at the ocean's floor where liquid chemical substances heated by tidal dissipation emerged from the rocky core under the sea ground [Spencer *et al.*, 2009]. Chemical energy is produced from reduced gases such as H_2S and H_2 that result from the vent interacting with an appropriate oxidant, e.g. CO_2 [Corliss *et al.*, 1981, Shock, 1990, Wächtershäuser 1992]. An illustration of the chemical processes is shown in Figure 3.3. One of the major proponents of the idea that life has a chemosynthetic origin is the German chemist Günter Wächtershäuser (born 1938) who formulated the iron-sulfur world theory, that proposes that life has formed on the surface of iron sulphides in the vicinity of hydrothermal vents exposed to high pressure and temperatures [Wächtershäuser 1992]. On Enceladus, that can be regarded as a geological active body, hydrothermal vents located at the bottom of the subsurface ocean are a quite reasonable possibility. According to this theory, the first life forms would be chemotrophic microorganisms that absorb inorganic substances wheras in the Miller-Urey or "Primordial Soup" scenario they would be heterothrophs consuming organic material. A very recent study by Khawaja *et al.* (2019), where O- and N-bearing organic compounds have been identified by analysing CDA spectra in more detail, suggests several possible reaction pathways for hydrothermal synthesis of biochemical precursors that might occur within Enceladus' subsurface ocean.

3.2 Possible Lifeforms on Enceladus

To detect extraterrestrial lifeforms is in princinple a hard task to accomplish, because one should have a clear idea what one is looking for at all, when one searches for life. Unfortunately, the definition of life is not unique, currently more than 300 proposals for life definitions exist, and these are still strongly discussed amongst scientists. The official NASA definition of life was formulated by Joyce (1994):

> "Life is a self-sustaining chemical system capable of undergoing Darwinian evolution"

However, this specific definition will be very difficult to be realized in practice. Instead of trying to

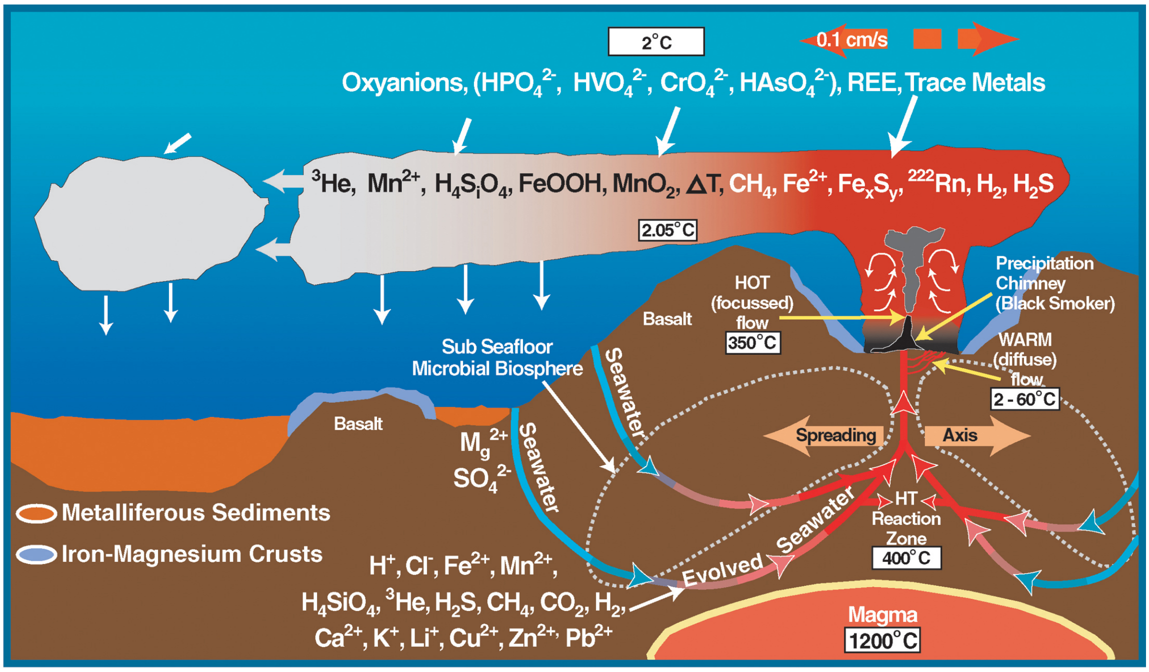

Figure 3.3: Schematic illustration of the chemical processes of the deep-sea hydrothermal vent biogeochemical cycle.
Source: US National Oceanic and Atmospheric Administration,
http://oceanexplorer.noaa.gov/explorations/02fire/background/hirez/chemistry-hires.jpg (accessed on July 27th, 2021).

find one unique, strict definition, it seems to be more appropriate to accept a number of working hypotheses that complement each other. Following this idea, Leitner and Firneis conceived a working hypothesis on the definition of (exotic) life comprising the following properties that have to be fulfilled by living organisms [Leitner and Firneis, 2012, Leitner, 2014]:

- "life is based on a metabolism, which is working symbiotically or asymbiotically" (i.e., "life is based on molecules which perform chemical reactions" [Taubner, 2012]).
- "life exploits a thermodynamic disequilibrium".
- "the macromolecules that enable the metabolisms, the building of structures, energy management and transfer of information, are a consequence of specific elements to form polymers with the ability to chemically bind functional groups".
- "the molecules of life interact with a solvent to be soluble (or not) or to react (or not) in a way that confers fitness of the life-form".
- "life has the ability to conserve its species".

These properties are very difficult to be verified outside a scientific laboratory even on Earth, and maybe almost inpossible to be monitored at other bodies of our Solar System by unmanned spacecrafts like e.g., Cassini's observations of the processes on Enceladus. Thus, the search for life has to be restricted to a few basic ingredients: according to Schulze-Makuch and Irwin (2008) there are three substantial "geoindicators":

1. an energy source,
2. the availability of a solvent (water preferred), and
3. the existence of essential nutrient matter.

On Enceladus all these fundamental factors might be available in the subsurface liquid water reservoir. The energy providing mechanism on this moon is mainly tidal heating (plus some contribution from radiogenic heating) that keeps the water liquid and might be also a possible energy source for potential life. Possible life forms could also retrieve energy by radiolysis and through redox gradients. Organic compounds could be produced around hydrothermal vents and/or might be externally acquired by material stemmimg from cometary or meteoritic impacts. Possible microorganisms could exist on the subsurface ocean's ground, preferentially in the vicinity of hydrothermal vents, but they could also be freely floating in the liquid reservoir. The first possibility would be analogous to the mechanism of Wächtershäuser's iron-sulphur world theory [Wächtershäuser 1992].

Category	**Definition**	**Examples**
I	"Presence of liquid water, available energy, organic compounds, atmospheric or surface shielding, evidence of biogenic processes"	Earth
II	"Evidence for past or present liquid water, availability of energy, inference of organic compounds, planetary history favorable for genesis of life"	Mars
III	"Physically extreme conditions, but with evidence of energy sources and complex chemistry possibly, suitable for life forms unknown to Earth"	Titan, Europe, Venus
IV	"Persistance of life very different from on Earth conceivable in isolated habitats, or reasonable, inference of past conditions suitable for the origin of life prior to the development of conditions so harsh as to make its perseverance at present unlikely but conceivable in isolated habitats"	Io, Triton, Enceladus, Gliese 581d
V	"Conditions so unfavorable for life by any reasonable definition that its origin or persistence cannot be rated a realistic probability"	Jupiter, Neptune, Gliese 581a,b HD 149026b, Sun, Moon

Table 3.1: Astrobiology plausibility categories ("Plausibility of Life (POL) index").
Source: Schulze-Makuch and Irwin (2008).

Schulze-Makuch and Irwin (2008) devised the so-called "Plausibility of Life (POL) index", its categorical definition is given in Table 3.1. Life in the subsurface of a planet or moon is faced with a fundamental problem, namely since a life habitat is an isolated system it will reach an equilibrium state where redox pairs will be exhausted. Thus, the existence of oxidizing agents is a crucial factor for life in a subsurface ocean that is isolated by an ice layer. However, this problem can be solved by the presence of an alternative energy, e.g., geochemical or geothermal energy. Conditions simimilar to those on early Earth might be possible when photosynthesis was not yet evolved, or when Earth might have been nearly entirely frozen ("Snowball Earth" occuring in the Neoproterozoic and in the Paleoproterozoic eras, [Kirschivink, 1992]).

On Earth there exist three microbial ecological systems that (i) are not exposed to sunlight, (ii) do not need oxygen, and (iii) do not depend on organic material that is created via photosynthesis, and, thus, can be regarded as analogous environments for a possible ecosystem on Enceladus [McKay *et al.*, 2008]. Two of these systems are based on methanogens using H_2 derived from water-rock reactions [Stevens and McKinley, 1995, Chapelle *et al.*, 2002], while the third is based on sulfur-reducing microorganisms using redox pairs created by radioctive decay [Lin *et al.*, 2006]. The first methanogen-based system was discovered in deep aquifers of the Columbia River Basin [Stevens and McKinley, 1995, Spencer *et al.*, 2009], and a second similar system was detected in the basalts in the Twin Falls region of Idaho [Chapelle *et al.*, 2002, McKay *et al.*, 2008].

An illustration of a hypothetical methane cycle, which could support methanogens in a subsurface liquid reservoir on Enceladus (or Europa), is shown in Figure 3.4 [McKay *et al.*, 2008].

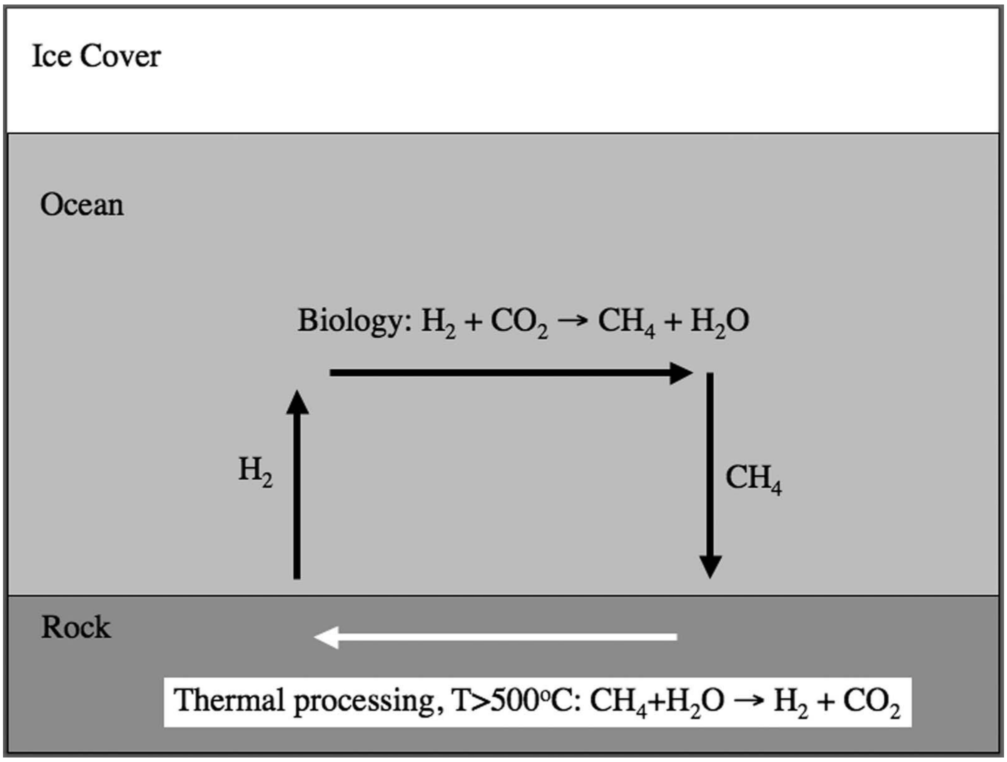

Figure 3.4: Schematic illustration of a possible methane cycle on Enceladus.
Source: C.P. McKay, *et al*, 2008, "The Possible Origin and Persistence of Life on Enceladus and Detection of Biomarkers in the Plume" [McKay *et al.*, 2008].

The microbial ecosystem proposed by Lin *et al.* (2006), where bacteria like *Desulfoprofundis tokoloshe* consume energy via a sulfur-reducing redox-reaction is sketched in Figure 3.5 [McKay *et al.*, 2008]. The microorganisms obtain energy through the following chemical redox reaction:

$$4\,H_2 + H^+ + SO_4^{2-} \longrightarrow H_2S + 2\,H_2O + 2\,OH^-\,. \tag{3.1}$$

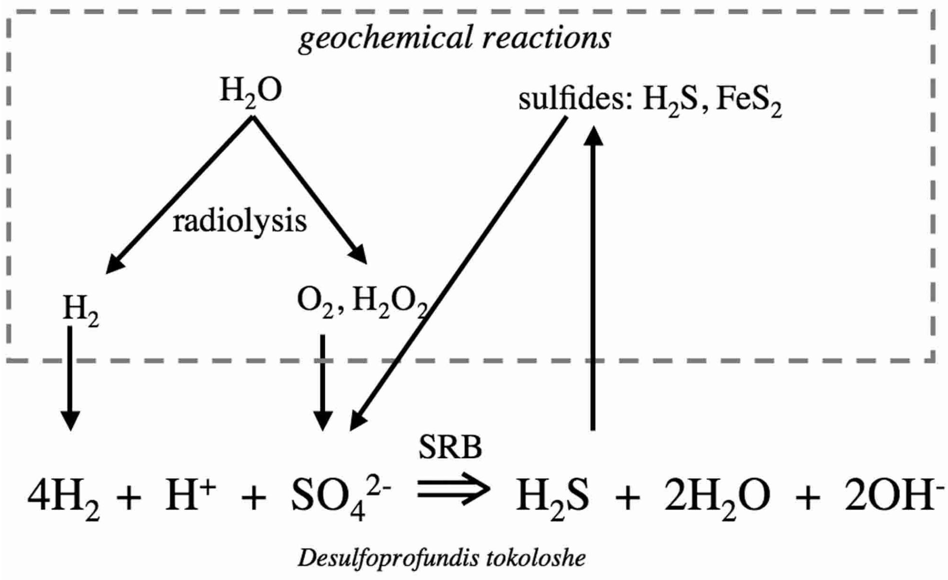

Figure 3.5: Processes of the possible biogeochemical cycle in the subsurface ocean on Enceladus where bacteria obtaining energy via a sulfur-reducing redox reaction produced by radiactive decay.
Source: C.P. McKay, *et al*, 2008, "The Possible Origin and Persistence of Life on Enceladus and Detection of Biomarkers in the Plume" [McKay *et al.*, 2008].

On Earth the radioactive decay of long-lived (half life time $\tau \approx$ several Gyrs) nuclids of U, Th, and K provides the necessary energy [Lin *et al.*, 2006, McKay *et al.*, 2008].

3.2.1 Detection of Life in the Plume

A promising way to find evidence for life on Enceladus would be the detection of biomarkers in the plume. The existence of CH_4 in the plume might indicate that there could be methanogens within an chemosynthetic ecological system similar to those in the Colombia River basalts [McKay *et al.*, 2008, Stevens and McKinley, 1995, Taubner, 2012, Taubner *et al.*, 2018a]. A sample return mission like *Stardust* (NASA, 2011) would be optimal to help clarifying if the plume actually contains biomarkers.

Assuming that both molecular hydrogen (H_2) and methane (CH_4) have been observed in the plume, methane producing microbiological life forms could find promising life conditions on Enceladus [Taubner *et al.*, 2018a, Taubner, 2018b, Taubner *et al.*, 2019]. Recent works by Taubner *et al.* (2018, 2019), where the growth of several methanogenic archaea have been studied in the laboratory on Earth, showed that one methanogenic archaeon, *Methanothermococcus okinawensis*, can produce CH_4 under physiochemical conditions extrapolated for Enceladus. The authors suggest that a portion of the CH_4 observed in Enceladus' plume could basically be created by similar methanogenic archaea. Biological CH_4 production of methanogens of the biochemical laboratory study under Enceladus-like conditions at high pressure is shown in Figure 3.6.

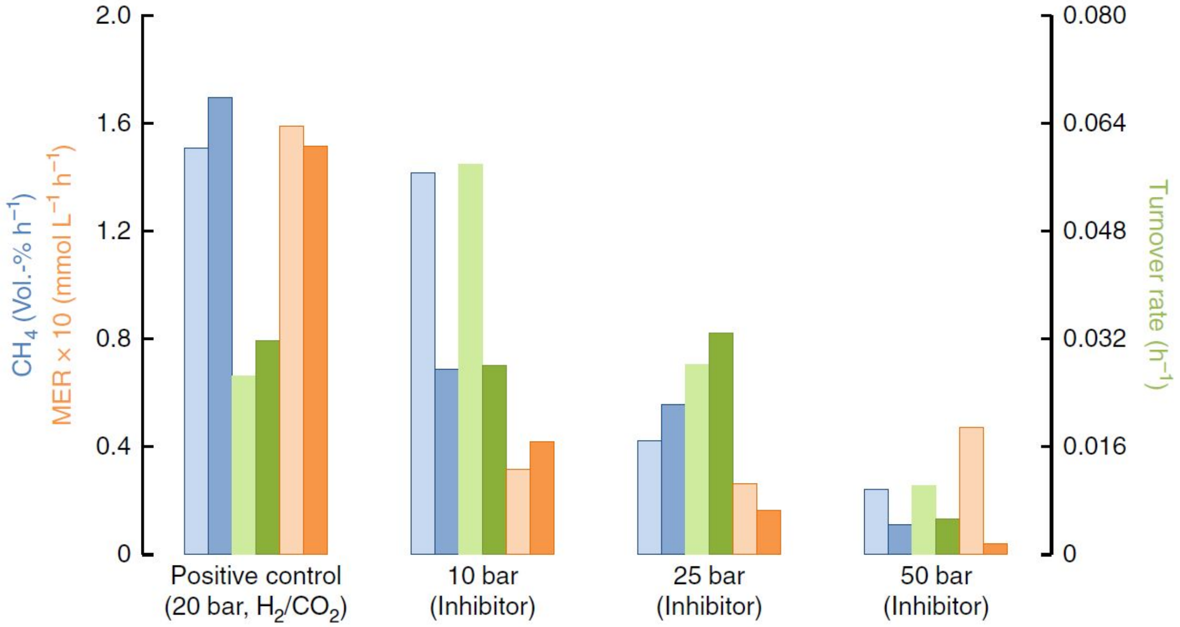

Figure 3.6: Biological CH_4 production (blue), turnover rates (green), and methane evolution rates (MER) (red) of the methanogenic archaeon *Methanothermococcus okinawensis* under Enceladus-like conditions at high pressure obtained in the study by Taubner *et al.* (2018a).

Source: R.-S. Taubner, *et al.*, 2018a, "Biological methane production under putative Enceladus-like conditions".

4. Plume

The NASA/ESA Cassini spacecraft discovered a plume of water vapor and ice particles over the south polar area during the Enceladus flybys in 2005 [Porco *et al.*, 2006, Spencer *et al.*, 2006, Hansen *et al.*, 2006, Waite *et al.*, 2006, Teolis *et al.*, 2017]. The first observation of a plume of ice grains came from Imaging Science Subsystem (ISS) pictures recorded in Jan and Feb 2005. Finally, the third close flyby in July 2005, where Cassini flew directly through the plume gas cloud, confirmed the presence of a plume of water vapor and small icy particles from warm fractures near the SPT [Porco *et al.*, 2006]. Figure 4.1 shows a high resolution plume jet image taken by Cassini's ISS on November 30$^{\text{th}}$ 2010.

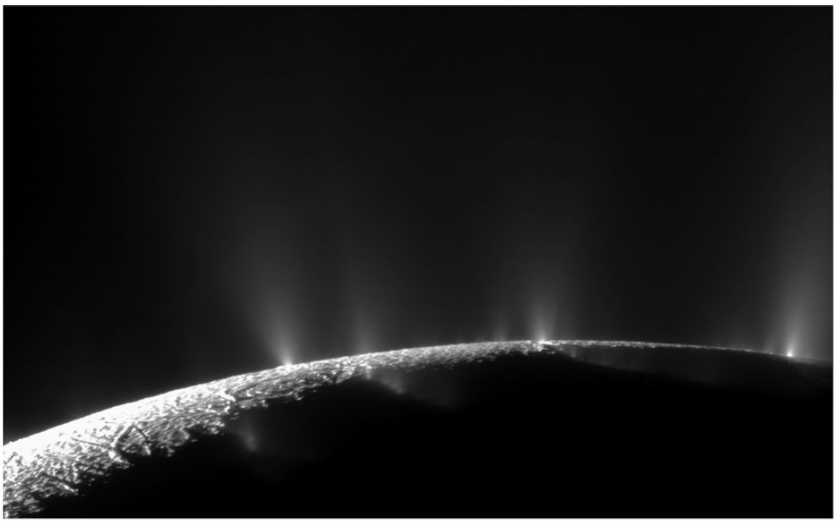

Figure 4.1: High resolution image of a plume jet taken by Cassini's ISS on November 30$^{\text{th}}$ 2010.
Source: Porco *et al.* (2014), *"How the Geysers, Tidal Stresses, and Thermal Emissions across the South Polar Terrain of Enceladus are related"* [Porco *et al.*, 2014].

Following the description of Spitale and Porco (2007), a plume is characterized as an "observed feature, as opposed to the individual 'jets' of material that can compose a plume, depending on the viewing geometry". For consistency's sake I follow in this thesis the convention to use the singular form 'plume' (as in Taubner, 2012; the present literature, however, speaks of both *plume* and the *plumes*).

The authors of one of the first plume studies analysing Cassini's CIRS data found eight sources of jets located on the four Tiger Stripes, Damascus, Baghdad, Cairo, and Alexandria [Spitale and Porco, 2007], but present day analysis of Cassini's data reveal that the plume is composed of about more than 100 discrete jets [Porco *et al.*, 2014]. Figure 4.2 shows a polar stereographic base map of the SPT where positions and directions of 100 jets have been drawn. Though the plume represents a kind of cryovolcanic activity, these plume jets are not violently erupting geysers like those on Earth, but they are rather steady jets of fine-grained particles of ice and vapour, and some of them are forming continous curtains [Spitale *et al.*, 2015]. At locations along the Tiger Stripes where plume activity is observed, also high thermal emission is present (see Figure 2.7). On the other hand, thermal emission peaks coincide at some positions (but not all) with individual plume jets observed by Cassini's ISS instrument [Helfenstein and Porco, 2015].

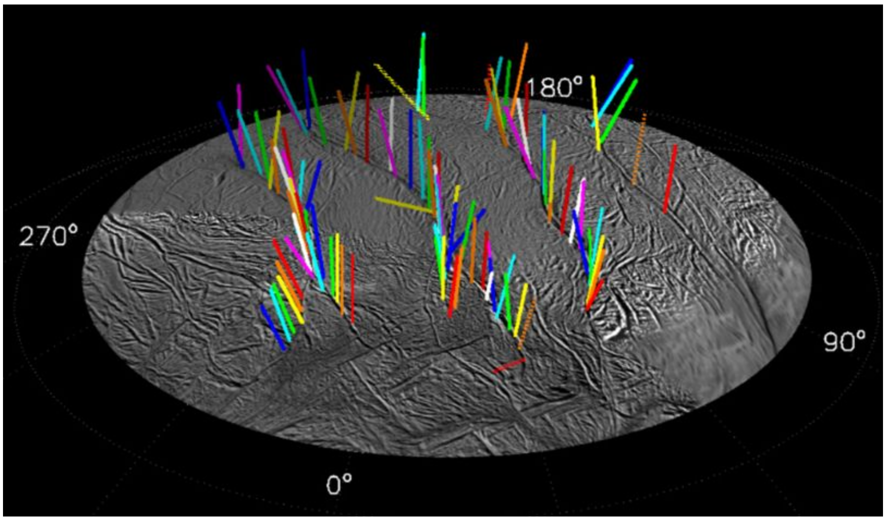

Figure 4.2: Polar stereographic basemap of Enceladus' South Polar Terrain (SPT) on which the locations and directions of 100 jets determined in Porco *et al.* (2014) have been plotted.
Source: Porco *et al.* (2014), *"How the Geysers, Tidal Stresses, and Thermal Emissions across the South Polar Terrain of Enceladus are related"*.

Enceladus' plume represents an exciting and fascinating active geological phenomenon in our Solar System. The moon is the fourth body in our Solar System that has confirmed present-day (cryo-)volcanic activity, along with Earth, Neptune's Triton, and Jupiter's Io (and maybe Europa).

However a lot of important questions concerning the plume arise: What is the source of heat that holds the plume active? Where is the origin of the heat located (at what depth)? How is it transferred to the surface? How deep is the ice layer above the liquid subsurface ocean? How deep and how thick are the cracks in the ice layer, which serve as channels, where the water vapor and ice particles are flowing through up to the surface? Do the plume jets show variation over time? What are the constituents of the gaseous and the solid particle plume components?

4.1 Gas and Dust Components

The plume of Enceladus consists of solid particles which are mostly water ice, and a gasous part whose major component is water vapor. Minor ingredients of the plume's gaseous part are CO_2, CH_4, NH_3, H_2, heavier organic molecules, and other items (e.g. ^{40}Ar) [Waite *et al.*, 2009, Hansen *et al.*, 2011, Waite *et al.*, 2017, Spencer *et al.*, 2018]. Figure 4.3 illustrates the mass spectrum of Enceladus' plume from the INMS measurements on October 9th, 2008, as given in Waite *et al.* (2009), and Table 4.1 shows the major species composition from a more recent study [Waite *et al.*, 2017].

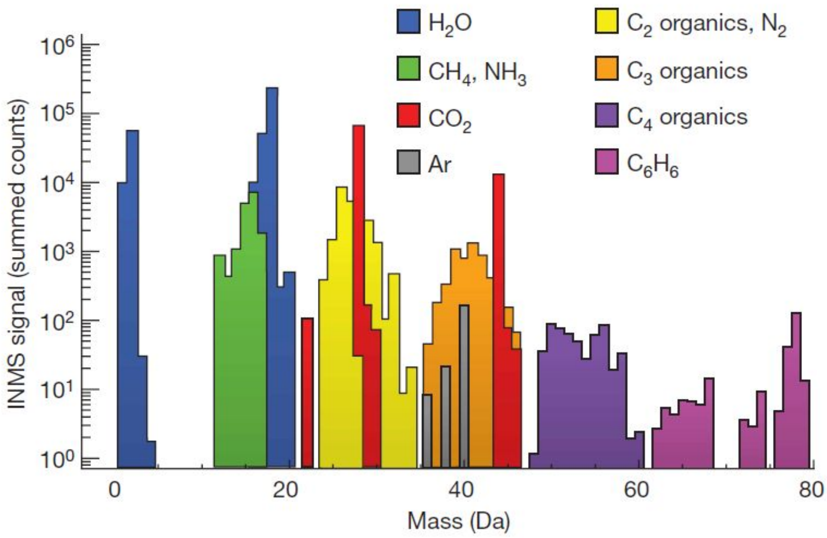

Figure 4.3: The mass spectrum of Enceladus' plume mesured by Cassini's INMS instrument during the October 9th, 2008, (E5) encounter.
Source: Waite *et al.* (2009), *"Liquid water on Enceladus from observations of ammonia and ^{40}Ar in the plume"*.

Constituent	Mixing ratio (%)
H_2O	96 to 99
CO_2	0.3 to 0.8
CH_4	0.1 to 0.3
NH_3	0.4 to 1.3
H_2	0.4 to 1.4

Table 4.1: Main components of the gaseous part of Enceladus' plume. Mixing ratios (Vol %) are obtained from Cassini's INMS measurements.
Source: Waite *et al.* (2017), *"Cassini finds molecular hydrogen in the Enceladus plume: Evidence for hydrothermal processes"*.

Model simulations provide evidence that the water molecules ejected along the Tiger Stripes have a vertical velocity of 300-500 $\mathrm{m\,s^{-1}}$ at the surface [Tian *et al.*, 2007], which is larger than Enceladus' escape velocity $v_{\mathrm{esc}} = 239\,\mathrm{m\,s^{-1}}$. Furthermore, the Cassini's Ultraviolet Imaging Spectrograph (UVIS) instrument observed parallel aligned gas jets in the plume that have Mach numbers of 5-8, indicating vertical gas velocities of more than 1000 $\mathrm{m\,s^{-1}}$ [Hansen *et al.*, 2011] (for simulation results, see e.g. Tucker *et al.* (2015)). The rate of water vapour injection to Saturn's E-ring is $\sim 200\,\mathrm{kg\,s^{-1}}$ [Hansen *et al.*, 2011].

The ejection velocity of the dust is an order of magnitude smaller, $v \sim 100\,\mathrm{m\,s^{-1}}$, which is below Enceladus' escape velocity, and depends on the size of the dust grains. [Porco *et al.*, 2006, Schmidt *et al.*, 2008, Hedman *et al.*, 2009] (small particles are systematically faster than larger ones), and the dust production rates are in the range of 5-50 $\mathrm{kg\,s^{-1}}$ [Schmidt *et al.*, 2008, Ingersoll and Ewald, 2011]. The larger salt-rich particles fall back onto Enceladus' surface, since they are thrown out at a lower velocity than the salt-poor ones. This explains why Schneider *et al.* (2009) could not detect atomic sodium (Na) or potassium (K) near Enceladus and Saturn's E ring using ground-based spectroscopy.

Postberg *et al.* (2009, 2011) analysed time-of-flight mass spectra of Enceladus' plume, that were produced by Cassini's Cosmic Dust Analyser (CDA), and they make a classification of the spectra into three compositional types (see Figure 4.4):

- Type I: almost pure water crystals, dominated by hydronium (H_3O^+) peak (and water cluster features if applicable), H_3O^+ peak larger than any Sodium Na^+ peak.
- Type II: dominated by water signatures, but also significant organic and/or siliceous impurities, H_3O^+ peak larger than any Sodium Na^+ peak (if present).
- Type III: dominated by Na-rich water ice, also rich in Sodium and Potassium salts, (e.g. NaCl, $NaHCO_3$, and/or Na_2CO_3, minor contribution from K-salts), Na^+ peak much larger than H_3O^+ peak (if present).

Since Type II particles contain organic and/or siliceous material, it is assumed that they are created in Enceladus' plume, wheras Type-I particles have been produced by micro-meteoroid impacts or by homogeneous nucleation from water vapor [Postberg *et al.*, 2009]. Type II grains are found in the dense core part of the plume [Postberg *et al.*, 2011].

Type III particles have more mass, and are agglomerated near the surface, indicating that they are ejected at speeds below the escape velocity $v_{\mathrm{esc}} = 239\,\mathrm{m\,s^{-1}}$ [Spencer *et al.*, 2018]. Postberg *et al.* strongly suppose that these Na-rich type III particles, that have their maximum density located in the vicinity of the SPT, are frozen droplets of size $< 1\,\mu\mathrm{m}$, which have to have their origin in a liquid reservoir. Additionally they noticed that the observed amount of sundry salt components together with its basic pH value shows a convincing resemblance to the proposed composition of a possible subsurface ocean simulated by Zolotov (2007).

The particle type classification has been extended by Horanyi *et al.* (2009) and Srama *et al.* (2008), who proposed a fourth population:

- Type IV: population of pure minerals, high sodium content, no pure water molecule clusters detected.

Using the Ion Neutral Mass Spectromenter (INMS) instrument H_2 was detected in the plume [Waite *et al.*, 2017]. This hydrogen is very likely produced by continuing hydrothermal reactions of rock carrying reduced materials and organic substances. The fact that a relatively large amount of hydrogen has been found favors the creation of CH_4 from CO_2 in Enceladus' subsurface ocean.

NH_3, that has been detected with a mixing ratio of about 0.4-1.4 [Waite *et al.*, 2009, Waite *et al.*, 2017], serves as an antifreeze, capable to lower the freezing point of water. The existence of NH_3 combined with the detection of Na- and K-salts in the plume and E-ring ice particles [Postberg *et al.*, 2009, Postberg *et al.*, 2011] seems to be a strong indication for a liquid subsurface water reservoir [Spencer *et al.*, 2018].

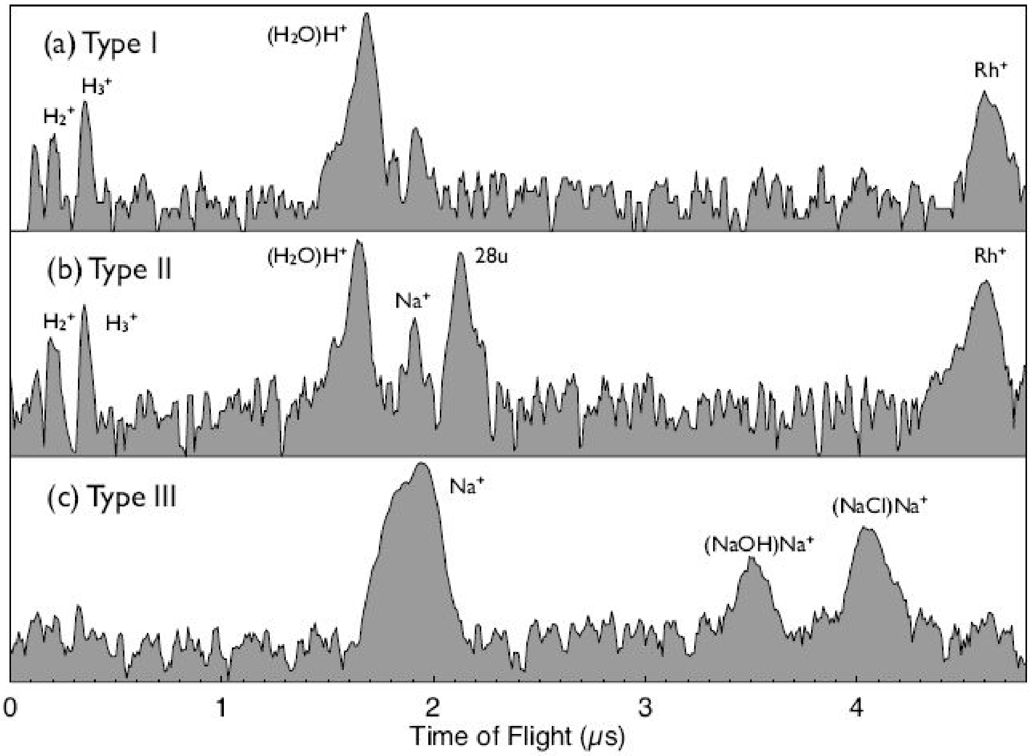

Figure 4.4: Comparison between a Type I (a), Type II (b), and a Type III (c) spectrum. Spectra were recorded during Cassini's E5 flyby of Enceladus.
Source: Postberg *et al.* (2011), *"A salt-water reservoir as the source of a compositially stratified plume on Enceladus"*, Supplementary Information.

The detection of icy grains with a high abundance of NaCl and $NaHCO_3$ probably is one of the strongest indicators that the plume originates from liquid water. The salt content of these grains gives highly evidence that they are formed by direct freezing of salty water at the plume origin, whereas the sodium-poor elements seem to be vapor condensates [Spencer *et al.*, 2009]. If the plume solids were created exclusively by condensation from the vapor, they would be more or less salt-free [Spencer *et al.*, 2018]. Thus, the presence of salty plume particles could not be explained in "dry" models, i.e. models that do not include a subsurface liquid reservoir. The salty grain components seem to be akin to those which are expected for an subsurface sea, that has been in touch with high temperature rocks at the ocean floor [Zolotov, 2007], hence indicating direct interchange of the plume source with the liquid reservoir. However, it could also be possible that the salinity is enhanced in the plume source reservoir only due to the predominantly evaporation of H_2O, while the subsurface sea itself is less saline [Schneider *et al.*, 2009]. Schneider *et al.* (2007, 2009) determined the atomic sodium content in the vapor part of the plume by ground-based spectroscopic measurements. The amount of sodium they found was by far too small to support the idea of a near-surface cryovolcanic geyser sourced by a salty sea.

But Postberg *et al.* (2009) explained that the observations by Schneider *et al.* (2009) are not in contradiction with their results, because due to the fact that most of the icy salty grains are falling back to Enceladus' surface the particle mass content of the E-ring is 200 times less than its

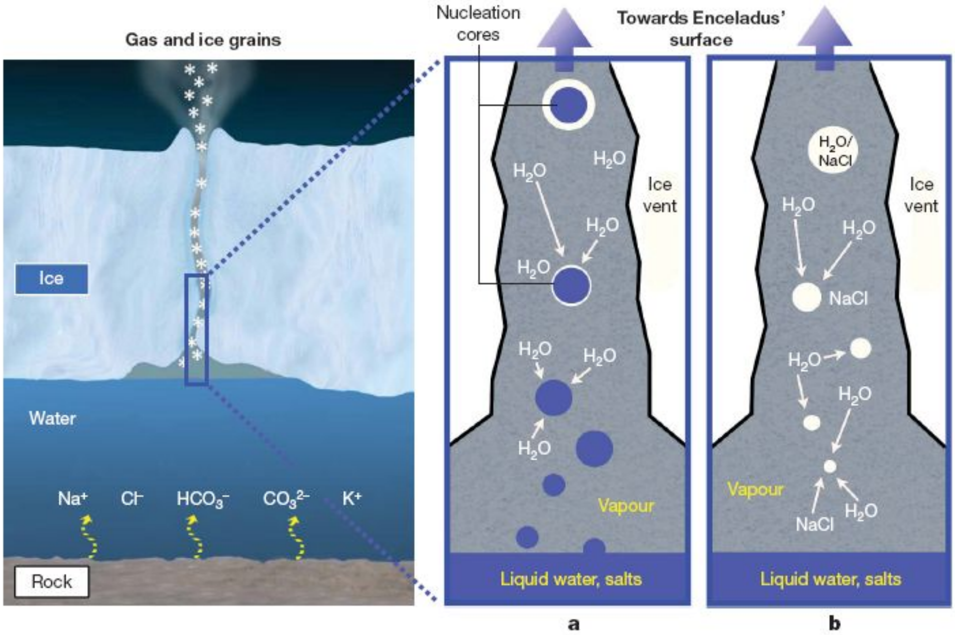

Figure 4.5: Schematic illustration of how salty ice grains with different Na content are built by liquid dispersion and condensation from vapor. a) Na-rich grains (Type III). Droplets are generated by dispersion above the salty liquid, they preserve the ocean's compositions. The salt content of the Type III Na-rich grains can be considered a lower limit for the surface of the subsurface ocean. b) Na-poor grains. They are created by condensation of water vapor rising from the subsurface sea. Initially the particles have the same low ratio of Na/H_2O as the gas. By interaction with the Na-rich grains they may be further enriched with Na-salt traces.

Source: Postberg *et al.* (2009), *"Sodium salts in E-ring ice grains from an ocean below the surface of Enceladus"*.

water vapor part, giving a Na/H_2O E-ring mixing ratio of about $10^{-7} - 10^{-6}$ that is below the optical detection limit [Postberg *et al.*, 2009]. Postberg *et al.* (2009) not even favor the idea of an liquid subsurface reservoir, they claim that the sodium detected in the plume particles has to have a liquid origin, and assume it to be a "soda-ocean", rich in bicarbonate and/or carbonate.

Additional evidence for liquid water in the interior of Enceladus is given by the existence of plenty of radiogenic ^{40}Ar in the plume, because hydrous processes can leach ^{40}Ar from the rocky core and concentrate it in the plume [Waite *et al.*, 2009].

The Cosmic Dust Analyzer (CDA) instrument of Cassini also detected nanometer-sized grains rich in silicon [Hsu *et al.*, 2015], most probably SiO_2. Size and composition of these particles indicate origination in a hydrothermal system inside Enceladus, that further supports a liquid water reservoir as plume source that is in direct contact with the rocky core [Glein *et al.*, 2008, Hsu *et al.*, 2015]. These nanosilica grains also constrain the conditions of the subsurface ocean to moderate salinity, an alkine pH, and relative warm temperature [Hsu *et al.*, 2015, Sekine *et al.*, 2015].

In a recent study by Postberg *et al.* (2018), the authors report detections of ejected ice particles containing complex organic molecules with masses of more than 200 amu (atomic mass units) Before, only simple organic compounds with molecular masses below 50 amu have been detected in the plume material [Waite *et al.*, 2006, Postberg *et al.*, 2008, Waite *et al.*, 2009].

The observed monomeric organic compounds are carbon-rich unsaturated molecules, which are chemically similar to simple liquids. The possibility of a pre-RNA Lipid World scenario for life's origin is described in Kahana *et al.* (2019). A picture of the possible components of the prebiotic soup and the plume is shown in Figure 4.6.

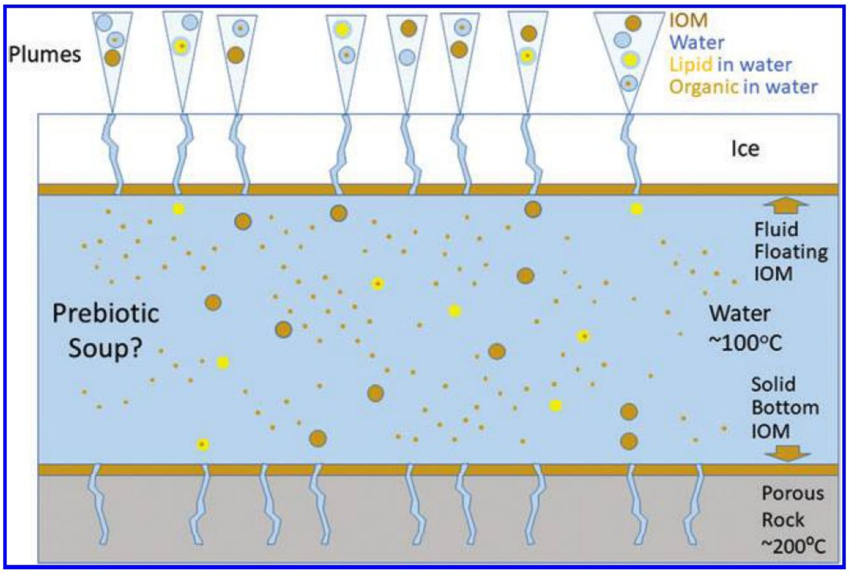

Figure 4.6: Cross section of Enceladus, showing the possible components of the prebiotic soup and the plume. IOM denotes insoluble, nondispersable organic matter, lipid in water can be realized as monomers and aggregates, e.g. vesicles and micelles, and organics in water occur in dispersed form, e.g. as microemulsion. Source: Kahana *et al.* (2019), *"Enceladus: First Observed Primordial Soup Could Arbitrate Origin-of-Life Debate"*.

Mass spectra from organic-bearing ice grains obtained by Cassini's Cosmic Dust Analyser (CDA) have been used for a broader compositional analysis performed by Khawaja, *et al.* (2019). This recently published study show that the ice particles of Enceladus' plume contain O- and N-bearing organic compounds. These compounds are (a) dissolved in the subsurface ocean, (b) evaporated at its surface, and (c) finally attached to the ice grains via adsorption. An overview of these processes inside Enceladus' ice vents is shown in Figure 4.7. The O- and N-containing compounds might participate in further chemical processes, e.g. mineral-catalysed Friedel-Crafts hydrothermal synthesis [Friedel and Crafts, 1877], that could produce biologically relevant compounds that might serve as building blocks for possible life.

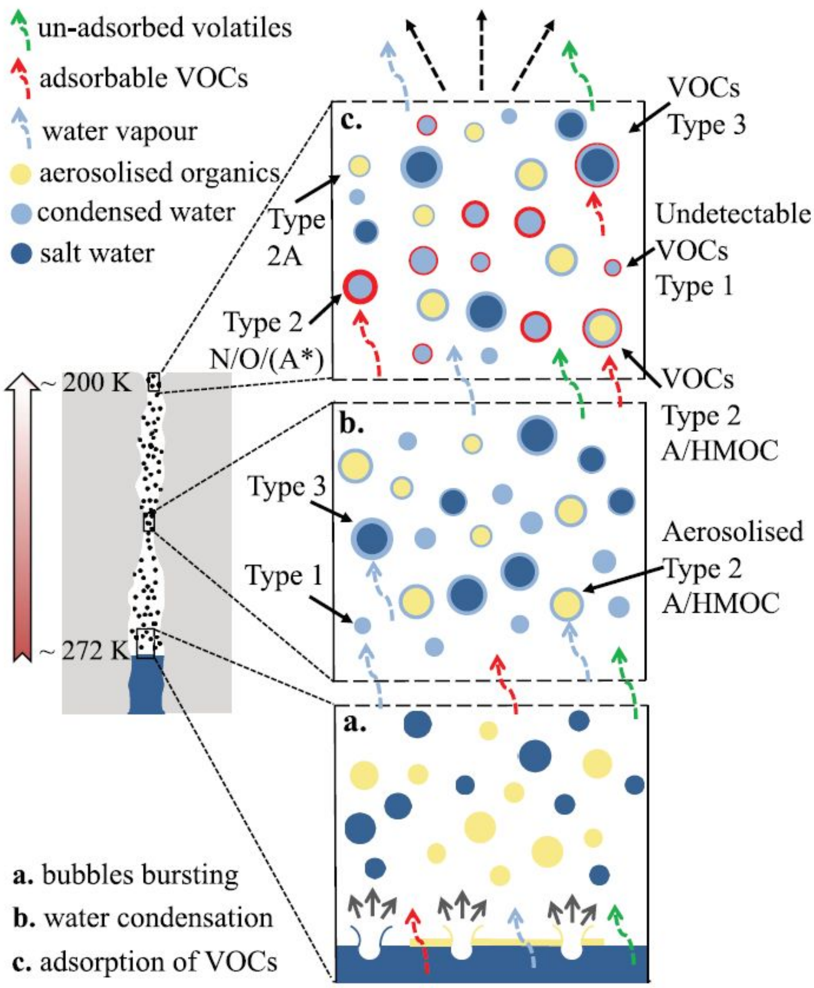

Figure 4.7: Schematic illustration of various creation paths of ice particles in the ice channels of Enceladus. **(a) Bubble bursting:** Water vapor and gas bubbles burst at the water surface, producing a spray of (not only salt-water) aerosols (dark blue) from the liquid reservoir and loft droplets of organic compounds (yellow). **(b) Water condensation:** Water becomes supersaturated at a tight throat of the ice channel, water vapour condenses into water ice particles (light blue), and also onto salt-water aerosols (dark blue) and aerosolized organic droplets (yellow). **(c) Adsorption of volatile organic material:** N- and O-carrying organic substances adsorb onto pre-existing icy particles in the channel. These N- and O-carrying compounds, amines, carbonyls, could be optimal basic material for mineral-catalysed Friedel-Crafts hydrothermal synthesis of biologically relevant organic compounds that might serve as building blocks of life.

Source: N. Khawaja, *et al.*, 2019, "Low-mass nitrogen-, oxygen-bearing, and aromatic compounds in Enceladean ice grains".

4.2 Plume formation scenarios

A model feasible to describe the plume and its physics must be able to explain several issues: The plume and its plumbing system seems to be a long-lived phenomenon. It is a crucial question if liquid water is a necessity to produce the plume, and if yes, the follow-up question is how near the water has to be to the surface, or in other words, how thick is the ice shell between a liquid water reservoir and the surface. Water originating from a subsurface reservoir has to perform a big effort to come up to the surface as a plume of icy grains and water vapor. A sufficient number of cracks and fractures within the ice mantle must exist connecting the subsurface ocean to the surface. These ocean-to-surface channels must be kept open despite of the creeping ice flow. Water must be able to flow through these channels without freezing, and it has to override its larger density compared to the surrounding ice. These issues define the so-called “plumbing-system problem” for hydrodynamic activities on Enceladus.

A considarable number of models have been devised up to now by several authors.

4.2.1 ’Cold Faithful’ model

The very first scenario of a plume formation model is the “Explosive Boiling” model, also known as “Near-Surface Geyser” or “Cold Faithful” model, proposed by Porco *et al.* (2006). It assumes that the liquid is present very close to the surface (liquid water of about 273 K, only 7-10 m below the surface), and that fractures, rapidly opening in the ice, suddenly expose the water to the vacuum. A schematic illustration of the “Cold Faithful” hypothesis is shown in Figure 4.8.

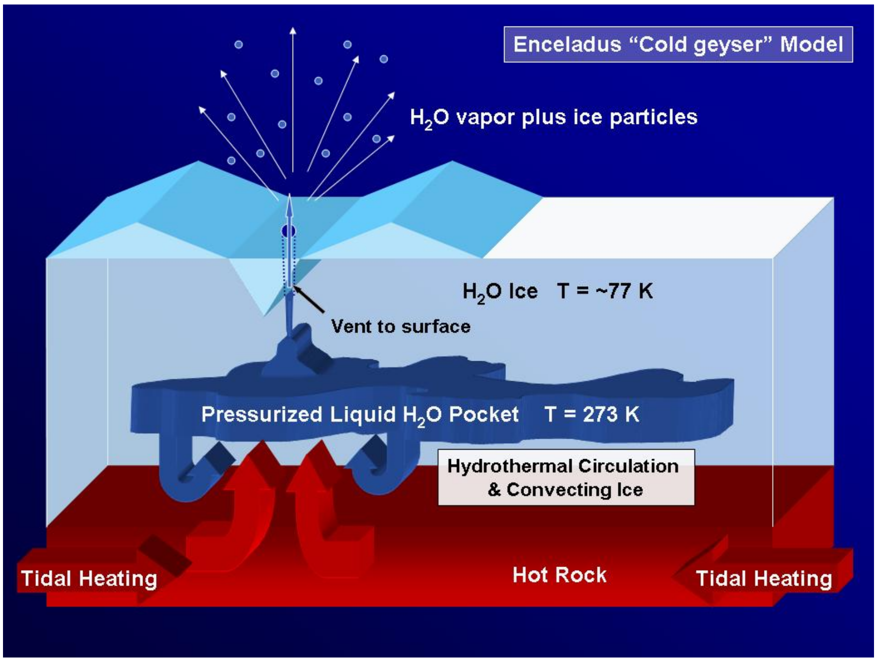

Figure 4.8: Schematic illustration of the Cold Faithful model.
Source: NASA/JPL/SSI PIA07799, https://photojournal.jpl.nasa.gov/jpeg/PIA07799.jpg (accessed on July 27th, 2021).

Due to the zero pressure condition at the surface the uppermost layer of the liquid should instantanously begin to boil, while some part of it also begins to freeze, thus, a plume of water vapor and icy particles erupts explosively, like a cold version of the Old Faithful Geyser in the Yellowstone National Park [Porco *et al.*, 2006]. Vapor bubbles enriched with the liquid are created that would explain the high liquid/vapour ratio observed by Cassini [Porco *et al.*, 2006]. The "liquid cools rapidly due to evaporation and freezes into a cloud of micron-sized particles" [Ingersoll and Ewald, 2011]. Part of the frozen particles are ejected as plume particles, are accelerated and dragged to space by the expanding gas. The whole process should be self-limiting, because any crack should be sealed fast by the freezing part of the liquid. However, this is contrary to the observed quasi-continuous activity which seems to be very stable over the last couple of years, which excludes such explosive and self-limiting geyser-like process. Furthermore, in this model both the gas stemming from the boiling phase and the frozen particles should have the same sodium content as the liquid they are originating from. But this could not be observed, the vapor part of the plume is practically sodium free [Schneider *et al.*, 2009]. In Brilliantov *et al.* (2008) the maximal velocity of ice particles stemmimg from freezed droplets that are sputtered from violently boiling water was estimated employing basic thermodynamical arguments. The authors found that for the "Cold Faithful" model the maximum speeds are only a few meters per second, which is significantly smaller than the velocity expected from observed plume properties, which is of the order of hundred meters per second. Thus, the "Explosive Boiling" model seems to be a less favored scenario.

4.2.2 'Frigid Faithful' model

Also a rather early model is the "Clathrate Reservoir" hypothesis by Kieffer *et al.* (2006), also known as "Frigid Faithful" model. In this scenario it is assumed that the plume activity is based on the decomposition of CO_2, CH_4, and N_2 clathrates located underneath an H_2O-CO_2 ice shell [Gioia *et al.*, 2007], see Figure 4.9 for a schematic picture.

Plume jets that are produced via this scenario are similar to jets ejecting from comets. The process does not require the presence of liquid water as plume source (→ "dry" model), so it can take place below 273 K. The clathrates containing plume gases like CO_2 or CH_4, that could be located below a 3.5 km thick H_2O-CO_2 ice cap seal [Kieffer *et al.*, 2006], become unstable at high temperatures and/or low pressures. So near cracks or heat sources the clathrates would decompose into (volatile) gas and solid ice. The volatile gases would advect up to the surface through the Tiger Stripe faults. But this process does not produce the water gas directly, water vapour would be created by sublimation of the ice particles that is caused by the drop of total pressure. But this might be difficult to be accomplished thermodynamically, especially at the low temperatures assumed in the "Frigid Faithful" model.

The "Clathrate Reservoir" model is capable to explain the large amount of volatile gases (CO_2, CH_4, N_2) in the plume (the solubility of these gases is much higher in clathrate hydrates than in liquid water). However, the most severe problem of this model, which is based on a "dry" scenario, where Enceladus is totally frozen, is that it cannot explain the observed sodium in the icy plume particles (Type III). A way out of this problem could be - supposed a liquid salt water reservoir had ever existed on Enceladus - to suggest a salty ice layer (brine pocket) below the surface that may supply the plume with salty particles. But (i) this salt storage will be depleted over time, and (ii) this assumption seems to be geophysically unlikely. Furthermore, the "Frigid Faithful" model can also not account for the detection of micrometer-sized plume particles since these cannot be produced by sublimation [Porco *et al.*, 2006]. And a quantitative study of Brilliantov *et al.* (2008)

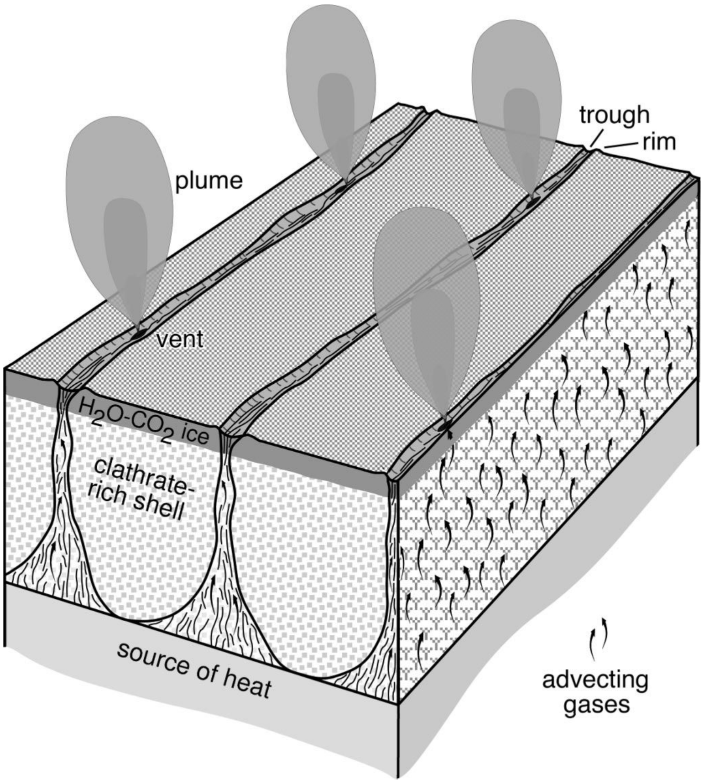

Figure 4.9: Schematic illustration of the Frigid Faithful model.
Source: G. Gioia *et al.* (2007), *"Unified model of tectonics and heat transport in a frigid Enceladus"*.

showed that for the Frigid Faithful hypothesis there might be an issue concerning the momentum transfer from gas to ice grains, because the low temperatures of this model ($\sim$ 140-170 K) suggest a vapor too thinned out which would not fit the detected high particle fluxes of the plume.

To conclude, though clathrate decomposition and sublimation may take place to produce the volatile gases, they seem not to be crucial processes for plume formation.

4.2.3 Shear Heating Model / Sublimation from Warm Ice

Another early plume formation scenario is the 'Shear Heating' model, also called 'Tectonic Meltwater' model, proposed by Nimmo *et al.* (2007). They postulated that tidally induced shearing motion in the South Polar ice cap, i.e. strike-slip motion along faults in the upper, brittle ice layer, and viscous heating in the ductile ice at depth, produces frictional heat. This energy produced by shearing is used both for heating and vapor sublimation. If an ocean exists between the rocky core and the ice mantle, so that the tidal displacements of the ice mantle can be large, the mechanism can be efficient. The heat generated can be transferred by conduction, by the flow of vapour through the cracks, and by diffusion of vapour (if the ice is porous). As a consequence, the ice should be warmed up in the vicinity of the Tiger Stripes along a relatively thin zone going downward into the ice mantle. The equilibrium temperature distribution cutting a shear zone in the South Polar ice cap is shown in Figure 4.10 [Nimmo *et al.*, 2007, Ingersoll and Pankine, 2010].

The heating produces low-salinity meltwater situated in the cracks. This model can explain the measured heat flow and the detected vapor production rate [Spencer *et al.*, 2009]. But the model cannot account directly for the observed non-water gases. Furthermore, the model overrates

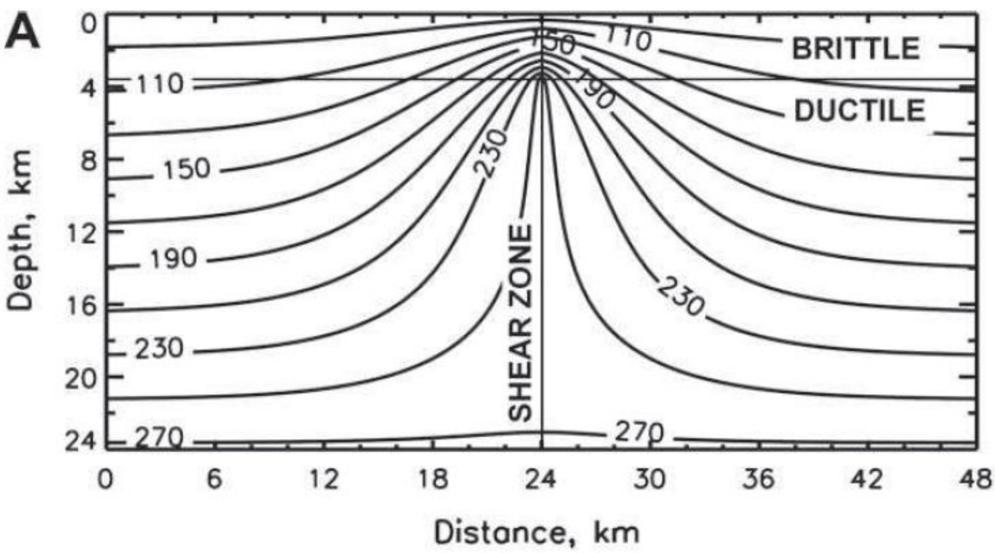

Figure 4.10: Equilibrium temperature distribution based on the 'Shear Heating' model in a vertical plane cutting a shear zone in the South Polar ice mantle. The original model was proposed by Nimmo *et al.* (2007), and then reproduced by Ingersoll and Pankine (2010).
Source: A.P. Ingersoll and A.A. Pankine (2010), *"Subsurface heat transfer on Enceladus: Conditions under which melting occurs"*.

the performance of vapor transport because it does not take condensation of the vapour on the enclosing ice walls into account, as remarked by Ingersoll and Pankine (2009).

If the subsurface liquid reservoir is a global one it separates the ice mantle from the rocky core, which leads to larger shear velocity and greater tidal heating. Assuming a global subsurface water reservoir one can explain the right shear velocities that are needed for appropriate values of the ice viscosity [Nimmo *et al.*, 2007]. Otherwise, if such an ocean is missing, unusual small numbers for the ice shell viscosity would be required. Nimmo *et al.* (2007) conclude that, in order to generate the required shear velocities, it might be probable that a subsurface ocean, either just locally or even globally, exists on Enceladus.

4.2.4 'Deep Source' model

The 'Deep Source' mechanism, proposed by Schmidt *et al.* (2008), states that a gas-particle mixture is flowing through fractures in Enceladus' ice crust, that extend down to a deep lying liquid-water reservoir. The vapour forms by evaporation at depth from the liquid-water reservoir at temperatures close to or at the triple point of water. Particles then condense on their way up through the fractures, the icy grains perform wall collisions and decelerate, and are then re-accelerated through the back-pressurized gas flow. Repeated wall collisions of grains induce an effective friction which explains the reduced grain velocity [Schmidt *et al.*, 2008]. The gas can be accelerated in the crack channels to high speeds. Variation of channel width causes transitions to supersonic velocities, just as in a nozzle [Schmidt *et al.*, 2008]. Figure 4.11 shows a schematic sketch of the gas flow and condensation in a crack channel within Enceladus' ice shell.

Ingersoll and Pankine (2010) emphasize that in a crack filled with gas, evaporation and condensation are so fast that the gas vapor pressure in the cells and in the open fractures is roughly equal to the saturation vapor pressure of the surrounding ice. This physical principle restricts the

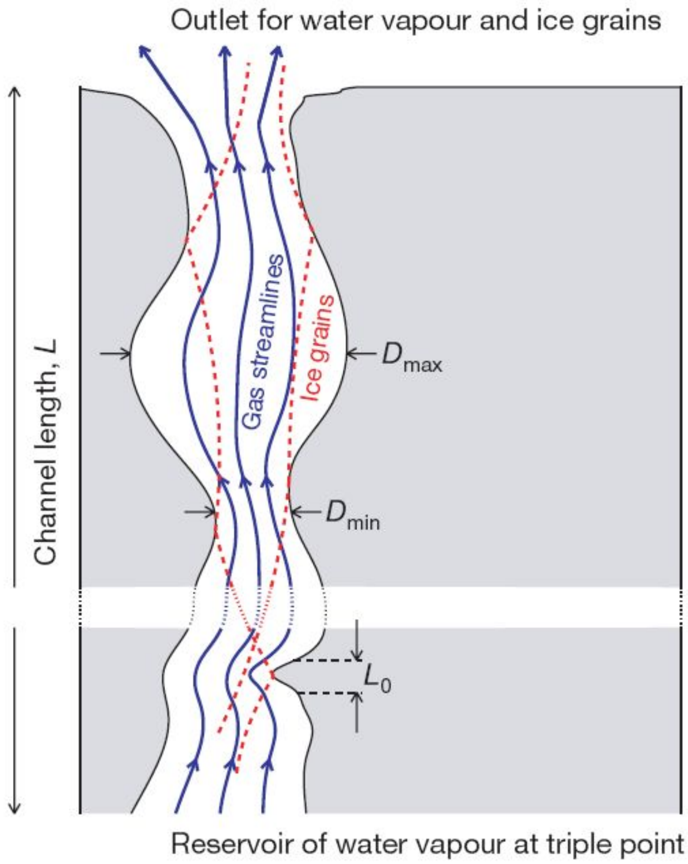

Figure 4.11: Schematic illustration of the gas flow and condensation in a crack channel through the ice mantle for the 'Deep Source' model.
Source: J. Schmidt *et al.* (2008), *"Slow dust in Enceladus' plume from condensation and wall collisions in tiger stripe fractures"*.

capability of ice to transport the detected heat to the surface without melting. Small differences between the gas and the saturation vapor pressure can cause large water mass fluxes between the walls and the gas. These fluxes are responsible that the gas pressure maintains a value at the ice wall saturation pressure. Evaporation and condensation occur under reversible, quasi-equilibrium conditions. Ingersoll and Pankine (2010) use a hydrodynamical model to demonstrate that if the heat is produced on $\lesssim$ 1 m wide fractures in the brittle ice region (which is near the surface), and if the fractures open and close during orbital motion [Hurford *et al.*, 2007], the upstreaming vapor flow is able to transport the heat away.

Postberg *et al.* (2009) showed that concerning vaporization from a water surface in a crack of constant width, heat cannot be carried upward within the water fast enough to restore the latent heat loss that is caused by evaporation at the water surface. The water column would quickly freeze at the water surface. For an assumed high evaporation rate of about 200 $\mathrm{kg\,s^{-1}}$, the cross-sectional area of the evaporation zone must be several orders of magnitude larger than the area venting to space, e.g. Postberg *et al.* (2009) estimated a surface area in the order of square kilometers. If the area were too small, inplausibly large temperature gradients would be required to counteract the loss due to latent heat generation. A sketch of this picture of having an outflow from a large evaporation area is shown in Figure 4.12.

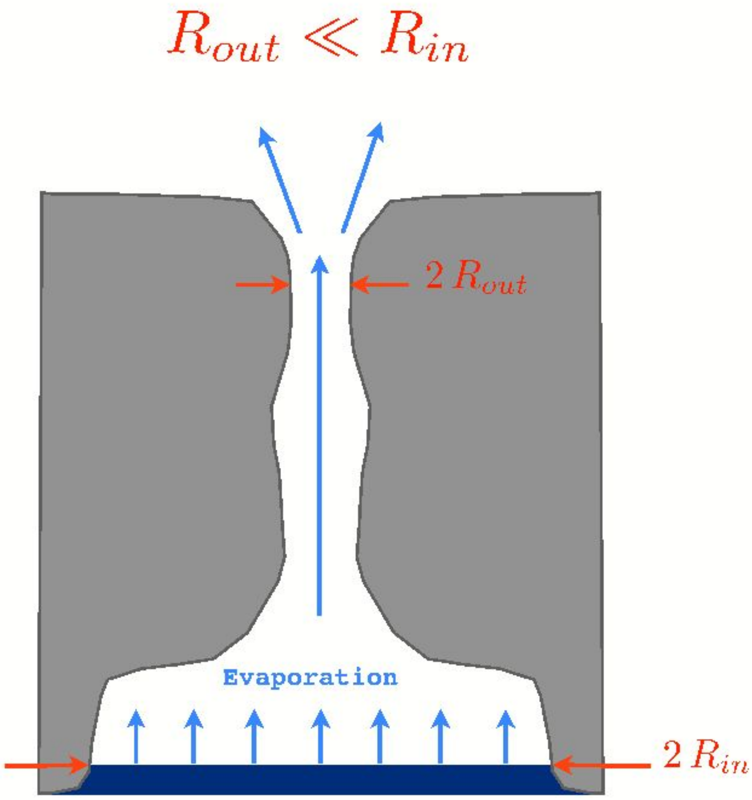

Figure 4.12: Illustrative sketch of gas evaporating from a subsurface liquid and flowing through cracks to vacuum following Postberg *et al.* (2009). A huge liquid/gas interface is assumed because it is argued that for a too small evaporation area inplausibly large temperature gradients would be needed to sustain the heat flow required for steady state gas evaporation.

Source: F. Postberg *et al.* (2009), *"Sodium salts in E-ring ice grains from an ocean below the surface of Enceladus"*, supplementary information.

Nakajima and Ingersoll (2016a) investigate how crack width and depth to the liquid water interface affect major physical plume properties, like mass flow rate and heat flow. They use a hydrodynamical model to calculate the flow dynamics in the fracture channel and the interaction between the flow and the ice walls. The model could explain the measured vapor mass flow rate of the plume when the channel width is 0.05-0.075 m for a fracture with a uniform width. Also a tapering crack, i.e. a crack which is wider ($\sim$1 m) at the bottom at the liquid-vapor interface and becomes tighter (0.05-0.075 m) at shallower depths, can explain the detected mass and heat flows. A wider width of about 1 m is necessary at the bottom to prevent freezing at the liquid-vapor interface. A schematic illustration of the model of Nakajima and Ingersoll (2016a) showing a uniform crack in the ice mantle and the basic mass flow and heat transfer processes is shown in Figure 4.13.

Ingersoll and Nakajima (2016b) studied how the liquid flows within the crack vent up to its height of zero buoyancy. They are critically questioning some assumptions in the calculations of Postberg *et al.* (2009) concerning the area of the evaporation zone. Using different parameters Ingersoll and Nakajima (2016b) found that the evaporating area can be small (e.g. the cross-section of a narrow crack), and thus a big vapor chamber acting as a plume source, as it was demanded by Postberg *et al.* (2009), is not necessary (e.g. the power radiated to space was not taken into

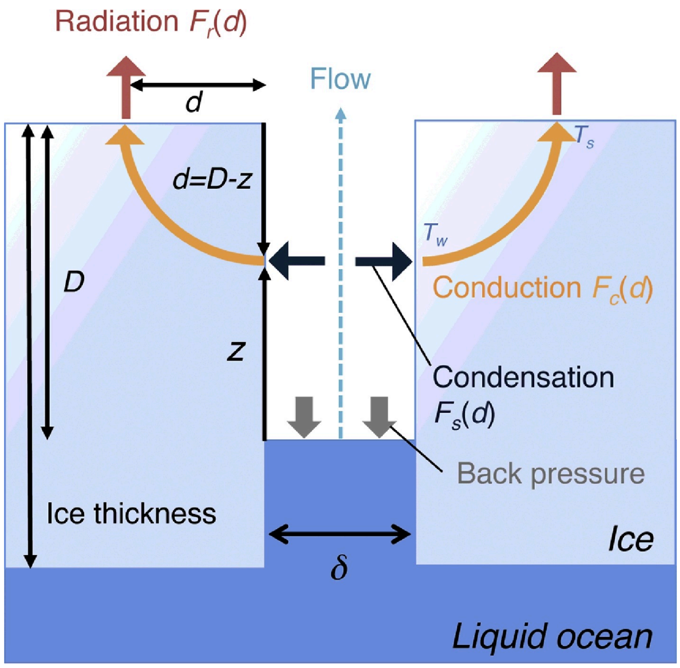

Figure 4.13: Schematic view of the model of Nakajima and Ingersoll (2016a) showing a uniform crack in the ice shell. The evaporation is controlled by the back pressure of the flow. Some of the vapor condenses onto the ice walls at each depth d, and latent heat is transferred to the ice walls ($F_s(d)$). The heat is conducted in the ice ($F_c(d)$) and eventually radiated to space ($F_r(d)$).
Source: M. Nakajima and A.P.Ingersoll (2016a), *"Controlled boiling on Enceladus. 1. Model of the vapor-driven jets"*.

account by the latter authors, and Ingersoll and Nakajima (2016b) use in their calculations a thermal expansion coefficient $\alpha = 26 \times 10^{-6}\,\mathrm{kg\,s^{-1}}$, which is about one order of magnitude smaller than that of Postberg *et al.* (2009), $\alpha = 200 \times 10^{-6}\,\mathrm{kg\,s^{-1}}$.

Geometry of the plumbing system

The plumbing system might be made up of concentrated flow in slots, cracks, fractures or channels, or distributed porous flow, or something in between [Spencer *et al.*, 2018]. Crack channels might exist in a variety of geometric forms, they may have kinks, narrowings, throats, branchings, etc., and they could be even connected to a complex network. Ocean-to-surface conduits can be initiated either from a crack at the ocean or a fracture from the surface. To form a conduit started from the surface would need tensile stresses that overcomes overburden pressure [Crawford and Stevenson, 1988] Fractures that initiates from the surface are able to propagate down for depth $D < 25$ km and ice tensile strength 3 MPa [Rudolph and Manga, 2009]. Water-filled fracture channels that start at the ocean can penetrate the ice shell more easily than cracks that start at the surface, and breaking of ice can occur even nearby its melting point [Schulson, 2001]. That behavior is due to the fact that the stress trying to close the fracture is the pressure head difference between the ice column and the water column, which is more effective than the pressure head difference between ice and vacuum [Crawford and Stevenson, 1988]. Additionally gas exsolution can also account for the buoyancy of the rising water column [Crawford and Stevenson, 1988]. The ocean could also be overpressured [Manga and Wang, 2007], which would favour crack propagation. Ocean-to-surface channels could build at the present moon's eccentricity if $D \lesssim 10$ km. But crack vents may have also built during a higher eccentricity episode in Enceladus' history, when stresses were larger.

From ice glacier theory it follows that a narrow channel undergoing unidirectional flow is unstable to the creation of discrete pipes [Walder, 1982]. However, this instability might be suppressed by horizontal water transport which is driven by tidal forces [Kite and Rubin, 2016]. A study of the cross-sectional evolution of englacial meltwater conduits [Dallaston and Hewitt, 2014] shows that pipes may also be unstable to perturbations perpendicular to the flow direction. It may be also unlikely for conduits or slots to pinch off at a certain depth since any turbulent dissipation would be concentrated at the pinch-point which would cause melt-back counteracting the squeezing.

Matson *et al.* (2012) propose a model describing an ongoing water circulation system below Enceladus' active south polar area, where a closed plumbing system reach a water table just about 1 km below the surface. An illustrative sketch of the model is shown in Figure 4.14.

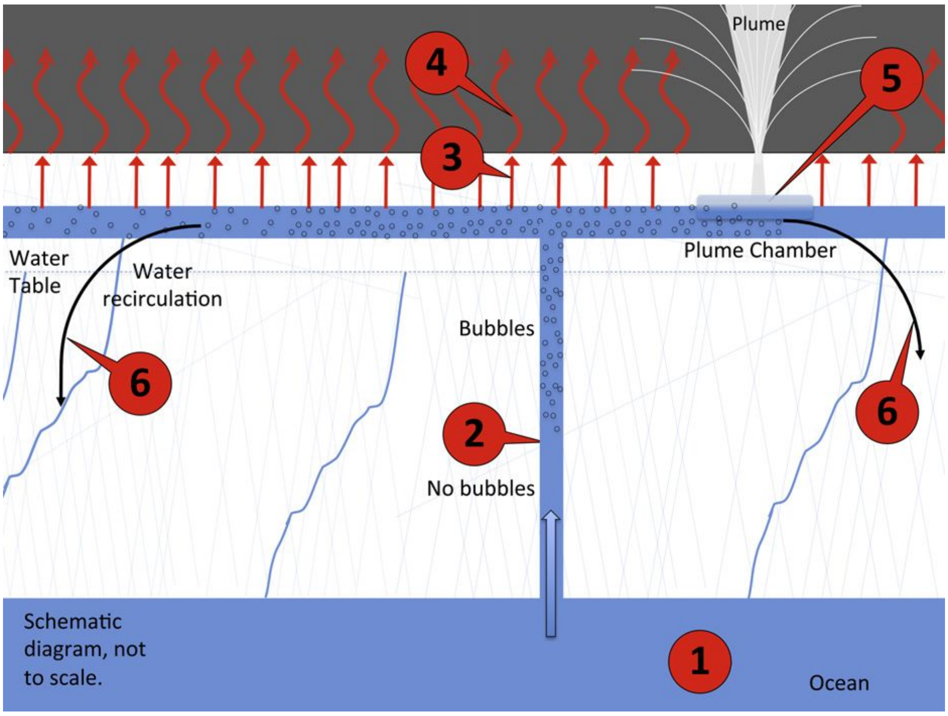

Figure 4.14: Illustrative sketch of the hypothesis of ocean water circulation by Matson *et al.* (2012).
Source: D.L. Matson *et al.* (2012), *"Enceladus: A hypothesis for bringing both heat and chemicals to the surface"*.

The model assumes a subsurface ocean below an estimated average crustal thickness of 10 km (Fig. 4.14:(1)). Dissolved gases that are contained in the ocean water can exsolve away when pressure drops below the saturation pressure for the specific gas type (the gas is primarily CO_2). When water rises towards the surface pressure decrease and exsolution takes place. If enough gas has exsolved, the seawater gets buoyant concerning the solid ice mantle and rises towards the surface provided cracks or fissures in the ice have builded appropriate channels (Fig. 4.14:(2)). Heat conduction to the surface and heat radiation to space is indicated in Fig. 4.14:(3),(4), respectively. The upward going column is a bubbly mixture, which enters a water brine reservoir located 1 km below the surface. Some of the water flows into plume chambers (Fig. 4.14:(5)), where ocean water and its contents are converted into vapor and aerosols. Water vapor and icy grains are then streaming through the plume conduits by the mechanism described by Schmidt *et al.* (2008), and finally erupting as plume on the surface. Heat is delivered by a temperature gradient of 2° C between the warm ocean (∼ 0° C) and the freezing salty water, and the gas loss is responsible for the density increase that causes the liquid to fall off via fissures or cracks back to the sea (Fig. 4.14:(6)), and thus closing the water circulation. However, the closed plumbing system might be unstable, the pipes could burst causing the system being reverted to a vapor deposition system.

Kite and Rubin (2016) use a model of tidally-flexed slots that penetrate the ice shell. An illustrative sketch of this mechanism is shown in Figure 4.15. This model is able (i) to explain the persistency of plume activity during the tidal period, (ii) the delay of eruptions relative to tidal stress, (iii) the continuity of plume activity over geological time scales, and (iv) the observed heat output of Enceladus [Kite and Rubin, 2016]. The tidally produced heat keeps off the cracks from being freezed-out and prevents the subsurface sea from freezing. The model of Kite and Rubin (2016) predicts crack widths of 1-2 m for the water-filled part of the slot. Channels with widths smaller than 1 m freeze shut in that model. These model calculations give larger crack widths than the estimations of Ingersoll and Pankine (2010) and Nakajima and Ingersoll (2016), which give values of about 0.05-0.1 m for channels at shallower depths. Thus, it seems plausible that cracks become narrower towards the surface.

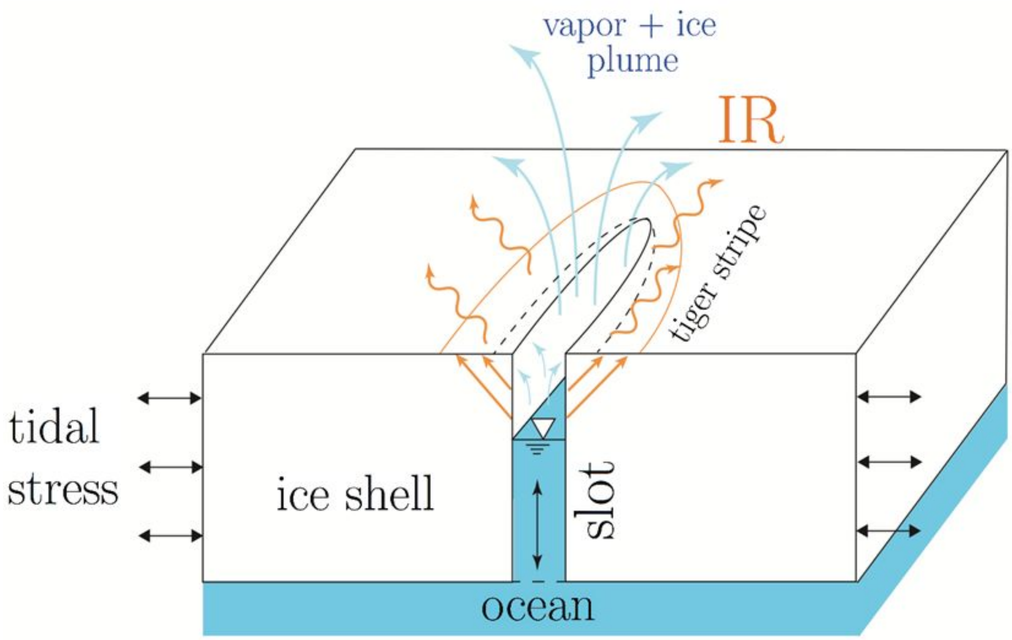

Figure 4.15: Schematic illustration of the model by Kite and Rubin (2016). In this picture, the plume activity varies on tidal timescales due to flexing of crack slots by tidal stresses. The heat produced prevents the slots against freeze-out.

Source: E.S. Kite and A.M. Rubin (2016), *"Sustained eruptions on Enceladus explained by turbulent dissipation in tiger stripes"*.

Today's accepted picture of the plume mechanism is based on the Deep Source model, i.e. it combines the original version of Schmidt *et al.* (2008), and the enhancements and modifications of Ingersoll and Pankine (2010), Postberg *et al.* (2009), Nakajima and Ingersoll (2016a), Ingersoll and Nakajima (2016b), Matson *et al.* (2012), and Kite and Rubin (2016). A summary of the current picture of the geometry and the main processes of the plumbing system is given in Figure 4.16.

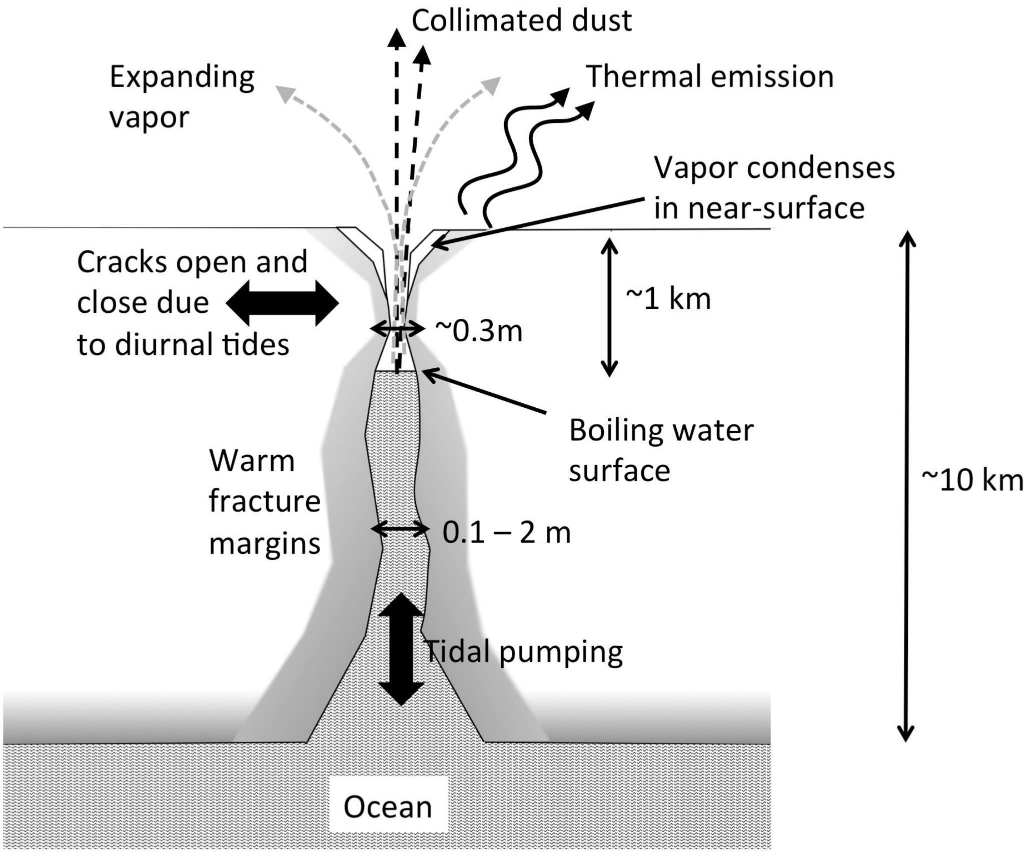

Figure 4.16: Illustrative sketch of the current picture of the principal mechanisms of the plumbing system which connects the subsurface liquid ocean with the surface south polar region.
Source: J.R. Spencer *et al.* (2018), *"Plume Origins and Plumbing: From Ocean to Surface"*.

4.2.5 Plume simulations

When talking about plume simulations one has to distinguish two main cases: (i) simulating the plumbing system from the subsurface ocean to the surface of Enceladus, and (ii) simulating the propagation of the gas and icy particle jets from Enceladus' surface up to space. Various physical simulation methods have been applied by several authors.

Schmidt *et al.* (2008) simulate the flow of vapour and grains through subsurface crack channels and calculate also nucleation and growth rates of icy particles. They use a hydrodynamical model and formulate a complete set of equations including conservation of mass, momentum, energy, and formulas describing the nucleation and growth rate. This set of equations is then solved numerically. Different channel geometries are considered in that study by using a random channel model, where the channel width $D(z)$ is given by a superposition of sine functions [Schmidt *et al.*, 2008]

$$D(z) = \sum_i A_i \sin(k_i z + 2\pi\xi)\,, \tag{4.1}$$

where A_i are the amplitudes, ξ is a uniformly distributed random variable, and the wave numbers k_i are defined as

$$k_i = \frac{1}{2}\Big(\frac{2\pi}{L}\Big)\, i \;<\; k_c = \Big(\frac{2\pi}{L_0}\Big)\,, \tag{4.2}$$

with the cutoff wave number k_c and the cutoff length L_0. An exponentially decaying correlation function is assumed:

$$< D(z)\, D(z') > - < D(z) >^2 \propto \exp\left[- \frac{|z - z'|}{L_0} \right], \tag{4.3}$$

where L_0 is associated with the correlation length. Channels are generated by choosing randomly the correlation length L_0 and the minimal width $D_{\min}/D_{\max}$ and the phase parameter ξ. Total channel length is fixed to $L = 150\,\mathrm{m}$, and the minimal widths and correlation lengths are uniformly distributed in the intervals $0.3 < D_{\min}/D_{\max} < 0.9$, and $5\,\mathrm{m} < L_0 < 40\,\mathrm{m}$, respectively.

A typical solution of a simulation of Schmidt *et al.* (2008) is shown in Figure 4.17, where gas density, mass fraction, gas speed and temperature is drawn along a random crack channel.

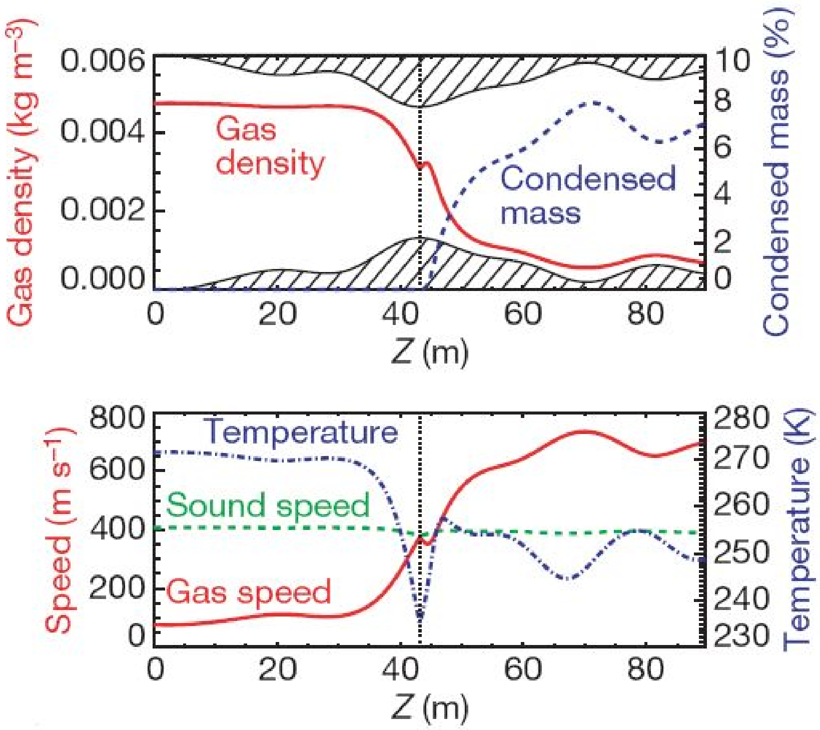

Figure 4.17: Solution of a typical simulation of Schmidt *et al.* (2008). The upper plot shows gas density and mass fraction of icy grains along a random crack channel. The lower graphic displays the gas velocity and temperature.
Source: J. Schmidt *et al.* (2008), *"Slow dust in Enceladus' plume from condensation and wall collisions in tiger stripe fractures"*.

The gas velocity rises significantly at the narrowest point in the channel (nozzle throat) and reaches supersonic speed, which is the same effect as in a turbine nozzle.

In the studies of Ingersoll and Pankine (2010) and Nakajima and Ingersoll (2016a) a one-dimensional hydrodynamical model is used to simulate the vapor and ice grain flow in the subsurface plumbing system where steady-state equations describing the flow and flow-wall interactions are solved. The governing equations represent conservation of mass, momentum and energy of the flow. Besides the flow driving terms, like pressure gradient, and gravitational force, terms characterizing the interaction with the walls are taken into account: terms describing (a) the vapor mass and energy fluxes from the ice walls, (b) the momentum loss because of vapor condensation on the walls, and (c) cooling effects due to heat transfers between flow and ice walls are included in these equations. They performed simulations with different crack geometries: (i) straight cracks, where the crack width is constant ($d\delta/dz = 0$) along the channel length, and (ii) non-uniform cracks ($d\delta/dz \neq 0$), where (a) a sine-shaped curve $\delta(z) = \delta_0(1 + X\sin(2n\pi z/D))$, and (b) an exponential curve $\delta(z) = \delta_{\text{top}} + (\delta_{\text{bottom}} - \delta_{\text{top}})\exp(-z/Y)$ is used. The crack depth is $D = 1.5 - 4.5\,\text{km}$, and crack width values δ range from 0.05 to 0.1 m. Simulation results of Nakajima and Ingersoll (2016a) for the velocity are given in Figure 4.18. The left plot (Figure 4.18a) shows the vertical profile of the velocity for the case of straight width cracks, the right graph (Figure 4.18b) depicts the case of non-straight cracks (where an exponential function is used).

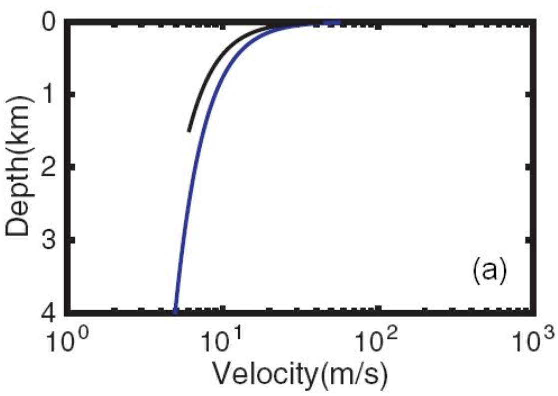

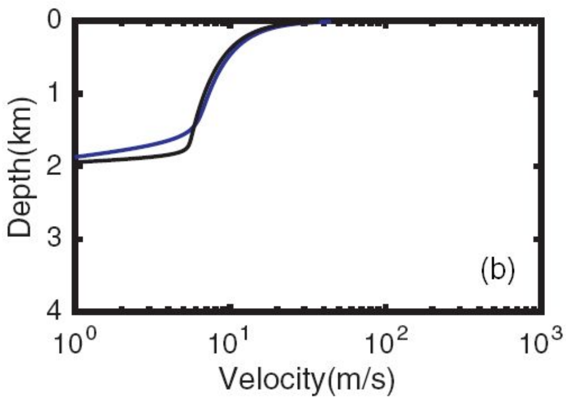

Figure 4.18: Vertical profile of the velocity for simulation results of Nakajima and Ingersoll (2016a) (Plots are adapted from [Nakajima and Ingersoll, 2016a]). (a) velocity profile for the case of straight widths, black line is for crack width $\delta = 0.05\,\text{m}$, crack depth $D = 1.5\,\text{km}$, blue line is for $\delta = 0.0075\,\text{m}$, $D = 4\,\text{km}$; (b) velocity profile for the case of non-straight widths $d\delta/dz \neq 0$, the crack width is wide at the bottom ($\delta = 1\,\text{m}$) and becomes narrower towards the surface, two cases $\delta(z) = 0.05 + 0.95\exp(-z/40)$ (black) and $\delta(z) = 0.05 + 0.95\exp(-z/100)$ (blue) are drawn.

Source: M. Nakajima and A.P. Ingersoll (2016), *"Controlled boiling on Enceladus. 1. Model of the vapor-driven jets"*.

The flow velocity increases on the way towards the surface, in the case of a straight crack the velocity increases moderately and stays below 100 $\text{m}\,\text{s}^{-1}$ even at the surface (Depth = 0 km) (Figure 4.18a), but for the non-straight crack case the simulations show a sharp increase at depths where the crack width δ sharply decreases ($\rightarrow$ nozzle effect).

Yeoh *et al.* (2015, 2017) performed plume simulations both for the subsurface plumbing system and the plume propagation from the surface up to higher altitudes. For the subsurface region they simulate an isentropic quasi-1-dimensional flow that expands trough a converging-diverging nozzle, see Figure 4.19.

The simulations show that the flow is subsonic before the narrowing nozzle and becomes supersonic after passing through the nozzle. To model the plume above ground Yeoh *et al.* (2015, 2017) use the Direct Simulation Monte Carlo (DSMC) method for the near-field ($\sim$ O(10 km)), where the gas is represented by a large number ($10^{12} - 10^{17}$) of discrete computational particles, and a free-molecular model for the far-field ($\sim$ O(100-1000 km)), see Figure 4.20.

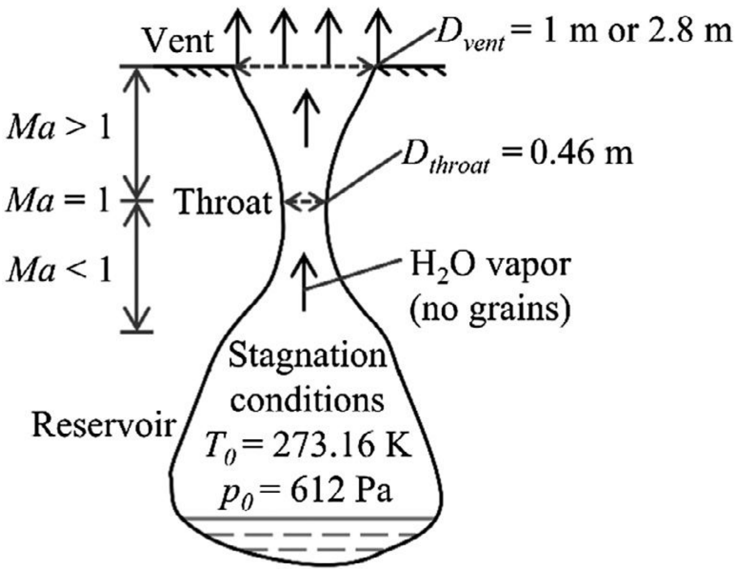

Figure 4.19: Schematic illustration of the subsurface flow model of Yeoh *et al.* (2015), where an isentropic 1-dim flow is simulated that expands through a narrowing nozzle.
Source: S.K. Yeoh *et al.* (2015), *"On understanding the physics of the Enceladus south polar plume via numerical simulation"*.

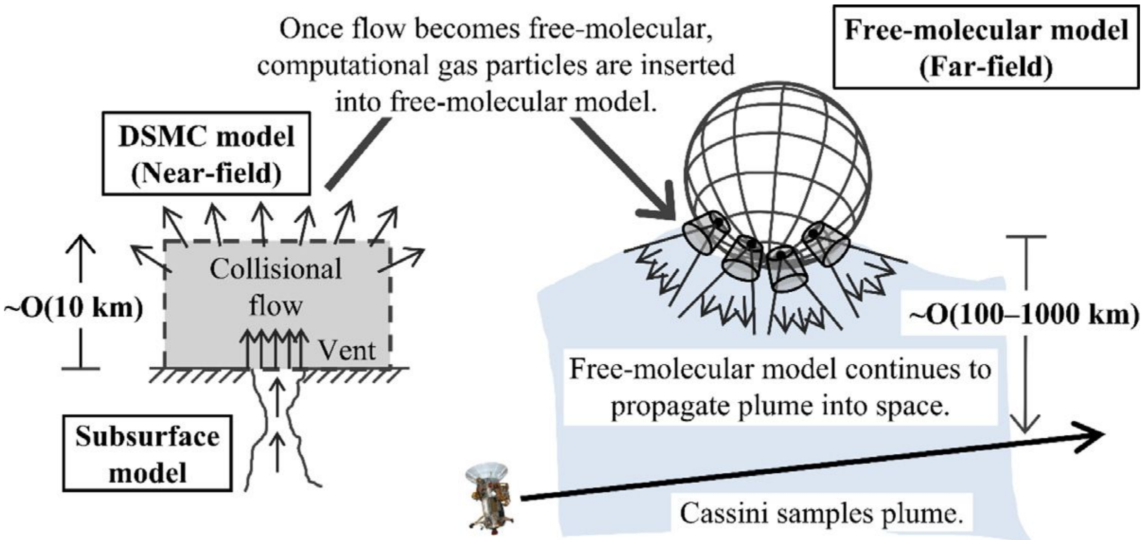

Figure 4.20: Schematic illustration of the plume model of Yeoh *et al.* (2017). The Plume is modeled by a large number of discrete point-like particles that move along ballistic trajectories and perform collisions. For statistical sampling the Direct Simulation Monte Carlo (DSMC) method is employed.
Source: S.K. Yeoh *et al.* (2017), *"Constraining the Enceladus plume using numerical simulation and Cassini data"*.

The movements of the discrete point-like particles (which travel along ballistic trajectories), and the collisions among the particles are computed in Monte Carlo simulations.

5. Ice Channel Thermodynamics

An important issue of the so-called "plumbing-system problem" is that the crack channels must be kept open, and water must be able to flow through the fractures and cracks without freezing. The heat contained in the water flow will be transferred to the surrounding ice, so there will be a significantly heat loss along the way up to the surface. If a crack's width is too small it will obviously freeze-out, and also water moving up a crack which is very long could have lost so much heat that its temperature drops down to $T \sim 0°$ C, i.e. to a point where it would start to freeze. So it is an interesting question which crack width and depth combinations produce stable situations where freezing inside the crack is avoided and the water plume flow is able to reach the surface.

5.1 Pipe model

To investigate the heat loss along a crack channel a simple model of a cylindrical hollow pipe of length L and radius r surrounded by an unbounded, infinitely extended block of ice is considered. Water flows through the pipe with velocity v, having an initial temperature T_{in} at $z = 0$, and a final temperature T_{out} at the end of the pipe ($z = L$). A schematic picture of this model is shown in Figure 5.1.

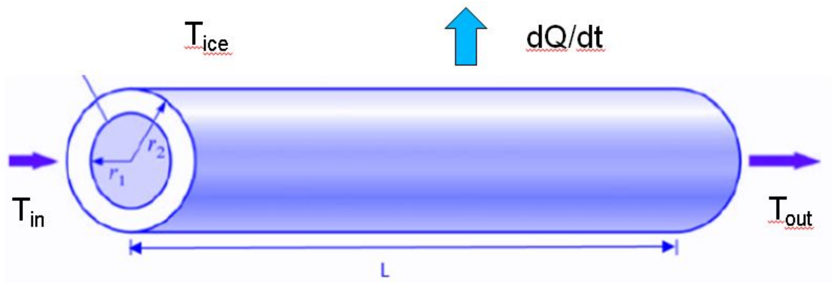

Figure 5.1: Schematic illustration of a cylindrical hollow pipe of length L and radius r surrounded by an infinitely extended block of ice.

The temperature T_{ice} of the embedding ice is for the general case a function of depth z, i.e. $T_{\text{ice}} = T_{\text{ice}}(z)$.

5.1.1 Case 1: $T_{\mathrm{ice}} = \mathbf{const}$

First, the more simple case is considered where the temperature of the surrounding ice T_{ice} does not depend on the depth z, i.e. $T_{\mathrm{ice}} = \mathrm{const}$. The heat loss of water (per time) is related to the fluid flow rate and the temperature drop between inlet and outlet:

$$\frac{dQ}{dt} = \frac{dm}{dt}\, c\, (T_{\mathrm{out}} - T_{\mathrm{in}})\,, \tag{5.1}$$

where dm/dt is the mass flow per time, c is the specific heat capacity, and T_{in}, T_{out} are the water temperatures when entering, leaving the pipe, respectively.

Generally, the heat transfer at an interface between two media 1 and 2 with temperatures T_1 and T_2, repectively, is described by the heat transfer formula

$$\frac{dQ}{dt} = h\, A\, (T_2 - T_1)\,, \tag{5.2}$$

where dQ/dt is the energy flow at the interface between medium 1 and 2 as seen from medium 1, i.e. if $dQ/dt > 0$ heat flows into medium 1 and increases the energy in it, if $dQ/dt < 0$ heat flows from medium 1 and decreases the energy in it; $h\,[\mathrm{W\,m^{-2}\,K^{-1}}]$ is the heat transfer coefficient between medium 1 and 2, which is a property of the system, and A is the characteristic area of the contact interface.

The heat change in an infinitesimal section of the pipe (cylinder with radius r and length dz, see Figure 5.2) is given by

$$d\,\frac{dQ}{dt} = \frac{dm}{dt}\, c\, dT(z) = \frac{dm}{dt}\, c\, \frac{dT(z)}{dz}\, dz\,, \tag{5.3}$$

and the heat transfer through the infinitesimal surface (ring with radius r and length dz) at the interface is described by

$$d\,\frac{dQ}{dt} = -\, h\, 2\pi r\, dz\, (T(z) - T_{\mathrm{ice}})\,, \tag{5.4}$$

where h is the heat transfer coefficient between water and ice, r is the pipe radius, and dz is the length of the infinitesimal pipe section.

Setting (5.3) equal (5.4) gives a differential equation

$$\frac{dT(z)}{dz} = -\, \alpha\, (T(z) - T_{\mathrm{ice}})\,, \tag{5.5}$$

where all factors have been condensed into a single constant α defined as

$$\alpha = \frac{h\, 2\pi r}{\frac{dm}{dt}\, c}\,. \tag{5.6}$$

Calculating the integral of (5.5)

$$\int_{T_{\mathrm{in}}}^{T(z)} \frac{dT'}{T' - T_{\mathrm{ice}}} = -\int_0^z \alpha\, dz'\,, \tag{5.7}$$

can be readily done and gives

$$\ln(T(z) - T_{\mathrm{ice}}) - \ln(T_{\mathrm{in}} - T_{\mathrm{ice}}) = -\, \alpha\, z\,. \tag{5.8}$$

The solution for the temperature T(z) along the pipe is then

$$T(z) = T_{\text{ice}} + (T_{\text{in}} - T_{\text{ice}}) \cdot \exp(-\,\alpha\, z)\,, \tag{5.9}$$

and the temperature at the end of the pipe is

$$T(z = L) = T_{\text{out}} = T_{\text{ice}} + (T_{\text{in}} - T_{\text{ice}}) \cdot \exp(-\alpha\, L)\,. \tag{5.10}$$

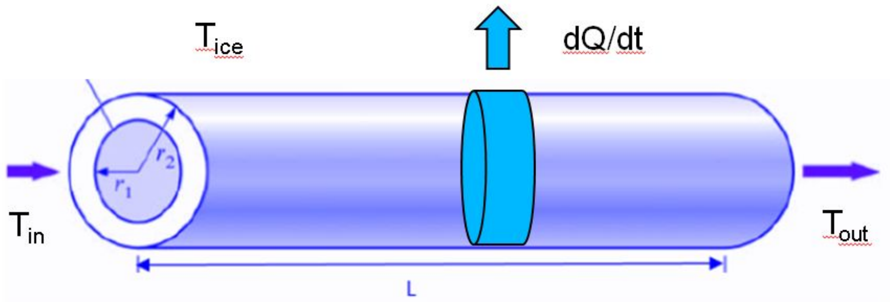

Figure 5.2: Heat flow dQ/dt through an infinitesimal pipe section, a ring with radius r and length dz.

Using equation (5.4) and (5.10), the complete heat transfer through the surface along the whole pipe of radius r and length L to the surrounding ice can be formulated as

$$\frac{dQ}{dt} = h\, 2\pi r\, L\, \theta_{\text{m}}\,, \tag{5.11}$$

where h is the heat transfer coefficient between water and ice, and θ_{m} is the logarithmic mean temperature difference (LMTD) given by

$$\theta_{\text{m}} = \frac{T_{\text{in}} - T_{\text{out}}}{\ln\left(\frac{T_{\text{in}} - T_{\text{ice}}}{T_{\text{out}} - T_{\text{ice}}}\right)}\,. \tag{5.12}$$

One important factor in (5.6) is the heat transfer coefficient h for the water-ice transition. Unfortunately, no explicit list values for $h_{\text{water-ice}}$ are available (compared to list values of various physical quantities available in engineering science, e.g. table of water density as function of temperature). But an answer can be found in the realm of glacier physics. Several glacier physics studies examine the flow of water in crevasses and meltwater channels [Lock, 1990, Shatalina, 1990, Isenko *et al.*, 2005, Vatne and Irvine-Fynn, 2016], and analyse the heat exchange between water and the surrounding ice on the channel wall, which causes ice freezing and melting. A schematic illustration of a general example of a glacier channel is given in Figure 5.3.
It is shown that the temperature of the water stream reaches exponentially an asymptotic non-zero equilibrium value when flowing through an englacial channel [Isenko *et al.*, 2005]:

$$T(x) = T_{\infty} + (T_0 - T_{\infty}) \cdot \exp\left(-\,\frac{x}{x_0}\right), \tag{5.13}$$

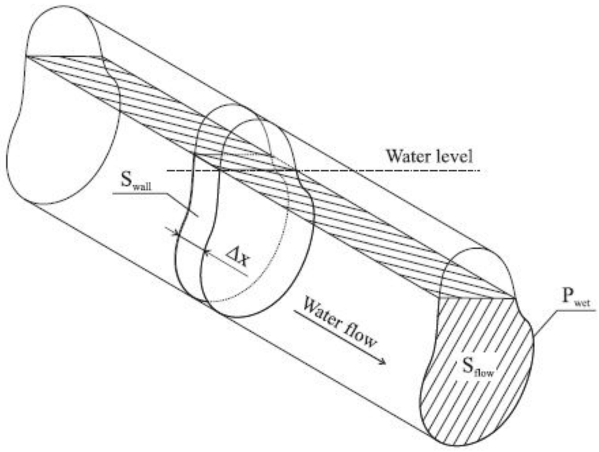

Figure 5.3: Schematic illustration of a general example of a glacier channel.
Source: E. Isenko *et al.* (2005), *"Water temperature in englacial and supraglacial channels: Change along the flow and contribution to ice melting on the channel wall"*.

where T_0 is the initial temperature, T_∞ is the equilibrium temperature, x denotes the length coordinate of the glacier channel, and the constant x_0 is given by

$$x_0 = \frac{c_{\mathrm{w}} \rho_{\mathrm{w}} R}{B}\,, \tag{5.14}$$

where c_{w} is the specific heat of water, ρ_{w} is the density of water, R is the hydraulic radius, and B equals $2.64 \times 10^3\,\mathrm{J\,m^{-3}\,K^{-1}}$ for turbulent flow at $0°\,C$ [Lock, 1990]. For a system of a solid surface in contact with a flowing liquid the constant B is the factor in the formula that relates the flux of the heat exchange j with the water flow velocity v and the temperature difference ΔT [Lock, 1990, Shatalina, 1990, Isenko *et al.*, 2005]:

$$j = B\,v\,\Delta T\,. \tag{5.15}$$

Writing the flux j as

$$j = \frac{1}{A}\frac{dQ}{dt}\,, \tag{5.16}$$

and comparing (5.15) with the heat transfer formula (5.2) one finds for the heat transfer coefficient h the relation

$$h = B\,v\,. \tag{5.17}$$

The exponential decay law (5.10) for the temperature of water flowing through a glacial channel has also been confirmed experimentally by Isenko *et al.* (2005). The experimental setup consisting of an ice sample where water flows through an artificial channel is shown in Figure 5.4.
There is good agreement between the measured results and the theoretical model of the temperature distribution along the channel [Isenko *et al.*, 2005]. It should be emphasized that the characteristic exponential decay length x_0 of equation (5.10) does not depend explicitly on the flow velocity v, i.e.

$$x_0 \neq x_0(v)\,. \tag{5.18}$$

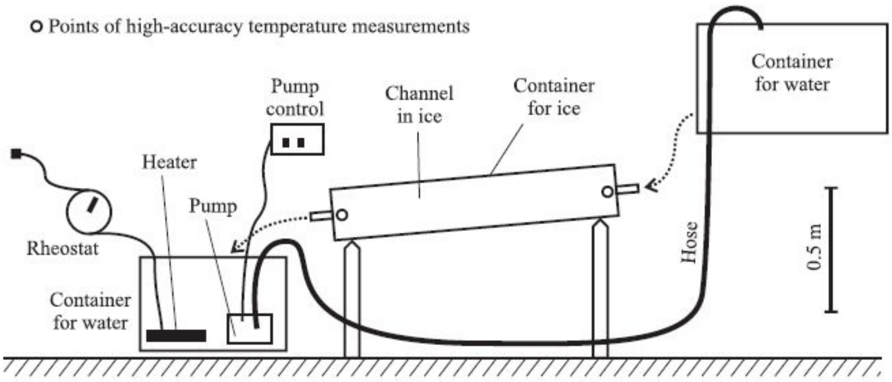

Figure 5.4: Illustration of the experimental setup by E. Isenko *et al.* (2005) containing an artificial ice channel.
Source: E. Isenko *et al.* (2005), *"Water temperature in englacial and supraglacial channels: Change along the flow and contribution to ice melting on the channel wall"*.

Heat Transfer Coefficient h for the Water-Ice Transition:

To determine the heat transfer coefficient h for the water-ice transition glacier studies use results from hydrodynamics of fluids in solid pipes. The basic results concerning the physics of heat transfer in pipe hydrodynamics go back to the early work obtained by Dittus and Boelter (1930).

The turbulent flow in a circular tube can be described by some characteristic numbers: the Nusselt number Nu, the Reynolds number Re, and the Prandtl number Pr (see e.g. Taler and Taler (2017)). The Nusselt number Nu is related to the heat transfer coefficient

$$\mathrm{Nu} = h\,\frac{d}{\lambda}\,, \tag{5.19}$$

where $d = 2r$ is the diameter of the pipe, and λ is the thermal conductivity,
the Reynolds number Re is defined as

$$\mathrm{Re} = \frac{\rho\, v\, d}{\eta}\,, \tag{5.20}$$

where ρ is the density of the fluid, v is the velocity of the fluid, and η is the dynamical viscosity, and the Prandtl number Pr is given as

$$\mathrm{Pr} = \frac{\eta\, c}{\lambda}\,, \tag{5.21}$$

where c is the heat capacity. The three numbers are not independent and are related by following empirical relationship that is known as the Dittus-Boelter equation [Dittus and Boelter, 1930, Winterton, 1998]:

$$\mathrm{Nu} = C\,\mathrm{Re}^{0.8}\,\mathrm{Pr}^{n}\,, \tag{5.22}$$

where C is an empirical constant, and the exponent of the Prandtl number is $n = 0.4$ for heating of the fluid ($T_{\mathrm{wall}} > T_{\mathrm{fluid}}$), and $n = 0.3$ if the fluid is being cooled ($T_{\mathrm{wall}} < T_{\mathrm{fluid}}$). For the case of water flowing in a channel within ice, the fluid will be cooled, thus $n = 0.3$, and with $C = 0.0265$ [Dittus and Boelter, 1930] equation (5.22) becomes

$$\mathrm{Nu} = 0.0265\,\mathrm{Re}^{0.8}\,\mathrm{Pr}^{0.3}\,. \tag{5.23}$$

The Dittus-Boelter equation is valid for smooth pipes and for the following conditions [Taler and Taler, 2017]:

$$
\begin{aligned}
0.6 &\leq \mathrm{Pr} \leq 160\,, && (5.24)\\
\mathrm{Re} &\geq 10^4\,, && (5.25)\\
L/d &\geq 60\,. && (5.26)
\end{aligned}
$$

With the relations worked out so far, one is now able to determine the heat transfer coefficient h for a water-ice pipe system. Proposing a sample calculation for water with an initial temperature of $T_{\mathrm{in}} = 100°\,\mathrm{C}$, and final temperature of $T_{\mathrm{out}} = 0°\,\mathrm{C}$, and under the assumption that several physical properties of water, namely density ρ, velocity v, dynamical viscosity η, specific heat c, and thermal conductivity λ are constant and have values for the reference point $\bar{T} = (0°\,\mathrm{C} + 100°\,\mathrm{C})/2 = 50°\,\mathrm{C}$. Taking values from a table of technical properties of water ["Table of Water Properties", 2006], water density $\rho = 988\,\mathrm{kg\,m^{-3}}$, and dynamical viscosity $\eta = 5.46 \cdot 10^{-4}\,\mathrm{Ns\,m^{-2}}$, and suggesting a fluid velocity $v = 240\,\mathrm{m\,s^{-1}}$ (that is the escape velocity of Enceladus), and a pipe diameter $d = 1\mathrm{m}$, the Reynolds number (5.20) calculates as

$$\mathrm{Re} = 4.34 \cdot 10^8\,. \tag{5.27}$$

With values for the specific heat of water $c = 4182\,\mathrm{J\,kg^{-1}\,K^{-1}}$, thermal conductivity $\lambda = 0.654$ $\mathrm{W\,m^{-1}\,K^{-1}}$, and the dynamical viscosity used for Re ["Table of Water Properties", 2006], one obtains for the Prandtl number

$$\mathrm{Pr} = 3.49\,. \tag{5.28}$$

Inserting the values for Re and Pr into (5.23) yields the Nusselt number value

$$\mathrm{Nu} = 313\,472\,. \tag{5.29}$$

The heat transfer coefficient h is given through (5.19)

$$h = \mathrm{Nu}\,\frac{\lambda}{d}\,, \tag{5.30}$$

and with the calculated Nusselt number one obtains

$$h = 205\,010\,\mathrm{W\,m^{-2}\,K^{-1}}\,. \tag{5.31}$$

5.1.2 Case 2: $T_{\mathrm{ice}} = T_{\mathrm{ice}}(z)$ linear function of z

As next step a more realistic case is examined where the ice temperature T_{ice} is a function of depth z, for simplicity a linear relation is assumed (which also seems not to be an unplausible suggestion). In this picture the ice temperature $T_{\mathrm{ice}}(z)$ is linearly decreasing towards the surface (increasing z) via following relation,

$$T_{\mathrm{ice}} = T_{\mathrm{ice}}(z) = T_{\mathrm{A}} - \frac{T_{\mathrm{A}} - T_{\mathrm{B}}}{L} \cdot z\,, \tag{5.32}$$

where $T_{\mathrm{A}} = T_{\mathrm{ice}}(0)$, $T_{\mathrm{B}} = T_{\mathrm{ice}}(L)$, $T_{\mathrm{A}} > T_{\mathrm{B}}$, see Figure 5.5 for a schematic illustration.

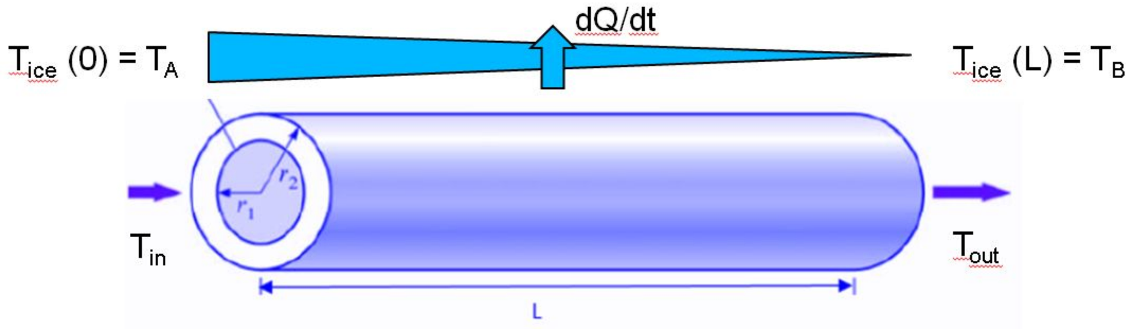

Figure 5.5: Heat flow through the surface of a cylindrical hollow pipe of length L and radius r surrounded by an infinitely extended block of ice for the case that the ice temperature $T_{\text{ice}}(z)$ decreases linearly with increasing z, i.e. towards the surface.

Taking equation (5.5) for the heat transfer and using the above linear expression (5.32) for the ice temperature $T_{\text{ice}}(z)$ yields

$$\frac{dT(z)}{dz} + \alpha\, T(z) = \alpha\, T_{\text{ice}}(z)\,, \tag{5.33}$$

$$\frac{dT(z)}{dz} + \alpha\, T(z) = \alpha\, T_{\text{A}} - \alpha\, \frac{T_{\text{A}} - T_{\text{B}}}{L} \cdot z\,, \tag{5.34}$$

$$\frac{dT(z)}{dz} + \alpha\, T(z) = f(z)\,, \tag{5.35}$$

which is a linear, inhomogenous 1st order ordinary differential equation (ODE).

This ODE can be readily solved:

(1) Solving the corresponding homogenous equation:

$$\frac{dT_{\text{h}}(z)}{dz} + \alpha\, T_{\text{h}}(z) = 0 \tag{5.36}$$

With the ansatz

$$T_{\text{h}}(z) = C\, \exp(\lambda\, z)\,, \tag{5.37}$$

one obtains the characteristic equation

$$\lambda + \alpha = 0 \;\Rightarrow\; \lambda = -\,\alpha\,, \tag{5.38}$$

and finally

$$T_{\text{h}}(z) = C\, \exp(-\alpha\, z)\,. \tag{5.39}$$

(2) Finding a particular solution $T_{\text{p}}(z)$:

Using the ansatz

$$T_{\text{p}}(z) = A\, z + B\,, \tag{5.40}$$

and inserting it into (5.34) one gets by comparison of coefficients the solution

$$T_{\text{p}}(z) = -\frac{T_{\text{A}} - T_{\text{B}}}{L} \cdot z + \left(T_{\text{A}} + \frac{T_{\text{A}} - T_{\text{B}}}{\alpha\, L}\right). \tag{5.41}$$

The general solution $T(z)$ is the sum of the solution of the homogenous ODE $T_{\mathrm{h}}(z)$ and the particular solution $T_{\mathrm{p}}(z)$

$$T(z) = T_{\mathrm{h}}(z) + T_{\mathrm{p}}(z)\,, \tag{5.42}$$

$$T(z) = C\,\exp(-\alpha\, z) - \frac{T_{\mathrm{A}} - T_{\mathrm{B}}}{L} \cdot z + \Big(T_{\mathrm{A}} + \frac{T_{\mathrm{A}} - T_{\mathrm{B}}}{\alpha\, L}\Big)\,. \tag{5.43}$$

The constant C is determined by imposing a boundary condition. Using the condition

$$T(z = 0) = T_0\,. \tag{5.44}$$

gives

$$C = T_0 - T_{\mathrm{A}} - \frac{T_{\mathrm{A}} - T_{\mathrm{B}}}{\alpha\, L}\,, \tag{5.45}$$

Thus, the final solution for the water temperature T(z) along the pipe channel within the ice in the case of linearly decreasing ice temperature has the following form

$$T(z) = \Big(T_0 - T_{\mathrm{A}} - \frac{T_{\mathrm{A}} - T_{\mathrm{B}}}{\alpha\, L}\Big) \cdot \exp(-\alpha\, z) \;-\; \frac{T_{\mathrm{A}} - T_{\mathrm{B}}}{L} \cdot z + \Big(T_{\mathrm{A}} + \frac{T_{\mathrm{A}} - T_{\mathrm{B}}}{\alpha\, L}\Big)\,. \tag{5.46}$$

Special cases:

$$T_{\mathrm{A}} = T_{\mathrm{B}} = T_{\mathrm{ice}} \neq T_{\mathrm{ice}}(z) \quad\Rightarrow\quad T(z) = (T_0 - T_{\mathrm{ice}}) \cdot \exp(-\alpha\, z) + T_{\mathrm{ice}}\,, \tag{5.47}$$

$$T(z = 0) = T_0\,, \tag{5.48}$$

$$T(z = L) = \Big(T_0 - T_{\mathrm{A}} - \frac{T_{\mathrm{A}} - T_{\mathrm{B}}}{\alpha\, L}\Big) \cdot \exp(-\alpha\, L) + T_{\mathrm{B}} + \frac{T_{\mathrm{A}} - T_{\mathrm{B}}}{\alpha\, L}\,, \tag{5.49}$$

$$T(z = L \to \infty) = T_{\mathrm{B}}\,, \tag{5.50}$$

$$T(z; \alpha \to 0) = T_0 \quad (\frac{dT}{dz} = 0 \;\Rightarrow\; T = \mathrm{const} = T_0)\,, \tag{5.51}$$

$$T(z; \alpha \to \infty) = T_{\mathrm{A}} - \frac{T_{\mathrm{A}} - T_{\mathrm{B}}}{L} \cdot z \overset{(5.32)}{=} T_{\mathrm{ice}}(z)\,. \tag{5.52}$$

5.1.3 Effect on gravity and pressure

Gravity and pressure can be taken into account on the heat transfer equation by defining a hydrostatic potential

$$\Phi(z) = \rho\, g\, z + p(z)\,, \tag{5.53}$$

where ρ is the density, g the gravitational acceleration, and $p(z)$ is the pressure (depending on z). The heat transfer equation will be modified by a potential term:

$$\begin{aligned} \frac{dm}{dt}\, c\, dT(z) &= -\,h\, 2\pi r\, dz\, (T(z) - T_{\mathrm{ice}}(z)) - dV\, \frac{d\Phi}{dt}\,, \\ &= -\,h\, 2\pi r\, dz\, (T(z) - T_{\mathrm{ice}}(z)) - dm\, g\, \frac{dz}{dt} - \frac{dm}{\rho}\, \frac{dp}{dz}\, \frac{dz}{dt}\,. \end{aligned} \tag{5.54}$$

This gives a differential equation equivalent to (5.33)

$$\frac{dT(z)}{dz} = -\alpha\,(T(z) - T_{\text{ice}}(z)) - \frac{g}{c} - \frac{1}{c\rho}\frac{dp}{dz} \tag{5.55}$$

$$\frac{dT(z)}{dz} = -\alpha\Big(T(z) - (T_{\text{ice}}(z) - \frac{g}{\alpha c} - \frac{1}{\alpha c\rho}\frac{dp}{dz})\Big)\,. \tag{5.56}$$

Comparing (5.56) with (5.33) one notices that the effect on gravity and pressure can be interpreted as an effective shifted ice temperature $T'_{\text{ice}}(z)$

$$T_{\text{ice}}(z) \;\rightarrow\; T'_{\text{ice}}(z) = T_{\text{ice}}(z) - \frac{1}{\alpha c}\Big(g + \frac{1}{\rho}\frac{dp}{dz}\Big)\,. \tag{5.57}$$

The solution of the heat transfer ODE including gravity and pressure is then given by

$$\begin{aligned} T(z) \;=\; & \Big(T_0 - T_{\text{A}} + \frac{g}{\alpha c} + \frac{1}{\alpha c\rho}\frac{dp}{dz} - \frac{T_{\text{A}} - T_{\text{B}}}{\alpha\,L}\Big)\cdot\exp(-\alpha\,z) \;- \\ & - \;\frac{T_{\text{A}} - T_{\text{B}}}{L}\cdot z + \Big(T_{\text{A}} - \frac{g}{\alpha c} - \frac{1}{\alpha c\rho}\frac{dp}{dz} + \frac{T_{\text{A}} - T_{\text{B}}}{\alpha\,L}\Big)\,. \end{aligned} \tag{5.58}$$

Pure hydrostatic pressure:

Considering pure hydrostatic pressure in a pipe of length L:

$$p(z) = \rho\,g\,(L - z)\,. \tag{5.59}$$

Deriving with respect to z gives the hydrostatic relation

$$\frac{dp}{dz} = -\rho\,g\,. \tag{5.60}$$

The derivative of the potential $\Phi(z) = \rho\,g\,z + p(z)$, which can be found on the r.h.s of (5.54), is then

$$\begin{aligned} \frac{d\Phi(z)}{dz} &= \frac{d}{dz}\Big(\rho\,g\,z + p(z)\Big) \\ &= \rho\,g + \frac{dp}{dz} \\ &= \rho\,g - \rho\,g \\ &= 0\,. \end{aligned} \tag{5.61}$$

Thus, having a pure hydrostatic pressure, i.e. a pressure caused by gravity alone, there is no effect on the heat transfer equation.

5.2 Numerical Calculations

The heat transfer of water flow in a hollow pipe inside an ice mantle is numerically calculated using a Python program which evaluates solution (5.46) for various set of parameters (the Python program can be provided by the author on request).

Case 1: T_{ice} **= const :**

Figure 5.6 shows the outlet temperature $T_{\text{out}}(L)$ as a function of pipe length L for different values of the initial temperature T_{in}, pipe radius $r = 1\,\text{m}$, for the case having a constant ice temperature $T_{\text{ice}} = 80\,\text{K}$ (latter value is based on the “Cold Faithful” model [Porco *et al.*, 2006]). The horizontal dashed line points out the $T_0 = 273.15\,\text{K}$ threshold, water temperatures below this threshold do not exist physically, because at $T_{\text{out}} = T_0$ freezing sets in. A significant temperature drop is visible. In the region above the $T_0 = 273.15\,\text{K}$ threshold an approximately linear dependency on the the initial temperature T_{in} can be deduced, because the distance between neighbouring curves stays nearly constant. Since the threshold is reached at pipe length $L \sim 1000\,\text{m}$ it can be suggested that the length of realistic ice pipes are also in that order of magnitude. This might also be an indication that the depth of the ice mantle at Enceladus’ south polar region is rather small, which is in agreement with current studies that propose ice depths of only a few km (e.g. [Čadek *et al.*, 2016, Le Gall *et al.*, 2017]).

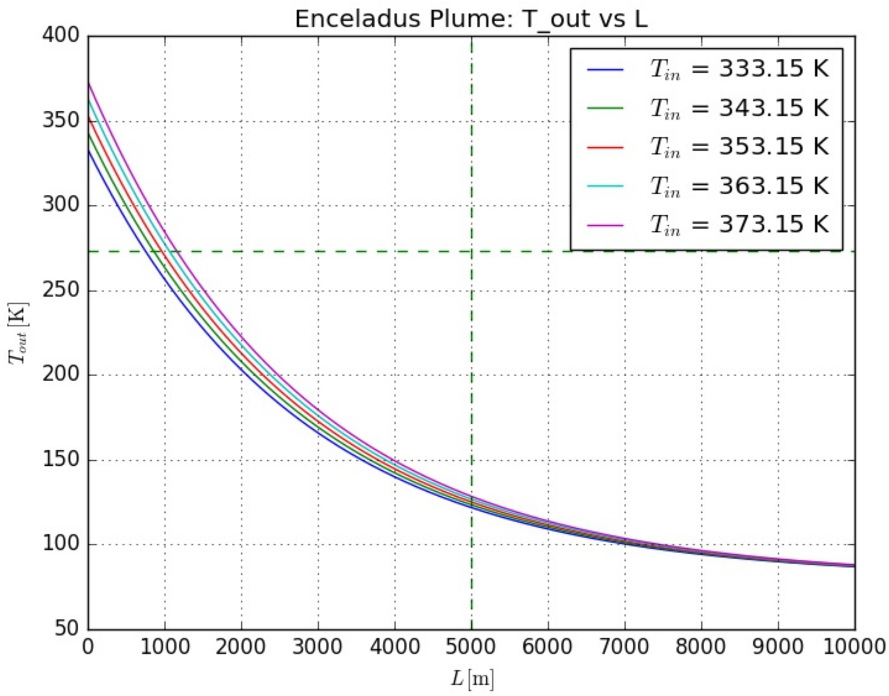

Figure 5.6: Temperature $T_{\text{out}}(L)$ of water flow in a hollow pipe inside an ice mantle of constant temperature $T_{\text{ice}} = 80\,\text{K}$ as a function of pipe length L for different values of the initial temperature $T_{\text{in}}(L)$, pipe radius $r = 1\,\text{m}$. The temperature drop reaches the $T_0 = 273.15\,\text{K}$ threshold (dashed green horizontal line) at pipe length $L \sim 1000\,\text{m}$. Above the threshold the solution curves $T_{\text{out}}(z; T_{\text{in}})$ show an (approximately) linear dependency on the initial temperature T_{in}.

In Figure 5.7 the dependence of the outlet temperature $T_{\text{out}}(L)$ on the pipe width $d = 2r$ is depicted for the case of constant ice temperature $T_{\text{ice}} = 80\,\text{K}$ ($T_{\text{in}} = 353.15\,\text{K}$ for all curves). One can clearly see a strong dependency for smaller pipe radii $r < 1\,\text{m}$ the temperature drops very steeply, wheras for larger radii $r > 1\,\text{m}$ the decrease is more moderately.

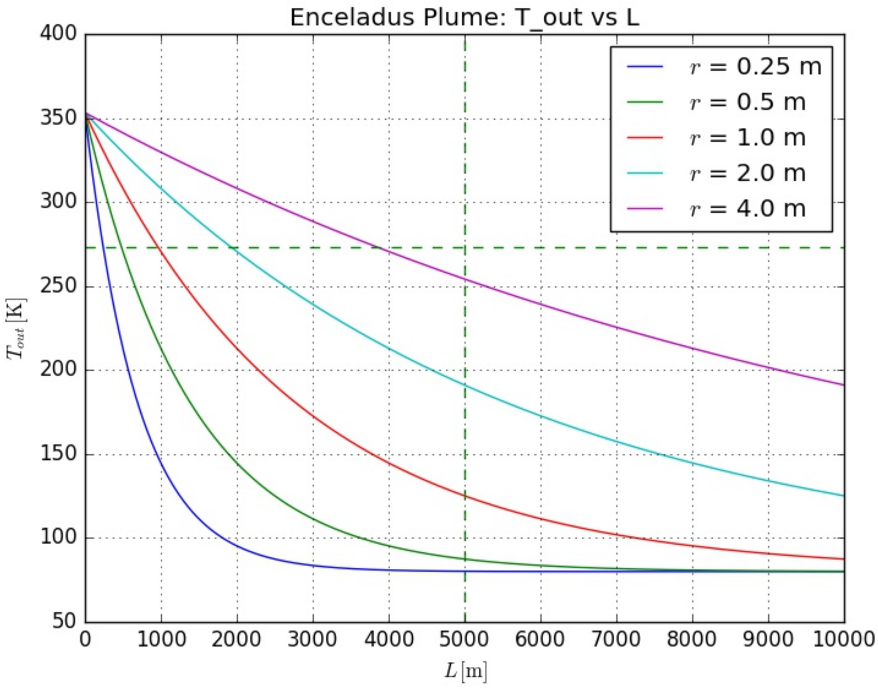

Figure 5.7: Temperature $T_{\text{out}}(L)$ of water flow in a hollow pipe inside an ice mantle of constant temperature $T_{\text{ice}} = 80\,\text{K}$ as a function of pipe length L for different values of the pipe radius r, $T_{\text{in}} = 353.15\,\text{K}$. The dashed green horizontal line represents the $T_0 = 273.15\,\text{K}$ threshold. For the smaller pipe radii $r < 1\,\text{m}$ temperature drops down significantly.

Case 2: $T_{\text{ice}} = T_{\text{ice}}(z)$ linear function of z:

The outlet temperature $T_{\text{out}}(L)$ as a function of pipe length L for different values of the initial temperature T_{in}, but same pipe radius $r = 1$, for the case where the ice temperature is a linear function of z, i.e. $T_{\text{ice}} = T_{\text{ice}}(z)$, is shown in Figure 5.8. The linear function of the ice temperature $T_{\text{ice}}(z) = T_{\text{A}} - (T_{\text{A}} - T_{\text{B}})/L \cdot z$ is fixed by the values $T_{\text{A}} = T_{\text{ice}}(z = 0\,\text{m}) = 270\,\text{K}$, $T_{\text{B}} = T_{\text{ice}}(z = L' = 5000\,\text{m}) = 80\,\text{K}$, pipe radius $r = 1\,\text{m}$, curves for different values of the initial temperature T_{in} are drawn. Also in this case the temperature drop is clearly visible, however it is more pronounced than in the constant ice temperature calculation (Figure 5.6). In the region above the $T_0 = 273.15\,\text{K}$ threshold the (absolute) slope value dT/dz increases with increasing initial temperature T_{in}, and the distance of neighbouring curves decreases with increasing distance z. Thus, in contrast to Figure 5.6 the dependency of $T(z)$ on the initial temperature T_{in} is no longer linear. The $T_0 = 273.15\,\text{K}$ threshold is reached at pipe length $L \sim 2500\,\text{m}$, which is a factor ~ 2.5 larger than for the constant ice temperature case.

Figure 5.9 depicts the dependence of the outlet temperature $T_{\text{out}}(L)$ on the pipe width $d = 2r$ for the case of linearly decreasing ice temperature $T_{\text{ice}}(z)$ ($T_{\text{in}} = 353.15\,\text{K}$ for all curves). A strong dependency on the pipe radius r can be seen also in this case, the temperature drop is more pronounced for smaller pipe radii $r < 1\,\text{m}$, but it is considerably slower than for the constant ice temperature case (Figure 5.7).

The dependency of the water flow temperature curve $T_{\text{out}}(L)$ on the exact form of the ice tem-

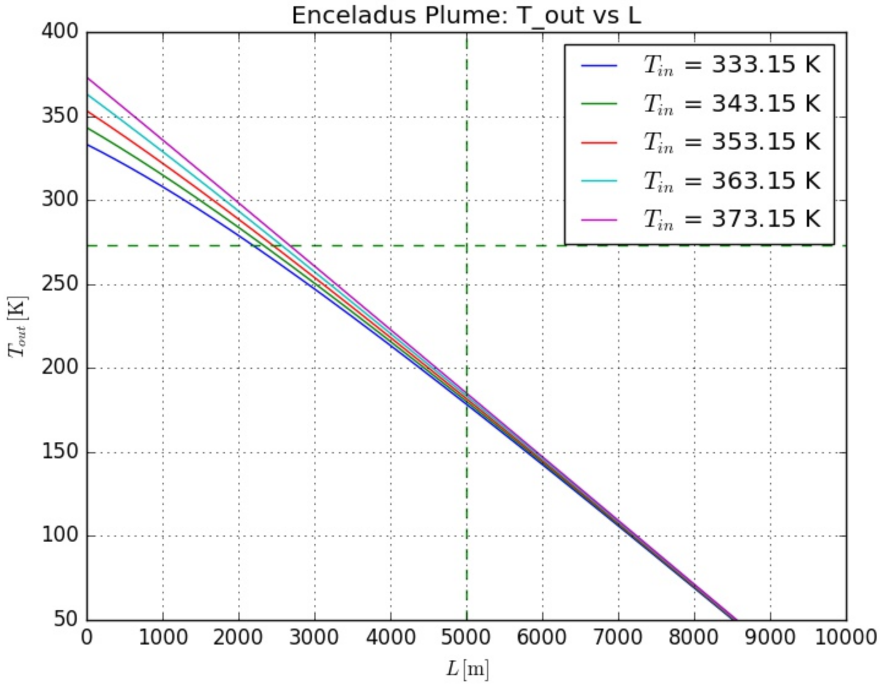

Figure 5.8: Temperature $T_{\text{out}}(L)$ of water flow in a hollow pipe inside an ice mantle, where the temperature $T_{\text{ice}}(z)$ is linearly decreasing towards the surface, as a function of pipe length L for different values of the initial temperature $T_{\text{in}}(L)$, pipe radius $r = 1$. The linear function $T_{\text{ice}}(z)$ is fixed by the values $T_{\text{ice}}(0\,\text{m}) = 270\,\text{K}$, $T_{\text{ice}}(L' = 5000\,\text{m}) = 80\,\text{K}$. The temperature decrease is slower than for the constant ice temperature case, and the dependency of $T_{\text{out}}(z; T_{\text{in}})$ on T_{in} is non-linear.

perature function $T_{\text{ice}}(z)$ has been studied by varying the fixing value $T_{\text{ice}}(z = L')$ that determines the slope of the linear function. Figure 5.10 shows the outlet temperature of the water flow for the case of linearly decreasing ice temperature $T_{\text{ice}}(L) = T_{\text{A}} - (T_{\text{A}} - T_{\text{B}})/L' \cdot z$ for different fixing values $T_{\text{ice}}(L' = 5000\,\text{m})$ (pipe radius $r = 1\,\text{m}$, inlet temperature $T_{\text{in}} = 353.15\,\text{K}$ for all curves). Increasing the fixing value $T_{\text{ice}}(L')$ means reducing the slope of the ice temperature function, which results in smaller heat loss so that the $T_0 = 273.15\,\text{K}$ threshold will be reached at a larger value of L.

In Figure 5.11 the calculation results of the outlet temperature $T_{\text{out}}(L)$ for constant pipe radius $r = 1\,\text{m}$ and varying inlet temperature T_{in} for the two cases, (a) constant ice temperature ($T_{\text{ice}} = 80\,\text{K}$), and (b) linearly decreasing ice temperature ($T_{\text{A}} = T_{\text{ice}}(0\,\text{m}) = 270\,\text{K}$, $T_{\text{B}} = T_{\text{ice}}(L' = 5000\,\text{m}) = 80\,\text{K}$), are compared. The decrease of temperature is much more pronounced for the constant ice temperature case.

Figure 5.12 shows a comparison of the calculation results of the outlet temperature $T_{\text{out}}(L)$ for constant inlet temperature ($T_{\text{in}} = 353.15\,\text{K}$), and varying pipe radius r for the two cases, (a) constant ice temperature ($T_{\text{ice}} = 80\,\text{K}$), and (b) linearly decreasing ice temperature ($T_{\text{A}} = T_{\text{ice}}(0\,\text{m}) = 270\,\text{K}$, $T_{\text{B}} = T_{\text{ice}}(L' = 5000\,\text{m}) = 80\,\text{K}$). The temperature drop is bigger for the constant ice temperature case, and the curves in (a) all have a convex shape, wheras the curves in (b) are concave for $r > 1\text{m}$.

An overview of the heat transfer scenarios that have been simulated and their respective parameters is shown in Table 5.1.

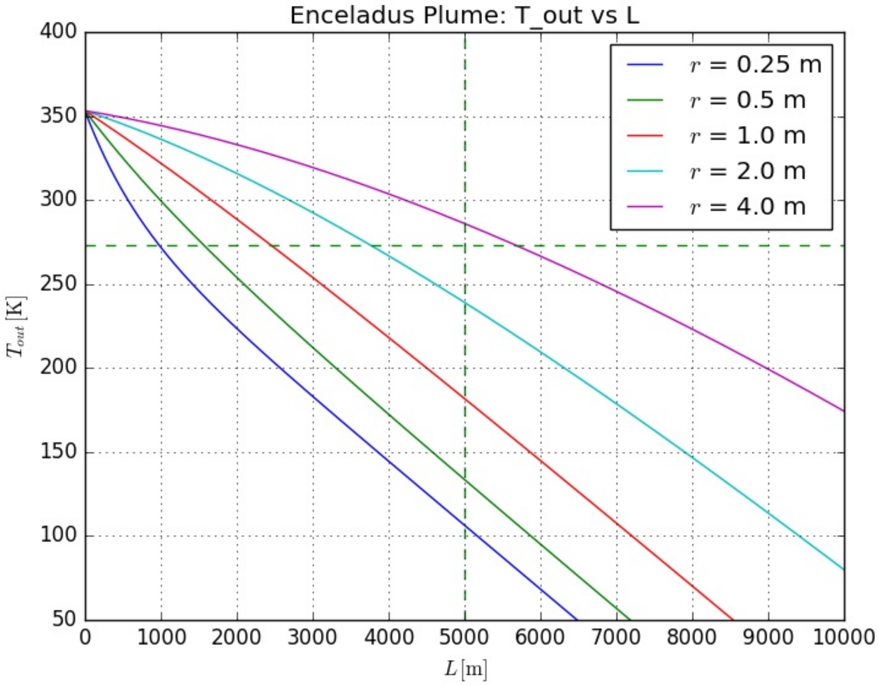

Figure 5.9: Temperature $T_{\text{out}}(L)$ of water flow in a hollow pipe inside an ice mantle for the linearly decreasing ice temperature case ($T_{\text{ice}} = T_{\text{ice}}(z)$), as a function of pipe length L for different values of the pipe radius r, $T_{\text{in}} = 353.15\,\text{K}$. For the smaller pipe radii $r < 1\,\text{m}$ the temperature drops down more rapidly, however, the decrease is not so fast as for the constant ice temperature case.

$T_{\text{ice}}(L)$	$T_{\text{ice}}(0)$ [K]	$T_{\text{ice}}(L')$ [K]	T_{in} [K]	r [m]
const.	80	80	333.15, 343.15, 353.15, 363.15, 373.15	1.0
const.	80	80	353.15	0.25, 0.5, 1.0, 2.0, 4.0,
linear	270	80	333.15, 343.15, 353.15, 363.15, 373.15	1.0
linear	270	80	353.15	0.25, 0.5, 1.0, 2.0, 4.0,
linear	270	80, 125, 170, 215, 260	353.15	1.0

Table 5.1: A list of the various heat transfer scenarios that have been calculated. The first column specifies the type of ice temperature function that have been used for the simulation, either 'constant' or 'linear'. Columns $T_{\text{ice}}(0)$, $T_{\text{ice}}(L')$ denote the ice temperatures at the lower end ($L = 0$) and the upper fixing value ($L = L'$) of the pipe, respectively.

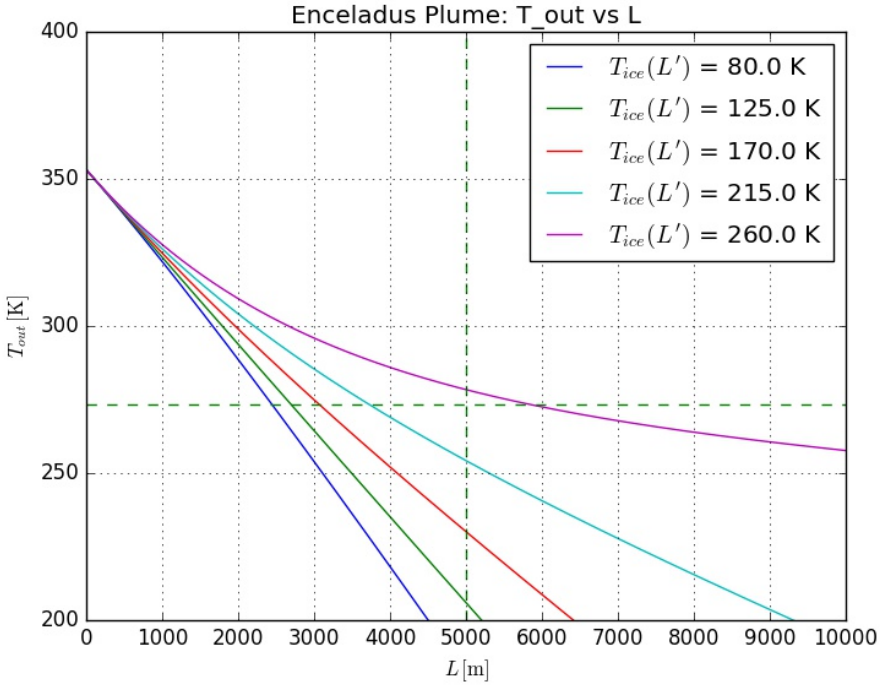

Figure 5.10: Temperature $T_{\text{out}}(L)$ of water flow in a hollow pipe inside an ice mantle for the linearly decreasing ice temperature case, $T_{\text{ice}}(L) = T_{\text{A}} - (T_{\text{A}} - T_{\text{B}})/L' \cdot z$, for different fixing values $T_{\text{B}} = T_{\text{ice}}(L' = 5000\,\text{m})$ (pipe radius $r = 1\,\text{m}$, inlet temperature $T_{\text{in}} = 353.15\,\text{K}$ for all curves). When decreasing the slope of the ice temperature function (by increasing the $T_{\text{ice}}(L')$ the $T_0 = 273.15\,\text{K}$ threshold will be reached at larger L values since the heat loss will be reduced.

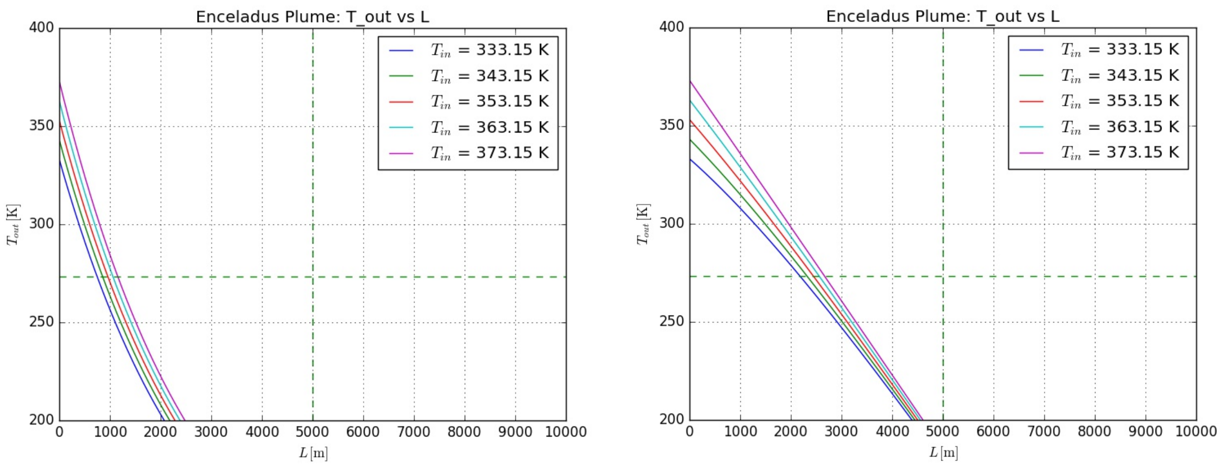

(a) $T_{\text{ice}} = \text{const}$ (b) $T_{\text{ice}} = T_{\text{ice}}(z) = T_{\text{A}} - \frac{T_{\text{A}} - T_{\text{B}}}{L} \cdot z$

Figure 5.11: Temperature $T_{\text{out}}(L)$ of water flow in a hollow pipe inside an ice mantle as a function of pipe length L for different values of the initial temperature $T_{\text{in}}(L)$, and pipe radius $r = 1\,\text{m}$. Comparison between (a) the constant ice temperature case and (b) the linearly decreasing ice temperature case. The temperature drops more rapidly (steeper slope) for the constant ice temperature case.

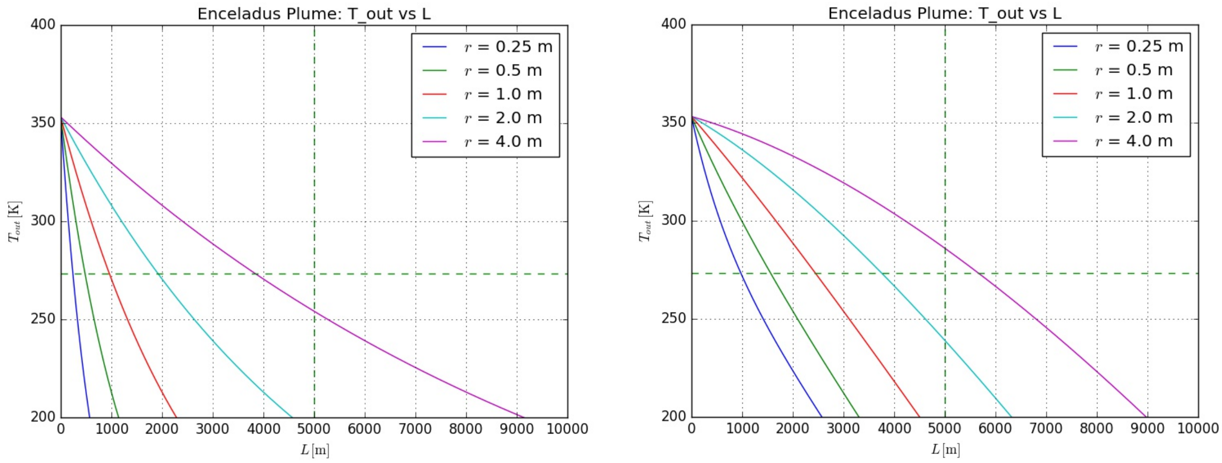

(a) $T_{\text{ice}} = \text{const}$

(b) $T_{\text{ice}} = T_{\text{ice}}(z) = T_{\text{A}} - \frac{T_{\text{A}} - T_{\text{B}}}{L} \cdot z$

Figure 5.12: Temperature $T_{\text{out}}(L)$ of water flow in a hollow pipe inside an ice mantle as a function of pipe length L for different values of the pipe radius r (initial temperature $T_{\text{in}} = 353.15\,\text{K}$). Comparison between (a) the constant ice temperature case and (b) the linearly decreasing ice temperature case. The temperature decreases faster (steeper slope) for the constant ice temperature case. All curves in (a) are convex, whereas curves in (b) are concave for a pipe radius $r > 1\,\text{m}$.

6. Vent Simulations

The physics of the water vapour flow through the subsurface plumbing system is studied in this work via numerical simulations of the underlying hydrodynamical equations, the Navier-Stokes equations. Subsurface crack channels are modelled as 2-dimensional geometrical objects, i.e. in this approximation it is assumed that the geometry of the crack is defined in x (width) and z (depth) coordinates, while it is infinitely extended in y (length) coordinate. This approach, namely to use effectively a (in one dimension infinitely extended) cuboid instead of a cylindrical shaped geometry, is justified in two respects: (i) symmetry arguments show that physical results are not restricted or truncated by the 2-dim approximation (it can be shown that the 2-dimensional model is the asymptotic limiting case of a 3-dimensional cylinder when the thickness of the cylinder converges to 0 [Vodák *et al.*, 2010]), and (ii) cracks that are extended in one (length) dimension are not an implausible conjecture since it has been observed that plume jets are forming continously extended curtains [Spitale *et al.*, 2015]. The distribution of pressure $p(\vec{r})$ and the velocity vector field $\vec{v}(\vec{r})$ inside the cracks are computed. An illustrative sketch of a water flow through a crack channel within the ice shell is shown in Figure 6.1.

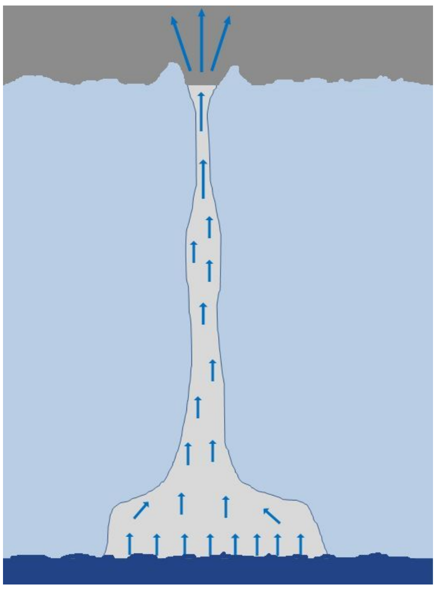

Figure 6.1: Illustrative sketch of a water vapour flow through a crack channel within the ice mantle from the subsurface ocean up to the moon's surface.

Simulations are performed for different vent geometries. Initially, simple geometries (2-dim rectangles) are studied to test and calibrate the simulation software modules (see Figure 6.2:(a)). Then, the calculations are extended to more complex crack channel geometries, including narrowings, throats, forking branches, and 'zig-zag' lines, which might represent physically more realistic fracture shapes (see Figure 6.2:(b)-(e)).

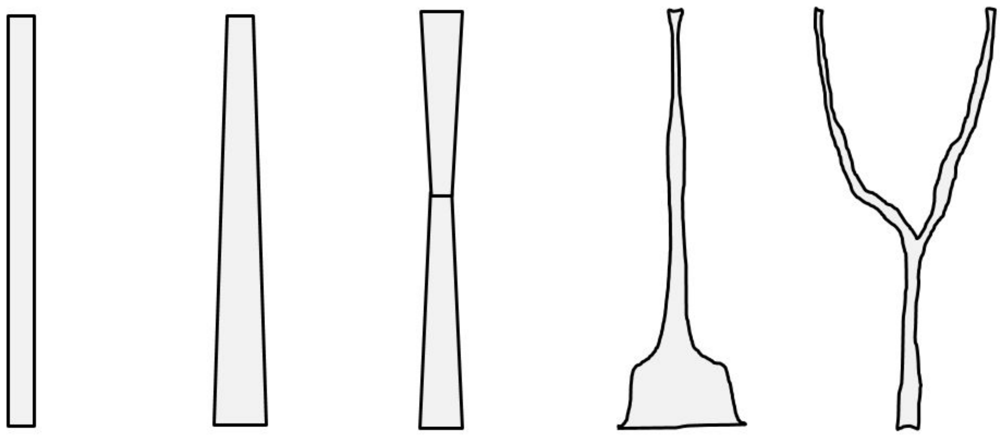

(a) (b) (c) (d) (e)

Figure 6.2: Vent geometries used for the numerical simulations: initially, simple rectangles (a) are simulated, then more complex geometries are considered (b)-(e), including narrowings, throats, kinks, forking branches, and 'zig-zag' lines.

6.1 Navier-Stokes Equations

The Navier-Stokes equations are the fundamental, general equations that describe the dynamics of viscous fluids. They are named after the French engineer and physicist Claude Luis Marie Henri Navier (1785-1836) and the Anglo-Irish physicist and mathematician George Gabriel Stokes (1819-1903), who developed the equations independently from each other. The Navier-Stokes equations are applied in various scientific and engineering areas. They are used to describe the water and vapour flow in a pipe, the air flow and turbulences around an aeroplane wing, the blood flow, ocean currents, atmospheric streams, and many more fluid phenomena.

The Navier-Stokes momentum equation is given by

$$\rho \left(\frac{\partial \vec{v}}{\partial t} + (\vec{v} \cdot \vec{\nabla}) \vec{v} \right) = -\vec{\nabla} p + \vec{\nabla} \cdot \bar{\bar{\sigma}} + \vec{f}\,, \tag{6.1}$$

where $\rho(\vec{r},t)$ is the fluid density, $\vec{v}(\vec{r},t)$ is the velocity field of the fluid, $p(\vec{r},t)$ is the fluid pressure, $\bar{\bar{\sigma}}(\vec{r},t)$ is the deviatoric stress tensor, and $f(\vec{r},t)$ is a general external force density (e.g. gravitational term $-\rho g\, \vec{e}_z$).

In addition the fluid has to obey the continuity equation which represents the mass conservation law

$$\frac{\partial \rho}{\partial t} + \vec{\nabla} \cdot (\rho \vec{v}) = 0\,. \tag{6.2}$$

The stress tensor $\bar{\bar{\sigma}}$ has the following general form

$$\bar{\bar{\sigma}} = \begin{pmatrix} \sigma_{xx} & \tau_{xy} & \tau_{xz} \\ \tau_{yx} & \sigma_{yy} & \tau_{yz} \\ \tau_{zx} & \tau_{zy} & \sigma_{zz} \end{pmatrix} , \tag{6.3}$$

with the diagonal elements σ_{ij}, and the off-diagonal elements τ_{ij} respectively given as

$$\begin{aligned} \sigma_{xx} &= -p + 2\mu\frac{\partial v_x}{\partial x} - \frac{2}{3}\mu\,\vec{\nabla}\cdot\vec{v}\,, & \tau_{xy} &= \tau_{yx} = \mu\left(\frac{\partial v_x}{\partial y} + \frac{\partial v_y}{\partial x}\right) \\ \sigma_{yy} &= -p + 2\mu\frac{\partial v_y}{\partial y} - \frac{2}{3}\mu\,\vec{\nabla}\cdot\vec{v}\,, & \tau_{yz} &= \tau_{zy} = \mu\left(\frac{\partial v_y}{\partial z} + \frac{\partial v_z}{\partial y}\right) \\ \sigma_{zz} &= -p + 2\mu\frac{\partial v_z}{\partial z} - \frac{2}{3}\mu\,\vec{\nabla}\cdot\vec{v}\,, & \tau_{zx} &= \tau_{xz} = \mu\left(\frac{\partial v_z}{\partial x} + \frac{\partial v_x}{\partial z}\right) \end{aligned} \tag{6.4}$$

where μ is the dynamical viscosity.

Writing down explicitely the components of the momemtum equation and inserting (6.4) one obtains the following set of equations

$$\begin{aligned} \rho\left(\frac{\partial v_x}{\partial t} + v_x\frac{\partial v_x}{\partial x} + v_y\frac{\partial v_x}{\partial y} + v_z\frac{\partial v_x}{\partial z}\right) &= -\frac{\partial p}{\partial x} + f_x + \mu\left(\frac{\partial^2 v_x}{\partial x^2} + \frac{\partial^2 v_x}{\partial y^2} + \frac{\partial^2 v_x}{\partial z^2}\right) \\ &\quad + \frac{1}{3}\mu\left[\frac{\partial}{\partial x}\left(\frac{\partial v_x}{\partial x} + \frac{\partial v_y}{\partial y} + \frac{\partial v_z}{\partial z}\right)\right] \\ \rho\left(\frac{\partial v_y}{\partial t} + v_x\frac{\partial v_y}{\partial x} + v_y\frac{\partial v_y}{\partial y} + v_z\frac{\partial v_y}{\partial z}\right) &= -\frac{\partial p}{\partial y} + f_y + \mu\left(\frac{\partial^2 v_y}{\partial x^2} + \frac{\partial^2 v_y}{\partial y^2} + \frac{\partial^2 v_y}{\partial z^2}\right) \\ &\quad + \frac{1}{3}\mu\left[\frac{\partial}{\partial y}\left(\frac{\partial v_x}{\partial x} + \frac{\partial v_y}{\partial y} + \frac{\partial v_z}{\partial z}\right)\right] \\ \rho\left(\frac{\partial v_z}{\partial t} + v_x\frac{\partial v_z}{\partial x} + v_y\frac{\partial v_z}{\partial y} + v_z\frac{\partial v_z}{\partial z}\right) &= -\frac{\partial p}{\partial z} + f_z + \mu\left(\frac{\partial^2 v_z}{\partial x^2} + \frac{\partial^2 v_z}{\partial y^2} + \frac{\partial^2 v_z}{\partial z^2}\right) \\ &\quad + \frac{1}{3}\mu\left[\frac{\partial}{\partial z}\left(\frac{\partial v_x}{\partial x} + \frac{\partial v_y}{\partial y} + \frac{\partial v_z}{\partial z}\right)\right]. \end{aligned} \tag{6.5}$$

These equations can be simplified for the actual vent simulations due to following assumptions:

1. the cracks are modelled as 2-dimensional geometrical objects $\rightarrow$ a 2-dim version of the Navier-Stokes equations can be used,
2. one is interested in a stable, stationary water flow $\rightarrow$ the time derivative terms can be omitted,
3. no external forces $\vec{f}$ are taken into account (e.g. gravitation is small on Enceladus compared to Earth, $g = 0.11\,\mathrm{m\,s^{-2}}$ only).

Thus, the momentum equations used for the simulations reduces to

$$\begin{aligned} \rho\left(v_x\frac{\partial v_x}{\partial x} + v_y\frac{\partial v_x}{\partial y}\right) &= -\frac{\partial p}{\partial x} + \mu\left(\frac{\partial^2 v_x}{\partial x^2} + \frac{\partial^2 v_x}{\partial y^2}\right) + \frac{1}{3}\mu\left[\frac{\partial}{\partial x}\left(\frac{\partial v_x}{\partial x} + \frac{\partial v_y}{\partial y}\right)\right] \\ \rho\left(v_x\frac{\partial v_y}{\partial x} + v_y\frac{\partial v_y}{\partial y}\right) &= -\frac{\partial p}{\partial y} + \mu\left(\frac{\partial^2 v_y}{\partial x^2} + \frac{\partial^2 v_y}{\partial y^2}\right) + \frac{1}{3}\mu\left[\frac{\partial}{\partial y}\left(\frac{\partial v_x}{\partial x} + \frac{\partial v_y}{\partial y}\right)\right]. \end{aligned} \tag{6.6}$$

6.2 Simulation method

Before running actual computer calculations, an evaluation of various numerical methods have been performed in order to decide which method seems to be appropriate for simulating the water vapor flow in subsurface crack channels. At the beginning of the numerical investigations, test simulations using the compressible 1-dimensional hydrodynamical equations have been executed. For these 1-dimensional computations, a self-written implementation of an N-body integrator has been used which was running on a dedicated high-performance server machine. However, 1-dimensional calculations are not appropriate to simulate the physical features of water vapor flow in a 3-dimensional crack channel, e.g. only boundary conditions at $z = 0$ and $z = L$ can be handled, thus, the boundary of ice around the tube cannot be taken into account. Since only a few use cases (e.g. shock waves, unsteady gas flows) can be examined by the 1-dim equations, one has to extend the computations to higher dimensions.

A reasonable and also practicable approach is to employ existing external software to solve the Navier-Stokes equations. Following this way has the advantage to use matured software that executes reliably and stable both from a pure technical and also from an algorithmic perspective. Coding an own new Navier-Stokes solver, however, would require to re-do steps that researchers of numerical algorithms have been done in pioneering works some time ago, and would bear the risk to re-run into well known problems that these people have already solved.

For the numerical simulations of this work the open-source computing platform FEniCS (Finite Element Computational Software) has been employed ["FEniCS Project", Alnaes *et al.*, 2015, Logg *et al.*, 2012]. The FEniCS Project is a research and software project that provides free and open-source software modules for solving partial differential equations (PDE), FEniCS is - as the name implies - based on finite element methods ["FEniCS Project"]. It was created in 2003 as a research collaboration between the University of Chicago and Chalmers University of Technology, and is currently developed in cooperation by software engineers and scientific researchers of many universities and institutes around the world [Logg *et al.*, 2012].

FEniCS consists of several software components that build together the whole FEniCS package: UFL (Unified Form Language), FIAT (Finite element Automatic Tabulator), FFC (FEniCS Form Compiler), UFC (Unified Form-assembly Code), and DOLFIN. One of the most important FEniCS components is DOLFIN, which is a C++/Python library that provides algorithms and data structures for finite element grids. DOLFIN is the computational high-performance C++ backend of FEniCS and represents the main problem-solving environment [Langtangen and Logg, 2017]. It contains C++ classes for meshes, function spaces, and the basic resource-intensive solving algorithms. A diagrammatic overview of the FEniCS software components and their relationships is given in Figure 6.3.

FEniCS solves differential equations by formulating the problem as variational boundary-value problem. This can be best demonstrated on the Poisson equation, which represents one of the most simple partial differential equation (see Langtangen and Logg, 2017, *Solving PDEs in Python - The FEniCS Tutorial Volume I*):

$$-\nabla^2 u(x) = f(x)\,, \quad x \text{ in } \Omega\,, \tag{6.7}$$

$$u(x) = u_{\mathrm{D}}(x)\,, \quad x \text{ on } \partial\Omega\,, \tag{6.8}$$

where $u = u(x)$ is the unknown function, $f = f(x)$ is a source function, $\nabla^2 = \Delta$ is the Laplace operator, Ω denotes the spatial domain, $\partial\Omega$ is the boundary of Ω, and $u_{\mathrm{D}}(x)$ is the boundary value of the function u on $\partial\Omega$ ($\rightarrow$ Dirichlet boundary condition).

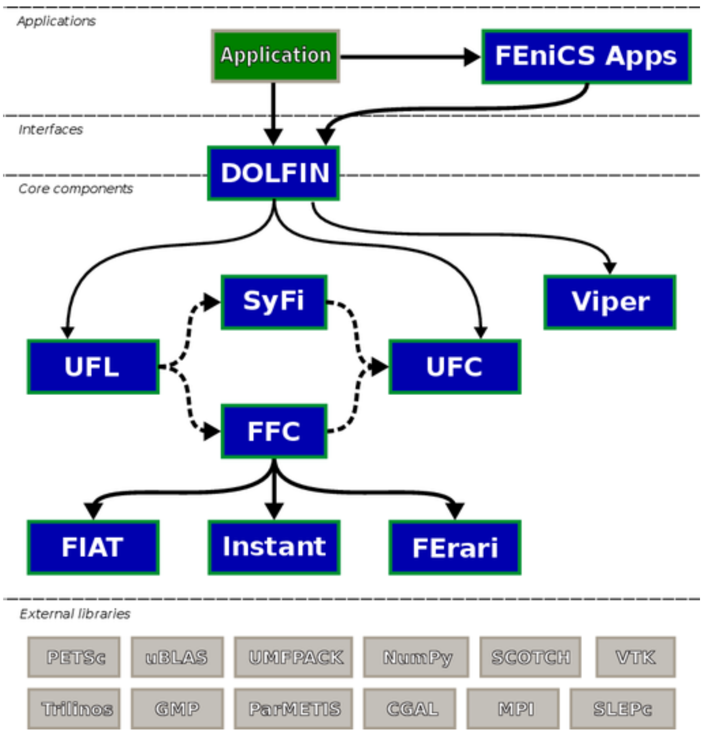

Figure 6.3: Diagrammatic overview of the FEniCS software components and their relationships.
Source: https://en.wikipedia.org/wiki/FEniCS_Project#/media/File:Fenics-map.png (accessed on July 27th, 2021).

In two dimensions the Poisson equation is given by

$$-\frac{\partial^2 u}{\partial x^2} - \frac{\partial^2 u}{\partial y^2} = f(x, y)\,. \tag{6.9}$$

The PDE will be reformulated as a finite element variational problem. The basic steps for putting a PDE into a variational problem are [Langtangen and Logg, 2017]:

1. multiply the PDE by a function v, which is called in the mathematical finite element literature a *test function*. The unknown function to be determined is termed a *trial function*.

2. integrate the resulting equation over the spatial domain Ω.

3. perform integration by parts while assuming that the surface term vanishes, i.e. the test function $v = 0$ on $\partial\Omega$.

Following the recipe described above the Poisson equation is multiplied by a test function v and then integrated over Ω:

$$-\int_\Omega (\nabla^2 u)\, v\, dx = \int_\Omega f v\, dx\,, \tag{6.10}$$

where dx denotes the differential element for integration over the domain Ω. Then integration by parts will be performed [Langtangen and Logg, 2017]:

$$\begin{aligned} -\int_\Omega (\nabla^2 u)\, v\, dx &= \int_\Omega \nabla u \cdot \nabla v\, dx - \int_\Omega \nabla \cdot (u \nabla v)\, dx \\ &= \int_\Omega \nabla u \cdot \nabla v\, dx - \int_{\partial\Omega} \frac{\partial u}{\partial n}\, v\, ds\,, \end{aligned} \tag{6.11}$$

where $\frac{\partial u}{\partial n}$ is the derivative of u with respect to the normal direction n on the boundary $\partial\Omega$, and ds is the differential element on the surface. Since the test function $v = 0$ on the surface $\partial\Omega$, the second term on the r.h.s of (6.11) vanishes. Taking (6.10) and (6.11) gives

$$\int_\Omega \nabla u \cdot \nabla v \, dx = \int_\Omega f v \, dx \, . \tag{6.12}$$

The test function v is element of a test function space $\hat{V}$ (e.g. space of polynomials of degree n), while the trial function u is member of a function space V, which can be different to $\hat{V}$.

It is now the challenge of the variational problem to find $u \in V$ such that

$$\int_\Omega \nabla u \cdot \nabla v \, dx = \int_\Omega f v \, dx \, , \quad \forall v \in \hat{V} \, , \tag{6.13}$$

i.e. a solution function u has to be found, such that equation (6.12) is fulfilled for all test functions v of the whole test function space $\hat{V}$. For the specific Poisson problem the trial and test spaces V and $\hat{V}$ are defined as

$$\begin{aligned} V &= u \in H^1(\Omega) : u = u_0 \text{ on } \partial\Omega \, , \\ V &= v \in H^1(\Omega) : v = 0 \text{ on } \partial\Omega \, , \end{aligned} \tag{6.14}$$

where $H^1(\Omega)$ is the so-called Sobolev space which contains functions v, such that integrals of v^2 and $|\nabla v|^2$ over Ω are finite.

However, to solve the Poisson equation numerically, one has to translate the continuous variational problem (6.13) into a discrete variational problem [Langtangen and Logg, 2017]. This is achieved by using finite-dimensional test and trial spaces, $V_h \subset V$, $\hat{V}_h \subset \hat{V}$. The discrete variational problem is then transformed into: determine numerically $u_h \in V_h \subset V$ such that

$$\int_\Omega \nabla u \cdot \nabla v \, dx = \int_\Omega f v \, dx \, , \quad \forall v \in \hat{V}_h \subset \hat{V} \, . \tag{6.15}$$

If a linear triangular element with three nodes is used then V and $\hat{V}$ are the spaces of all piecewise linear functions over a mesh of triangles [Logg *et al.*, 2012].

For the general case, one starts with a PDE, then one derives a variational equation

$$a(u, v) = L(v) \, , \tag{6.16}$$

where $u \in V$ and $v \in \hat{V}$, and finally the problem is discretized via using finite dimensional spaces for V and $\hat{V}$. In the case of the Poisson equation, one has

$$a(u, v) = \int_\Omega \nabla u \cdot \nabla v \, dx \tag{6.17}$$

$$L(v) = \int_\Omega f v \, dx \, . \tag{6.18}$$

So before actually coding a FEniCS program that solves a PDE one has to perform the following steps [Logg *et al.*, 2012]:

1. Transform the PDE into a discrete variational problem, i.e. find $u \in V$ such that

$$a(u, v) = L(v) \quad \forall v \in \hat{V} \, . \tag{6.19}$$

2. Choose appropriate spaces V and $\hat{V}$, that is, specify the mesh and type of finite elements.

6.2.1 Simulating Navier-Stokes equation

The Navier-Stokes equations for the velocity u and pressure p is given by Landau and Lifshitz (1966):

$$\rho\Big(\frac{\partial\vec{u}}{\partial t}+(\vec{u}\cdot\vec{\nabla})\vec{u}\Big)=\vec{\nabla}\cdot\bar{\bar{\sigma}}(u,p)+\vec{f}\,, \tag{6.20}$$

$$\frac{\partial\rho}{\partial t}+\vec{\nabla}\cdot(\rho\vec{v})=0\,. \tag{6.21}$$

where ρ is the fluid density, f is an external force, and $\bar{\bar{\sigma}}(u,p)$ denotes the Cauchy stress tensor (including the pressure p), which is the sum of the deviatoric stress tensor $\bar{\bar{\tau}}(u)=2\mu\bar{\bar{\epsilon}}(u)$ and the pressure term $-p\mathbb{1}$, given by

$$\bar{\bar{\sigma}}(u,p)=\bar{\bar{\tau}}(u)-p\mathbb{1}=2\mu\bar{\bar{\epsilon}}(u)-p\mathbb{1}\,, \tag{6.22}$$

where $\bar{\bar{\epsilon}}(u)$ is the strain-rate tensor

$$\bar{\bar{\epsilon}}(u)=\frac{1}{2}\big(\,\vec{\nabla}\vec{u}+(\vec{\nabla}\vec{u})^T\,\big)\,, \tag{6.23}$$

with the dynamic viscosity μ. Integrating the nonlinear term $(\vec{u}\cdot\vec{\nabla})\vec{u}$ against a test function $\vec{v}$ one obtains the term $a(\vec{u},\vec{v})$ used in the variational form (6.16) [Logg *et al.*, 2012]

$$a(\vec{u},\vec{v})=\int_\Omega(\vec{u}\cdot\vec{\nabla})\vec{u}\cdot\vec{v}\,dx\,. \tag{6.24}$$

To solve the Navier-Stokes equations, FEniCS applies the so-called *splitting method* [Langtangen and Logg, 2017]. Using this method the two equations (6.20) and (6.21) are handled separately. A standard procedure is the splitting method suggested by Chorin [Chorin, 1968] and Temam [Temam, 1969], also known as *Chorin's method.* FEniCS applies a modified version of Chorin's method, the so-called incremental pressure correction scheme (IPCS). The IPCS scheme consists of three main steps [Langtangen and Logg, 2017]:

1. computation of a tentative velocity u^* while taking the pressure p^n from the previous time step n, and linearizing the non-linear convective term $(\vec{u}^n\cdot\vec{\nabla})\vec{u}^n$ by taking the velocity $\vec{u}^n$ from the previous time interval. The variational problem for this first step is then given by

$$\begin{aligned}\langle\rho(\vec{u}^*-\vec{u}^n)/\Delta t,\vec{v}\rangle\;+\;\langle\rho(\vec{u}^n\cdot\vec{\nabla})\vec{u}^n,\vec{v}\rangle\;+\;\langle\bar{\bar{\sigma}}(\vec{u}^{n+\frac{1}{2}},p^n),\epsilon(\vec{v})\rangle\\ +\;\langle p^n\vec{n},\vec{v}\rangle_{\partial\Omega}\;-\;\langle\mu\vec{\nabla}\vec{u}^{n+\frac{1}{2}}\cdot\vec{n},\vec{v}\rangle_{\partial\Omega}=\langle\vec{f}^{n+1},\vec{v}\rangle\,.\end{aligned} \tag{6.25}$$

   The bracket term $\langle v,w\rangle$ denotes a generialized scalar product on a continuum function space:

$$\langle v,w\rangle=\int_\Omega vw\,dx\,,\qquad\langle v,w\rangle_{\partial\Omega}=\int_{\partial\Omega}vw\,ds\,. \tag{6.26}$$

2. The term $\vec{u}^{n+\frac{1}{2}}$ represents the value of $\vec{u}$ at the middle of the interval, which corresponds approximately to the arithmetic mean:

$$\vec{u}^{n+\frac{1}{2}}\approx(\vec{u}^n+\vec{u}^{n+1})/2\,. \tag{6.27}$$

3. Integration by parts of the expression $\langle -\vec{\nabla}\cdot\bar{\bar{\sigma}}, \vec{v}\rangle$ leads to the variational problem (6.25). One obtains for the integration by parts portion

$$\langle -\vec{\nabla}\cdot\bar{\bar{\sigma}}, \vec{v}\rangle = \langle \bar{\bar{\sigma}}, \epsilon(\vec{v})\rangle - \langle \vec{T}, \vec{v}\rangle_{\partial\Omega} \tag{6.28}$$

where $\vec{T} = \bar{\bar{\sigma}}\cdot\vec{n}$ is the boundary surface term, e.g. assuming a free boundary problem, then $\vec{T} = \vec{0}$ on the boundary.

In the first step one computes a tentative velocity u^* where the pressure p^n from the previous time step is used as input. This computed tentative velocity is then taken to calculate the new pressure p^{n+1}:

$$\langle \vec{\nabla}p^{n+1}, \vec{\nabla}q\rangle = \langle \vec{\nabla}p^n, \vec{\nabla}q\rangle - \Delta t^{-1}\langle \bar{\bar{\sigma}}\cdot u^*, q\rangle\,, \tag{6.29}$$

where q is a scalar-like test function in pressure space (the test function $\vec{v}$ in (6.28) on the other hand is a vector-like test function in velocity space). Subtracting the momentum equation (6.20) expressed in terms of the tentative velocity u^* and the pressure p^n from the momentum equation expressed in terms of the velovity u^{n+1} and the pressure p^{n+1} of the next time slice leads to

$$(\vec{u}^{\,n+1} - \vec{u}^{\,*})/\Delta t + \vec{\nabla}p^{n+1} - \vec{\nabla}p^n = \vec{0}\,. \tag{6.30}$$

Taking into account the continuity equation the following Poisson problem for the pressure p^{n+1} is obtained:

$$-\vec{\nabla}\cdot\vec{u}^{\,*}/\Delta t + \nabla^2 p^{n+1} - \nabla^2 p^n = 0\,. \tag{6.31}$$

Finally, the corrected velocity $\vec{u}^{\,n+1}$ is computed from equation (6.30). To get a variational problem this equation is multiplied by a test function $\vec{v}$, i.e. the scalar product is calculated:

$$\langle \vec{u}^{\,n+1}, \vec{v}\rangle = \langle \vec{u}^{\,*}, \vec{v}\rangle - \Delta t\langle\, \vec{\nabla}(p^{n+1} - p^n), \vec{v}\rangle = 0\,. \tag{6.32}$$

To summarize the Navier-Stokes equations are solved by determining the solutions of three successive variational problems.

6.2.2 Mesh generation

To create the various vent geometries the freely available tool 'Gmsh' has been applied. Gmsh is a free 2D/3D finite element mesh generator with a built-in CAD engine and post-processor [Geuzaine and Remacle, 2009]. It provides a user interface to construct 2-dim or 3-dim finite element meshes. The created mesh grid can be saved as human-readable ASCII file using a simple standard format.

At the beginning, simulations with simple geometries have been performed on the one hand to get familiar with the tool and on the other hand to calibrate and fine-tune the algorithm. The most simple geometry in 2-dim is a rectangle, see Figure 6.4.

The coarseness of the mesh can be controlled by the number of times the 'refine by splitting' button is pressed in the 'Gmsh' Graphical User Interface (GUI). In Figure 6.5 the triangulated grids are shown for different refinement levels for the same rectangle, ranging from level zero (a) up to level three (d).

A somewhat more complex vent is shown in Figure 6.6, where two different triangulation levels are presented ((a),(b) refinement level 0,1, respectively). The width of this vent varies and has a minimum (kink).

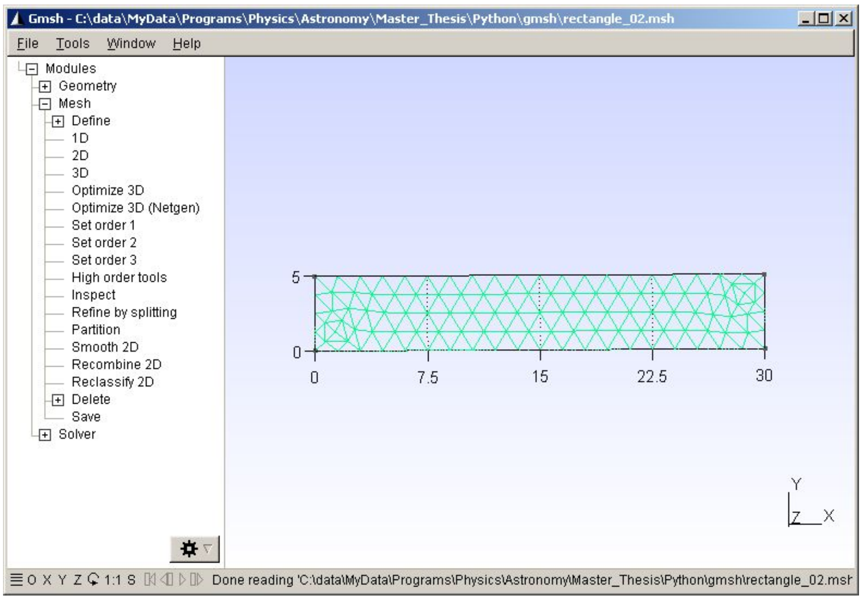

Figure 6.4: Vent geometries are generated by the open source tool 'Gmsh'. In this example a simple rectangle has been created and a triangulated mesh has been produced with a refinement degree of one (default grid splitted once). Length unit is 1 m.

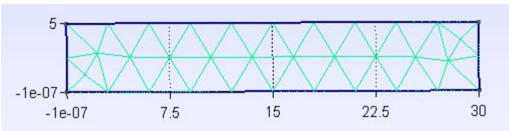

(a) refinement level 0

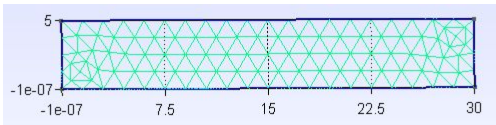

(b) refinement level 1

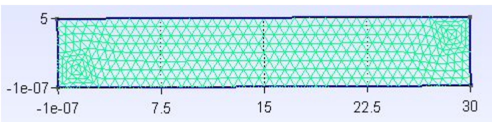

(c) refinement level 2

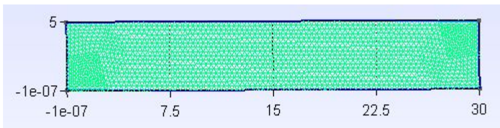

(d) refinement level 3

Figure 6.5: Triangulated grids for different refinement levels for the same rectangle (length unit is 1 m). (a)-(d) refinement level 0-3.

Crack channels that occur in real ice mantles might build branches or bifurcations. A modelled vent containing a bifurcated branch is depicted in Figure 6.7. Since this geometry also contains throats and several kinks, it is informally called the 'zig-zag' vent. Simulations have been performed using the zig-zig vent geometry for different triangulation granularity levels. Detail sections of the finest triangulation grid (refinement level 2) of the zig-zag vent are shown in Figure 6.8.

In a final stage the calculations have been extended to 3-dimensional vent geometries. A triangulation of a 3-dim crack channel geometry including kinks, throats, and a cave-like area at the bottom is depicted in Figure 6.9.

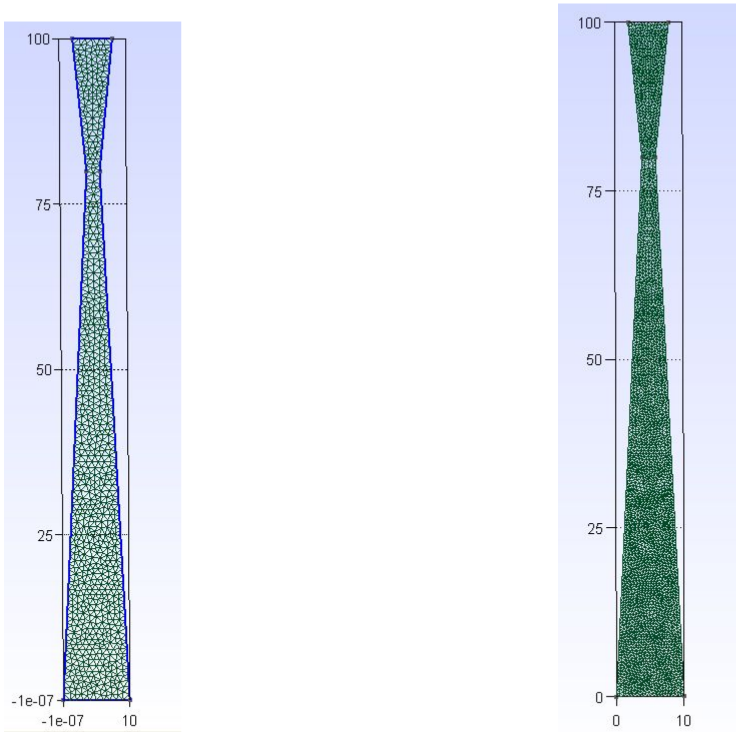

(a) refinement level 0 (b) refinement level 1

Figure 6.6: Vent with varying width having a minimum (kink). Two different traingulation refinement levels are shown (length unit is 1 m). a) refinement level 0, b) refinement level 1.

6.3 Simulation results

6.3.1 Calibration

Before starting the proper simulations using physical geometries several test runs have to be performed. At the very beginning, test runs for trivial geometries, namely 2-dim rectangles, have been executed. The first simulation with the FEniCS package has been done for a rectangle of dimension $4\,\mathrm{m} \times 20\,\mathrm{m}$ with the initial condition that velocity u is zero at t $= 0$:

$$u_0 = u(\vec{x}, t = 0) = 0\,\mathrm{m\,s^{-1}}\,, \tag{6.33}$$

and the boundary conditions such that (i) velocity is zero at the bottom ($z = 0$), (ii) also zero at the wall boundaries (no-slip condition), and (iii) pressure p is zero at top ($z = L$), and the bottom ($z = 0$) (the coordinate origin is set to the point at depth L):

$$u(z = 0) = 0 \quad , \quad u(\text{wall} = 0)\,, \tag{6.34}$$

$$p(z = 0) = 0 \quad , \quad p(z = L) = 0\,. \tag{6.35}$$

This trivial test case must produce a trivial result, namely a stationary time-independent solution where velocity u and pressure p are zero within the whole rectangle. This trivial outcome has been observed in the actual FEniCS simulation (see the upper rectangle in Figure 6.10).

The next step was to modify the boundary condition such that the pressure is non-zero at the bottom ($p(z = 0) = p_0$), which represent some hydrostatic pressure. For this case the solution is also known theoretically, the velocity u is independent in z and a quadratic function in x, i.e. $u = u(z)$ (see the lower rectangle in Figure 6.10).

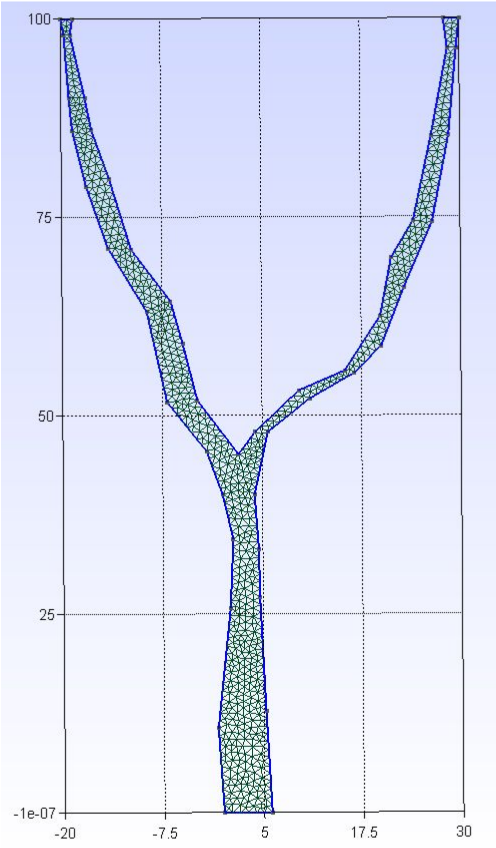

(a) refinement level 0

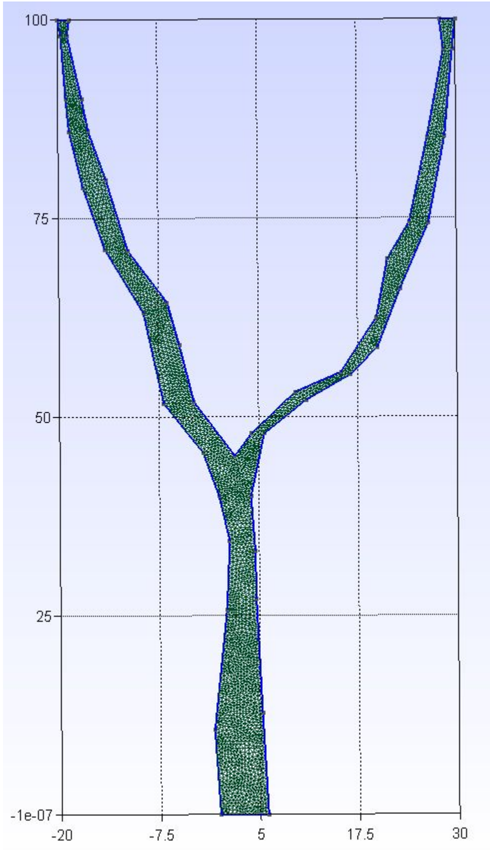

(b) refinement level 1

Figure 6.7: Vent containing a bifurcated branch. Two different traingulation refinement levels are shown (length unit is 1 m). a) refinement level 0, b) refinement level 1.

A next calibration test series has been performed by varying both length and width of the rectangle. The results are again consistent with the theoretical solution for the velocity u. Some cases (varying length L, width $w = 4\,\mathrm{m}$) from this test series are shown in Figure 6.11.

To visualize the results in an optically optimal way the graphical application 'ParaView' has been employed. 'ParaView' is an open-source, multi-platform data analysis and visualization tool [Ahrens *et al.*, 2005, Ayachit, 2015]. The tool is able to handle large amounts of data, and data can be visualized in 2-dim and 3-dim. A screenshot of 'ParaView' taken during the calibration phase where the velocity and pressure distributions of a simple rectangle geometry have been analyzed is shown in Figure 6.12.

6.3.2 2-dim case

As next step, 2-dimensional simulations with realistic boundary conditions have been performed, also starting with simple rectangle geometries. The boundary conditions are given as:

- Bottom (basis of the vent): $u(z = 0) = 0$, $p(z = 0) = \rho g L$ (hydrostatic pressure)
- Top (at the surface): $p(z = L) = 0$, no restriction for the velocity u
- Wall: $u(\text{wall}) = 0$, 'no slip' condition.

For the viscosity of water a reference value of $5.46 \cdot 10^{-4}\,\mathrm{Ns\,m^{-2}}$ has been applied. This viscosity value has been taken for nearly all simulations, only for two simulations (of type 2-dim 'zig-zag' geometry containing throats and a bifurcated branch) the value $1.00 \cdot 10^{-5}\,\mathrm{Ns\,m^{-2}}$ has been used for comparison reasons. An overview of the water vapor flow simulations and their respective parameters is given in Table 6.1. Figure 6.13 shows the velocity and pressure distribution within a rectangular vent with dimensions length $L = 20\,\mathrm{m}$, width $w = 4\,\mathrm{m}$. The velocity and pressure distributions represent stationary solutions, i.e. simulation iterations have been performed until a stationary state has been reached. For the simple rectangle the velocity u in the inner part of the vent has a more or less constant value and does not depend on z, $u_{\mathrm{inner}}(z) = u_{\mathrm{inner}} \simeq$ const.. The velocity drops towards the walls due to the 'no-slip' wall condition ($u(\mathrm{wall}) = 0$). The distribution of the pressure $p(z)$ is displayed via color coding, ranging from red for higher values at the bottom up to blue for low values at the top ($p(z = 0) = 0$ at the surface $\equiv$ no atmosphere, vaccum conditions).

The results for a rectangular vent with dimensions length $L = 100\,\mathrm{m}$, width $w = 4\,\mathrm{m}$, are given in Figure 6.14. Qualitatively they are similar to those of Figure 6.13.

Simulation results for a rectangular channel with the same length $L = 100\,\mathrm{m}$ as in the previous case (Figure 6.15) but for smaller width $w = 1\,\mathrm{m}$ is shown in Figure 6.15.

An enhancement of the geometry where a kink has been added is depicted in Figure 6.16. The length L of this vent is 100 m as in the previous rectangular cases, but now the width w varies: value at the bottom $w(z = 0) = 10\,\mathrm{m}$, minimum value (kink at $z = 80\,\mathrm{m}$) $w_{\mathrm{min}} = 2\,\mathrm{m}$, value at the top $w(z = L) = 6\,\mathrm{m}$. The velocity u is increasing towards the kink, reflecting the Venturi effect, which can be seen on the r.h.s of Figure 6.16, where the vicinity of the kink is zoomed out. For better visibility the magnitude of the velocity is illustrated by size, length and color of the velocity vector.

A similar geometry is shown in Figure 6.17, where the kink is extended to a throat. The absolute value of the velocity vector is enlarged within the throat as a consequence of the Venturi effect, analogous to the previous kink case. The maximum absolute value of the velocity is in this geometry larger than for the pure kink case (Figure 6.16).

As next step, geometries are considered where features are added that might occur in Enceladus' fracture channels. At the bottom of the channel a larger cave-like area is assumed that represents the liquid/gas interface where evaporation takes place [Postberg *et al.*, 2009, Ingersoll and Nakajima, 2016b]. A vent containing two throats and equipped with such an evaporation area is shown in Figure 6.18. The channel length $L = 100\,\mathrm{m}$ and a triangulation grid with medium resolution has been used for the simulation. It can be clearly seen that the velocity u is enhanced in the vicinity of the throats, the effect is more pronounced at the second throat at the top of the vent. The results of a simulation of a length $L = 100\,\mathrm{m}$ and two throat ice channel analogous to Figure 6.18, but with slightly modified parameters, is shown in Figure 6.19.

The results for a simulation of a vent containing two throats where the channel length has been increased to $L = 1000\,\mathrm{m}$ is given in Figure 6.20. For this calculation a triangulation grid with high resolution has been employed. Enlarged detail plots of the $L = 1000\,\mathrm{m}$ two throat vent are shown in Figures 6.21-6.25. Zooming out the region around the top of the channel (6.25) one can clearly see the increased velocities of the water vapor at the ejection point.

Results of a similar simulation using the same geometry as in the previous case (Figure 6.20), $L = 1000\,\mathrm{m}$ vent with two throats and a cave-like evaporation area at the bottom, but with a smaller value of $\rho_0 = 0.5\,\mathrm{kgm^{-3}}$ is presented in Figure 6.26. The large velocity values reflecting the

Venturi effect at the emission point at the top of the vent are higher than in Figure 6.20.

The most sophisticated ice channel structure that has been investigated is a geometry that contains a bifurcated branch and several throats and kinks, informally named the 'zig-zag' vent. Such structure includes elements that could occur in real ice mantles, and thus represents approximatively a physical ice crack channel. The simulated structure has following characteristic sizes: length $L = 100\,\mathrm{m}$, values of width w: at the bottom $w(z=0) = 6\,\mathrm{m}$, at the top $w_{\mathrm{top\_left}}(z=L) = 1.5\,\mathrm{m}$, $w_{\mathrm{top\_right}}(z=L) = 2.0\,\mathrm{m}$. Simulation results using a triangulation grid with medium resolution (refinement level 1) are presented in Figures 6.27-6.29. The Venturi effect of higher velocities occurs at tight throats and at the ejection points on the top of the vent. On the left bifurcation branch, the effect on the top is more pronounced because the opening width ($w_{\mathrm{top\_left}}(z=L) = 1.5\,\mathrm{m}$) is smaller than at the right branch ($w_{\mathrm{top\_right}}(z=L) = 2.0\,\mathrm{m}$). Velocity and pressure distributions of a simulation of a 'zig-zag' bifurcated branch geometry using a triangulation mesh of high resolution (refinement level 2) is displayed in Figures 6.30-6.33. The simulated structure has following characteristic sizes: length $L = 100\,\mathrm{m}$, values of width w: at the bottom $w(z=0) = 6\,\mathrm{m}$, at the top $w_{\mathrm{top\_left}}(z=L) = 0.8\,\mathrm{m}$, $w_{\mathrm{top\_right}}(z=L) = 1.5\,\mathrm{m}$. For this high resolution 'zig-zag' bifurcated vent simulation a smaller dynamic viscosity value $\mu = 1.00 \cdot 10^{-5}\,\mathrm{Ns\,m^{-2}}$ has been used, that leads to higher absolute values in the velocity field (compared to simulations where all the other parameters are kept unchanged). Thus, also the maximum value of the velocity field v_{max} is significantly higher (see Table 6.1: simulation Id = 17 where $\mu = 1.00 \cdot 10^{-5}$ yields $v_{\mathrm{max}} = 1105\ \mathrm{m\,s^{-1}}$, whereas simulation Id = 15 where $\mu = 5.46 \cdot 10^{-4}$ has $v_{\mathrm{max}} = 403\ \mathrm{m\,s^{-1}}$). This is in principle qualitatively in agreement with the Hagen-Poiseuille law of fluid dynamics, that describes the volume flow of a laminar, stationary Newtonian fluid through a pipe.

The volume flow $\dot{V}$ of a fluid with dynamical viscosity μ through a cylindrical pipe of radius r, and length L is given by

$$\dot{V} = \frac{dV}{dt} = \frac{\pi}{8}\frac{r^4\,\Delta p}{\mu\,L}\,, \tag{6.36}$$

where Δp is the pressure difference between the two ends of the pipe.
With the relation

$$v_{\mathrm{max}} = \frac{\dot{V}_{\mathrm{max}}}{\pi r^2}\,, \tag{6.37}$$

it follows

$$v_{\mathrm{max}} = \frac{r^2\,\Delta p}{8\mu\,L} \quad \Rightarrow \quad v_{\mathrm{max}} \propto \frac{1}{\mu}\,. \tag{6.38}$$

Though the Hagen-Poiseuille law for the laminar flow of a cylindrical pipe cannot be applied exactly to the dynamical simulation of the 'zig-zag' geometry, the simulation results, namely that decreasing the viscosity yields to increased velocities, are at least qualitatively consistent with it.

The high velocity values v_{max} of the simulations of this work are qualitatively in agreement with studies obtained via different methods, e.g. (a) Yeoh *et al.* (2015, 2017) (numerical Monte Carlo simulation of particles moving in a nozzle-like vent) (b) Schmidt *et al.* (2008) (simulation of the 1-dim flow of vapour and ice grains through random crack channels) (c) Ingersoll and Pankine (2010) and Nakajima and Ingersoll (2016a) (investigation of vapor and grain flow in the plumbing system including flow-wall interactions using a 1-dim hydrodynamical model) and (d) velocity values obtained via statistical flux models applied on data measured by the Cassini Ultraviolet Imaging Spectrograph (UVIS) and Cassini's Infrared Spectrometer (CIRS) [Spencer *et al.*, 2009, Hansen *et al.*, 2011].

6.3.3 3-dim case

The simulations have been further extended to 3-dimensional geometries. At the beginning of the 3-dimensional computation series several tests and calibrations have been performed. The first simulated 3-dim geometries are simple cylinders which correspond to rectangles in two dimensions since a rectangle is the cross section in a plane parallel to the z-axis of the cylinder (a 3-dim cylinder with length L, diameter $w = 2r$ corresponds to a 2-dim rectangle with length L, width w). The boundary conditions for the 3-dim geometries are analogue to the two dimensional case:

- Bottom area (basis of the vent): $u(z = 0) = 0$, $p(z = 0) = \rho_{\mathrm{ice}} g L$ (hydrostatic pressure)
- Top area (at the surface): $p(z = L) = 0$, no restriction for the velocity u
- Wall (= 2-dim mantle of 3-dim volume): $u(\mathrm{wall}) = 0$, 'no slip' condition.

A list of the 3-dim vent simulations and their parameters is given in Table 6.1. Figure 6.34 shows the velocity (at the top) and pressure distribution of a cylindrical vent with length $L = 20\,\mathrm{m}$, diameter $w = 2r = 4\,\mathrm{m}$ (Table 6.1: Id = 18, the corresponding 2-dim simulation, where an exact rectangle geometry is used, has Id = 2, see also Figure 6.13). The velocity distribution inside the cylinder ($L = 20\,\mathrm{m}$, $w = 4\,\mathrm{m}$) is drawn in Figure 6.35. The results for the 3-dim cylindrical case are trivial as were the results for the 2-dim rectangle case: the pressure drops linearly from the hydrostatic value at the bottom down to zero at the top (moon's surface), the velocity distribution in a perfect cylinder does not depend on z and the azimutal coordinate ϕ, it is only a function of radial distance r, i.e. $v_{\mathrm{cylinder}}(r, \phi, z) = v_{\mathrm{cylinder}}(r)$. Comparing the maximum value of the velocity field of the 3-dim simulation with that of the 2-dim rectangle computation, one can see that though the two values are not exactly equal they are of the same order of magnitude (Table 6.1: $v_{\max} = 29$ and $11\,\mathrm{m\,s^{-1}}$ for the rectangular (Id = 2), cylindrical case (Id = 18), respectively). A deeper zoom into the interior of the cylinder ($L = 20\,\mathrm{m}$, $w = 4\,\mathrm{m}$) from a viewing perspective from above is shown in Figure 6.36.

Simulation results for a cylindrical vent with larger length $L = 100\,\mathrm{m}$, and $w = 4\,\mathrm{m}$, is shown in Figures 6.37-6.39. These are qualitatively similar to those of the previous $L = 20\,\mathrm{m}$ case.

Calculation outcome for a cylindrical tube channel with the same length $L = 100\,\mathrm{m}$ as in the previous case but for smaller diameter $w = 2r = 1\,\mathrm{m}$ is presented in Figure 6.40.

A physically more interesting 3-dim channel geometry containing kinks, throats and a cave-like evaporation area is depicted in Figures 6.41-6.44. This geometry is the 3-dim analogon of the 2-dim vent-with-throats case (Table 6.1: Id = 10). The length L of this vent is 100 m as in the previous cylindrical cases, but now the width w varies: value at the bottom $w(z = 0) = 10\,\mathrm{m}$, value at the top $w(z = L) = 2\,\mathrm{m}$, at throat 1 (right after the cave) $w_{\mathrm{min1}} = 1\,\mathrm{m}$, at throat 2 (at the top) $w_{\mathrm{min2}} = 0.6\,\mathrm{m}$. Figure 6.41 shows the velocity vectors at the top and the pressure distribution from a perspective looking from above at the vent. Velocity distributions inside the 3-dim vent-with-throats geometry are visualized in Figures 6.42-6.44. One can see that velocities are enhanced at the kinks and throats reflecting the Venturi effect, qualitatively similar to the 2-dim case (Table 6.1: Id = 10).

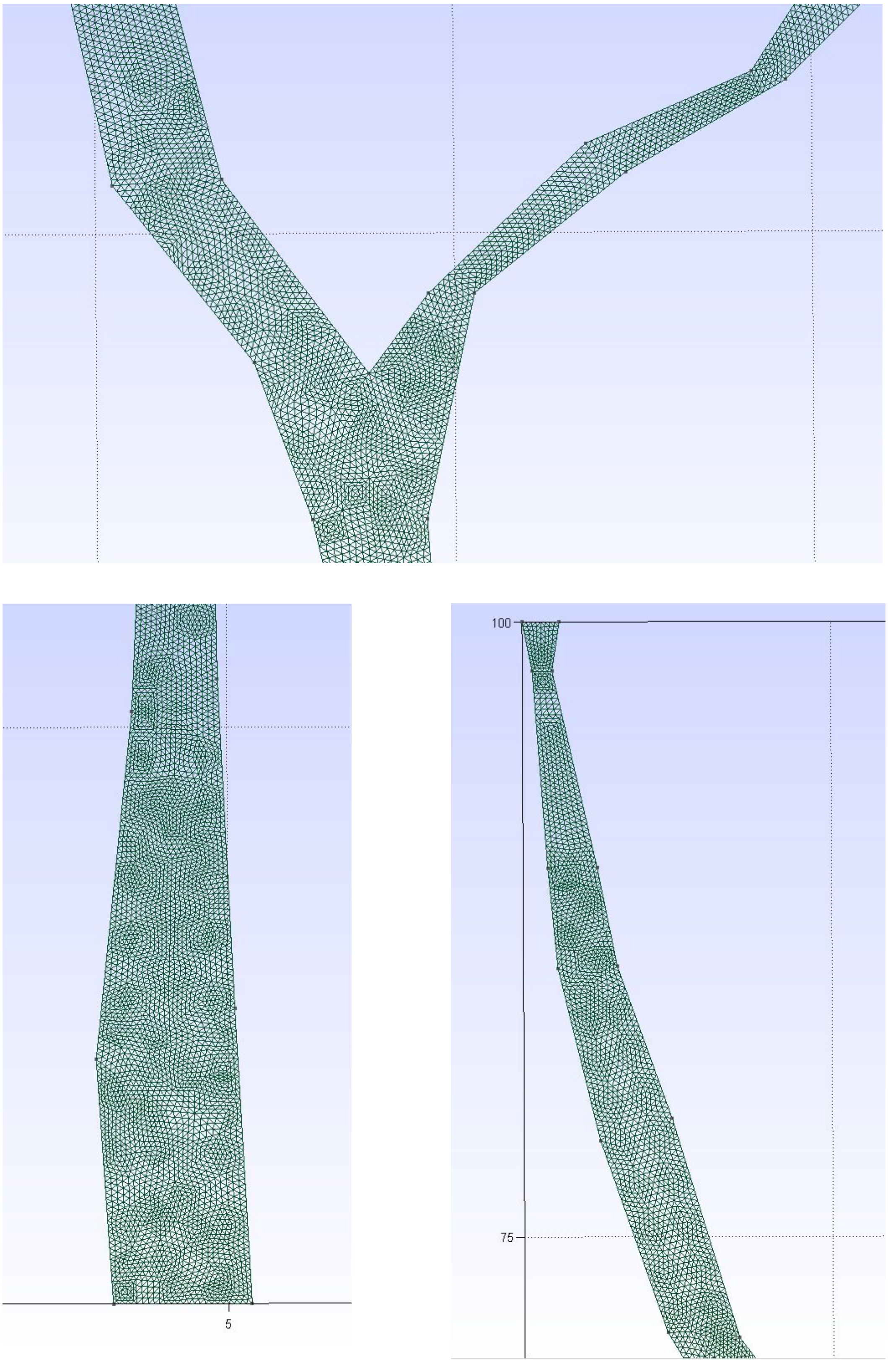

Figure 6.8: Detail sections of the zig-zag geometry containing a bifurcated branch, throats and kinks, covered with a very fine triangulation mesh (refinement level 2, length unit is 1 m).

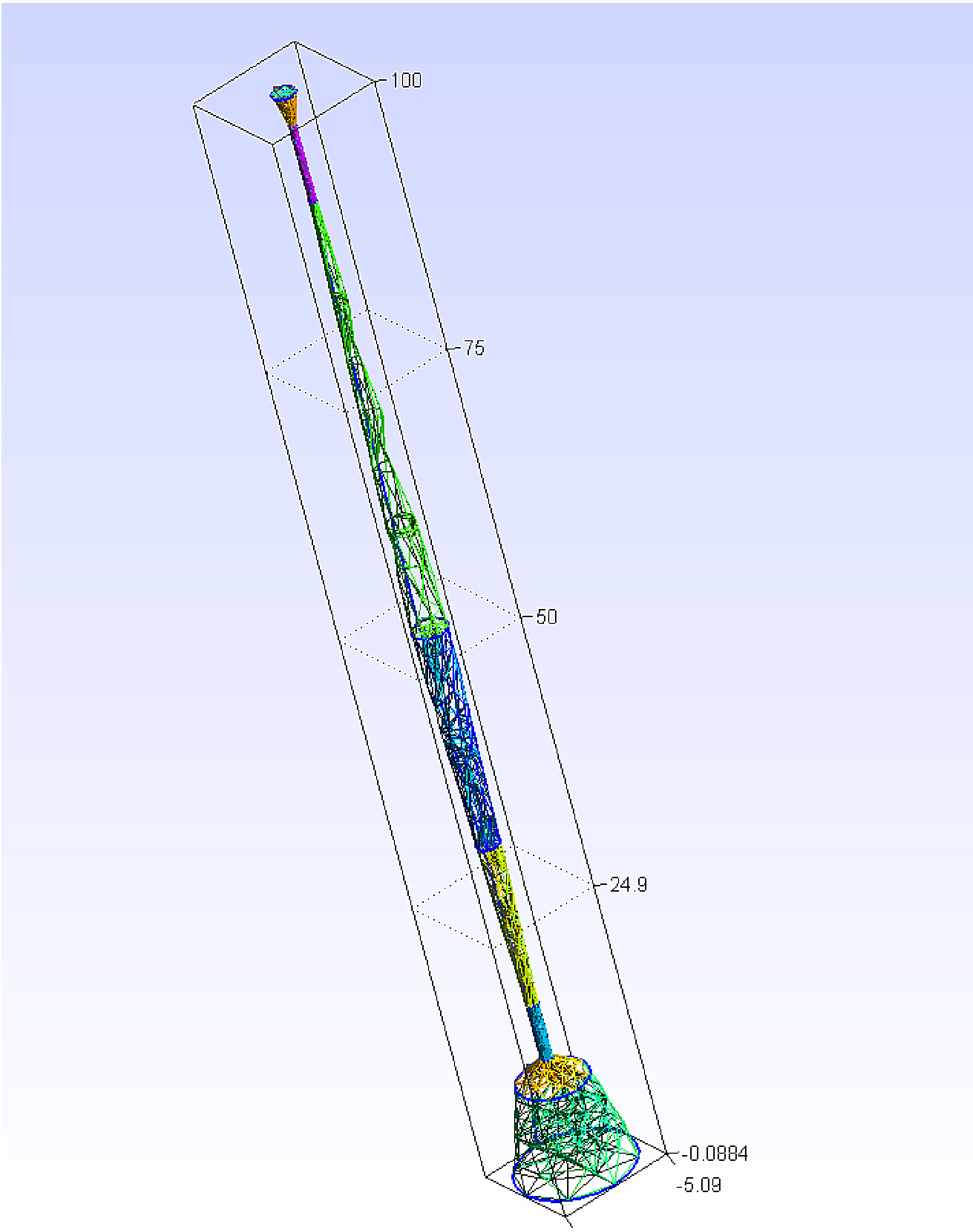

Figure 6.9: Triangulation of a 3-dim vent geometry including kinks, throats, and a cave-like area at the bottom (length unit is 1 m).

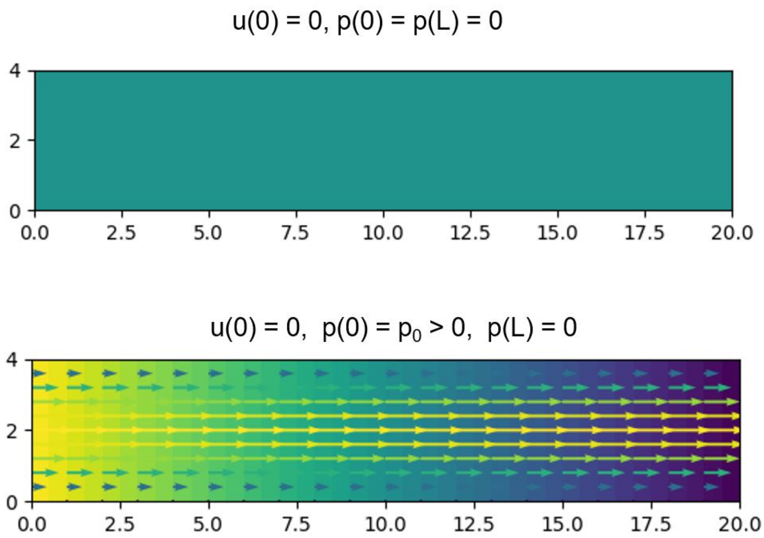

Figure 6.10: Test simulations employing the FEniCS package for a simple rectangle geometry. Upper plot: trial case where $u = 0$ at bottom and walls, and pressure $p = 0$ at top and bottom results to trial stationary solution where $u = 0$ and $p = 0$ for the whole rectangle. Lower plot: similar boundary condition as the upper plot, except that $p(z = 0) = p_0$ at the bottom, which represents a hydrostatic pressure at depth. The well known quadratic solution for velocity u in dimension x is perfectly reproduced.

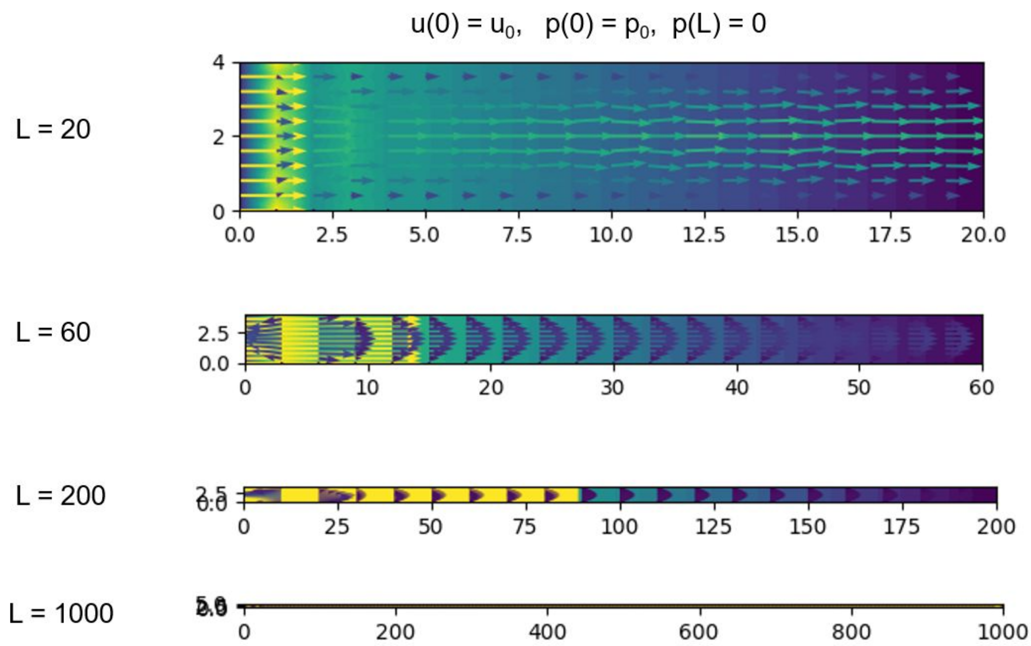

Figure 6.11: A series of test simulations using a simple rectangle geometry where the length L of the rectangle is varied (width w is 4 m for the simulations shown). The quadratic solution for the velocity u in x is well reproduced.

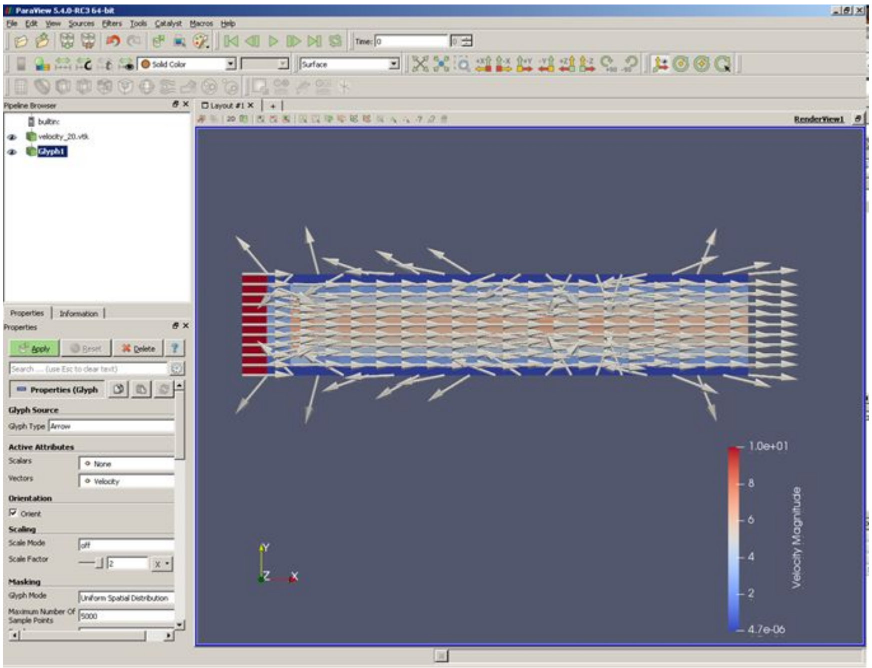

Figure 6.12: Screenshot of a working session with the graphical application 'ParaView', which has been used for visualization of the velocity and pressure data resulting from the FEniCS simulations. Here the velocity and pressure distributions of a simple rectangle geometry are shown that has been analyzed during the calibration phase (the colorbar specifies the velocity values in $\mathrm{m\,s^{-1}}$).

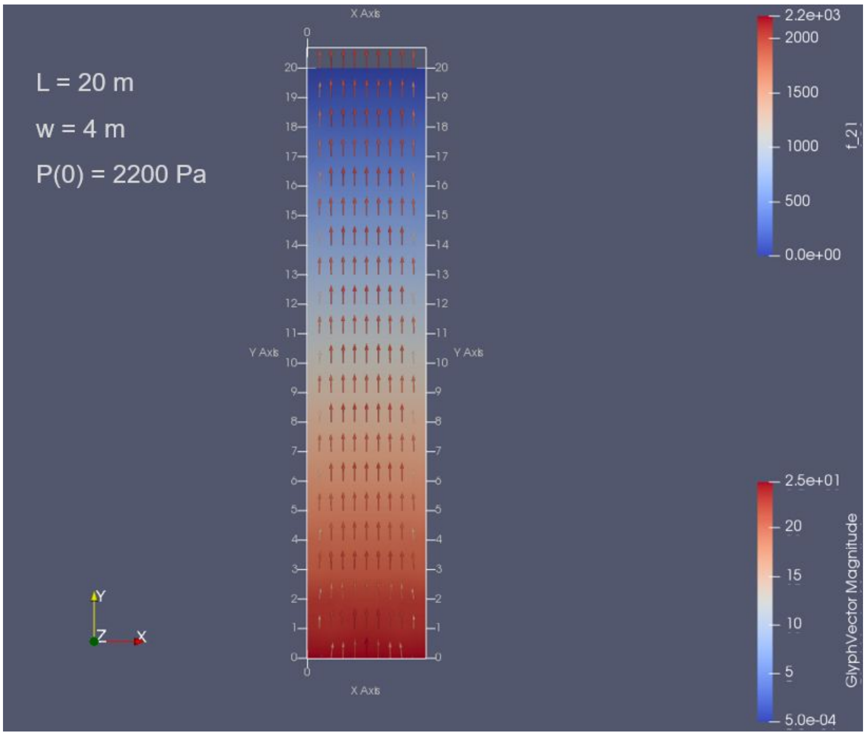

Figure 6.13: Velocity and pressure distribution within a 2-dimensional rectangular vent with dimension length $L = 20\,\mathrm{m}$, width $w = 4\,\mathrm{m}$ (Table 6.1: Id = 2). At the bottom a hydrostatic pressure $p(z = 0) = \rho g L = 2200\,\mathrm{Pa}$ is assumed (Enceladus' gravitational acceleration $g = 0.11\,\mathrm{m\,s^{-2}}$, $\rho \simeq \rho_{\mathrm{ice}} \simeq \rho_{\mathrm{water}} \simeq 1000\,\mathrm{kg\,m^{-3}}$), the velocity is zero at the bottom and at the wall ('no slip' condition). The pressure is zero at the surface, representing vacuum conditions. Upper colorbar: pressure in Pa, lower colorbar: velocity in $\mathrm{m\,s^{-1}}$.

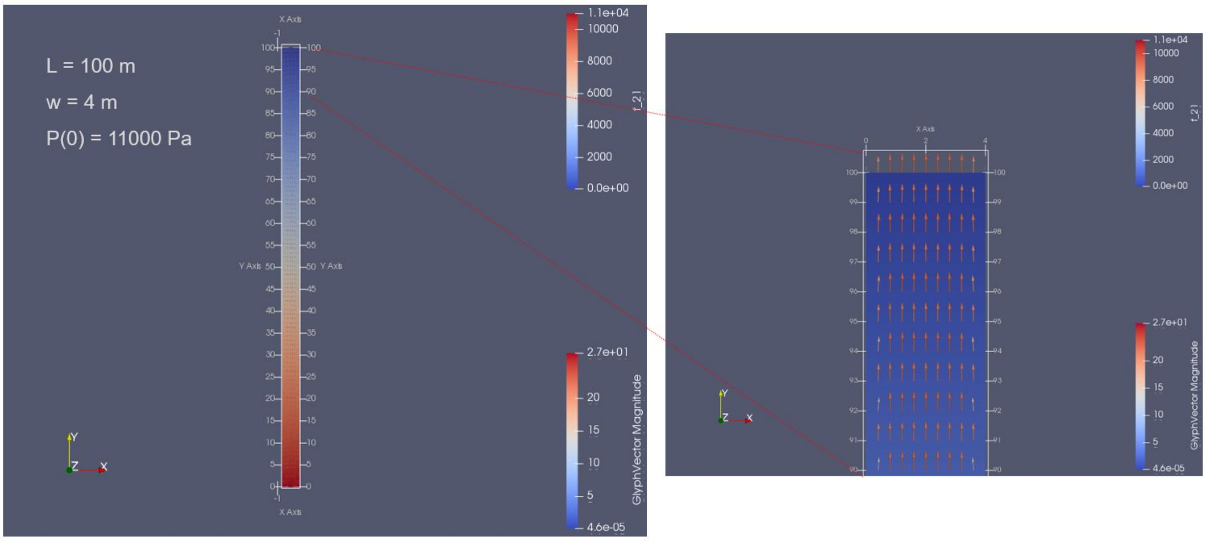

Figure 6.14: Left: Velocity and pressure distribution within a 2-dimensional rectangular vent with dimensions length $L = 100\,\mathrm{m}$, width $w = 4\,\mathrm{m}$ (Table 6.1: Id = 5). Boundary conditions are analogue to Figure 6.13, assuming a hydrostatic pressure at the bottom $p(z = 0) = \rho g L = 11000\,\mathrm{Pa}$. Right: Zoom into upper part (surface) of the vent.

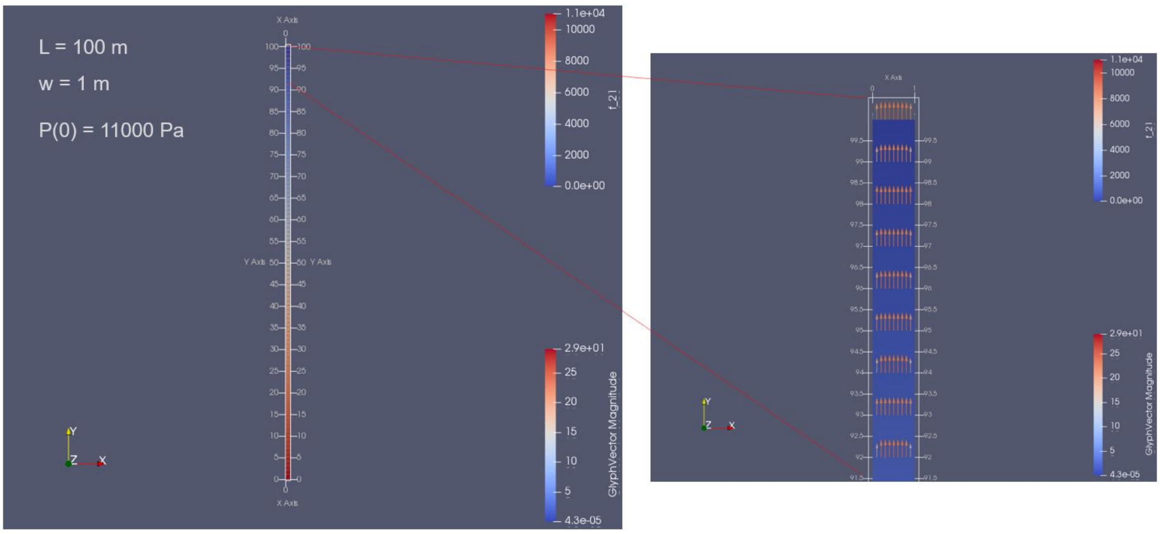

Figure 6.15: Left: Velocity and pressure distribution within a 2-dim rectangular channel with dimensions length $L = 100\,\mathrm{m}$, width $w = 1\,\mathrm{m}$ (Table 6.1: Id = 6). Boundary conditions are analogue to Figure 6.14. Right: Zoom into upper part (surface) of the vent.

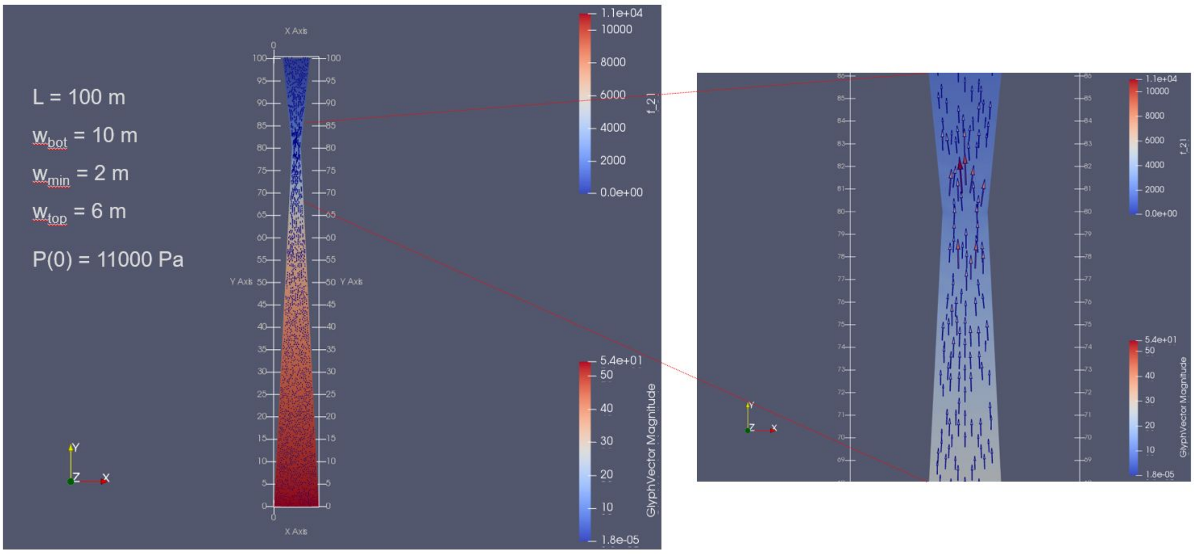

Figure 6.16: Left: Velocity and pressure distribution within a channel having a kink (Table 6.1: Id = 8). The length $L = 100\,\mathrm{m}$, as in the rectangular cases, but the width w varies from $w(z = 0) = 10\,\mathrm{m}$ at the bottom to a minimum value $w_{\mathrm{min}} = 2\,\mathrm{m}$ (at the kink), and raising to $w(z = L) = 6\,\mathrm{m}$ at the surface. The velocity u increases towards the kink reflecting the Venturi effect, which is visible on the enlarged frame at the r.h.s. Right: Zoom into kink at upper part of the vent.

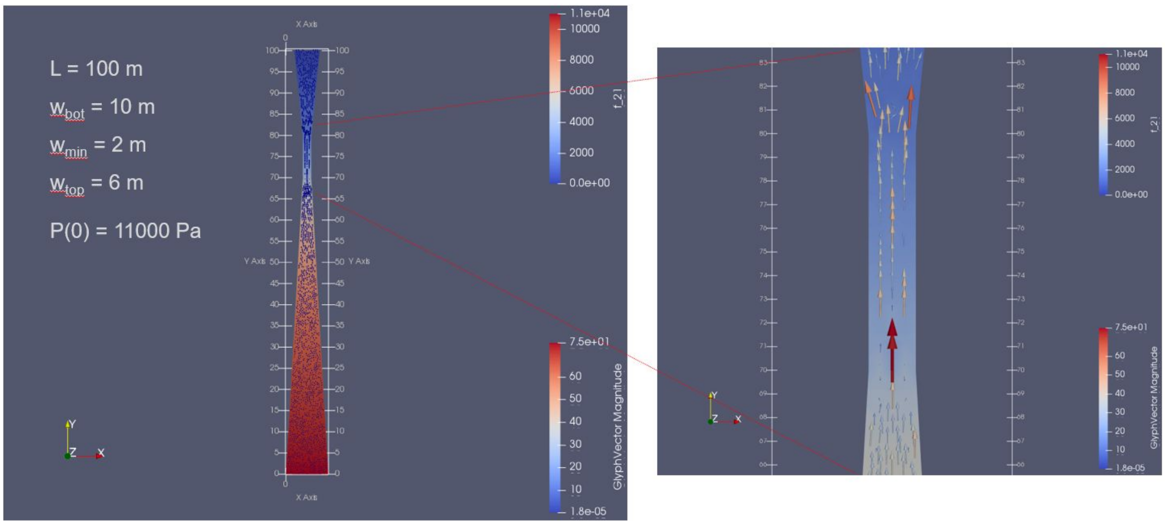

Figure 6.17: Left: Velocity and pressure distribution within a vent having a throat (Table 6.1: Id = 9). The length $L = 100\,\mathrm{m}$ as in the rectangular cases, values of width w: at the bottom $w(z = 0) = 10\,\mathrm{m}$, at the top $w(z = L) = 6\,\mathrm{m}$, within the throat $w_{\mathrm{min}} = 2\,\mathrm{m}$ ($70\,\mathrm{m} \leq z \leq 80\,\mathrm{m}$), respectively. The velocity u is enlarged within the throat due to the Venturi effect. Right: Zoom into throat at upper part of the vent.

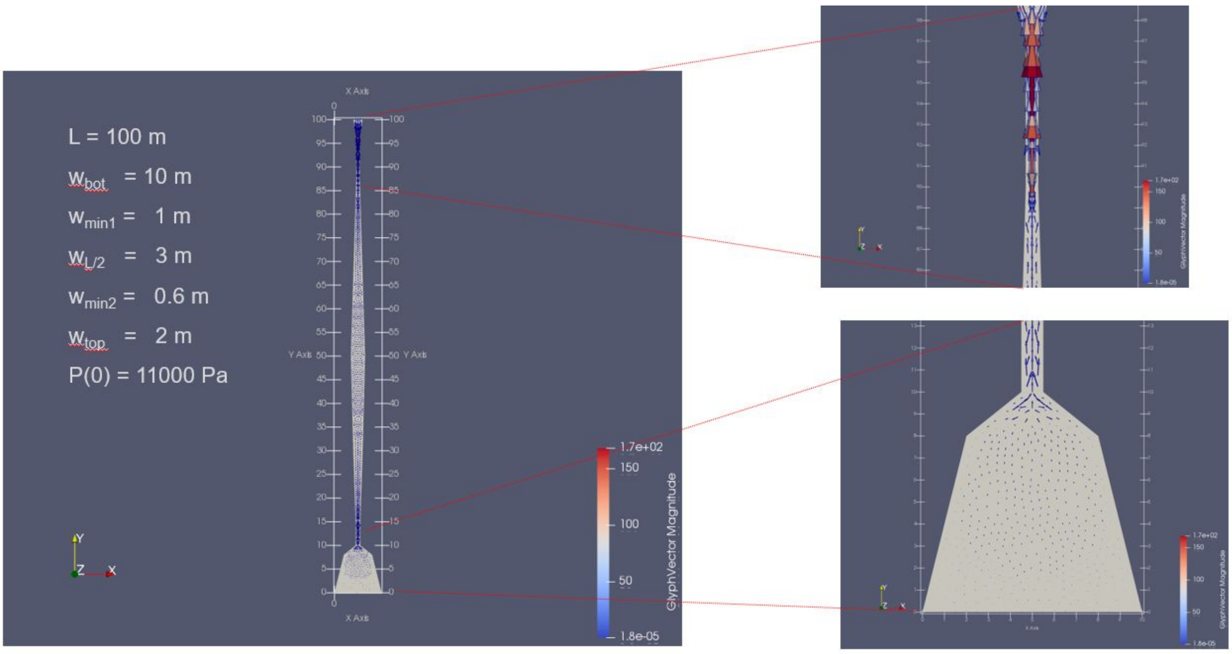

Figure 6.18: Velocity distribution within a vent containg two throats and a cave-like evaporation area at the bottom. The length $L = 100\,\mathrm{m}$, values of width w: at the bottom $w(z = 0) = 10\,\mathrm{m}$, at the top $w(z = L) = 2\,\mathrm{m}$, at throat 1 (right after the cave) $w_{\min1} = 1\,\mathrm{m}$, at throat 2 (at the top): $w_{\min2} = 0.6\,\mathrm{m}$, respectively. The velocity u is enhanced in the vicinity of the throats reflecting the Venturi effect.

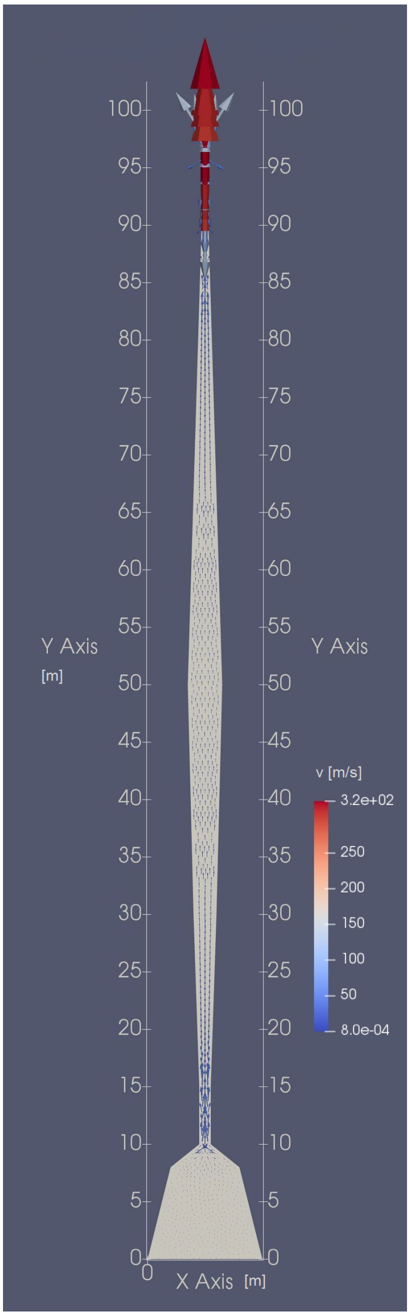

Figure 6.19: Velocity distribution within a vent containg two throats and a cave-like evaporation area at the bottom (Table 6.1: Id = 10). The length $L = 100\,\text{m}$, values of width w: at the bottom $w(z = 0) = 10\,\text{m}$, at the top $w(z = L) = 2\,\text{m}$, at throat 1 (right after the cave) $w_{\text{min1}} = 1\,\text{m}$, at throat 2 (at the top): $w_{\text{min2}} = 0.6\,\text{m}$, respectively. The Venturi effect of increased velocity u is strongly pronounced in the vicinity of the ejection point at the top of the channel.

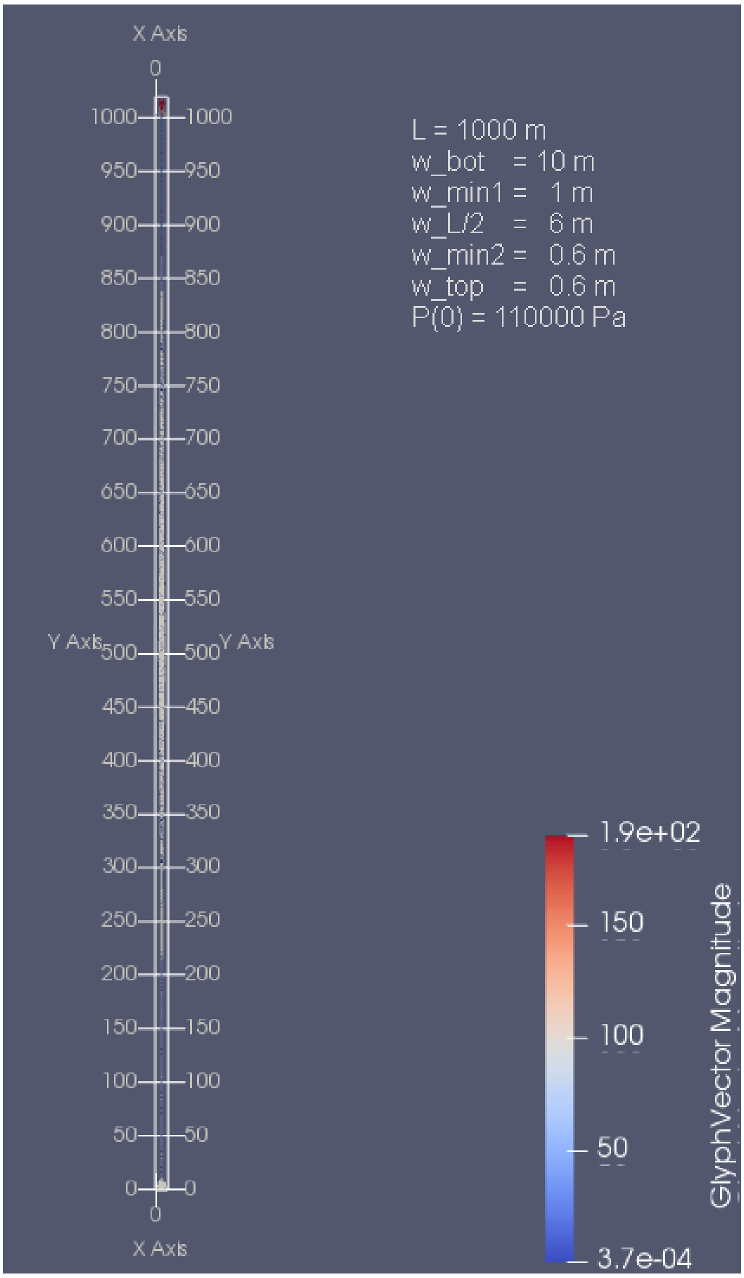

Figure 6.20: Velocity distribution within a vent containg two throats and a cave-like evaporation area at the bottom (Table 6.1: Id = 11). The length $L = 1000\,\mathrm{m}$, values of width w: at the bottom $w(z = 0) = 10\,\mathrm{m}$, at the top $w(z = L) = 0.6\,\mathrm{m}$, at throat 1 (right after the cave) $w_{\mathrm{min1}} = 1\,\mathrm{m}$, at throat 2 (at the top): $w_{\mathrm{min2}} = 0.6\,\mathrm{m}$, respectively. The Venturi effect of increased velocity u is clearly pronounced in the vicinity of the throat at the top of the vent. See also Figure 6.21 - Figure 6.25 for more details.

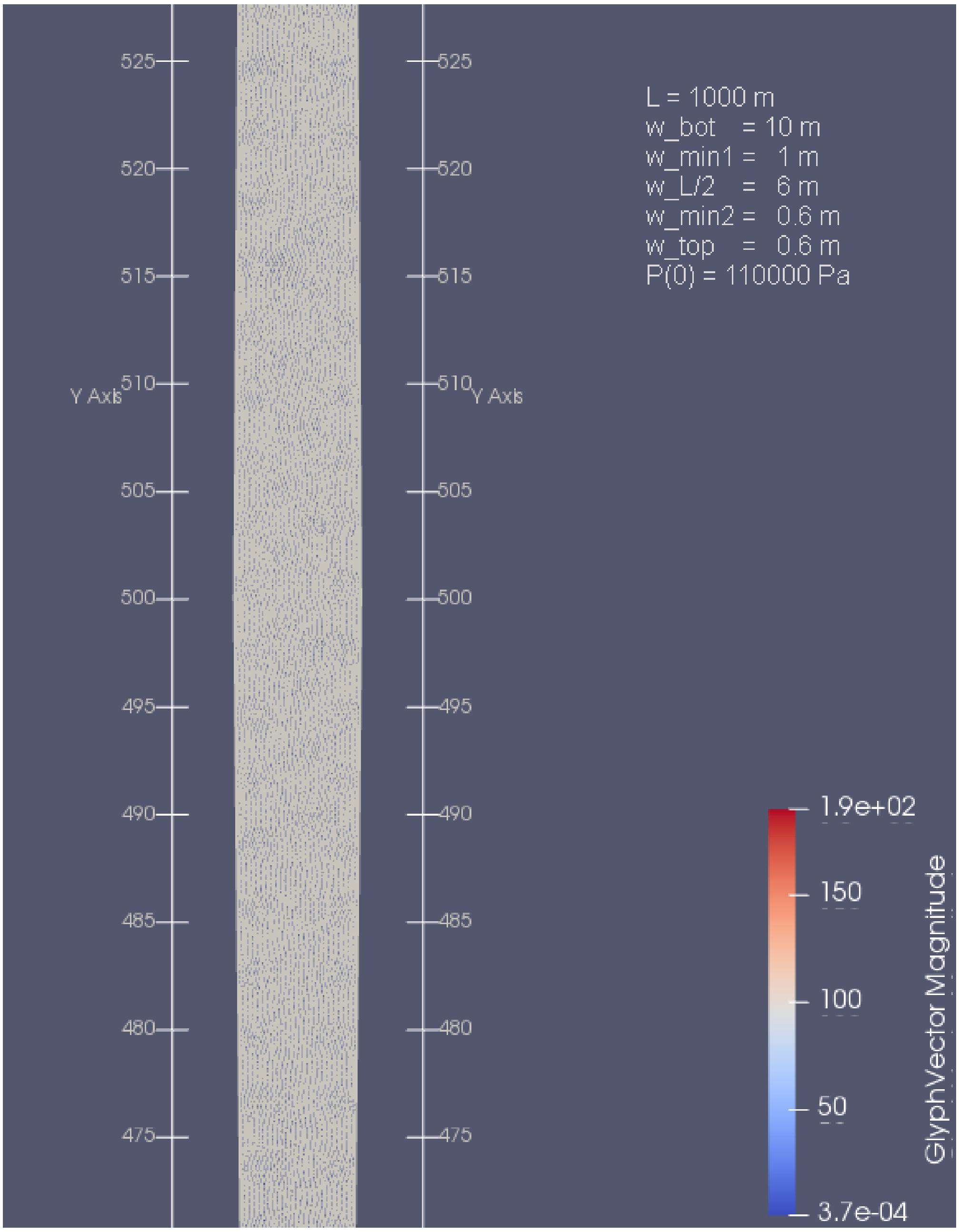

Figure 6.21: High resolution detail plot of the $L = 1000\,\mathrm{m}$ two throat vent (Figure 6.20) showing the velocity distribution of the middle part of the channel around $z = 500\,\mathrm{m}$.

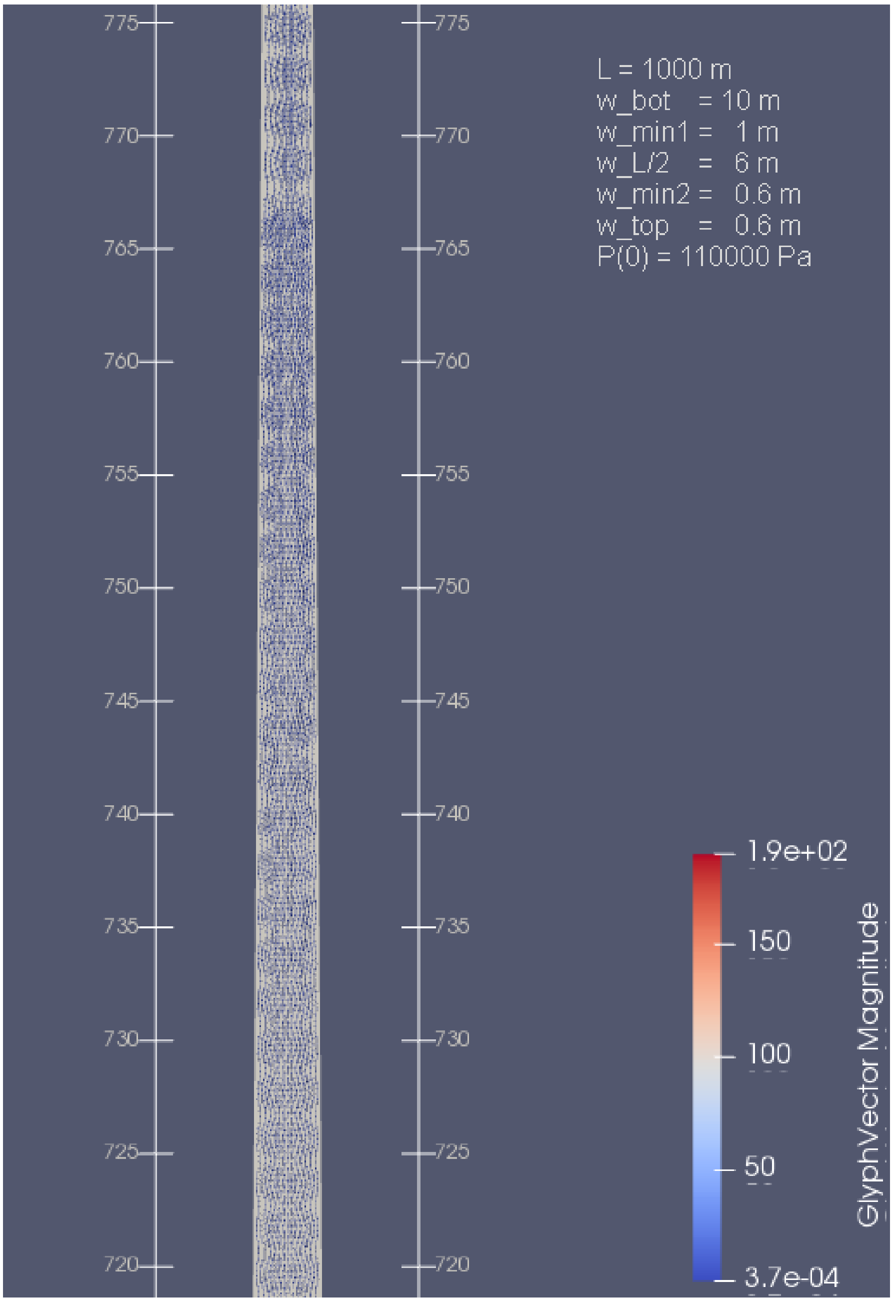

Figure 6.22: High resolution detail plot of the $L = 1000\,\mathrm{m}$ two throat vent (Figure 6.20) showing the velocity distribution of the upper part of the channel ($720 \leq z \leq 775\,\mathrm{m}$).

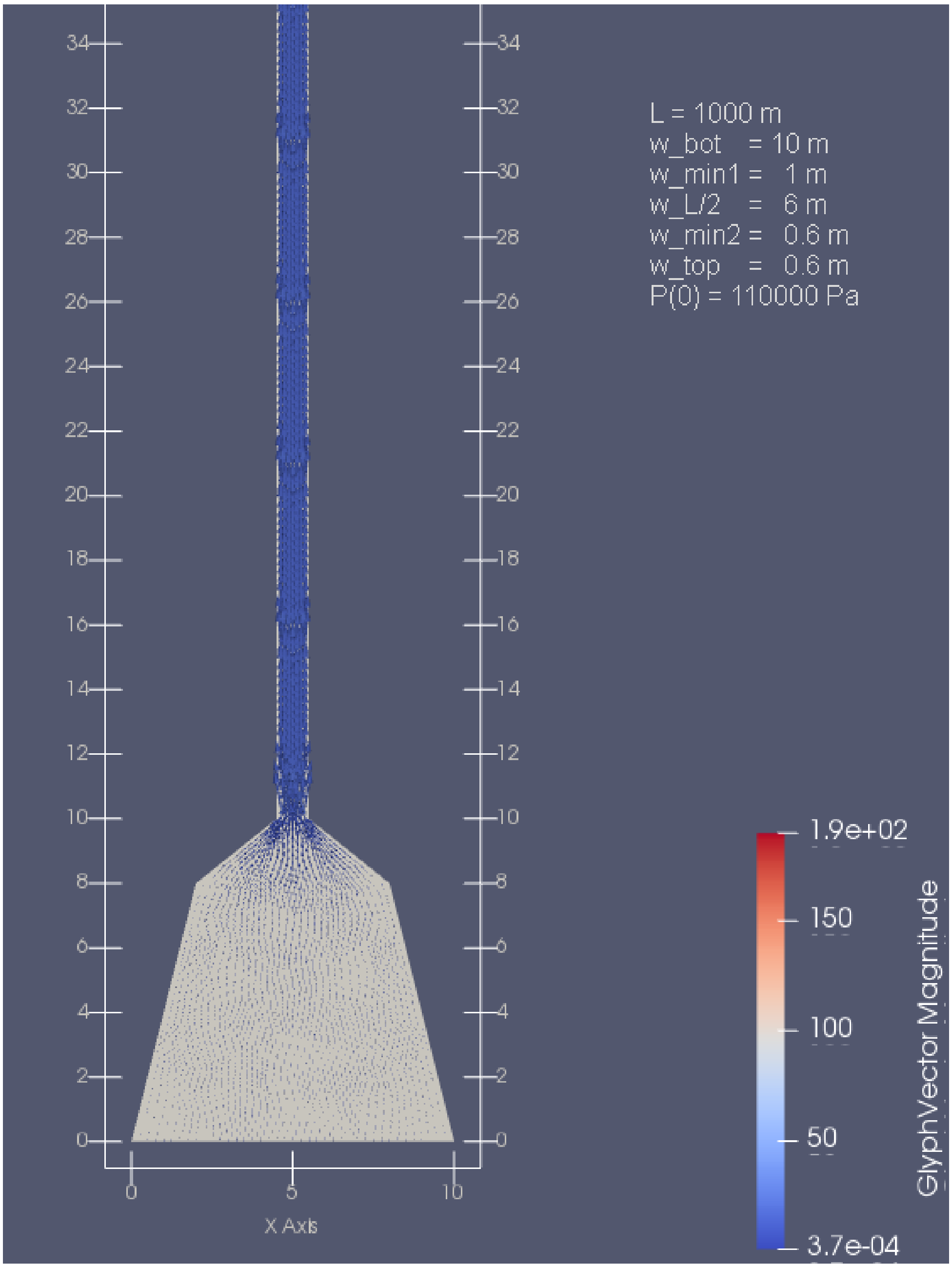

Figure 6.23: High resolution detail plot of the $L = 1000\,\mathrm{m}$ two throat vent (Figure 6.20) showing the velocity distribution at the bottom part ($0 \le z \le 34\,\mathrm{m}$).

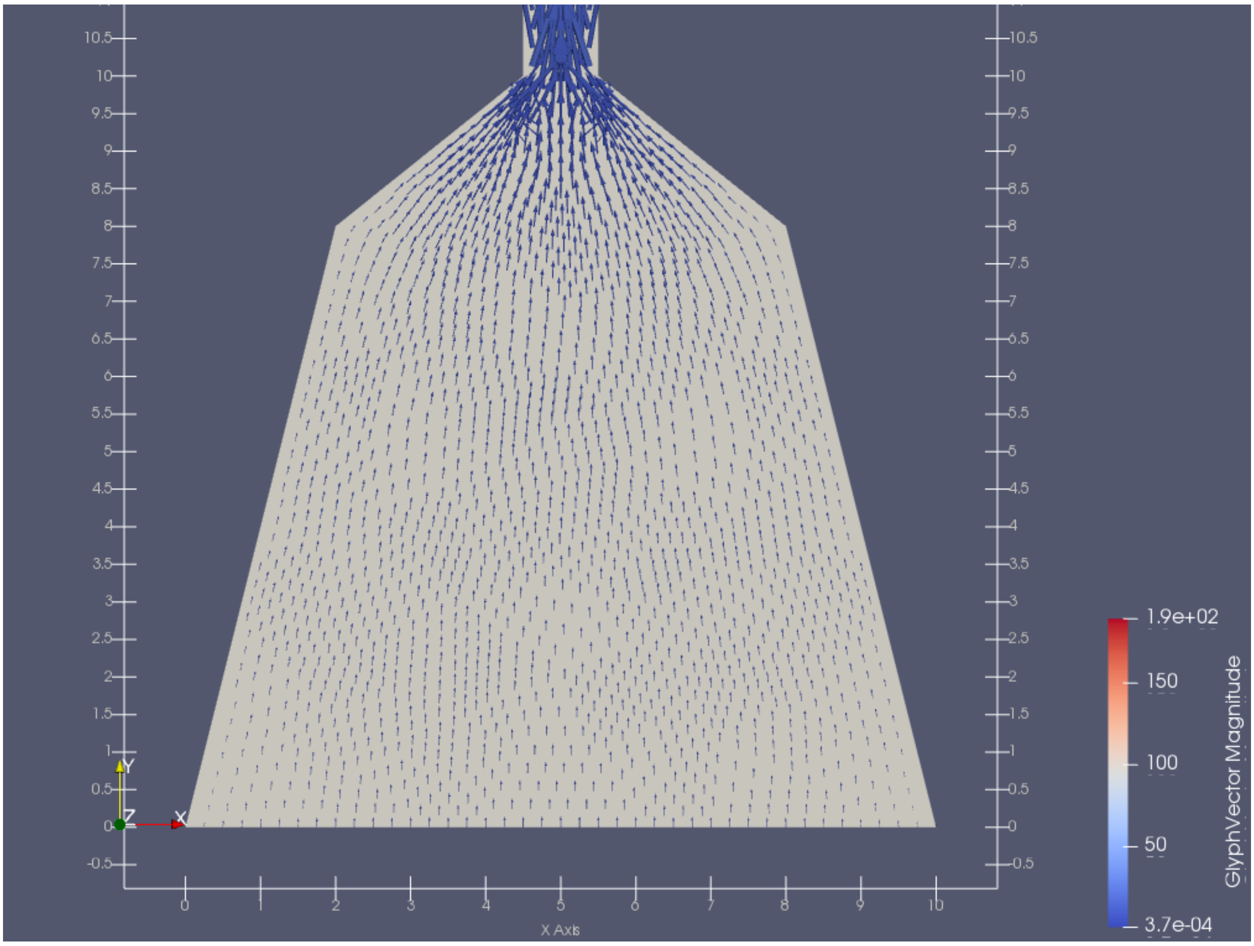

Figure 6.24: High resolution detail plot of the $L = 1000\,\mathrm{m}$ two throat vent (Figure 6.20) showing the velocity distribution in the cave-like area at the bottom.

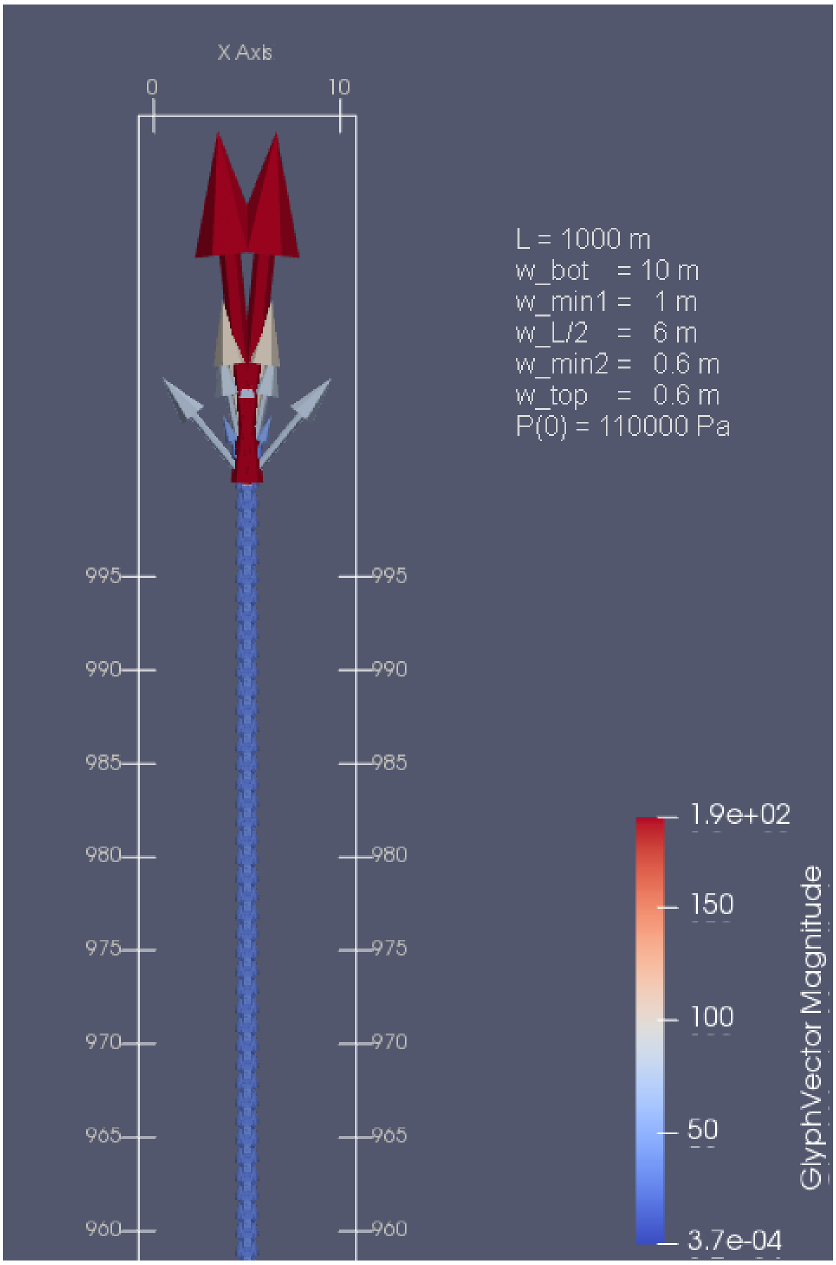

Figure 6.25: High resolution detail plot of the $L = 1000\,\mathrm{m}$ two throat vent (Figure 6.20) showing the velocity distribution at the top ($960 \leq z \leq 1000\,\mathrm{m}$). The enhanced high velocities of the water vapour at the emission point on the surface is clearly visible.

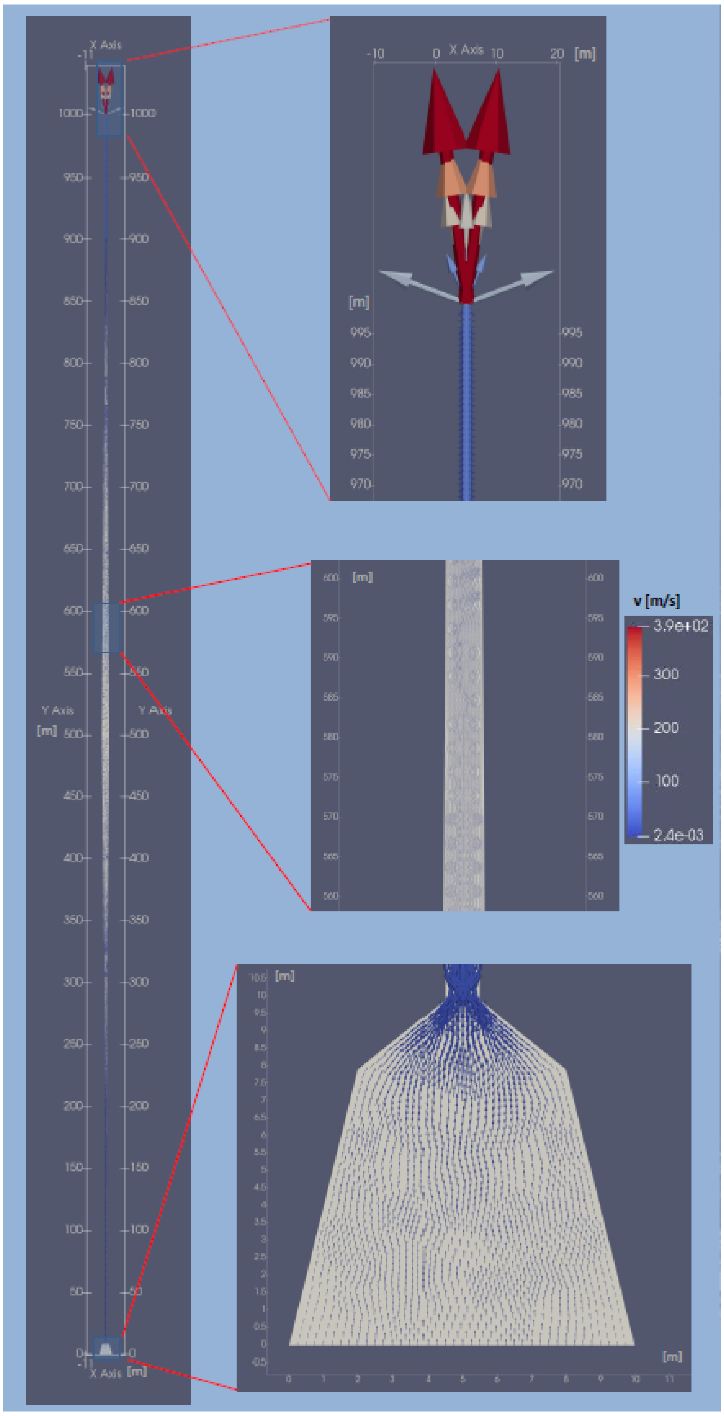

Figure 6.26: Velocity distribution within a vent containg two throats and a cave-like evaporation area at the bottom, same geometry as in Figure 6.20, but with a smaller value of $\rho_0 = 0.5\,\mathrm{kgm}^{-3}$ (Table 6.1: Id = 12). The length $L = 1000\,\mathrm{m}$, values of width w: at the bottom $w(z=0) = 10\,\mathrm{m}$, at the top $w(z=L) = 0.6\,\mathrm{m}$, at throat 1 (right after the cave) $w_{\mathrm{min1}} = 1\,\mathrm{m}$, at throat 2 (at the top): $w_{\mathrm{min2}} = 0.6\,\mathrm{m}$, respectively. The Venturi effect of increased velocity u is strongly expressed in the vicinity of the throat at the top of the vent, the maximum velocity value is higher than in Figure 6.20.

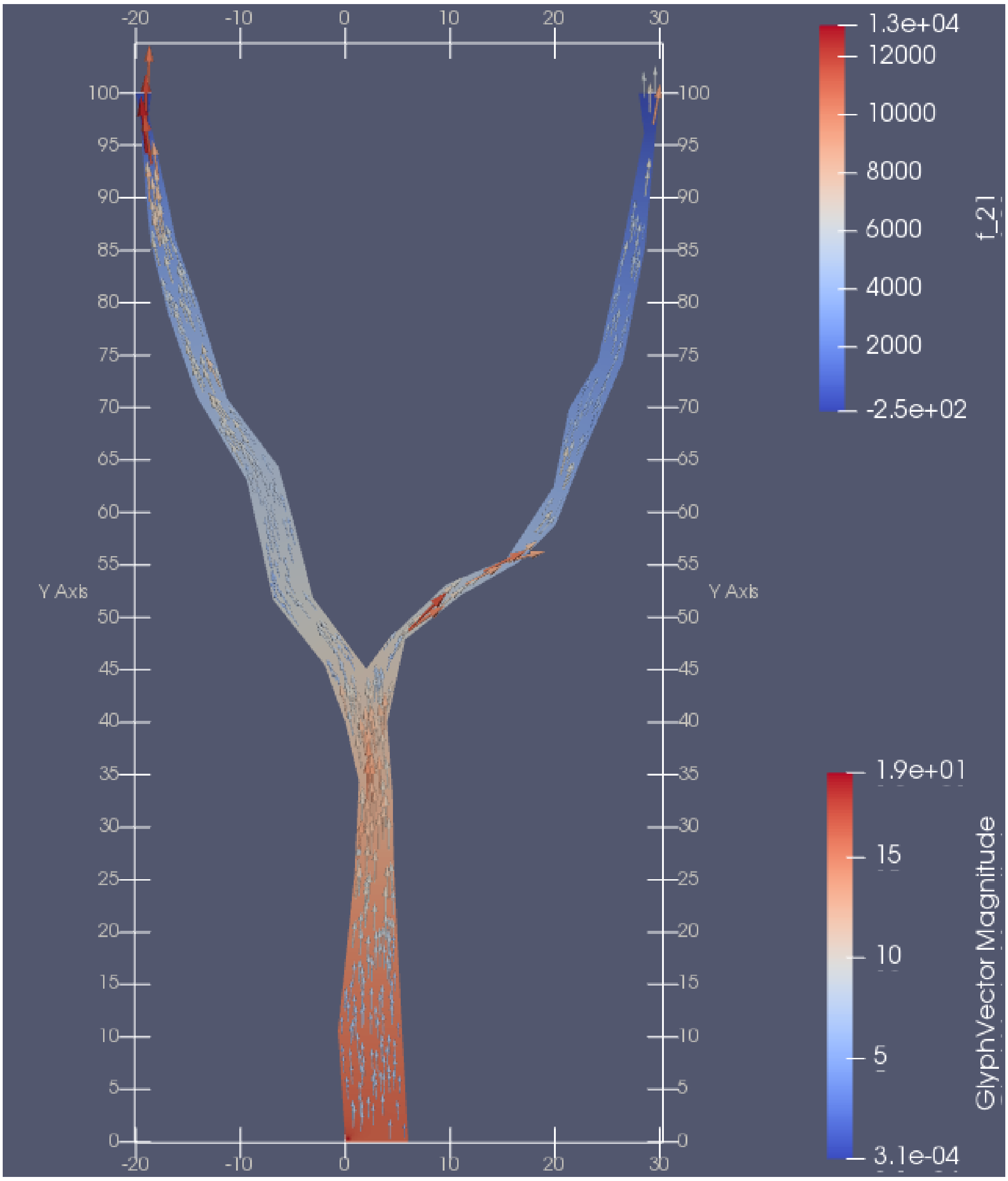

Figure 6.27: Velocity and pressure distributions within a vent containing a bifurcated branch and several throats and kinks ('zig-zag' geometry) using a triangulation grid with medium resolution (refinement level 1) (Table 6.1: Id = 14). The length $L = 100\,\mathrm{m}$, values of width w: at the bottom $w(z = 0) = 6\,\mathrm{m}$, at the top $w_{\mathrm{top\_left}}(z = L) = 1.5\,\mathrm{m}$, $w_{\mathrm{top\_right}}(z = L) = 2.0\,\mathrm{m}$. The Venturi effect of increased velocity u is visible at tight throats and at the emission points on the top of the vent (the effect is more pronounced on the left branch since it has a tighter opening width at the top).

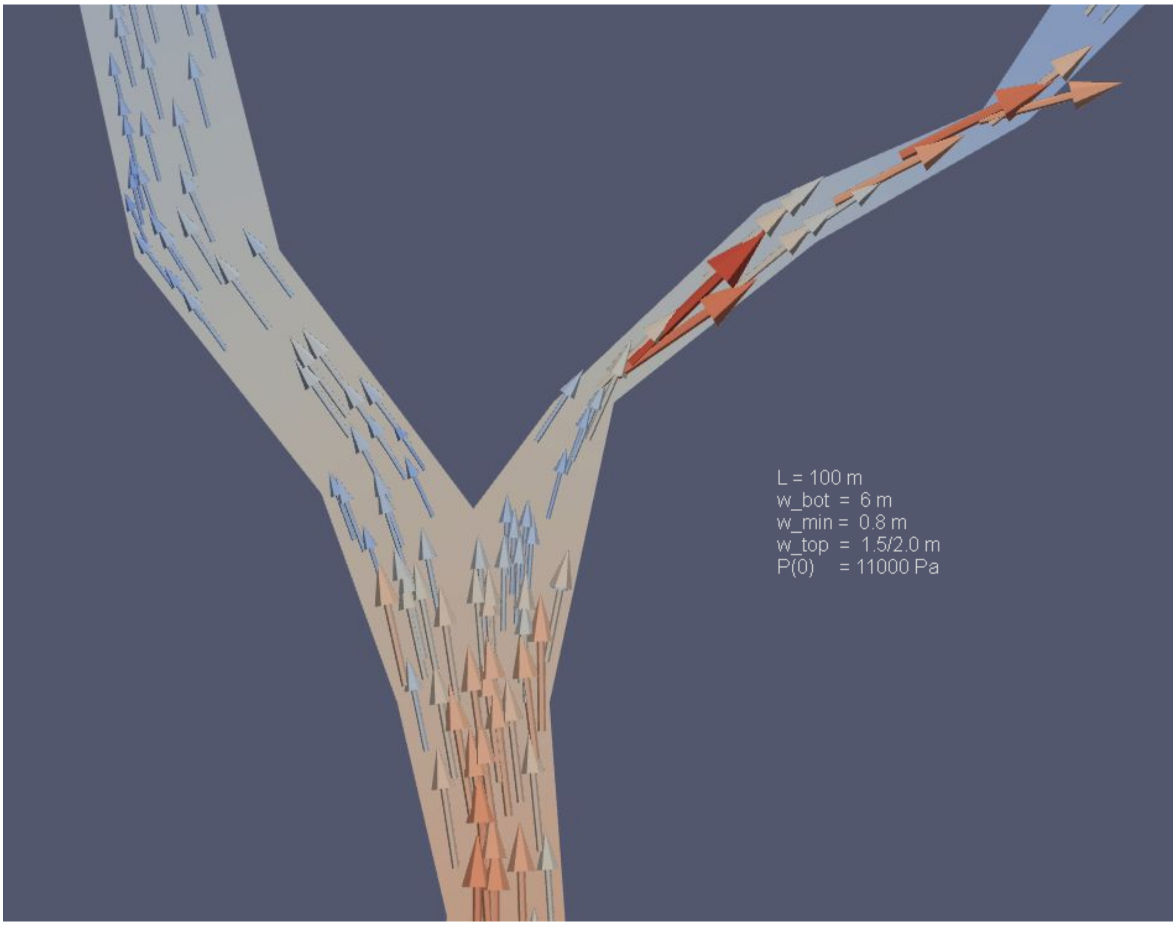

Figure 6.28: Detail plot of the $L = 100\,\mathrm{m}$ 'zig-zag' geometry vent containing a bifurcated branch (Figure 6.27) showing the velocity and pressure distribution around the bifurcation. The velocity is increased at tight throats reflecting the Venturi effect.

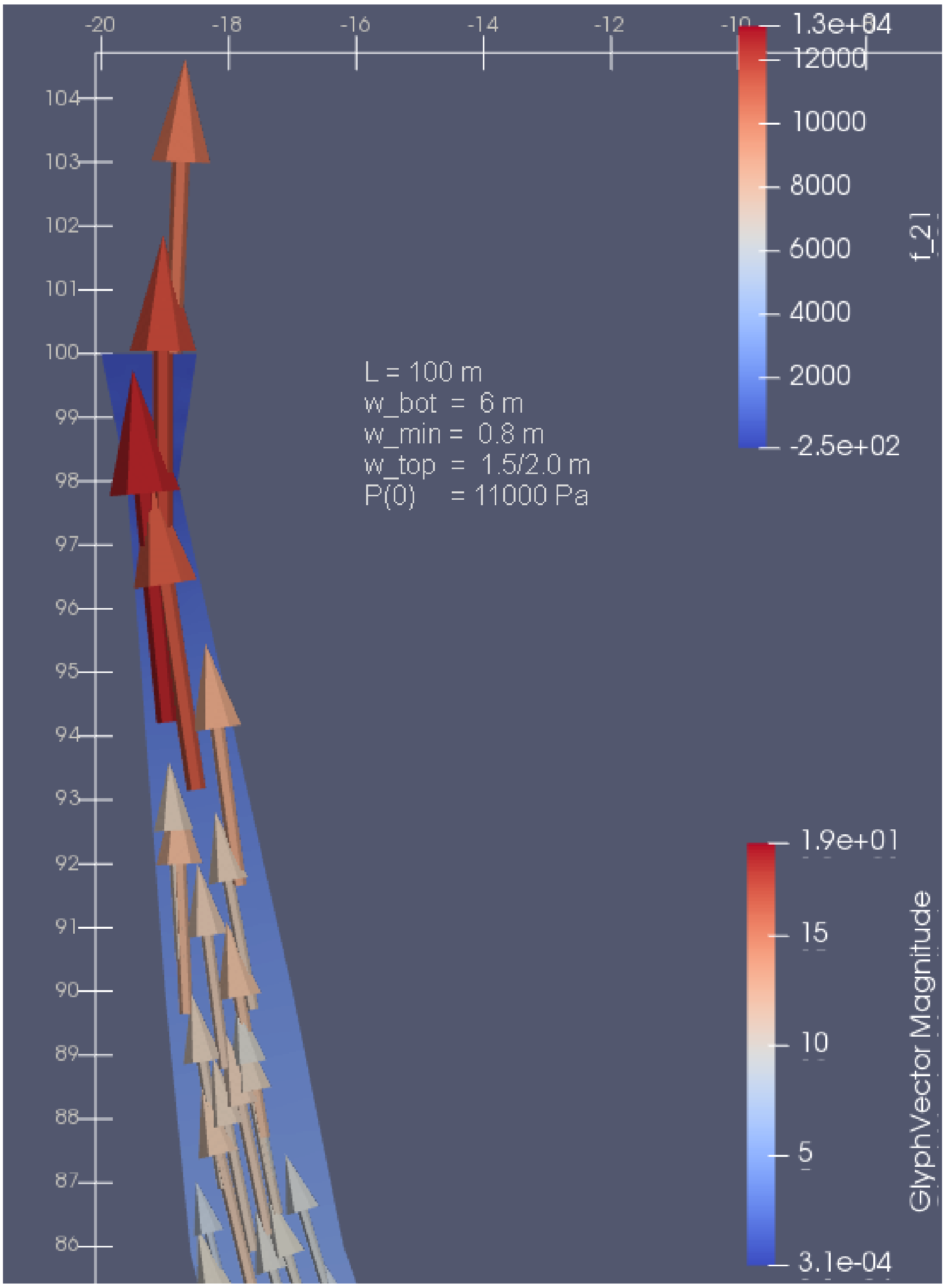

Figure 6.29: Detail plot of the $L = 100\,\mathrm{m}$ 'zig-zag' geometry vent containing a bifurcated branch (Figure 6.27) showing the velocity and pressure distribution in the vicinity of the emission point of the left bifurcation branch. The velocity is considerably enhanced at the emission point where the water vapour erupts on the surface.

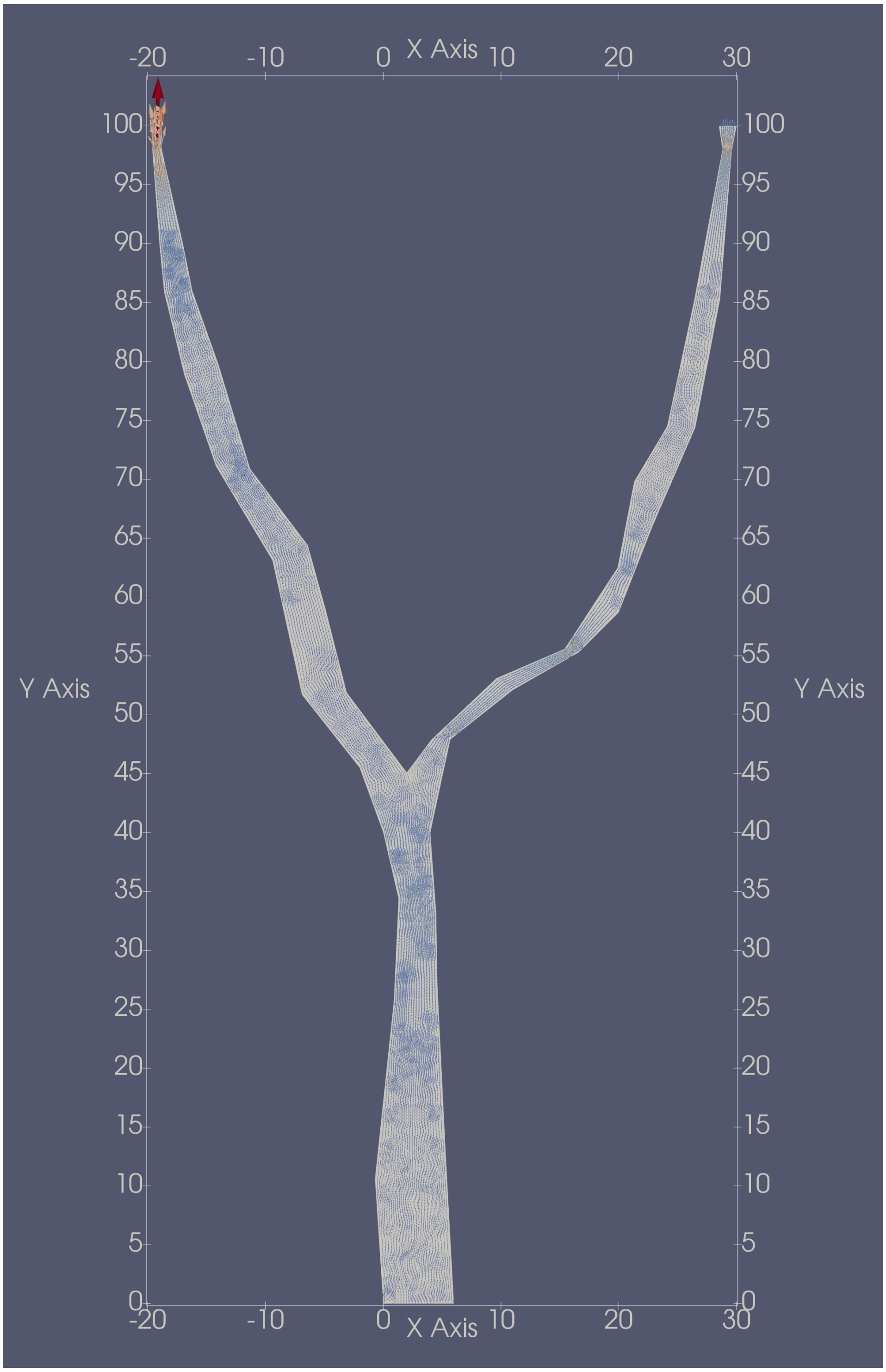

Figure 6.30: Velocity distribution within a vent containing a bifurcated branch and several throats and kinks ('zig-zag' geometry) using a triangulation grid with high resolution (refinement level 2) (Table 6.1: Id = 17). The length $L = 100\,\mathrm{m}$, values of width w: at the bottom $w(z=0) = 6\,\mathrm{m}$, at the top $w_{\mathrm{top\_left}}(z=L) = 0.8\,\mathrm{m}$, $w_{\mathrm{top\_right}}(z=L) = 1.5\,\mathrm{m}$, The Venturi effect of increased velocity u is visible at throats especially at the emission points on the top of the vent (the effect is more pronounced on the left branch since it has a tighter opening width at the top).

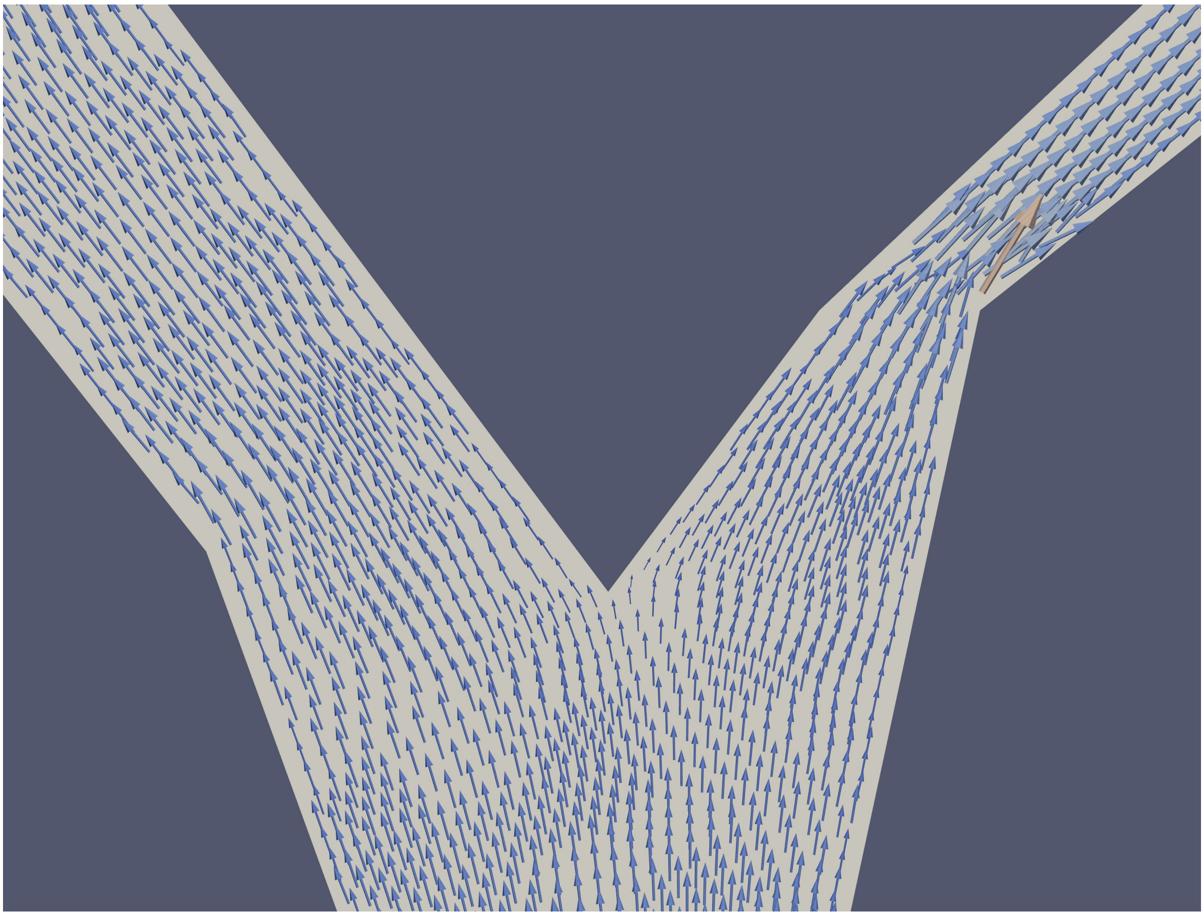

Figure 6.31: Detail plot of the high resolution simulation of the $L = 100\,\mathrm{m}$ 'zig-zag' geometry vent containing a bifurcated branch (Figure 6.30) showing the velocity distribution around the bifurcation. The velocity is increased at tight throats reflecting the Venturi effect.

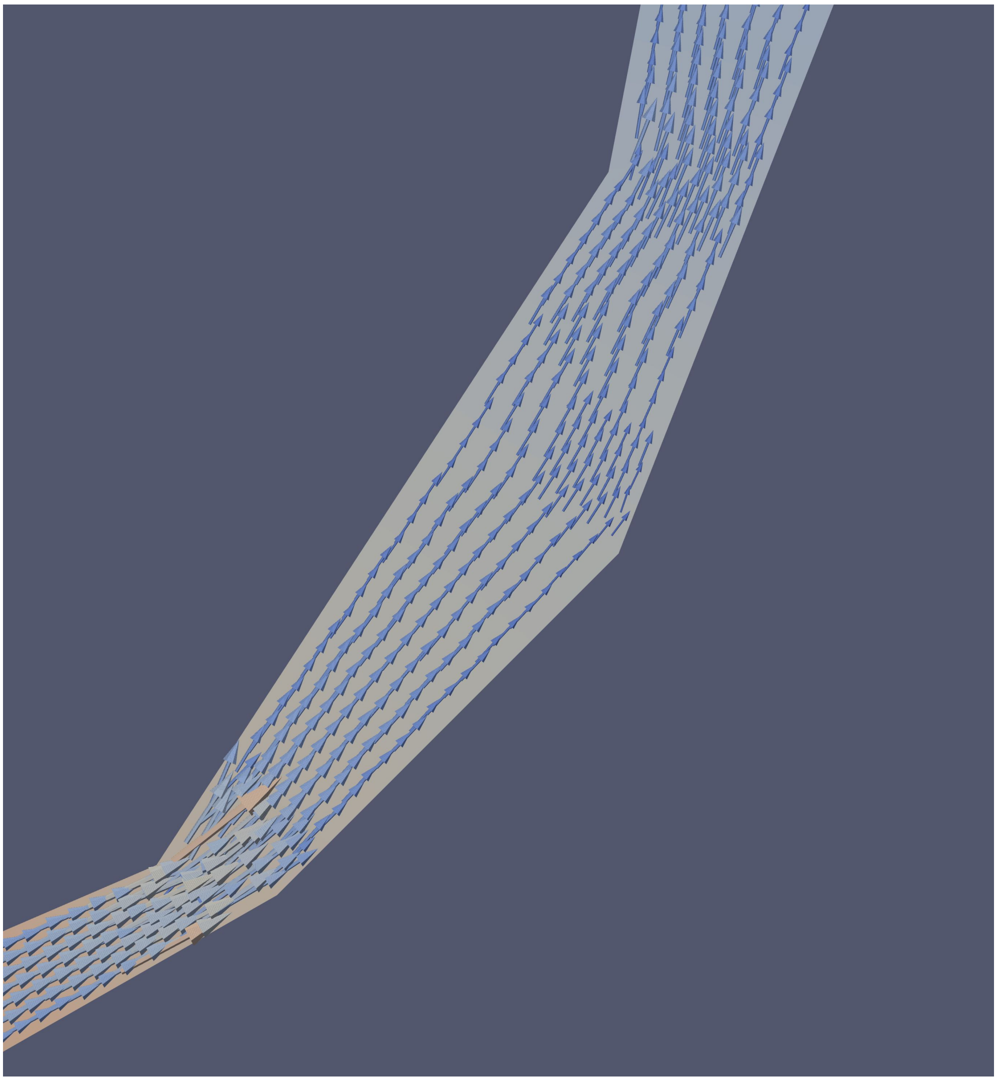

Figure 6.32: Detail plot of the high resolution simulation of the $L = 100\,\mathrm{m}$ 'zig-zag' geometry vent containing a bifurcated branch (Figure 6.30) showing the velocity and pressure distributions in a region in the right branch. The velocity is increased at tight throats reflecting the Venturi effect.

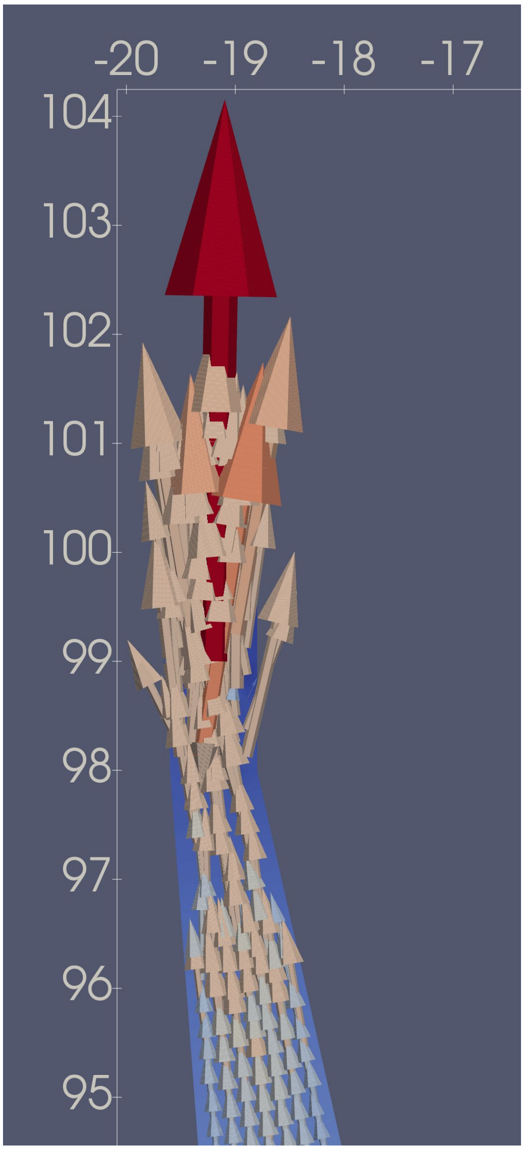

Figure 6.33: Detail plot of the high resolution simulation of the $L = 100\,\mathrm{m}$ 'zig-zag' geometry vent containing a bifurcated branch (Figure 6.30) showing the velocity distribution in the vicinity of the emission point of the left bifurcation branch. The velocity is considerably enhanced at the emission point where the water vapour erupts on the surface.

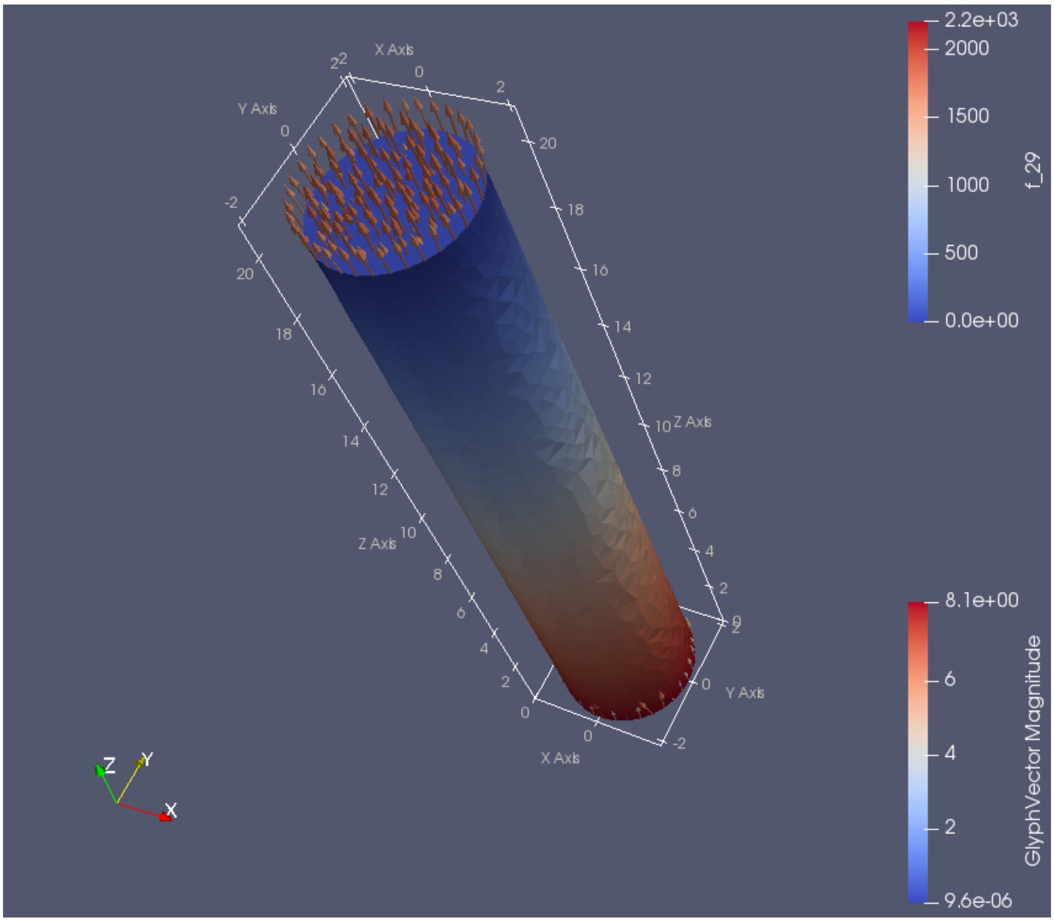

Figure 6.34: Velocity vectors (at the top) and pressure distribution of a 3-dimensional cylindrical vent with dimension length $L = 20\,\mathrm{m}$, diameter $w = 2r = 4\,\mathrm{m}$ (Table 6.1: Id = 18). At the bottom area a hydrostatic pressure $p(z = 0) = \rho g L = 2200\,\mathrm{Pa}$ is assumed (Enceladus' gravitational acceleration $g = 0.11\,\mathrm{m\,s^{-2}}$, $\rho \simeq \rho_{\mathrm{ice}} \simeq \rho_{\mathrm{water}} \simeq 1000\,\mathrm{kg\,m^{-3}}$), the velocity is zero at the bottom area and at the cylinder mantle ('no slip' condition). The pressure is zero at the surface at the top, representing vacuum conditions.

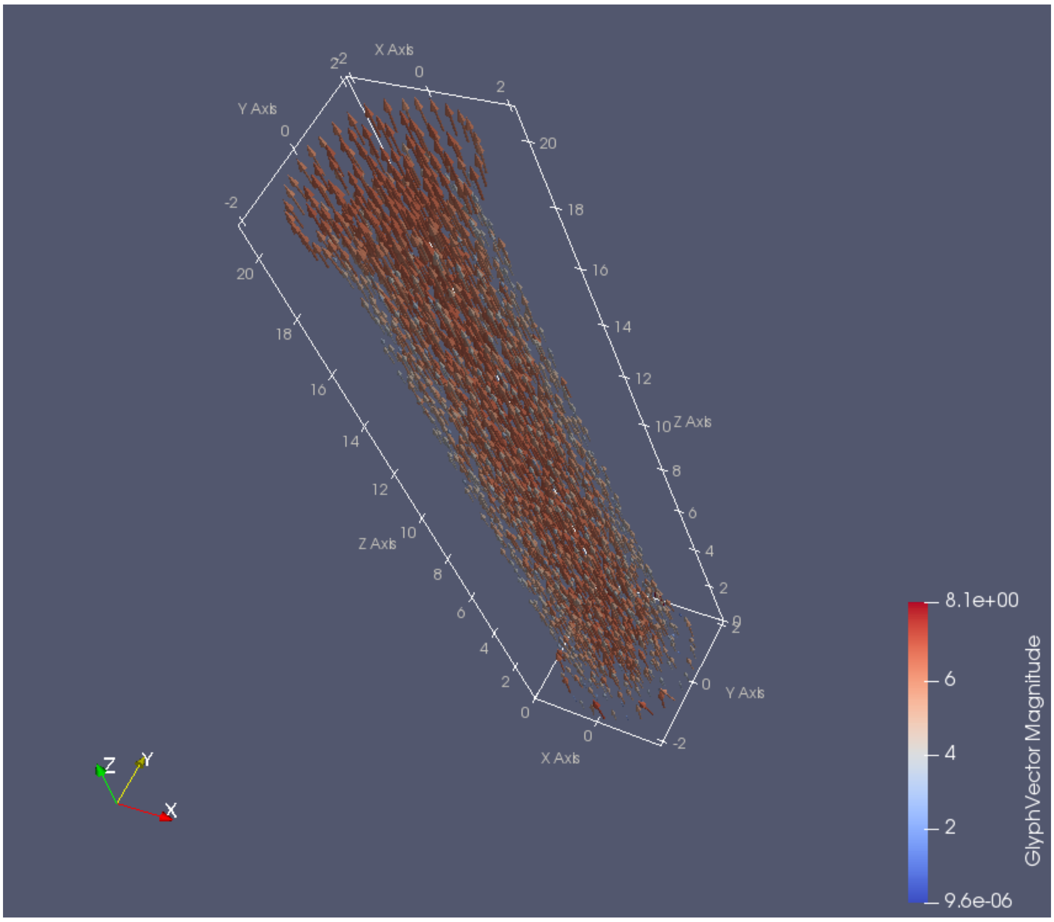

Figure 6.35: Velocity distribution inside the 3-dimensional cylindrical vent with dimension length $L = 20\,\mathrm{m}$, diameter $w = 2r = 4\,\mathrm{m}$ (Figure 6.34, Table 6.1: Id = 18).

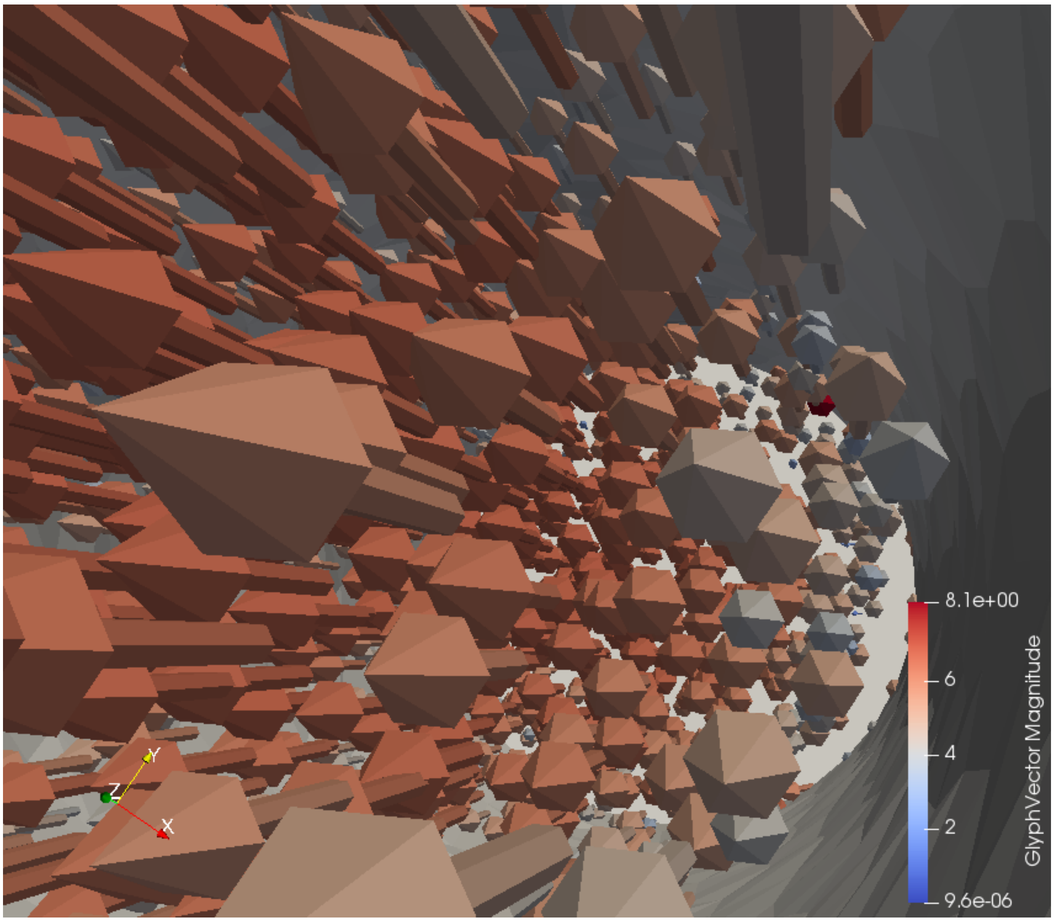

Figure 6.36: Velocity distribution in the interior of the 3-dimensional cylindrical vent with dimension length $L = 20\,\mathrm{m}$, diameter $w = 2r = 4\,\mathrm{m}$ (looking from above) (Figure 6.34, Table 6.1: Id = 18).

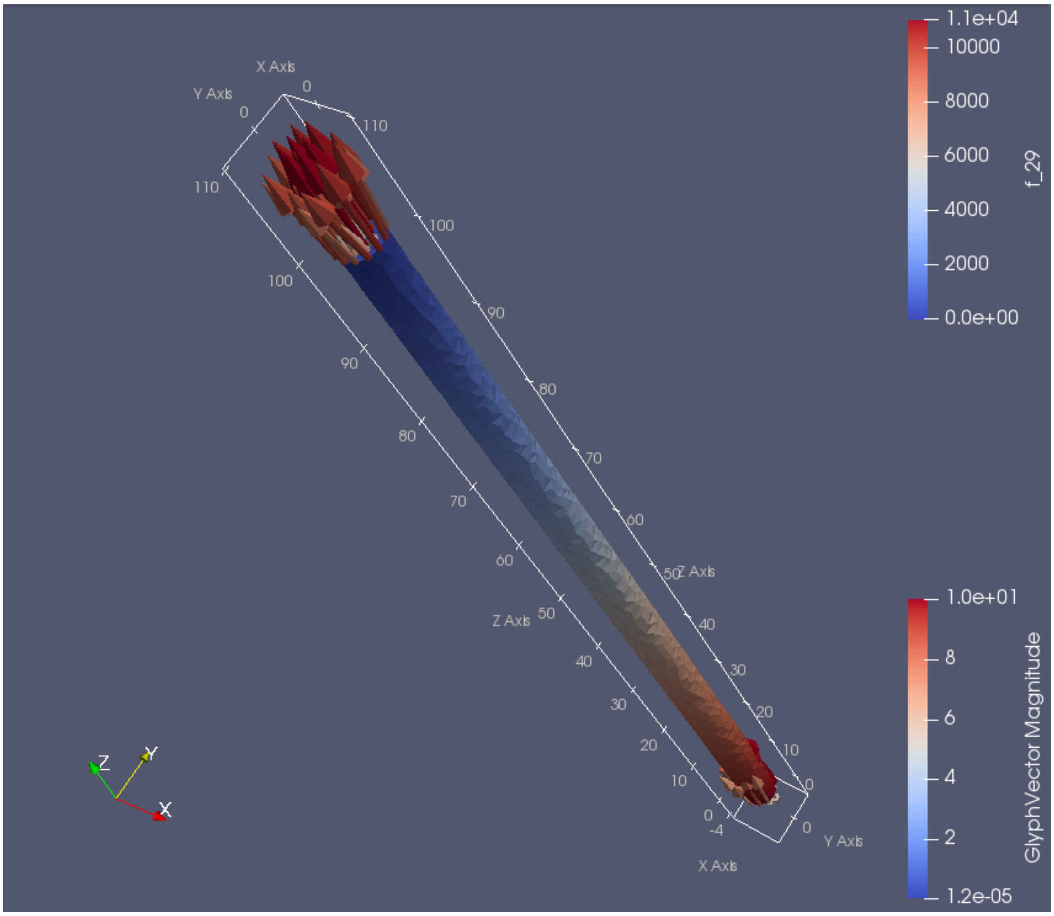

Figure 6.37: Velocity vectors (at the top) and pressure distribution of a 3-dimensional cylindrical vent with dimension length $L = 100\,\mathrm{m}$, diameter $w = 2r = 4\,\mathrm{m}$ (Table 6.1: Id = 20). Boundary conditions are analogue to Figure 6.34, assuming a hydrostatic pressure at the bottom $p(z = 0) = \rho g L = 11000\,\mathrm{Pa}$.

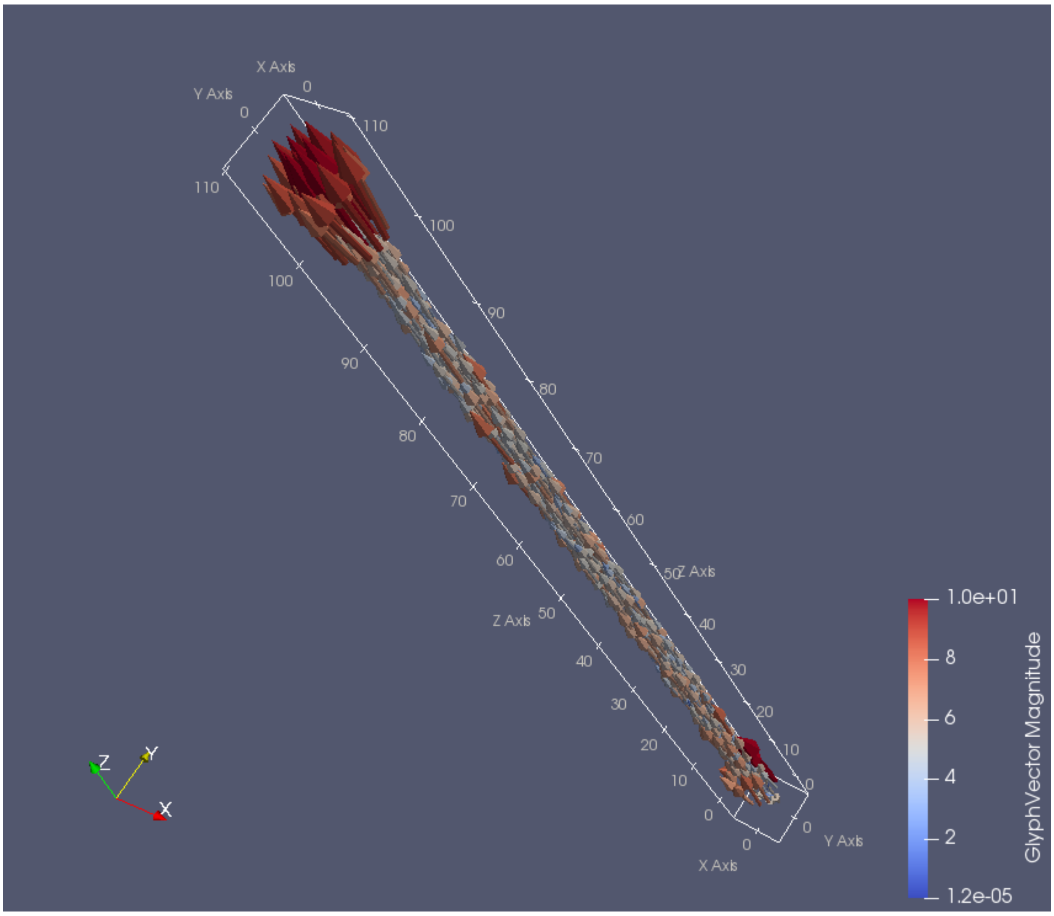

Figure 6.38: Velocity distribution inside the 3-dimensional cylindrical vent with dimension length $L = 100\,\mathrm{m}$, diameter $w = 2r = 4\,\mathrm{m}$ (Figure 6.37, Table 6.1: Id = 20).

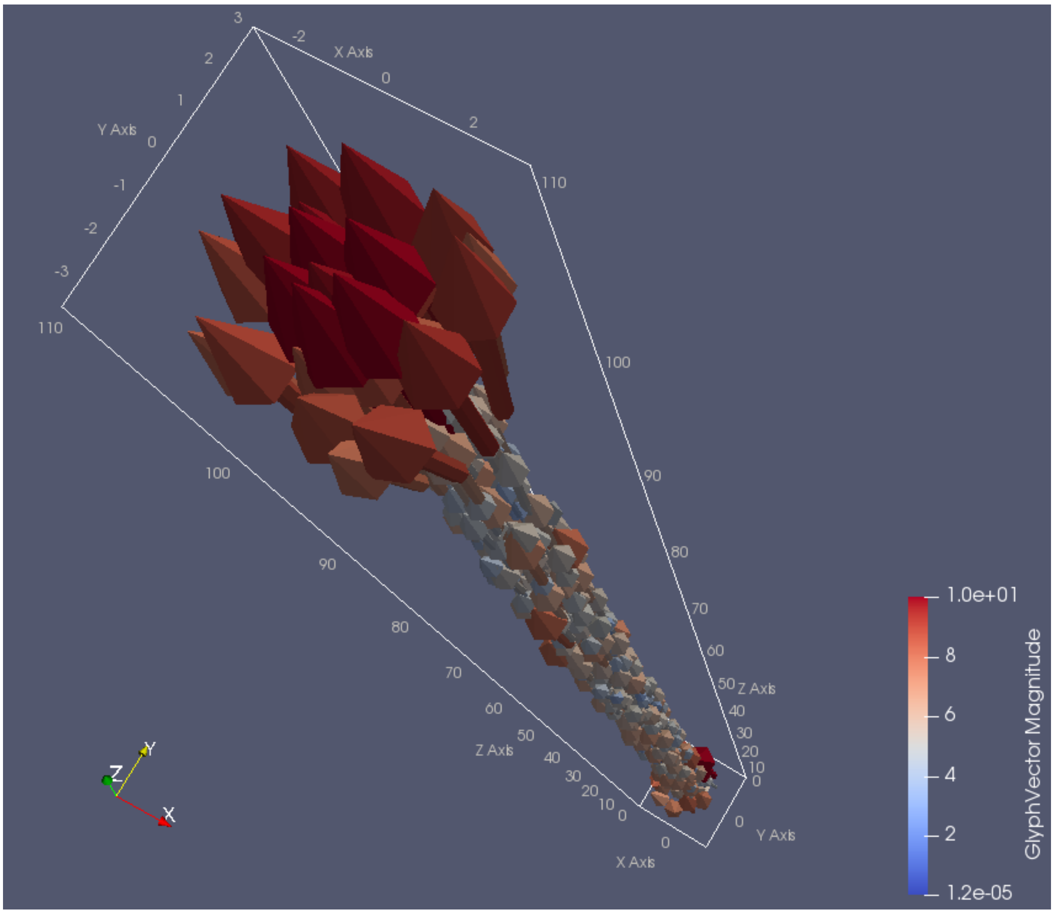

Figure 6.39: Velocity distribution inside the 3-dimensional cylindrical vent with dimension length $L = 100\,\mathrm{m}$, diameter $w = 2r = 4\,\mathrm{m}$ seen from a nearer viewing perspective from above (Figure 6.37, Table 6.1: Id = 20).

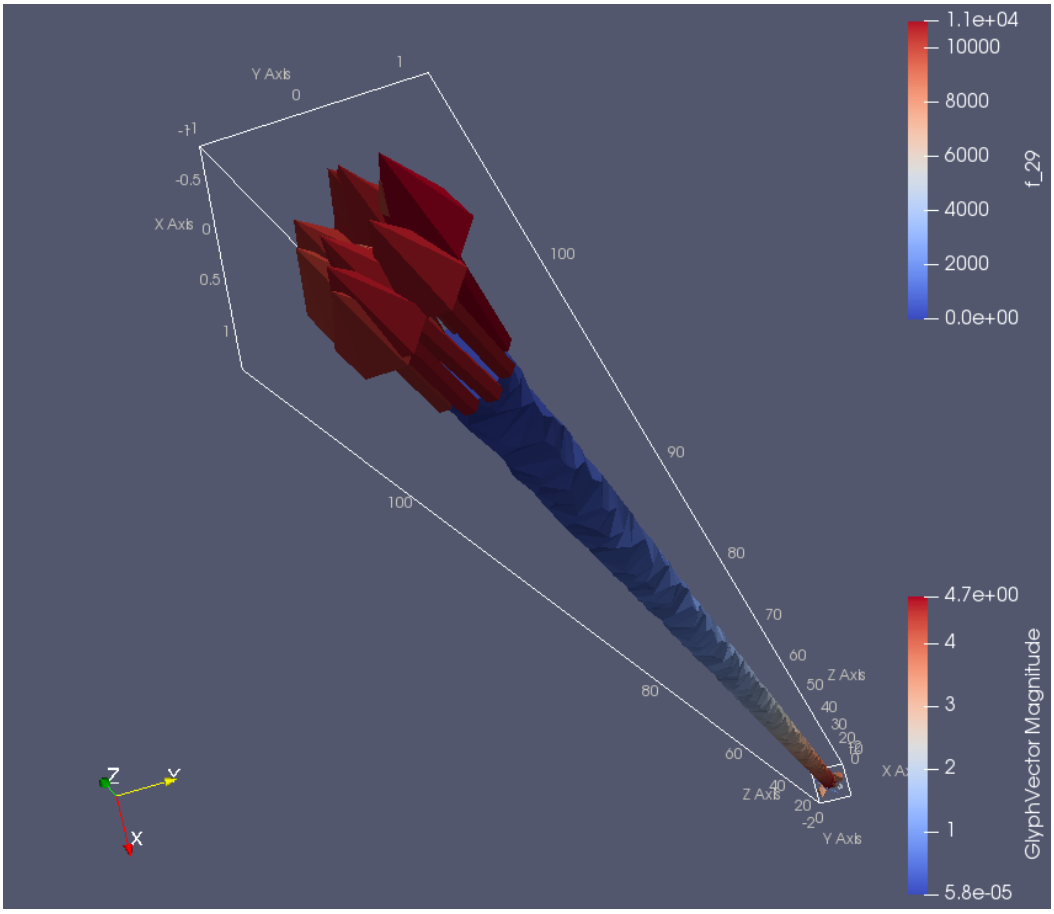

Figure 6.40: Velocity vectors (at the top) and pressure distribution of a 3-dimensional cylindrical vent with dimension length $L = 100\,\mathrm{m}$, diameter $w = 2r = 1\,\mathrm{m}$ (Table 6.1: Id = 21). Boundary conditions are analogue to Figure 6.37.

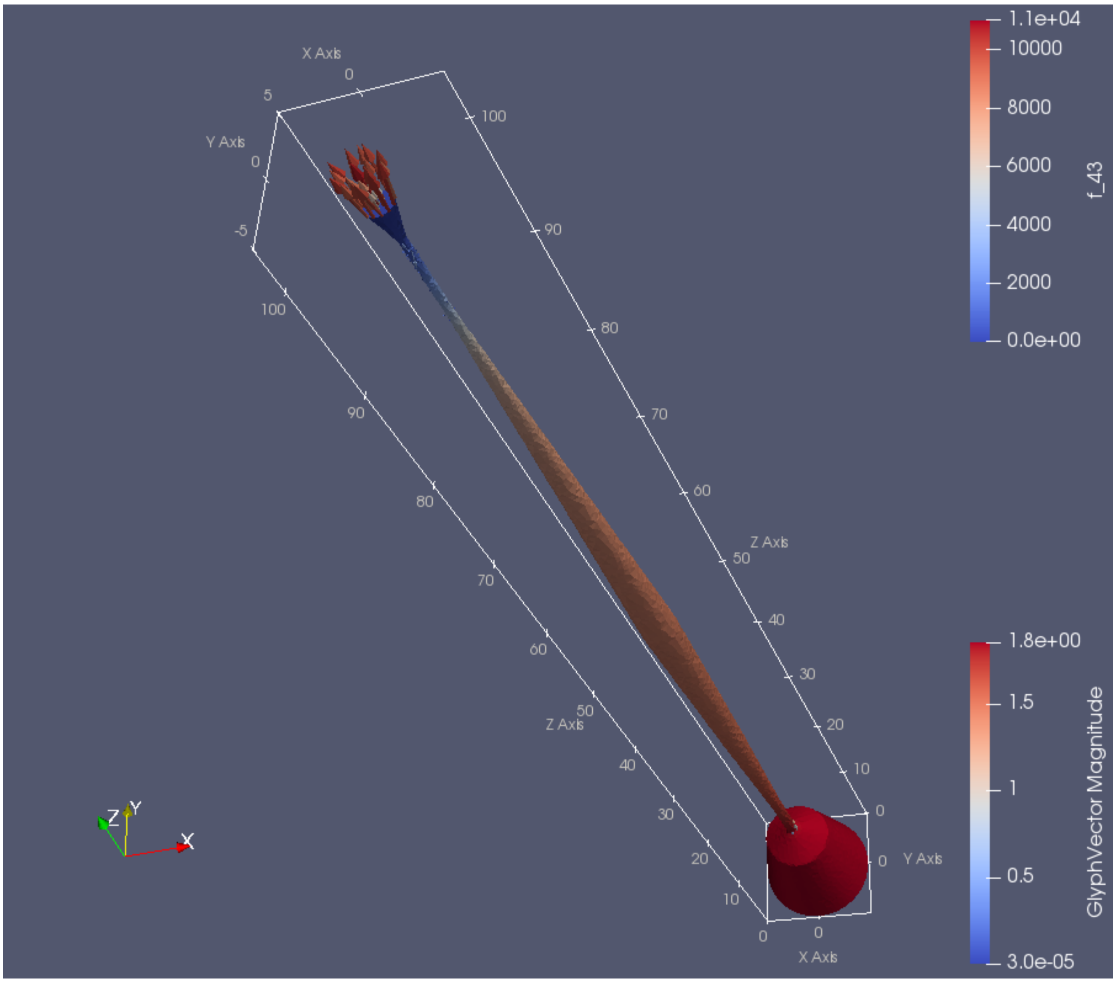

Figure 6.41: Velocity vectors (at the top) and pressure distribution of a 3-dim vent containing two throats and a cave-like evaporation area at the bottom (for all parameters see Table 6.1: Id = 22). This 3-dim geometry is the analogon to the 2-dim vent-with-throats shape (Table 6.1: Id = 10). The length $L = 100\,\mathrm{m}$, values of width w: at the bottom $w(z = 0) = 10\,\mathrm{m}$, at the top $w(z = L) = 2\,\mathrm{m}$, at throat 1 (right after the cave) $w_{\mathrm{min1}} = 1\,\mathrm{m}$, at throat 2 (at the top): $w_{\mathrm{min2}} = 0.6\,\mathrm{m}$, respectively.

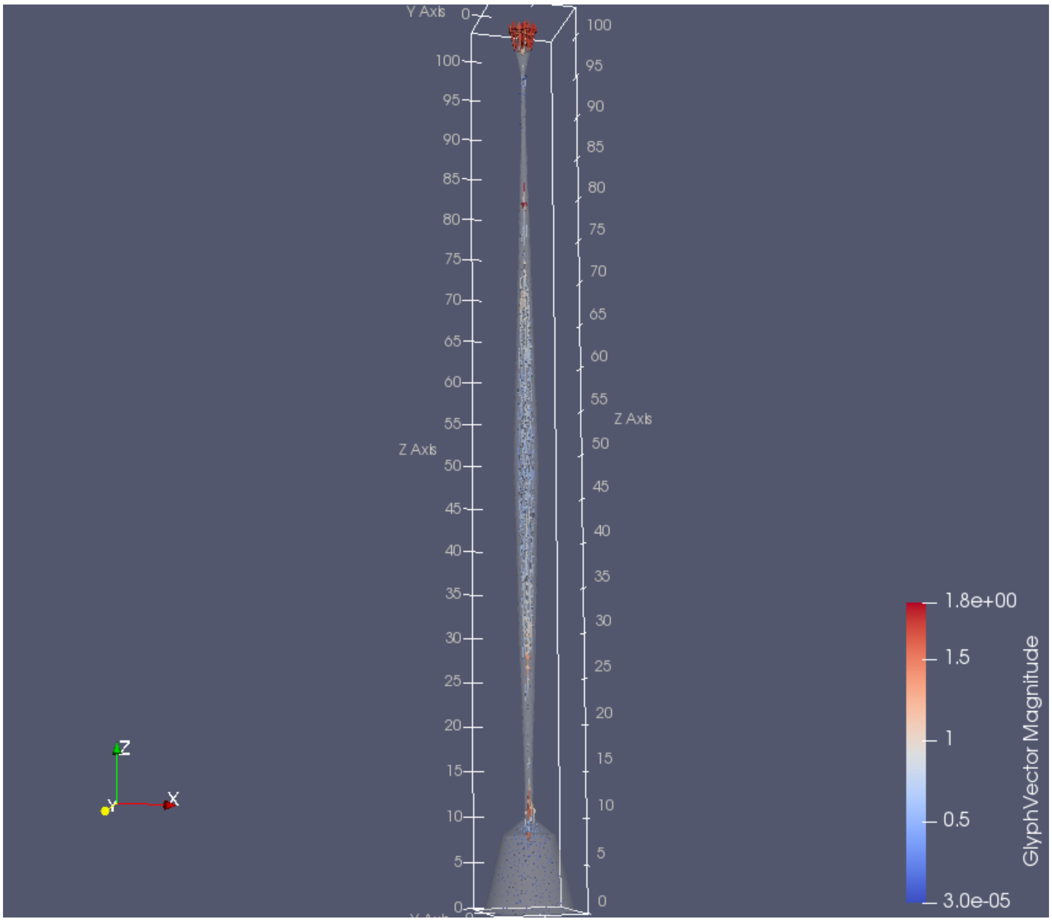

Figure 6.42: Velocity distribution inside the 3-dim vent containing two throats and a cave-like evaporation area at the bottom (see Figure 6.41, Table 6.1: Id = 22). This 3-dim geometry is the analogon to the 2-dim vent-with-throats shape (Table 6.1: Id = 10) and has dimension length $L = 100\,\mathrm{m}$, values of width w: at the bottom $w(z = 0) = 10\,\mathrm{m}$, at the top $w(z = L) = 2\,\mathrm{m}$, at throat 1 (right after the cave) $w_{\mathrm{min}1} = 1\,\mathrm{m}$, at throat 2 (at the top): $w_{\mathrm{min}2} = 0.6\,\mathrm{m}$, respectively.

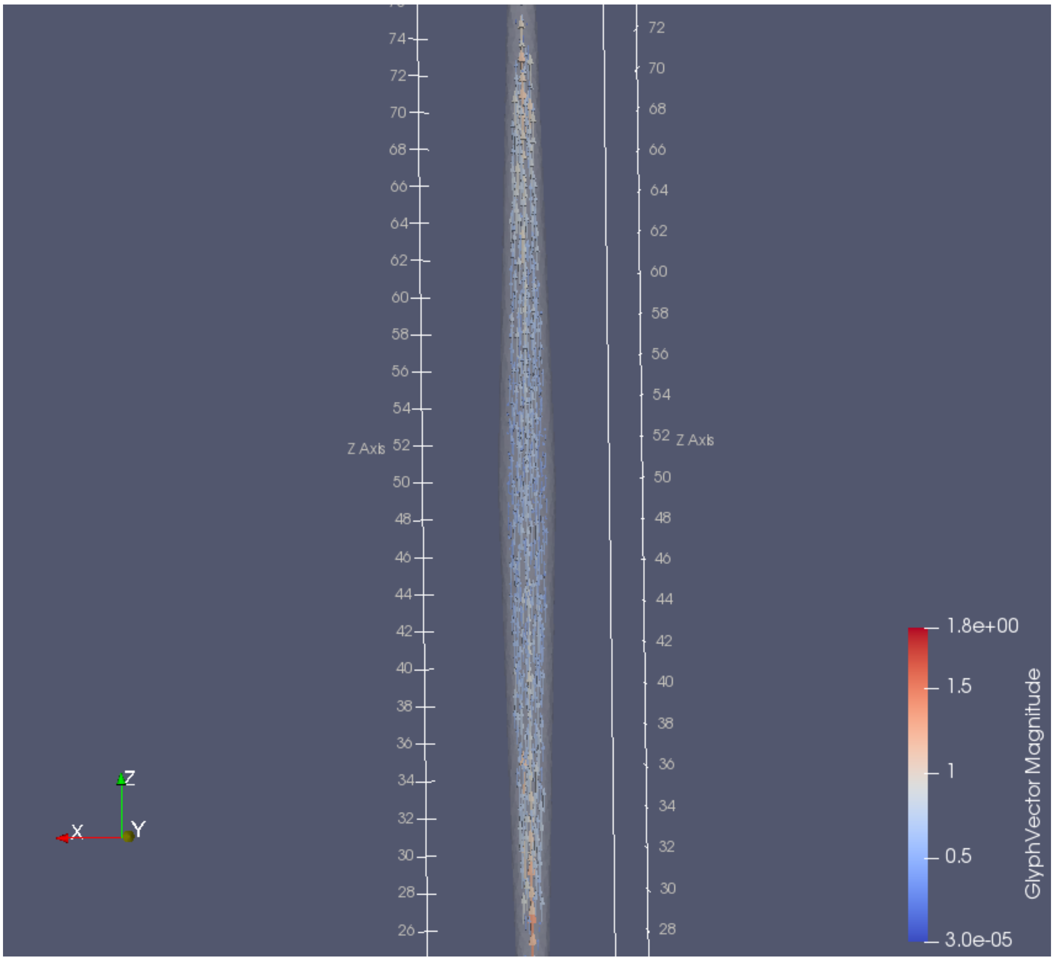

Figure 6.43: Zoomed detail of the velocity distribution inside the 3-dim vent-with-throats geometry (see Figure 6.41, Table 6.1: Id = 22) showing the middle part of the vent. This 3-dim geometry is the analogon to the 2-dim vent-with-throats shape (Table 6.1: Id = 10) and has dimension length $L = 100\,\mathrm{m}$, values of width w: at the bottom $w(z = 0) = 10\,\mathrm{m}$, at the top $w(z = L) = 2\,\mathrm{m}$, at throat 1 (right after the cave) $w_{\min 1} = 1\,\mathrm{m}$, at throat 2 (at the top): $w_{\min 2} = 0.6\,\mathrm{m}$, respectively.

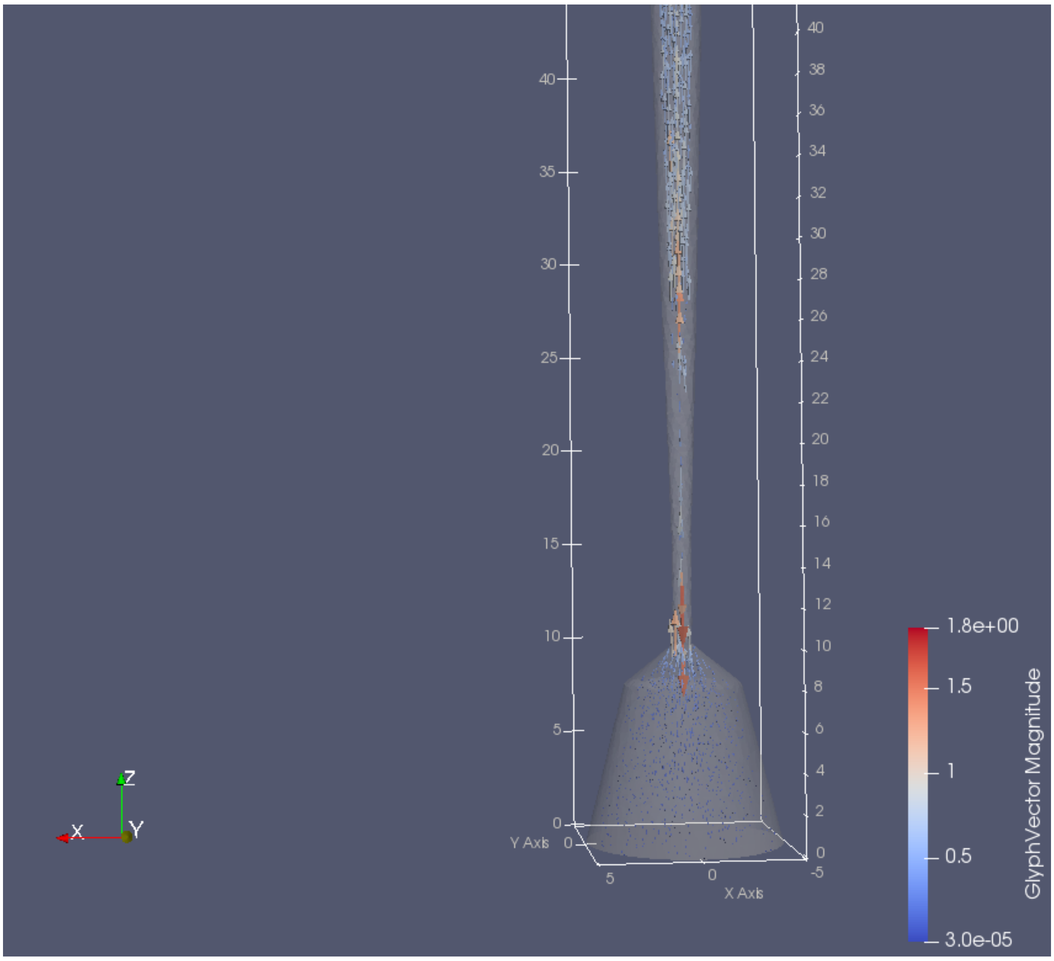

Figure 6.44: Zoomed detail of the velocity distribution inside the 3-dim vent-with-throats geometry (see Figure 6.41, Table 6.1: Id = 22) showing the cave-like evaporation area at the bottom of the vent. This 3-dim geometry is the analogon to the 2-dim vent-with-throats shape (Table 6.1: Id = 10) and has dimension length $L = 100\,\mathrm{m}$, values of width w: at the bottom $w(z = 0) = 10\,\mathrm{m}$, at the top $w(z = L) = 2\,\mathrm{m}$, at throat 1 (right after the cave) $w_{\min1} = 1\,\mathrm{m}$, at throat 2 (at the top): $w_{\min2} = 0.6\,\mathrm{m}$, respectively.

Id	Dim	Geometry	μ [kg/(ms)]	ρ_0 [kg/m^3]	L [m]	w [m]	p_{in} [Pa]	$v_{\max}$ [m/s]
1	2-dim	rectangle	$5.46 \cdot 10^{-4}$	1.0	20	4	611	18
2	2-dim	rectangle	$5.46 \cdot 10^{-4}$	1.0	20	4	2200	29
3	2-dim	rectangle	$5.46 \cdot 10^{-4}$	1.0	20	1	611	19
4	2-dim	rectangle	$5.46 \cdot 10^{-4}$	1.0	50	1	611	6
5	2-dim	rectangle	$5.46 \cdot 10^{-4}$	1.0	100	4	11000	29
6	2-dim	rectangle	$5.46 \cdot 10^{-4}$	1.0	100	1	11000	30
7	2-dim	vent with kink	$5.46 \cdot 10^{-4}$	1.0	100	1	611	5
8	2-dim	vent with kink	$5.46 \cdot 10^{-4}$	1.0	100	1	11000	54
9	2-dim	vent with throat	$5.46 \cdot 10^{-4}$	1.0	100	1	11000	134
10	2-dim	vent with throat	$5.46 \cdot 10^{-4}$	0.5	100	1	11000	322
11	2-dim	vent with throat	$5.46 \cdot 10^{-4}$	1.0	1000	1	110000	188
12	2-dim	vent with throat	$5.46 \cdot 10^{-4}$	0.5	1000	1	110000	386
13	2-dim	zigzag with fork	$5.46 \cdot 10^{-4}$	1.0	100	6, 2	11000	388
14	2-dim	zigzag with fork	$5.46 \cdot 10^{-4}$	1.0	100	6, 1.5/2.0	11000	116
15	2-dim	zigzag with fork	$5.46 \cdot 10^{-4}$	0.5	100	6, 1.5/2.0	11000	403
16	2-dim	zigzag with fork	$1.00 \cdot 10^{-5}$	1.0	100	6, 1.5/2.0	11000	193
17	2-dim	zigzag with fork	$1.00 \cdot 10^{-5}$	0.5	100	6, 1.5/2.0	11000	1105
18	3-dim	cylinder	$5.46 \cdot 10^{-4}$	1.0	20	4	2200	11
19	3-dim	cylinder	$5.46 \cdot 10^{-4}$	1.0	20	1	2200	40
20	3-dim	cylinder	$5.46 \cdot 10^{-4}$	1.0	100	4	11000	19
21	3-dim	cylinder	$5.46 \cdot 10^{-4}$	1.0	100	1	11000	21
22	3-dim	vent with throat	$5.46 \cdot 10^{-4}$	0.5	100	1	11000	340

Table 6.1: A list of the various water vapour flow scenarios that have been simulated. The 'Id' value specifies each simulation scenario, simulations have been performed for 2-dim (Id = 1-17) and 3-dim (Id = 18-21) geometries. $v_{\max}$ is the maximum value of the velocity field of a single simulation. Increasing the pressure p_{in} at the bottom (while keeping the other parameters unchanged) clearly also increases $v_{\max}$. Using the hydrostatic pressure for the value at the bottom, $p_{\text{in}} = p(z = 0) = \rho_{\text{ice}} g L$, represents a natural boundary condition. Decreasing the dynamic viscosity μ (while keeping the other parameters constant) leads to higher values of $v_{\max}$ in agreement with the Hagen-Poiseuille law. The trivial rectangle vent geometries yield small $v_{\max}$ values of a few $\mathrm{m\,s^{-1}}$ only (Id = 1-6). Introducing a kink enhances somewhat $v_{\max}$ (Id = 8), the velocity is increased around the kink reflecting the Venturi effect (the simulation with Id = 7 is similar to Id = 8, but a hypothetically small value for the pressure has been choosen for testing reasons). The geometry effect is stronger when extending the kink into a throat, the maximum values of the velocity field which are located within the throats are in the order of several hundred $\mathrm{m\,s^{-1}}$ (Id = 9-12). The Venturi effect of increased velocity is also well pronounced for vents containing a bifurcated branch and several throats and kinks ('zig-zag' geometry) that represent the most complex geometry simulated. Maximal velocity values are reached at the emission point where the water vapour erupts on the surface, values of several 100 $\mathrm{m\,s^{-1}}$ up to top values of more than 1000 $\mathrm{m\,s^{-1}}$ are observed in the simulations (Id = 13-17). Simple cylinders (Id = 18-21) and a throat geometry (Id = 22) have been analysed in the 3-dimensional case. The 3-dim cylinder simulations correspond to the 2-dim rectangle cases since a rectangle is the cross section in a plane parallel to the z-axis of the cylinder (cylinder length L, diameter $w = 2r$ correspond to rectangle length L, width w). The results for the trivial 3-dim cylinder geometries are qualitatively quite similar to the 2-dim rectangle geometries. Maximum velocities $v_{\max}$ for the cylinder cases are also in the same order of magnitude as the corresponding rectangle results. Non-trivial results are obtained for the 3-dim geometry including kinks and throats (Id = 22), which is the 3-dim analogon to the 2-dim vent-with-throat geometry (Id = 10). Enhanced velocities are detected at the throats, the maximum velocity for the 3-dim channel with throats (Id = 22) is in agreement with the 2-dim case (Id = 10).

7. Summary

The observation of a plume of water vapor and icy particles [Porco *et al.*, 2006, Spencer *et al.*, 2006, Hansen *et al.*, 2006, Waite *et al.*, 2006] enriched with sodium salts and interesting organic compounds [Hsu *et al.*, 2015, Postberg *et al.*, 2009, 2011, 2018, Khawaja *et al.*, 2019], together with the strong indication that a subsurface ocean might exist that is in contact with a warm rocky core [Nimmo and Porco, 2014, Hsu *et al.*, 2015, Spencer *et al.*, 2018], makes Saturn's tiny moon Enceladus one of the most promising candidates for possible extraterrestrial life in our Solar System [McKay *et al.*, 2008, 2014]. Jets of gas and icy grains are emerging from prominent fractures in the South Polar Terrain (SPT) reaching velocities of several 100 $\mathrm{m\,s^{-1}}$ up to 1000 $\mathrm{m\,s^{-1}}$ [Hansen *et al.*, 2015, Yeoh *et al.*, 2015, 2017]. The water vapor is formed via evaporation at depth from the liquid-water reservoir and moves upwards through a system of fractures, cracks, and vents, the so-called plumbing system, within Enceladus' ice mantle [Spencer *et al.*, 2018]. Ice shell thickness at the South Polar Terrain ranges between 1.5 and 23 km [McKinnon, 2015, Thomas *et al.*, 2016, Kamata and Nimmo, 2017, Čadek *et al.*, 2016, Le Gall *et al.*, 2017, Beuthe, 2018], an average value calculated by the present author gives $\langle d_{\mathrm{ice@SPT}} \rangle = 9.2 \pm 7.5\,\mathrm{km}$.

In this work, a model of a cylindrical pipe surrounded by an ice mantle has been used to analyze the heat loss along a crack channel. Heat loss is the crucial issue of the so-called "plumbing-system problem", because the crack channels have to be kept open such that water can flow through the ice fractures without freezing. Differential equations describing the heat transfer have been formulated in this thesis and explicit solutions have been worked out by the author for several use cases and boundary conditions. The temperature $T_{\mathrm{out}}(L)$ of the water flow as a function of pipe length L has been computed in this thesis for different values of the initial temperature $T_{\mathrm{in}}(L)$ and for several values of the pipe radius r to determine which pipe length/width value combinations yield a stable non-freezing water flow. For smaller pipe radii $r < 1\,\mathrm{m}$ the temperature falls off steeply, whereas for bigger radii $r > 1\,\mathrm{m}$ the decrease is more moderate. The model calculations of this work show that for vent radius of $r \gtrsim 1\,\mathrm{m}$ water remains liquid when flowing along a channel of several km length. These results are qualitatively in agreement with the literature where crack widths $w = 2r \sim 1 - 2\,\mathrm{m}$ are proposed to fulfill the non-freezing criterion [Kite and Rubin, 2016, Spencer *et al.*, 2018, Yeoh *et al.*, 2015].

The water vapour flow through the plumbing system consisting of cracks and vents has been studied in this thesis via numerical simulations of the Navier-Stokes equations, which describe the motion of viscous fluids. Crack channels have been modelled in this work as 2-dimensional and 3-dimensional geometrical objects, their shapes range from simple rectangles and cylinders up to more complex forms including narrowings, throats, forking branches, and 'zig-zag' lines, where the latter ones represent physically more realistic fracture shapes that could be present in a similar way inside an icy moon like Enceladus. For the numerical simulations performed in this work the open-source computing platform FEniCS has been utilized ["FEniCS Project", Alnaes *et al.*, 2015, Logg *et al.*, 2012], which provides modules for solving partial differential equations based on finite element methods. With this toolset the discretized Navier-Stokes equations have been solved for the various 2-dim and 3-dim crack channel geometries. The vent geometries conceived by the author have been created via a finite element mesh generator, that can produce triangulated grids with different refinement levels. Velocity and pressure distributions of vents of length $L = 20\,\mathrm{m}$ (just for calibration), $100\,\mathrm{m}$, and $1000\,\mathrm{m}$ with widths varying from $w = 0.6 - 6\,\mathrm{m}$ have been determined in this thesis. While the results for the simple geometries (rectangles, cylinders) are trivial (the velocity in the inner part of the vent is constant and independent on the z coordinate), the enhanced channel geometries containing kinks and throats show clearly that the velocity u is obviously enlarged in the vicinity of kinks and narrowings, which is a consequence of the Venturi effect that describes the velocity increase of a fluid flowing through a constricted pipe. The effect is stronger for a throat geometry than for a single kink case, the highest velocity values are localized within the throats of the ice channel, v_{max} (defined as the maximum value of the velocity field of a single specific simulation) is in the order of several $100\,\mathrm{m\,s^{-1}}$.

The most sophisticated ice vent structure that has been studied in this work in 2-dim is a geometry that contains a bifurcated branch and includes several throats and kinks (informally called 'zig-zag' vent). Such a structure comprises elements that could be definitely present within real ice mantles, and thus can represent approximately a physical ice crack channel. Highest velocity values of such 'zig-zag' vents occur at ejection points where the water vapour erupts on the surface. The numerical simulations of this work yield values of several $100\,\mathrm{m\,s^{-1}}$ up to peak values of more than $1000\,\mathrm{m\,s^{-1}}$, thus clearly exceeding the escape velocity of Enceladus, $v_{\mathrm{esc}} = 239\,\mathrm{m\,s^{-1}}$ [NASA, 2013]. These maximum velocity numbers obtained in this thesis are consistent with results in the literature obtained via various different methods, e.g. (a) Yeoh *et al.* (2015, 2017), who performed numerical Monte Carlo simulation of particles propagating in a nozzle-like vent, (b) Schmidt *et al.* (2008), who simulated the 1-dim flow of vapour and grains through random crack channels, (c) Ingersoll and Pankine (2010) and Nakajima and Ingersoll (2016a), who used a 1-dim hydrodynamical model to study the vapor and ice grain flow in the plumbing system including flow-wall interactions, and (d) applying statistical flux models on data measured by the Cassini Ultraviolet Imaging Spectrograph (UVIS) and Cassini's Infrared Spectrometer (CIRS) [Spencer *et al.*, 2009, Hansen *et al.*, 2011].

In this work the fundamental differential equations describing velocity and pressure of the water vapor flow are solved using finite element methods. The approach is in some respects different to previous studies (Yeoh *et al.* (2015, 2017), Schmidt *et al.* (2008), Ingersoll and Pankine (2010), Nakajima and Ingersoll (2016a)), and it might illuminate the mechanisms of the plume formation from another angle. An essential advantage of the chosen method is that one can perform simulations in 2-dim and 3-dim with complex geometries (some methods used in previous studies are restricted to the 1-dim case). The elaborated software modules of the FEniCS package ["FEniCS Project", Alnaes *et al.*, 2015, Logg *et al.*, 2012] based on the finite element method allow to construct even intricate 2-dim and 3-dim geometries in a comfortable way. Another characteristics of this work's approach is the fact that the subject going to be solved is the set of the underlying fundamental hydrodynamical equations. The calculations of this work can be considered as an extension and supplementary complement of previous studies, especially the dimensionality has been increased as far as hydrodynamical computations are concerned. Before, simulations based on hydrodynamical equations have been performed by several groups just in one dimension (Schmidt *et al.* (2008), Ingersoll and Pankine (2010), Nakajima and Ingersoll (2016a)). In this work, computations of similar hydrodynamical equations have been accomplished in two and three dimensions. The basic results of this work, namely that velocities of several $100\,\mathrm{m\,s^{-1}}$ are obtained, are qualitatively in agreement with the results obtained by the 1-dim studies. Some 1-dim computations also include terms or equations describing the interactions of the plume particles with the ice wall, e.g. in Schmidt *et al.* (2008) the collisions between ice grains with the wall are described by a Poisson process, and in Ingersoll and Pankine (2010), Nakajima and Ingersoll (2016a), the hydrodynamical equations contain terms describing condensation and evaporation of water vapour on the wall. Though these interaction terms might in principle describe the underlying physics in more detail, these terms contain several additional parameters that have to be guessed or estimated. Explicit flow-wall interaction terms have not been considered in this current work. It would be an interesting extension to include such flow-wall interaction terms in a forthcoming study employing the framework of this work, i.e. solving the fundamental hydrodynamical Navier-Stokes equations containing water vapour flow-wall interactions using the FEniCS package. Another challenge of a possible future study would be the task to transform the 2-dim 'zig-zag' vent geometry containing throats, narrowings, and forking branches, into 3-dim cracks and pipes, and to perform finite elements calculations with the FEniCS framework on these highly complex 3-dim geometries.

Since the discovery of the cryovolcanic activitiy by the Cassini spacecraft various studies and model calculations have been performed to investigate the underlying physics and mechanism of the vapour and particle flow in the ice cracks, which shed some light into the plumbing system problem and the nature of the plume jets of Enceladus. However, several detail questions are currently still open concerning the plumbing system: (i) The exact magnitude, the exact distribution, and the temporal continuity or variability of the heat source around and within the tiger stripes are not known. (ii) It is not quite clear if the plume is manifested in perfect jets or rather in curtains or in a combination of both. (iii) Space and time variability of the plume jets/curtains are not completely understood. (iv) Also, the exact shape and width of the crack vents is not fully explained: Concerning the water filled-part of a crack some authors claim that widths of 1 m are optimal [Ingersoll and Nakajima, 2016b, Kite and Rubin, 2016], while considering the vapour filled-part some studies suggesting that widths of 0.1 m might be best [Schmidt *et al.*, 2008, Postberg *et al.*, 2011, Nakajima and Ingersoll, 2016a].

Forthcoming investigations applying models that (a) include the hydrodynamical equations (2-dim at least, 3-dim optimally), (b) consider terms describing interactions between water vapour, ice particles, and the channel wall, and (c) that take heat flow and tidal effects into account, might further explain the complex physical mechanisms behind Enceladus' plumbing system. Future space missions that follow the spirit of Cassini-Huygens, e.g. NASA's Enceladus Orbiter (EO) mission [Spencer *et al.*, 2010a], NASA's JPL Rapid Mission Architecture (RMA) [Spencer *et al.*, 2010b], the joint NASA-ESA Titan and Enceladus Mission (TandEM) [Coustenis *et al.*, 2009], NASA's Enceladus Life Finder (ELF) mission [Lunine *et al.*, 2015], ESA's Voyage 2050 programme [Choblet *et al.*, 2019, Sulaiman *et al.*, 2019], or NASA's Enceladus Orbilander mission [MacKenzie *et al.*, 2021], that plan (i) to perform flybys through the plume of Enceladus with more sophisticated instruments, and/or (ii) to land on the surface and take samples from the ground, hopefully might answer some of the open plume mechanism issues and might further clarify the fascinating and exciting question whether life is possible on Enceladus.

Bibliography

Ahrens, J., *et al.* (2005) ParaView: An End-User Tool for Large Data Visualization *Visualization Handbook, Elsevier*, ISBN-13: 978-0123875822.

Alnaes, M.S., *et al.* (2015) The FEniCS Project Version 1.5. *Archive of Numerical Software* vol.3.

Ayachit, U. (2015) The ParaView Guide: A Parallel Visualization Application *Kitware*, ISBN 978-1930934306.

Baum, W.A., *et al.* (1981) Saturn's E ring. *Icarus* 47:84-96.

Barr, A.C., McKinnon, W.B. (2007) Convection in Enceladus' ice shell: Conditions for initiation. *Geophys. Res. Lett.* 112, E02012.

Beuthe, M. (2018) Enceladus's crust as a non-uniform thin shell: I tidal deformations. *Icarus* 302:145-174.

Brilliantov, N.V., *et al.* (2008) Geysers of Enceladus: Quantitative analysis of qualitative models. *Planetary and Space Science* 56:1596-1606.

Čadek, O., *et al.* (2016) Enceladus's internal ocean and ice shell constrained from Cassini gravity, shape, and libration data. *Geophys. Res. Lett.* 43:5653-5660.

Cassidy, T.A., Johnson, R.E. (2010) Collisional spreading of Enceladus' neutral cloud. *Icarus* 209:696-703.

Chapelle, F.H., *et al.* (2002) A hydrogen-based subsurface microbial community dominated by methanogens. *Nature* 415:312-315.

Chen, E.M.A., Nimmo, F. (2011) Obliquity tides do not significantly heat Enceladus. *Icarus* 214:779-781.

Choblet, G., *et al.* (2019) Enceladus as a potential Oasis of Life. *ESA Voyage 2050 White Paper.*

Chorin, A.J. (1968) Numerical solution of the Navier-Stokes equations. *Math. Comp.* 22:745-762.

Collins, G.C., Goodman, J.C. (2007) Enceladus' south polar sea. *Icarus* 189:72-82.

Cook, J.C., *et al.* (2013) "Hubble Sees Evidence of Water Vapor at Jupiter Moon" *NASA*, https://www.jpl.nasa.gov/news/hubble-sees-evidence-of-water-vapor-at-jupiter-moon (accessed on July 27^{th}, 2021).

Corliss, J., Baross, J., Hoffman, S. (1981) An Hypothesis Concerning the Relationship Between Submarine Hot Springs and the Origin of Life on Earth. *Oceanologica Acta* 4:59-69.

Coustenis, A., *et al.* (2009) TandEM: Titan and Enceladus mission. *Exp Astron* 23:893-946.

Crawford, G.D., Stevenson, D.J. (1988) Gas-driven water volcanism in the resurfacing of Europe. *Icarus* 73:66-79.

Crick, F.H., Orgel, L.E. (1973) Directed Panspermia. *Icarus* 19(3):341-348.

Czechowski, L., Kopystyński, F. (2005) Convection driven by tidal and radiogenic heating in medium size icy satellites. *Planetary and Space Science* 53:749-769.

Dallaston, M.C., Hewitt, I.J. (2014) Free-boundary models of a meltwater conduit. *Physics of Fluids* 26, id.083101.

Davis, W.L., McKay, C.P. (1996) Origins of life: a comparison of theories and application to Mars. *Orig. Life Evol. Biosph.* 26:61-73.

Dittus, F.W., Boelter, L.M.K. (1930) Heat transfer in automobile radiators of the tubular type. *The University of California Publications on Engineering* 2:443-461, Reprinted in Int. Commun. Heat Mass 12:3-22.

Dougherty, M.K., *et al.* (2006) Identification of a Dynamic Atmosphere at Enceladus with the Cassini Magnetometer. *Science* 311:1406-1409.

ESA, Cassini Huygens - Cassini Instruments, https://sci.esa.int/web/cassini-huygens/-/34962-cassini-tour-prime-mission (last updated: September 1, 2019, accessed on July 27th, 2021).

Esposito, L.W., *et al.* (2005) Ultraviolet imaging spectroscopy shows an active Saturnian system. *Science* 307:1251-1255.

“The FEniCS Project page”, https://fenicsproject.org/ (accessed on July 27th, 2021).

Friedel, C., Crafts, J.M. (1877) Sur une nouvelle méthode générale de synthèse d’hydrocarbures, d’acétones, etc. *Compt. Rend.* 84:1392-1450.

Fuller, J.L., *et al.* (2016) Resonance locking as the source of rapid tidal migration in the Jupiter and Saturn moon systems. *Mon. Not. R. Astron. Soc.* 458:3867-3879.

Geuzaine, C., Remacle, J.-F. (2009) Gmsh: a three-dimensional finite element mesh generator with built-in pre- and post-processing facilities. *Intenational Journal for Numerical Methods in Engineering* 79(11):1309-1331.

Giese, B., *et al.* (2017) An exceptionally high standing ridge on Enceladus. *EPSC Abstracts* European Planetary Science Congress 2017, Vol. 11, EPSC2017-28-1.

Gioia, G., *et al.* (2007) Unified model of tectonics and heat transport in a frigid Enceladus. *Proceedings of the National Acedemy of Sciences* 104(34):13578-13581.

Glein, C.R., *et al.* (2008) The oxidation state of hydrothermal systems on early Enceladus. *Icarus* 197:157-163.

Glein, C.R., *et al.* (2015) The pH of Enceladus' ocean. *Geochimica et Cosmochimica Acta* 162:202-219.

Gold, T.R. (1960) Cosmic Garbage. *Air Force and Space Digest* 65.

Haff, P.K., Siscoe, G.L., Eviatar, A. (1983) Ring and plasma - The enigmae of Enceladus. *Icarus* 56:426-438.

Haldane, J.B.S. (1929) The Origin of Life. *The Rationalist Annual* 148:3-10.

Hansen, C.J., *et al.* (2006) Enceladus' water vapor plume plume. *Science* 311:1422-1425.

Hansen, C.J., *et al.* (2011) The composition and structure of the Enceladus plume. *Geophysical research Letters* 38, L11202.

Hedman, M.M., *et al.* (2009) Spectral observations of the Enceladus plume with Cassini-VIMS. *Astronomical Journal* 693:1749-1762.

Hedman, M.M., *et al.* (2012) The three-dimensional structure of Saturn's E ring. *Icarus* 217(1):322-338.

Helfenstein, P., Porco, C.C. (2015) Enceladus' Geysers: Relation to Geological Features. *The Astronomical Journal* 150:96.

Herschel, W. (1790) Account of the Discovery of a Sixth and Seventh Satellite of the Planet Saturn; With Remarks on the Construction of Its Ring, Its Atmosphere, Its Rotation on an Axis, and Its Spheroidal Figure. *Philosophical Transactions of the Royal Society of London.* 80:1-20.

Herschel, W. (1795) Description of a Forty-feet Reflecting Telescope. Philosophical Transactions of the Royal Society of London. *Philosophical Transactions of the Royal Society of London.* 85:347-409.

Hillier, J.K., *et al.* (2007) The composition of Saturn's E ring. *Mon. Not. R. Astronom. Soc.* 377:1588-1596.

Horányi, M., *et al.* (2009) *Diffuse Rings*, pages 511-536, doi: 10.1007/978-1-4020-9217-6_21.

Howett, C.J.A., *et al.* (2010) Thermal inertia and bolometric Bond albedo values for Mimas, Enceladus, Tethys, Dione, Rhea and Iapetus as derived from Cassini/CIRS measurements. *Icarus* 206(2):573-593.

Howett, C.J.A., *et al.* (2011) High heat flow from Enceladus' south polar region measured using 10-600 cm^{-1} Cassini/CIRS data. *Journal of Geophysical Research (Planets)* 116, E03003.

Hoyle, F., Wickramasinghe, N.C. (1981) *Evolution from Space.* Simon & Schuster Inc., NY, and J.M. Dent and Son, London, ch3 pages 35-49.

Hoyle, F., *et al.* (1986) *Viruses from Space and Related Matters.* University College Cardiff Press.

Hsu, H-W., *et al.* (2015) Ongoing hydrothermal activities within Enceladus. *Nature* 519:207-210.

Hurford, T.A., *et al.* (2007) Eruptions arising from tidally controlled periodic openings of rifts on Enceladus. *Nature* 447:292-294.

Iess, L., *et al.* (2014) The Gravity Field and Interior Structure of Enceladus. *Science* 344(6179):78-80.

Ingersoll, A.P., Pankine, A.A. (2010) Subsurface heat transfer on Enceladus: Conditions under which melting occurs. *Icarus* 206:594-607.

Ingersoll, A.P., Ewald, S.P. (2011) Total particulate mass in Enceladus plumes and mass of Saturn's E ring inferred from Cassini ISS images. *Icarus* 216:492-506.

Ingersoll, A.P., Nakajima, M. (2016b) Controlled boiling on Enceladus. 2. Model of the liquid-filled cracks. *Icarus* 272:319-326.

Isenko, E., *et al.* (2005) Water temperature in englacial and supraglacial channels: Change along the flow and contribution to ice melting on the channel wall. *Cold Regions Science and Technology* 42:53-62.

Jacobson, R.A., *et al.* (2006) The Gravity Field of the Saturnian System from Satellite Observations and Spacecraft Tracking Data. *The Astronomical Journal* 132(6):2520-2526.

Jebbar, M., *et al.* (2020) Microbial Diversity and Biosignatures: An Icy Moons Perspective. *Space Sci Rev* 216(1):10.

Jia, X., *et al.* (2018) Evidence of a plume on Europa from Galileo magnetic and plasma wave signatures. *Nature Astronomy* 2(6):459-464.

Joyce, G. (1994) *Origins of Life: The Central Concepts*, chapter: Foreword, pages xi-xii. Boston: Jones and Barlett Publishers.

Jones, G.H., *et al.* (2006) Enceladus' Varying Imprint on the Magnetosphere of Saturn. *Science* 311:1412-1415.

Kahana, A., *et al.* (2019) Enceladus: First Observed Primordial Soup Could Arbitrate Origin-of-Life Debate. *Astrobiology* 19(10):1263-1278.

Kamata, S., Nimmo, F. (2017) Interior thermal state of Enceladus inferred from the viscoelastic state of the ice shell. *Icarus* 284:387-393.

Kempf, S., *et al.* (2008) How the Enceladus dust plume feeds Saturn's E ring. *Icarus* 206:446-457.

Khawaja, N., *et al.* (2019) Low-mass nitrogen-, oxygen-bearing, and aromatic compounds in Enceladean ice grains. *Monthly Notices of he Royal Astronomical Society* 489:5231-5243.

Kieffer, S.W., *et al.* (2006) A Clathrate Reservoir Hypothesis for Enceladus' South Polar Plume. *Science* 314:1764-1766.

Kirschivink, J. (1992) Late Proterozoic Low-Latitude Global Glaciation: the Snowball Earth. In J.W. Schopf and C. Klein, editors, *The Proterozoic Biosphere: A Multidisciplinary Study*, pages 51-52. Cambridge University Press, New York.

Kite, E.S., Rubin, A.M. (2016) Sustained eruptions on Enceladus explained by turbulent dissipation in tiger stripes. *Proceedings of the National Academy of Science* 113:3972-3975.

Konstantinidis, K., *et al.* (2015) A lander mission to probe subglacial water on Saturn's moon Enceladus for life. *Acta Astronautica* 106:63-89.

Landau, L.D., Lifshitz, E.M. (1966) *Fluid Mechanics - Course of Theoretical Physics.* Institute of Physical Problems, U.S.S.R. Academy of Sciences, Pergamon Press, pages 47-53.

Langtangen, H.P., Logg, A. (2017) *Solving PDEs in Python. The FEniCS Tutorial I.*, Simula SpringerBriefs on Computing (3), Springer, 2017.

Le Gall, A., *et al.* (2017) Thermally anomalous features in the subsurface of Enceladus's south polar terrain. *Nature Astronomy* 1, id. 0063.

Leitner, J., Firneis, M. (2012) How can we detect Life when we Cannot Define It in a General Way? International Workshop on Extraterrestrial Life - Beyond our Expectations, held in Vienna, Austria, May 21-22, 2012.

Leitner, J. (2014) Exotic Life and the Life Supporting Zone as a Basis for the Search for Extraterrestrial Life. Dissertation/Doctoral thesis, University of Vienna.

Lin, L.-H., *et al.* (2006) Long-Term Sustainability of a High-Energy, Low-Diversity Crustal Biome. *Science* 314(5798):479-482.

Lissauer, J.J., *et al.* (2017) Ring torque on Janus and the melting of Enceladus. *Icarus* 58:159-168.

Lock, G.S.N. (1990) *The Growth and Decay of Ice.* Cambridge University Press, Cambridge.

Logg, A., Mardal, K.A., Wells, G. (2012) Automated Solution of Differential Equations by the Finite Element Method: The FEniCS Book (Lecture Notes in Computational Science and Engineering), Springer.

Lunine, J.I., *et al.* (2015) Enceladus Life Finder: The Search for Life in a Habitable Moon. 46th Lunar and Planetary Science Conference, held in The Woodlands, Texas, USA, March 16-20, 2015.

MacKenzie, S.M., *et al.* (2021) The Enceladus Orbilander Mission Concept: Balancing Return and Resources in the Search for Life. *The Planetary Science Journal* 2(2):77-94.

Manga, M., Wang, C.-Y. (2007) Pressurized oceans and the eruption of liquid water on Europa and Enceladus. *Geophysical Research Letters* 34, L07202.

McKay, C.P., *et al.* (2008) The Possible Origin and Persistence of Life on Enceladus and Detection of Biomarkers in the Plume. *Astrobiology* 8(5):909-924.

McKay, C.P., *et al.* (2014) Follow the Plume: The Habitability of Enceladus. *Astrobiology* 14(4):352-355.

McKinnon, W.B. (2015) Effect of Enceladus's rapid synchronous spin on interpretation of Cassini gravity. *Geophys. Res. Lett.* 42:2137-2143.

Meyer, J., Wisdom, R.T. (2007) Tidal heating in Enceladus. *Icarus* 188:535-539.

Meyer, J., Wisdom, R.T. (2008) Episodic volcanism on Enceladus: Application of the Ojakansas-Stevenson model. *Icarus* 198:178-180.

Miller, S. (1953) A Production of Amino Acids Under Possible Primitive Earth Conditions. *Science* 117(3046):528-529.

Miller, S., Urey, H. (1959) Organic Compound Synthesis on the Primitive Earth. *Science* 130(3370):245-251.

Miller, S. (1998) The endogenous synthesis of organic compounds. In *The Molecular Origins of Life* (A. Brack, ed), Cambridge University Press, chapter 3, pages 59-85.

Murray, C., Dermott, S. (1999) *Solar System Dynamics*. Cambridge University Press, Cambridge, 1999.

Nakajima, M., Ingersoll, A.P. (2016a) Controlled boiling on Enceladus. 1. Model of the vapor-driven jets. *Icarus* 272:309-318.

NASA (2011) Stardust - NASA's Comet Sample Return Mission, Jet Propulsion Laboratory, California Institute of Technology, https://solarsystem.nasa.gov/stardust/home/index.html (accessed on July 27$^{\text{th}}$, 2021).

NASA (2013) Solar System Exploration - Enceladus: Facts and Figures.
https://web.archive.org/web/20131016093801/http://solarsystem.nasa.gov/planets/profile.cfm?Object=Sat_Enceladus&Display=Facts (accessed on July 27$^{\text{th}}$, 2021).

Nimmo, F., Pappalardo, R.T. (2006) Diapir-induced reorientation of Saturn's moon Enceladus. *Nature* 441:614-616.

Nimmo, F., *et al.* (2007) Shear heating as the origin of the plumes and heat flux on Enceladus.*Nature* 447:289-291.

Nimmo, F., Porco, C. (2014) Enceladus. In *Encylopedia of the Solar System, Third Edition 2014* pages 851-859.

Nimmo, F., *et al.* (2017) The thermal and orbital evolution of Enceladus: observational constraints and models. In *Enceladus and the Icy Moons of Saturn* (P.M. Schenk et al., eds), pages 79-94. Univ. of Arizona, Tucson, doi: 10.2458/azu_uapress_9780816537075-ch005.

O'Leary, M. (2008) *Anaxagoras and the Origin of Panspermia Theory.* iUniverse publishing Group.

O'Neill, C., Nimmo, F. (2010) The role of episodic overturn in generating the surface geology and heat flow on Enceladus. *Nature Geoscience* 3:88-91.

Oparin, A. (1924) *The Origin of Life* Proiskhozhdenie zhizny, Moscow.

Oparin, A. (1967) *The Origin of Life*, translation by Ann Synge. In: Bernal, J.D. (ed), *The Origin of Life*, Weidenfeld & Nicolson, London, 1967, pages 199-234.

Orton, G.S., *et al.* (2009) *Review of Knowledge Prior to the Cassini-Huygens Mission and Concurrent Research*, page 9.

Pang, K.D., *et al.* (1984) The E ring of Saturn and satellite Enceladus. *J. Geophys. Res.* 89:9459-9470.

Peale, S.J., Cassen, P. (1978) Contribution of tidal dissipation to lunar thermal history. *Icarus* 36:245-269.

Peale, S.J. (2003) Tidally Induced Volcanism. *Celestial Mechanics and Dynamical Astronomy* 87:129-155.

Platt, J., Bell, B. (2014) NASA Space Assets Detect Ocean inside Saturn Moon. *NASA* Retrieved April 16, 2015.

Porco, C., *et al.* (2006) Cassini observes the active south pole of Enceladus. *Science* 311:1393-1401.

Porco, C., DiNino, D., Nimmo, F. (2014) How the Geysers, Tidal Stresses, and Thermal Emissions across the South Polar Terrain of Enceladus are related. *The Astronomical Journal* 148(3):45.

Postberg, F., *et al.* (2008) The E ring in the vicinity of Enceladus. II. Probing the moon's interior - the composition of E-ring particles. *Icarus* 193:438-454.

Postberg, F., *et al.* (2009) Sodium salts in E-ring ice grains from an ocean below the surface of Enceladus. *Nature* 459:1098-1101.

Postberg, F., *et al.* (2011) A salt-water reservoir as the source of a compositionally stratified plume of Enceladus. *Nature* 474:620-622.

Postberg, F., *et al.* (2018) Macromolecular organic compounds from the depths of Enceladus. *Nature* 558:564-568.

Vittorio, S.A. (2006) Cassini visits Enceladus - New light on a bright world. *Cambridge Scientific Abstracts (CSA)*, Released July 2006.

Rappaport, N.J., *et al.* (2007) Mass and interior of Enceladus from Cassini data analysis. *Icarus* 190:175-178.

Roatsch, T., *et al.* (2009) Cartographic Mapping of the Icy Satellites Using ISS and VIMS Data. *Saturn from Cassini-Huygens* pages 763-781.

Robidel, R., *et al.* (2020) Photometrically-corrected global infrared mosaics of Enceladus: New implications for its spectral diversity and geological activity. *Icarus* 349(1):113848.

Rudolph, M.L., Manga, M. (2009) Fracture penetration in planetary ice shells. *Icarus* 199:536-541.

Schmidt, J., *et al.* (2008) Slow dust in Enceladus' plume from condensation and wall collisions in tiger stripe fractures. *Nature* 451:685-688.

Schneider, N.M., *et al.* (2009) No sodium in the vapour plumes of Enceladus. *Nature* 459:1102-1104.

Schubert, G., *et al.* (1986) *Thermal histories, compositions and internal structures of the moons of the solar system* pages 224-292.

Schubert, G., *et al.* (2007) Enceladus: Present internal structure and differentiation by early and long-term radiogenic heating. *Icarus* 188:345-355.

Schubert, G., *et al.* (2010) Evolution of Icy Satellites. *Space Science Reviews* 153:447-484.

Schulson, E.M. (2001) Brittle failure of ice. *Engineering Fracture Mechanics* 68:1839-1887.

Schulze-Makuch, D., Irwin, L.N. (2008) *Life in the Universe.* 2nd edition, Springer, Berlin, doi:10.1007/978-3-540-76817-3.

Seal, D.A., Buffington, B.B. (2009) *The Cassini Extended Mission*, In: Dougherty M.K., Esposito L.W., Krimigis S.M. (eds) Saturn from Cassini-Huygens. Springer, Dordrecht, pages 725-744, doi:10.1007/978-1-4020-9217-6_22.

Sekine, Y., *et al.* (2015) High-temperature water-rock interactions and hydrothermal environments in the chondrite-like core of Enceladus. *Nature Communications* 6, 8604.

Shapiro, R. (1987) *Origins: A Skeptic's Guide to the Creation of Life on Earth.* Bantam Books, Toronto, New York.

Shatalina, I.N. (1990) Heat exchange in the processes of ice freezing and melting. *Library of hydroengineering* vol. 95, Energoizdat, Leningrad. 120p. (In Russian).

Shemansky, D.E., *et al.* (1993) Detection of the hydroxyl radical in the saturn magnetosphere. *Nature* 363:329-331.

Shock, E.L. (1990) Geochemical constraints on the origin of organic compounds in hydrothermal systems. *Origins of Life and Evolution of the Biosphere* 20:331-367.

Shoji, D., *et al.* (2014) Non-steady state tidal heating of Enceladus. *Icarus* 235:75-85.

Smith, B.A., *et al.* (1982) A new look at the Saturn system - The Voyager2 images. *Science* 215:504-537.

Spahn, F., *et al.* (2006) Cassini dust measurements at Enceladus and implications for the origin of the E ring. *Science* 311:1416-1418.

Spencer, J.R., *et al.* (2006) Cassini Encounters Enceladus: Background and the Discovery of a South Polar Hot Spot. *Science* 311:1401-1405.

Spencer, J.R., *et al.* (2009) *Enceladus: An Active Cryovolcanic Satellite.* In *Saturn from Cassini-Huygens* (M. Dougherty et al., eds), pages 683-724. doi: 10.1007/978-1-4020-9217-6_21.

Spencer, J.R., *et al.* (2010a) Planetary Science Decadal Survey - Enceladus Orbiter. *NASA Mission Concept Study 2010.*

Spencer, J.R., *et al.* (2010b) Planetary Science Decadal Survey - JPL Rapid Mission Architecture (RMA) - Enceladus Study Final Report. *NASA Mission Concept Study 2010.*

Spencer, J.R., Nimmo, F. (2013a) An Active Ice World in the Saturn System. *Annual Review of Earth and Planetary Sciences* 41:693-717.

Spencer, J.R., *et al.* (2013b) Enceladus Heat Flow from High Spatial Resolution Thermal Emission Observations. European Planetary Science Congress 2013, held 8-13 September in London, UK.

Spencer, J.R., *et al.* (2018) Plume Origins and Plumbing: From Ocean to Surface. In *Enceladus and the Icy Moons of Saturn* (P.M. Schenk et al., eds), Space Science Series. University of Arizona Press, Tucson, pages 163-174.

Spilker, L. (2009) Cassini-Huygens solstice mission. In *Draft White paper for Solar System Decadal Survey 2013-2023.*

Spitale, J.N., Porco, C.C. (2007) Association of the jets of Enceladus with the warmest regions on its south-polar fractures. *Nature* 521:57-60.

Spitale, J.N., *et al.* (2015) Curtain eruptions from Enceladus' south polar terrain. *Nature* 521:57-60.

Srama, R., *et al.* (2008) The Dust Environment at Saturn - Measurements by the Cassini Cosmic-Dust-Analyzer. Poster presented at the Cosmic Dust - Near & Far meeting in Heidelberg (September 8-12, 2008), online: http://www.mpiahd.mpg.de/DNF08/Posters/Ralf_Srama1_3MB.pdf, Sept. 2008.

Stevens, T.O., McKinley, J.P. (1995) Lithoautotrrophic Microbial Ecosystems in Deep Basalt Aquifers. *Science* 270(5235):450-455.

Sulaiman, A., *et al.* (2019) Enceladus and Titan: Emerging Worlds of the Solar System. *ESA Voyage 2050 White Paper.*

"Eigenschaften von Wasser in Tabellen". *www.wissenschaft-technik-ethik.de*, http://www.wissenschaft-technik-ethik.de/wasser_eigenschaften.html (last updated: April 27th, 2006, accessed on July 27th, 2021).

Taler, D., Taler, J. (2017) Simple heat transfer correlations for turbulent tube flow. *E3S Web of Conferences* 13, 02008, doi: 10.1051/e3sconf/20171302008.

Taubner, R-S. (2012) The possibility of the existence of a nitrogen cycle within Enceladus. Master thesis, University of Vienna.

Taubner, R-S., *et al.* (2018a) Biological methane production under putative Enceladus-like conditions. *Nature Communications* 9(1):748.

Taubner, R-S. (2018b) An interdisciplinary Approach: On the Habitability of Enceladus' Potential Subsurface Water Reservoir. Dissertation/Doctoral thesis, University of Vienna.

Taubner, R-S., *et al.* (2019) Membrane Lipid Composition and Amino Acid Excretion Patterns of Methanothermococcus okinawensis Grown in the Presence of Inhibitors Detected in the Enceladian Plume. *Life* 9(4):85.

Taubner, R-S., *et al.* (2020) Experimental and Simulation Efforts in the Astrobiological Exploration of Exooceans. *Space Sci Rev* 216(1):9.

Temam, R. (1969) Sur l'approximation de la solution des équations de Navier-Stokes. *Arc. Ration. Mech. Anal.* 32:377-385.

Teolis, B.D., *et al.* (2017) Enceladus Plume Structure and Time Variability: Comparison of Cassini Observations. *Astrobiology.* 17(9):926-940.

Thomas, P.C., *et al.* (2007) Shapes of the saturnian icy satellites and their significance. *Icarus* 190:573-584.

Thomas, P.C. (2010) Sizes, shapes, and derived properties of the saturnian satellites after the Cassini nominal mission. *Icarus* 208:395-401.

Thomas, P.C., *et al.* (2016) Enceladus's measured physical libration requires a global subsurface ocean. *Icarus* 264:37-47.

Thomson (Lord Kelvin), W. (1871) Inaugural Address to the British Association Edinburgh. 'We must regard it as probably to the highest degree that there are countless seed-bearing meteoritic stones moving through space'. *Nature* 4(92):261-278.

Tian, F., *et al.* (2007) Monte Carlo simulations of the water plumes on Enceladus. *Icarus* 188:154-161.

Tokar, R.L., *et al.* (2006) The Interaction of the Atmossphere of Enceladus with Saturn's Plasma. *Science* 311:1409-1412.

Tucker, O.J., *et al.* (2015) 2D models of gas flow and ice grain acceleration in Enceladus' vents using DSMC methods. *Icarus* 257:362-376.

Turcotte, D., Schubert, G. (2002) *Geodynamics* Cambridge University Press, Cambridge, United Kingdom.

USGS (2015) Planetary Body Names and Discoverers. *Gazetteer of Planetary Nomenclature.* USGS Astrogeology Science Center. https://planetarynames.wr.usgs.gov/Page/Planets (accessed on July 27th, 2021).

Vatne, G., Irvine-Fynn, T.D.L. (2016) Morphological dynamics of an englacial channel. *Hydrol. Earth Syst. Sci.* 20:2947-2964.

Verbiscer, A., *et al.* (2007) Enceladus: Cosmic Graffiti Artist Caught in the Act. *Science* 315(5813):815.

Veeder, G.J., *et al.* (1994) Io's heat flow from infrared radiometry: 1983-1993. *Journal of Geophysical Research* 99:17095-17162.

Vodák, R. (2010) Justification of Asymptotic Two-dimensional Model for Steady Navier-Stokes Equations for Incompressible Flow. *Acta Appl Math* 112:21-33.

Wächtershäuser, G. (1992) Groundworks for an evolutionary biochemistry: The iron-sulphur world. *Progress on Biophysics and Molecular Biology* 58(2):85-201.

Waite, J.H.Jr., *et al.* (2006) Cassini Ion and Neutral Mass Spectrometer: Enceladus plume composition and structure. *Science* 311:1419-1422.

Waite, J.H.Jr., Magee, B.A., Teolis, B.D. (2008) The Gas Composition of the Plume of Enceladus. In *European Planetary Science Congress 2008* page 692, held in Münster, Germany, 21-26 September, 2008.

Waite, J.H.Jr., *et al.* (2009) Liquid water on Enceladus from observations of ammonia and ^{40}Ar in the plume. *Nature* 460:487-490.

Waite, J.H.Jr., *et al.* (2017) Cassini finds molecular hydrogen in the Enceladus plume: Evidence for hydrothermal processes. *Science* 356:155-159.

Walder, J. (1982) Stability of sheet flow of water beneath temperature glaciers and implications for glacier surging. *Journal of Glaciology* 28:273-293.

Wickramasinghe, J., Wickramasinghe, C., Napier, W. (2010) *Comets and the Origin of Life*, World Scientific Publishing, Singapore.

Wickramasinghe, C. (2010) The astrobiological case for our cosmic ancestry. *International Journal of Astrobiology.* 9(2):119-129.

Wickramasinghe, C. (2011) Bacterial morphologies supporting cometary panspermia: a reappraisal. *International Journal of Astrobiology.* 10(1):25-30.

Winterton, R.H.S. (1998) Where did the Dittus and Boelter equation come from?. *Int J. Heat Mass Tran.* 41:809-810.

Wisdom, J. (2004) Spin-Orbit Secondary Resonance Dynamics of Enceladus. *Astrophysical Journal* 128:484-491.

Witze, A. (2014) Icy Enceladus hides a watery ocean. *Nature* doi:10.1038/nature.2014.14985;

Yeoh, S.K., *et al.* (2015) On understanding the physics of the Enceladus south polar plume via numerical simulation. *Icarus* 253:205-222.

Yeoh, S.K., *et al.* (2017) Constraining the Enceladus plume using numerical simulation and Cassini data. *Icarus* 281:357-378.

Zolotov, M.Y. (2007) An oceanic composition on early and today's Enceladus. *Geophysical Research Letter* 34, L23203.

Abstract (in German)

Der kleine Saturnmond Enceladus ist eines der faszinierendsten und spannendsten Objekte in unserem Sonnensystem. Die NASA Raumsonde Cassini entdeckte beim Vorbeiflug eine anomale Zone erhöhter Temperatur in der Südpolarregion, und geysirartige Fontänen aus Wasserdampf und Wassereisteilchen (engl. "Plume"), die von Bruchlinien in der Südpolarregion, den sogenannten "Tiger-Streifen", ausgehen, und die bis in eine Höhe von 500 km zu beobachten sind.

Die Entdeckung dieser kryovulkanischen Geysire macht Enceladus einzigartig: er ist der einzige Eismond unseres Sonnensystems auf dem aktuell eine bekannte permanente geologische Aktivität stattfindet. Die Fontänen aus Wasserdampf und Eispartikeln erreichen Geschwindigkeiten von bis zu 1000 $\mathrm{m\,s^{-1}}$, und übersteigen die Fluchtgeschwindigkeit von Enceladus ($v_{\mathrm{esc}} = 239\,\mathrm{m\,s^{-1}}$). Der Nachweis von Natriumsalzen und Siliziumhaltigen Molekülen im Plume legt nahe, dass die Eispartikeln aus einem flüssigen Wasserreservoir stammen, welches in Kontakt mit dem heißen, felsigen Kern von Enceladus steht. Es gibt starke Anzeichen, dass dieses flüssige Reservoir ein unterirdischer Ozean ist, der 8-30 km dick ist und sich in der Südpolarregion unter einem Eismantel von 2-40 km Dicke befindet. Neuere Arbeiten deuten darauf hin, dass es sich dabei nicht nur um einen lokalen polaren See handelt, sondern vielmehr sogar um einen globalen unterirdischen Ozean.

Es ist durchaus möglich, dass am Grund dieses unterirdischen Ozeans hydrothermale Quellen existieren, analog den "Schwarzen" bzw. "Weißen Rauchern" am Grund der Tiefsee auf der Erde. Die hydrothermalen Quellen auf der Erde und die in deren Umgebung stattfindenden chemischen Reaktionen, die die Existenz von chemolithotroph aktiver Bakterien und Archaeen ermöglicht, stellen eine potentielle Erklärung für den Ursprung des irdischen Lebens dar. Aus diesem Grund ist der kleine Mond Enceladus für die Astrobiologie von großem Interesse, da er einen äußerst interessanten Kandidaten für mögliches außerirdisches Leben in unserem eigenen Sonnensystem repräsentiert.

Der Wasserdampf in den Fontänen entsteht durch Verdampfung in der Tiefe in Kammern an der Oberfläche des unterirdischen Wasserreservoirs, und bewegt sich im Eismantel durch ein System von Brüchen, Rissen, Spalten und Röhren, quasi einem Rohrleitungs-System (engl. "Plumbing System") im Eis, aufwärts. In dieser Arbeit wurde anhand eines Models einer zylindrischen Eisröhre, welche von einem Eismantel umgeben ist, der Wärmeverlust entlang eines Eisspalt-Kanals analysiert. Der Wärmeverlust beim Aufsteigen durch die Eiskanäle ist ein wesentlicher Aspekt des sogenannten "Plumbing-System Problems", denn falls dieser zu groß ist, drohen die Kanäle zuzufrieren. Doch die Risse und Spalten, durch die Wasserdampf und Eispartikel vom unterirdischen Ozean bis zur Oberfläche strömen, müssen lange genug offen bleiben, d.h. sie dürfen nicht zu schnell zufrieren. Die Differentialgleichungen, die den Wärmetransfer bzw. den Wärmeverlust des Wassers beim Transport durch eine Eisröhre beschreiben, wurden in dieser Arbeit aufgestellt, und es wurden Lösungen für diese Differentialgleichungen für verschiedene Umgebungsparameter und Randbedin-

gungen ausgearbeitet. Der Verlauf der Temperatur $T_{\rm out}(L)$ des Wassers/Wasserdampfes entlang der Eisröhre wurde als Funktion der Kanallänge L für verschiedene Werte der Anfangstemperatur $T_{\rm in}(L)$ und diverse Werte des Röhrenradius r berechnet, um zu bestimmen, welche Kombinationen von Röhrenlängen L und Röhrendicken $w = 2r$ stabile Parameter darstellen, bei denen der Eiskanal nicht zufriert. Die in dieser Arbeit durchgeführten Berechnungen veranschaulichen, dass bei kleineren Eisröhrenradien $r < 1\,\rm m$ die Temperatur steil abfällt, wohingegen bei größeren Radien $r > 1\,\rm m$ der Abfall moderater ausgeprägt ist. Weiters zeigen die Modellrechnungen dieser Arbeit, dass bei Röhrenradii $r \gtrsim 1\,\rm m$ Wasser entlang eines Kanals von mehreren km Länge flüssig bleibt. Diese Resultate sind qualitativ in Übereinstimmung mit der aktuellen Literatur, wo Röhrendurchmesser $w = 2r \sim 1 - 2\,\rm m$ vorgeschlagen werden, um ein Nicht-Zufrieren der Eiskanäle zu garantieren.

Der Hauptteil dieser Arbeit ist der Untersuchung des Durchflusses des Wasserdampfes durch das aus Brüchen, Rissen, Spalten und Röhren bestehende “Plumbing-System” gewidmet. Die physikalischen Größen, die diesen Durchfluß beschreiben, nämlich Druck- und Geschwindigkeits-Verteilungen, wurden mittels numerischer Simulationen der Navier-Stokes Gleichungen bestimmt, welche die Dynamik viskoser Flüssigkeiten beschreiben. Die durch Risse und Brüche entstandenen Eiskanäle wurden als 2-dimensionale bzw. 3-dimensionale geometrische Objekte modelliert, die verwendeten Geometrien erstrecken sich von einfachen Formen wie Rechtecken und Zylindern bis zu komplexeren Ausprägungen, welche Verengungen, Einschnürungen, Knicke, Verzweigungen, und ’Zick-Zack’ Linien beinhalten, wobei letztere Formen tatsächliche physikalische Strukturen, wie sie möglicherweise auf Enceladus vorkommen, realistischer abbilden.

Für die numerischen Simulationen wurde in dieser Arbeit die Open-Source Berechnungs-Plattform FEniCS verwendet, welche eine Vielzahl von Modulen zum Lösen partieller Differentialgleichungen bereitstellt, die auf der Methode der finiten Elemente basieren. Mit Hilfe dieses Werkzeuges wurden die diskretisierten Navier-Stokes Gleichungen für verschiedene 2-dim und 3-dim Eiskanal-Geometrien auf numerischem Wege gelöst. Es wurden die Geschwindigkeits- und Druckverteilungen von Flußröhren bestimmt, deren Längen von $L = 20\,\rm m$ (nur zur Kalibrierung), $100\,\rm m$ and $1000\,\rm m$ und deren Durchmesser von $w = 0.6 - 6\,\rm m$ variieren. Während einfache Geometrien (Rechtecke, Zylinder) naturgemäß triviale Resultate liefern (die Geschwindigkeit im inneren Teil der Röhre ist konstant und unabhängig von der z-Koordinate), zeigen die Ergebnisse dieser Arbeit für komplexere Geometrien, die Knicke und Einschnürungen beinhalten, sehr klar, dass die Geschwindigkeit u in der Umgebung dieser Knicke und Verengungen deutlich erhöht ist, was eine Folge des Venturi-Effektes ist, der den Geschwindigkeitsanstieg eines durch eine verengte Röhre strömenden Fluids beschreibt. Dieser Effekt ist für eine Form mit einer Einschnürung stärker ausgeprägt als für eine Geometrie mit nur einem einfachen Knick. Die höchsten Geschwindigkeits-Werte sind innerhalb der Einengungen eines Eiskanals lokalisiert, die Maximalgeschwindigkeit $v_{\rm max}$ (definiert als Maximalwert des Geschwindigkeitsfeldes einer bestimmten einzelnen Computersimulation) liegt in der Größenordnung von mehreren $100\,\rm m\,s^{-1}$.

Die numerisch anspruchsvollste und komplexeste Eiskanal-Struktur, die in dieser Arbeit im 2-dimensionalen Fall untersucht wurde, ist eine Geometrie, welche eine Verzweigung und mehrere Einengungen und Knicke beinhaltet (in der Arbeit informell als ’Zick-Zack’ Schlot bezeichnet). Eine solche Struktur enthält Elemente, die in einem echten Eismantel durchaus vorkommen können, und die somit einem physikalischen Eisbruchkanal näherungsweise entsprechen könnte. Die höchsten Geschwindigkeiten in solchen ’Zick-Zack’ Schloten treten an den Ausstoß-Punkten auf, wo der Wasserdampf eruptiv an der Oberfläche austritt. Die Simulationen dieser Arbeit liefern an diesen

Extremstellen Werte von $100\,\mathrm{m\,s^{-1}}$ bis zu Spitzenwerte von mehr als $1000\,\mathrm{m\,s^{-1}}$, welche die Entweichgeschwindigkeit von Enceladus, $v_{\mathrm{esc}} = 239\,\mathrm{m\,s^{-1}}$, klar überschreiten. Diese Zahlenwerte für die Maximalgeschwindigkeit der Plume-Jets sind mit Resultaten aus der Literatur konsistent, die mit diversen, (auch im Vergleich zu dieser Arbeit) qualitativ unterschiedlichen Methoden ermittelt wurden.